UC-25
LBL-23879 c.1

Center for Advanced Materials

CAM REPORT

RECEIVED
LAWRENCE
BERKELEY LABORATORY

NOV 6 1987

LIBRARY AND
DOCUMENTS SECTION

Microstructural Observations of the Sn-Pb Solder/Cu System and Thermal Fatigue of the Solder Joint

D.R. Frear
(Ph.D. Thesis)

June 1987

For Reference

Not to be taken from this room

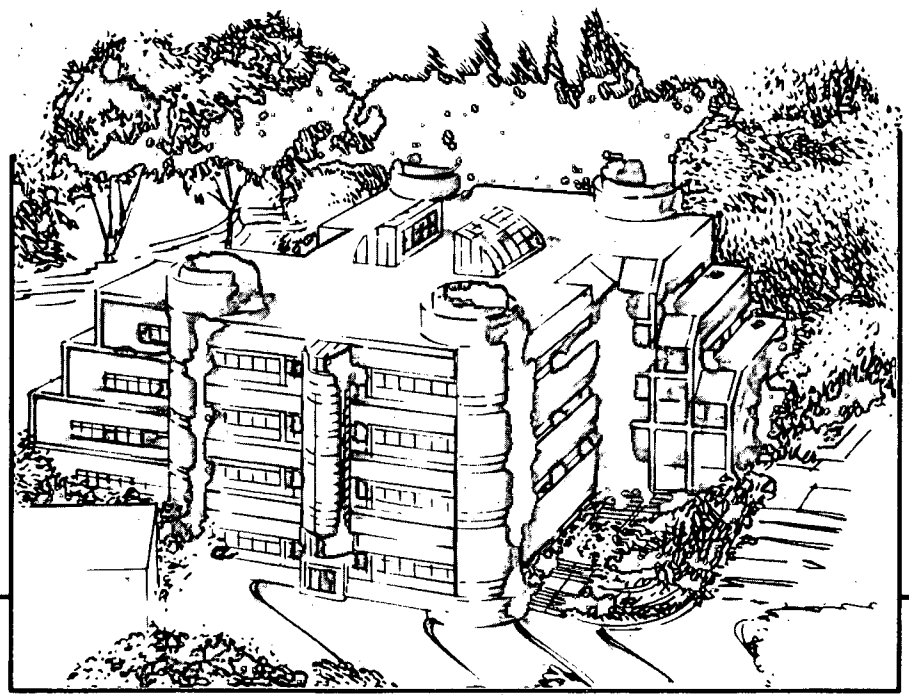

Materials and Chemical Sciences Division
Lawrence Berkeley Laboratory • University of California
ONE CYCLOTRON ROAD, BERKELEY, CA 94720 • (415) 486-4755

Prepared for the U.S. Department of Energy under Contract DE-AC03-76SF00098

LBL-23879 c.1

DISCLAIMER

This document was prepared as an account of work sponsored by the United States Government. While this document is believed to contain correct information, neither the United States Government nor any agency thereof, nor the Regents of the University of California, nor any of their employees, makes any warranty, express or implied, or assumes any legal responsibility for the accuracy, completeness, or usefulness of any information, apparatus, product, or process disclosed, or represents that its use would not infringe privately owned rights. Reference herein to any specific commercial product, process, or service by its trade name, trademark, manufacturer, or otherwise, does not necessarily constitute or imply its endorsement, recommendation, or favoring by the United States Government or any agency thereof, or the Regents of the University of California. The views and opinions of authors expressed herein do not necessarily state or reflect those of the United States Government or any agency thereof or the Regents of the University of California.

LBL - 23879

Microstructural Observations of the Sn-Pb Solder/Cu System and Thermal Fatigue of the Solder Joint.

Darrel Richard Frear
Ph.D. Thesis

Department of Materials Science and Mineral Engineering
University of California, Berkeley
and
Center for Advanced Materials
Materials and Chemical Sciences Division
Lawrence Berkeley Laboratory
University of California
Berkeley, California 94720

This work was supported by the Director, Office of Energy Research, Office of Basic Energy Sciences, Materials Sciences Division of the U. S. Department of Energy under contract # DE-AC03-76SF00098.

Microstructural Observations of the Sn-Pb Solder/Cu System and Thermal Fatigue of the Solder Joint.

Copyright © 1987

Darrel Richard Frear

Ph.D. Thesis

The United States Department of Energy has the right to use this thesis for any purpose whatsoever including the right to reproduce all or any part thereof.

MICROSTRUCTURAL OBSERVATIONS OF THE Sn-Pb SOLDER/CU SYSTEM AND THERMAL FATIGUE OF THE SOLDER JOINT.

Darrel Richard Frear

ABSTRACT

When an electronic package encounters thermal fluctuations, cyclical shear strain is imposed on the solder joint interconnections. The thermal cycling leads to a condition of thermal fatigue and eventual solder joint failure. This study was performed in order to understand the microstructural mechanisms that lead to solder joint failures in thermal fatigue.

The solders studied were 5Sn-95Pb and 60Sn-40Pb joined to Cu. The precipitation process of β-Sn in 5Sn-95Pb was fully characterized. On fast cooling from single phase α-Pb the Sn precipitates homogeneously. On slow cooling the precipitation process is cellular. Both precipitate structures overage and soften rapidly. The 60Sn-40Pb had a two phase microstructure. The Sn-rich phase was interconnected and polygranular. Both phases, and Sn grains, coarsened with time at 125°C. Coarsened 60Sn-40Pb microstructure was deleterious to the mechanical properties. The 5Sn-95Pb solder on Cu formed a single phase columnar interfacial intermetallic. The 60Sn-40Pb on Cu formed columnar Cu_3Sn adjacent to the Cu and rod-like Cu_6Sn_5 adjacent to the solder. Failures initiated and propagated through interfacial intermetallics only at extremely fast strain rates. Interfacial intermetallics had no influence on thermal fatigue properties. Cu_6Sn_5 η-phase whiskers formed at the intermetallic solder interface. The whiskers break off into the molten solder, the dislocation core dissolves, resulting in hexagonal tubes of Cu_6Sn_5 in the bulk solder.

Thermal cycling tests were performed on both 5Sn-95Pb and 60Sn-40Pb joints using a -55°C to 125°C cycle and 19% imposed shear strain. Failures in 5Sn-95Pb occurred at Pb

grain boundaries. Isothermal fatigue tests on 5Sn-95Pb give similar results when compared to thermal fatigue. A heterogeneously coarsened region of both Pb and Sn-rich phases develops within the 60Sn-40Pb solder joints. Cracks initiate and propagate through the heterogeneously coarsened region. Cracks initiate at the Sn-Sn grain boundaries due to their inability to accommodate the strain. Heterogeneous coarsening and failure occurs in high (35°C to 125°C) and low (-55°C to 35°C) thermal cycles. Isothermal fatigue cannot be compared to thermal fatigue results of 60Sn-40Pb on Cu because heterogeneous coarsening in isothermal fatigue occurs to a lesser extent than in thermal fatigue.

ACKNOWLEDGEMENTS

Although the research and writing of a Ph.D. thesis is an individual labor, it also requires the assistance, and patience, of a large number of people. This work was certainly no exception.

I would first like to thank my parents and my grandmother for their unceasing support and encouragement. Their faith in my ability to finish often exceeded my own.

Prof. J. W. Morris, Jr. was my advisor for this work and his guidance, support, and insight to the fundamentals of research were invaluable. I really can not see any way that this kind of work could have been performed outside of Bill's research group.

I would like to thank my co-workers, and fellow graduate students in the Morris research group, especially: Dan Dietderich, Lenora Quan, Mark McCormack, Dana Tribula, Judy Glazer, Pat Johnson, and Dr. Mike Strum for their discussions related to this work. I am grateful for the invaluable expertise and discussions of Dr. John Posthill in the High Resolution Microscopy studies. My special thanks go to Dr. Dennis Grivas whose discussions, insight, knowledge, and friendship helped make this to be an enjoyable project.

The High Voltage and High Resolution Electron Microscopy was performed at the National Center for Electron Microscopy at Lawrence Berkeley Laboratory. I appreciate the assistance of Dave Ackland in showing me the "ropes" on the Kratos HVEM.

The technical assistance and advice of John Holthius and James Wu in materials fabrication and experimental operation are of special note and were greatly appreciated. The assistance of Herb Riebe and Weylond Wong, in the machine shop, was also appreciated.

The patience to read this thesis and constructive criticisms of Prof. Ron Gronsky and Prof. H. Dharan were greatly appreciated.

This work was supported by the Director, Office of Basic Energy Sciences, U.S. Department of Energy under contract number DE-ACO3-76F0098.

TABLE OF CONTENTS

1.0 INTRODUCTION 1
FIGURES SECTION 1.0 5

2.0 BACKGROUND 8
2.0.1 Strains Induced in Solder Joints in Thermal Cycling 8
2.0.2 Solder Alloys 9
2.0.3 Temperature Fluctuations 10
2.1 Previous Metallurgical Observations of Thermal Fatigue Failures 11
2.1.1 Failure Through Interfacial Intermetallics 11
2.1.2 Failures Through Bulk Solder 12
2.1.3 Oxidation 13
2.1.4 Voids 13
2.1.5 No Effect of Microstructure 13
2.2 Fatigue Life Determination 14
FIGURES SECTION 2.0 15

2.1 PURPOSE 20

3.0 EXPERIMENTAL PROCEDURE 21
3.1 Joint Manufacture 21
3.2 Testing Procedure 22
3.3 Optical Polishing Techniques 23
3.4 Transmission Electron Microscopy 24
FIGURES SECTION 3.0 26

4.0 RESULTS 31

4.1 BULK SOLDER MICROSTRUCTURE 32
4.1.1 5Sn-95Pb Solder 32
4.1.1.1 Introduction 32
4.1.1.2 Experimental Procedure 32
4.1.1.3 Results 33
4.1.1.4 Discussion 36
4.1.1.5 Summary and Conclusions 38
FIGURES SECTION 4.1.1 40
4.1.2 60Sn-40Pb Solder 60
4.1.2.1 Introduction 60
4.1.2.2 Experimental Procedure 60
4.1.2.3 Results and Discussion 61
4.1.2.4 Summary and Conclusions 62
FIGURES SECTION 4.1.2.0 63

4.2 INTERFACIAL INTERMETALLIC MICROSTRUCTURE 71
4.2.1 Introduction 71
4.2.2 Background 71
4.2.3 Experimental Procedure 72
4.2.4 Results and Discussion 73
4.2.4.1 5Sn-95Pb on Cu 73
4.2.4.2 60Sn-40Pb on Cu 75
4.2.5 Conclusions 79
FIGURES SECTION 4.2.0 80

4.3 INTERMETALLIC WHISKERS IN 60Sn-40Pb JOINTS 100
4.3.1 Introduction 100
4.3.2 Experimental Procedure 100
4.3.3 Results and Discussion 100
4.3.4 Summary and Conclusions 104
FIGURES SECTION 4.3.0 106

4.4 MECHANICAL PROPERTIES OF SOLDER AND SOLDER JOINTS 123
4.4.1 Introduction 123
4.4.2 Specimen Design 123
4.4.3 Results and Discussion 125
4.4.3.1 Solder Joints in Shear 125
4.4.3.2 Bulk Solder 126
4.4.4 Summary and Conclusions 128
FIGURES SECTION 4..4.0 129

4.5 THERMAL FATIGUE 136
4.5.1 Introduction 136
4.5.2 Experimental Procedure 136
4.5.3 Results 138
4.5.3.1 5Sn-95Pb Joints 138
4.5.3.2 60Sn-40Pb Joints 139
4.5.3.2.1 -55°C to 125°C Thermal Cycle 139
4.5.3.2.2 High and Low Temperature Thermal Cycling 140
4.5.3.3 Thermal Cycling (-55°C to 125°C) of Bulk Solder 141
4.5.3.4 Thermal Cycling of Cu/Solder/Cu Joints (-55°C to 125°C) 142
4.5.4 Discussion 142
4.5.5 Summary and Conclusions 147
FIGURES SECTION 4.5.0 149

5.0 DISCUSSION SUMMARY 171

6.0 FUTURE WORK 175

7.0 SUMMARY AND CONCLUSIONS 178

8.0 REFERENCES 182

APPENDIX I ELECTRONIC PACKAGING 192
Figures Appendix I 196

APPENDIX II TRANSMISSION ELECTRON MICROSCOPY 201
Figures Appendix II 205

APPENDIX REFERENCES 209

1.0 INTRODUCTION

Soldering is one of the oldest and most widely used metallurgical joining techniques. The soldering process produces a coalescence of materials by heating them to a suitable temperature and joining the base materials with a filler metal. The filler metal must have a liquidus temperature below 450°C, and also below the solidus temperature of the base materials. The filler metal is the solder and it must wet and metallurgically bond the base materials. Joining processes that use a filler metal with a liquidus above 450°C are defined as brazing. The filler metal most commonly used in soldering is a Sn-Pb alloy.

The first evidence of soldering was found in Mesopotamia in 4000 BC in the form of hard soldered art objects. The ancient Egyption and Greek cultures used similar techniques as those developed in Mesopotamia. The common solders in these ancient times were Au-Cu, Ag, and Cu-Pb. The use of solder is first mentioned about 3000 years ago in the Bible (Isaiah 41:7). The first use of soft Sn-Pb solders is found in 800 BC. Strangely enough it was the Celts, not the classical cultures, that first developed low melting soldering techniques. The Celts were highly skilled in the art of tinning and the use of low melting Sn and Sn-Pb alloys. The Romans borrowed from the expertise of the Celts and used Pb solders for their aqueducts[1]. Soldering has found continued use through the ages as a joining method in plumbing, to an even more modern use as an electrical connector in the packaging of microelectronic devices. It is in this last area, the electronic packaging of microelectronic components (especially high speed digital computers) that the solder joint is extremely critical as it must act as an electrical, mechanical, and thermal conductor with the highest reliability possible.

The function of an electronic package is to interconnect integrated circuit chips and devices, distribute electric power to the system, and to provide a suitable environment for the devices. This description implies that the electronic package is incidental to the machine design. However, for high speed data processing units the electronic package is the limiting factor in cost, performance, and reliability. The importance of the package arises from the need for compactness in high speed data processing units. As the package size decreases more components can be fit into a smaller area resulting in very compact machines. Furthermore a compact package is necessary to accommodate the extremely fast switching speeds in modern integrated devices. As switching speeds drop to an order of a few nanoseconds the distance electronic signals travel becomes the limiting factor in

speed.* Therefore the following electronic packaging scheme has evolved to make the package more compact. (A more thorough description of electronic packaging and other problems associated therein is found in Appendix I.)

Figure 1.1 is an illustration of state of the art packaging of microelectronics. The hierarchy of the package can be divided up into three levels. Figure 1.2 is an illustration of the 1st and 2nd levels of the package in cross section.

• First level: The integrated circuit chip is permanently mounted in the chip carrier. Electrical connections can be made from the chip to the carrier by one of two methods: thermosonic wire bonding, or flip chip technology which is used extensively by IBM[2] and is shown schematically in Figure 1.2. In flip chip technology device pads on the chip are directly soldered to the carrier. A Pb-rich Sn-Pb solder is commonly used in the 1st level package.

• Second level: Chip carriers and other discrete components are soldered to a printed circuit board made of polyimide or fiberglass impregnated with epoxy. The chip carrier is a space transformer, it serves as a bridge between the small and closely spaced contact pads on the chip to the larger wiring network of the board. An important, and space saving technique is to use Surface Mount Technology (SMT) to directly solder the Leadless Chip Carriers (LCC's) to the circuit board, Figure 1.2. A near-eutectic Sn-Pb solder that has a low melting temperature is commonly used to bond the 2nd level package.

• Third level: Here the printed circuit boards are hard wired together in a chassis to form the machine.

The solder joint in the first and second levels of the electronic package are critical because the solder not only bonds the components mechanically but also passes electrical signals. The failure of a single solder joint could conceivably render a device or an entire machine inoperable. It is therefore critical to fully understand the metallurgy and physical nature of solder joints to insure reliability in electronic packaging.

A major requirement of the solder joints in an electronic package is that they absorb strains arising from thermal expansion mismatch of unlike materials within the package. For instance, the mismatch between a polyimide circuit board and a leadless ceramic chip carrier (or between a Si chip and the ceramic carrier) produces a shearing strain on the

---

* For a wire in an atmosphere with a dielectric constant of 1 (air) electrons travel at 30 cm/nanosecond. However, most electronic connections are associated with a fiberglass board that has a dielectric constant of 4 and then the electronic signals travel at 15 cm/nanosecond. In a package signals may have to travel further than 15 cm so the propagation delay becomes significant.

solder joints when the package encounters thermal fluctuations. This situation is shown schematically in Figure 1.3. The repetition of the shearing strain results in a condition of cyclical strain in the solder joint. This condition is referred to as thermal fatigue of the solder joint. The temperature fluctuations arise from both environmental and power cycling conditions. Environmental thermal fluctuations occur when the package is subjected to varying ambient temperatures. A testing standard for these fluctuations is -55°C to 125°C.[3] Thermal fluctuations from power cycling occur when a device is turned on and heats up the entire package, due to the internal Joule heating by the device, and cools down when the device is turned off. The temperature variation for power cycling ranges from 20°C to 150°C. In making the overall electronic package compact the actual size of chips and chip carriers has increased which exacerbates the amount of strain imposed upon the solder joints. The large fluctuating shear strains that occur in thermal cycling create cracks in the solder joints that have led to early catastrophic failures[4-6]. Therefore there is a significant need to better understand the thermal fatigue properties of solder joints used in electronic packaging.

The purpose of this study is to investigate the thermal fatigue characteristics of Sn-Pb solder joints and relate these results to the microstructural mechanisms that determine fatigue life. Before the thermal fatigue characteristics can be understood the microstructure of the Sn-Pb solder joint must be fully characterized, as well as some of the basic mechanical properties of the solder and solder joint. The two solders studied in this program were 5Sn-95Pb and 60Sn-40Pb. Both compositions are commonly used in the microelectronics industry. The solders were studied in a joint configuration soldered to Cu, which is also commonly used industrially as a base metal for Sn-Pb solders. The focus of the characterization studies was on the following areas of the solder joint: the bulk of the solder, the interfacial structure between the Cu and the solder, the isothermal mechanical behavior of the solder and the solder joints, and finally the microstructural development of solder joints that have undergone thermal fatigue.

Finally a note on the organization of the way this material is presented. This work is divided up into modular sections that discuss the various microstructural observations of the solder joint. Each section is written so that it can stand individually. The sections combined together present on overall picture of the microstructure of the solder joint from a fundamental point of view, and how the microstructure develops in thermal fatigue. Due to the fact that each section is modular an experimental procedure is presented in each section highlighting important procedures for pertinent observations. Therefore some procedures are repeated. Section 3.0 presents a summary of all experimental procedures

used in this work. In a similar manner section 5.0 combines and discusses all experimental observations in relation to thermal fatigue.

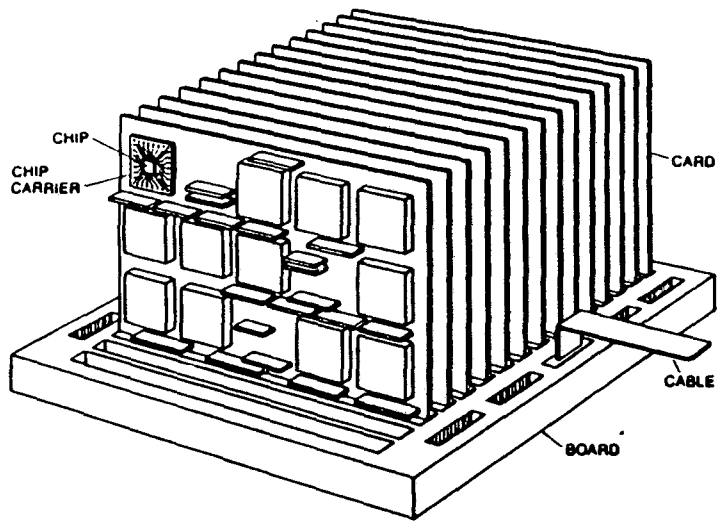

Electronic Packaging is a method of housing and interconnecting semiconductor chips. Traditionally packaging in large digital computers has had three levels. In the first level the semiconductor chip is bonded to the carrier by 95Pb-5Sn solder. In the second level the chip carrier is bonded to a card by 60Sn-40Pb solder. The third level has the cards joined together in a board. A schematic of the hierarchy is shown at the left.

Packaging thechnology today is the factor that limits cost, performance and reliability in high speed data processing units. This importance has led to the present fundamental investigation of solder.

XBL 862-466

Figure 1.1. Illustration of the three levels of an electronic package.

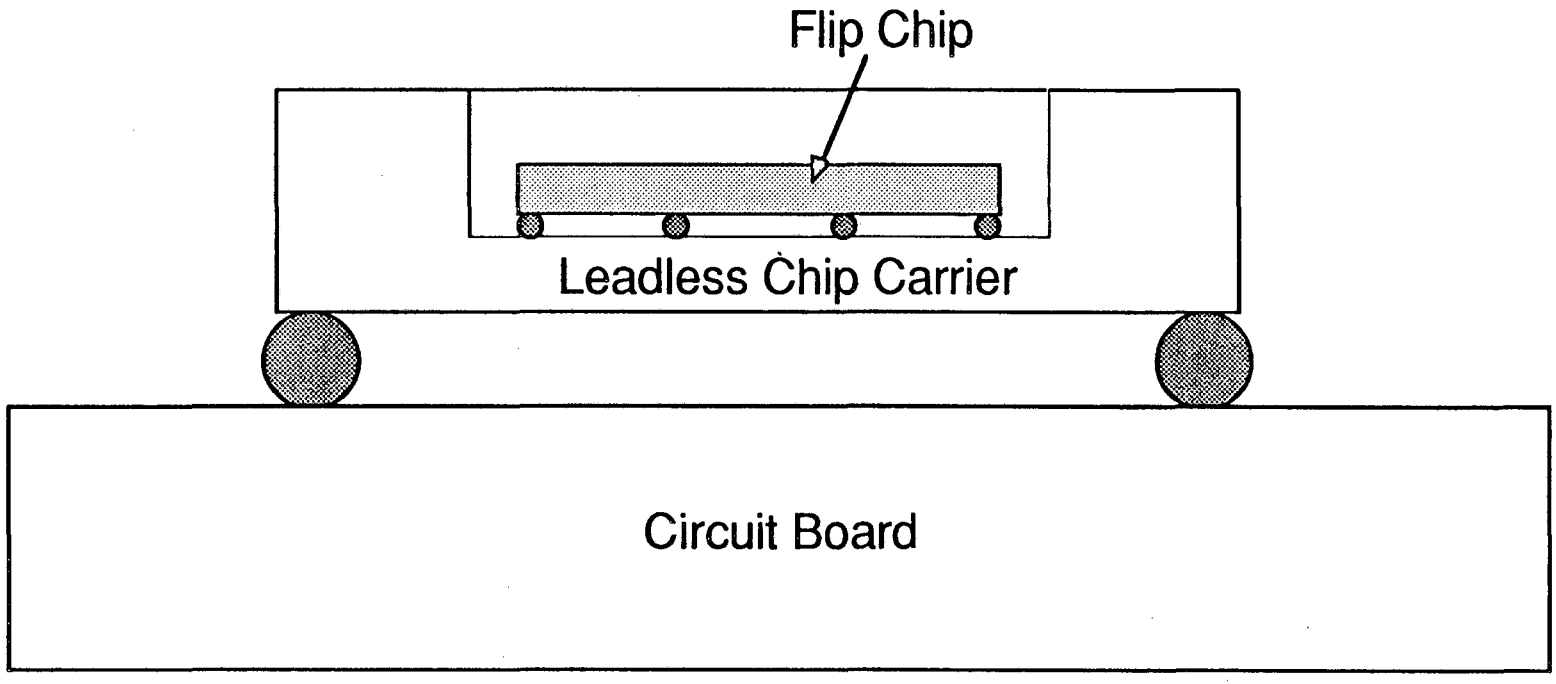

Figure 1.2 Cross section illustration of the first and second levels of an electronic package. Both Surface Mount (second level), and flip chip technology (first level), are shown.

Origin of Thermal Fatigue

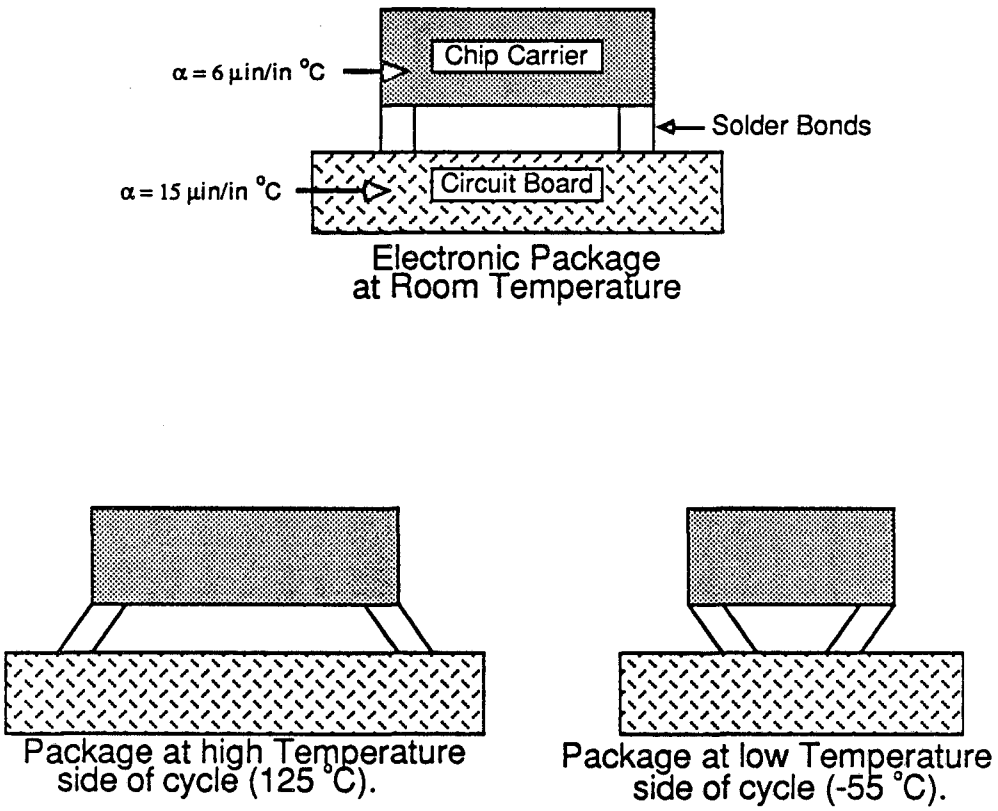

Figure 1.3 Schematic illustration of the origin of cyclical strain imposed upon solder joints when an electronic package encounters thermal fluctuations.

2.0 BACKGROUND

Catastrophic failures of solder joints in electronic packages have been observed after thermal cycling[4-15]. An SEM micrograph that shows a typical failure in solder joints after thermal cycling is shown in Figure 2.1. Previous investigations have attempted to characterize and interpret the failures of solder joints in thermal fatigue. A summary of these studies is presented in this section. Included in this section is a description of studies that investigate: a) the strains that a solder joint experiences in thermal fatigue, b) the alloys used to withstand the strains present in solder joints, c) sources of thermal fluctuations, and d) mechanisms and modes of failure of solder joints in thermal fatigue.

2.0.1 STRAINS INDUCED IN SOLDER JOINTS IN THERMAL CYCLING

As described in the Introduction (section 1.0) strains arise in solder joints due to the thermal expansion mismatch of unlike materials within the electronic package. Hall, Dudderrar, and Argyle[16] studied the three modes of deformation a joint experiences in a Leadless Chip Carrier (LCC) bonded to a Printed Wiring Board (PWB) in thermal cycling. These modes are illustrated in Figure 2.2.

- Mode A: In plane shear displacement which is characterized by a difference in the in-plane displacement between the LCC and the PWB.
- Mode B: Out of plane rotation due to the bending of the less stiff component, in this case the PWB.
- Mode C: Out of plane displacement (tension or compression). This can be caused by the "oil-canning" phenomenon[7] where localized heating creates non-uniform expansion or contraction, Figure 2.3.

Hall et. al.[16] quantitatively determined these strains by holographic interferometry and micro-strain gauges and found that the joints experience a complicated mixture of all three modes of deformation. Mode A (shear deformation) was found to be the most severe and therefore dominates the deformation process. Further work by Hall[17] found the solder joints to develop fully plastic flow when deformed in shear between an LCC and PWB during thermal cycling.

The shear strains a solder joint experiences in thermal cycling follow the equation:

$$\Delta\gamma = \frac{\Delta\alpha\ \Delta T\ l}{h}$$

where:

$\Delta\gamma$ = shear strain
ΔT = change in temperature in thermal cycling
l = distance form center of component to solder joint
h = thickness of solder joint.

The two plots in Figure 2.4 show percent shear strain as a function of joint thickness (h), component size (l), and two differential temperatures (ΔT). As an example the typical size of an LCC is 1 in. (2.54 cm) and l = 0.5 in. (1.27 cm) and a joint thickness of 0.005 in (0.127 mm) results in a 24% shear strain for the temperature range of -55°C to 125°C. This indicates that solder joints experience more than sufficient strain to be fully plastic in thermal fatigue.

Chen and Nelson[18] theoretically calculated the stresses present in soldered and adhesive joints due to differential expansion and contraction in a lap joint model. They found the shear stress in a joint displaced in shear is concentrated at the very end of the lap joint. The major assumption (unrealistic in the case of soft solders) is that the joint takes up all the stress elastically. Similar work by Weitsman[19] performed the same theoretical calculation for a viscoelastic adhesive lap joint and found the stress still concentrated at the edge of the specimen, but decreased in magnitude due to time dependant deformation (creep). Again Weitsman assumed the initial displacement of the joint was elastic in nature. No theoretical calculations are found in the literature for a fully plastic joint deformed in shear due to the complexity of the problem.

2.0.2 SOLDER ALLOYS

Two types of solders have been proposed for use as a joining material in an electronic package: hard solders (i.e. Au-Si eutectic), and soft solders (Sn-Pb). A comparison of mechanical properties of these solders is found elsewhere[20-22]. A synopsis of the comparison is that hard solders are not as susceptible to fatigue failures as are soft solders, but hard solders impose strain upon the components they join. The magnitude of the strain is large enough to cause failures in components joined by hard solder alloys[21]. However, for small strain applications Burgess et. al.[20] suggest that hard solders be used.

The large strains present in an electronic package suggests soft solder alloys are more applicable.

A variety of soft solder alloys are used industrially[23]. Sn-Pb solders find the majority of current use because of ready availability, and that these alloys have been used for a long period of time. Some Pb-In, Pb-Bi, and Pb-Ag alloys are finding some use[24-26] but not to the same extent as Sn-Pb.

Two types of Sn-Pb alloys are commonly used in electronic packaging. These compositions are shown in the Sn-Pb phase diagram in Figure 2.5. First is the Pb-rich solder (5Sn-95Pb), used in the first level of electronic packaging for the flip chip technology[2]. The Pb-rich solder has the highest melting point in the Sn-Pb system. The second type of solder used is the near-eutectic solder 60Sn-40Pb, commonly used in the second level of electronic packaging. Near-eutectic solders have a much lower melting point than Pb-rich solder and for this reason can be used as a reflow solder (a solder that is re-melted for joining purposes) in the second level without disturbing or melting the first level bonds.

A variety of ternary alloy additions have been made to Sn-Pb solders and are discussed by MacKay[25] and Thwaites[26]. For instance Sb is added in small amounts to resist the $\beta - \alpha$ transition in Sn (the so called "tin pest" phenomenon). Work is currently in progress to investigate the effect of ternary additions to the mechanical properties of Sn-Pb binary alloys[27,28]. Preliminary results of this work suggests that small additions of Sb, Mg, and Bi are beneficial to joint strength.

2.0.3 TEMPERATURE FLUCTUATIONS

The fluctuations that cause strains to be imposed on solder joints arise from two sources: external environmental fluctuations and power cycling. The environmental fluctuations are the special concern of the military where packages may encounter large temperature fluctuations in aerospace vehicles. For example a package on board a jet aircraft stationed in the desert encounters elevated temperatures on the ground and low temperatures in flight. A military standard (MIL-STD-883C)[3] uses the -55°C to 125°C thermal cycle to simulate environmental cycling.

Power cycling has a much wider area of concern. Power cycling occurs every time a device is turned on and off which can account for over 1000 cycles a year in consumer applications. Thermal fluctuations arise in power cycling because a device dissipates heat (by Joule heating) when in operation. Transient conditions of strain arise in power cycling[7] because, for example, the chip carrier heats up faster than the board imposing an initial strain on the 2nd level solder joints. The board then heats up and expands further

than the chip carrier imposing additional reversed shear strain. This transient condition is diagrammed in Figure 2.3. "Oil-canning", Figure 2.3, can arise from non-uniform dissipation of heat on the chip[7]. Englemaier[29] discusses environmental and power cycling and found that environmental cycling, though a problem, may not fully describe the condition of solder joints in thermal cycling. He states that power cycling exacerbates the fatigue of solder joints. Olsen and Berg[22] describe how solder joints fail in conditions of power cycling and describe the mechanical properties of solder under these conditions.

2.1 Previous Metallurgical Observations of Thermal Fatigue Failures

Observations have been made to determine the metallurgical causes of the failure of solder joints in thermal fatigue. The tests have been performed on both electronic packages and specimens designed to imitate the solder joints in electronic packages (these are described in section 4.4.1). Although most of the work was performed under similar conditions there is a great deal of confusion over the actual metallurgical reasons for failures. The following is a brief description of these observations organized with respect to proposed mechanisms of failure.

2.1.1 Failure Through Interfacial Intermetallics

A number of studies claim the failure of solder joints in thermal fatigue is through the interfacial intermetallics that form when Sn-Pb solder is joined to Cu, Ni, or Au based metals. Blum et. al.[30] studied the formation of intermetallics when Cu reacts with molten Sn. They found the interfacial Cu-Sn intermetallics to be very brittle and failures to occur intergranularly and transgranularly through the intermetallics.

Kang et. al.[9] thermally cycled Si power transistors soldered with 60Sn-40Pb and 5Sn-95Pb to a Ni base metal. For both solders the interfacial intermetallics were thought to create a structural inhomogeneity that altered the mechanical properties of the joint and lowered the fatigue life. However, the micrographs of the failed joints showed completely ductile fracture surfaces rather than the brittle cleavage associated with intermetallic fracture.

Keller[31] thermally cycled 60Sn-40Pb solder that joined Printed Wire Boards (PWBs) to hybrid integrated circuit packages. The thermal cycle in this study was between -40° and 130°C. Before and after cycling the terminals joined by the solder were pulled to failure at a 0.1 meter/minute strain rate, which is an extremely rapid deformation rate. Before cycling the joints failed through the bulk solder, but after thermal cycling the joints failed through the interfacial intermetallic.

Hall[32] aged Leadless Chip Carriers (LCCs) soldered to PWBs with 60Sn-40Pb solder and then performed torque tests on the joints before and after thermal cycling. He

found that after aging, and thus subsequent coarsening of the intermetallic layer, the joints failed in torque testing at lower strengths. Failures occurred through the Cu-Sn interfacial intermetallic layer. Similar results were found by both Stone et. al.[33] and Wright[34]. Wright used 60Sn-36Pb-4Ag solder and copper lap shear joints that were aged and isothermally fatigued to failure. Stone et. al. used ring and plug specimens joined with 60Sn-40Pb solder that were aged and fatigued at room temperature. Both Wright and Stone et. al. blamed the fatigue failures of the solder joints on the Cu-Sn interfacial intermetallics.

Dunlinger and Becker[35] claimed the thermal fatigue life of joints improved using a Pb-Cd-Zn solder that formed no interfacial intermetallics. Although little microstructural analysis was presented the increase in fatigue life was deemed to be due to the suppressed formation of interfacial intermetallics.

2.1.2 FAILURES THROUGH BULK SOLDER

Other work has suggested that failures do not occur through the intermetallic but rather through the bulk solder of the joint in thermal fatigue.

Levine and Ordenez[8] thermally cycled Controlled Collapse Ceramic Chips (C-4) joined with 5Sn-95Pb solder joints between the Si chips and alumina chip carriers. Deformation and cracking were found to occur randomly throughout the joint. Failures were explained as being due to Pb grain boundary sliding, particle-matrix cracking and cracking at grain triple points. Most failures were thought to be due to grain boundary sliding.

Rathore et. al.[36] tested 5Sn-95Pb solder in bulk using bending fatigue at 0.5% strain. They determined that fatigue in 5Sn-95Pb to have a three stage process: 1) formation of slip bands in Pb (independent of any Sn precipitates), 2) localized deformation at grain boundaries, 3) final crack propagation and failure. Interestingly, the same failure mechanism occurred for both high cycle (1800 cycles/min.) and low cycle (450 cycles/day) fatigue. When intermetallics were introduced to the bulk solder the brittle intermetallics provided initiation sites for fatigue cracks.

For near eutectic solders some investigators have traced thermal fatigue failures to coarsening of the solder microstructure. Bangs and Beal[37] thermally cycled Dual-in-Line Packages (DiPs) on PWBs between -65°C and 150°C using 63Sn-37Pb solder. They observed that the solder coarsened in regions of high strain in the joint. Failures were explained as being due to twinning and slip in the Pb rich phase with cracks propagating solely through the Pb. Wild[12] used a -62°C to 140°C thermal cycle on DiPs soldered with 63Sn-37Pb to polyimide circuit boards. In high stress low cycle fatigue Wild claims to have observed slip across multiple phase regions followed by recrystallization and growth

of the solder in the joint. Failures were found only through the soft Pb-rich phase[38]. Similar work was performed by Yenawine et. al.[14] using 60Sn-40Pb solder cycled from -50°C to 120°C with LCCs on PWBs. They found a large amount of phase coarsening followed by cracking through the Pb-rich phase. They postulate most of the damage occurs in the Pb on the cold portion of the thermal cycle. However, Lynch et. al.[39] cycled leaded chip carriers from -65°C to 150°C and found coarsening in 60Sn-40Pb but with only superficial cracking. When Lynch[10] cycled these same carriers from 20°C to 150°C he found extensive failures through the Pb-rich phase indicating that, contrary to previous work[14], damage occurs at the high temperature portion of the thermal cycle.

Dreyer et. al.[40] and Kinser et. al.[41] claim failures through near-eutectic solders are due to refinement of the microstructure, not coarsening. They claim the solder recrystallizes but does not go through grain growth. The refined microstructure then has a high yield strength resulting in fracture rather than plastic deformation and therefore a longer fatigue life.

2.1.3 OXIDATION

The oxidation of Pb has also been proposed as the primary cause of failures in the fatigue of solder[15,38,14]. Snowden[42] found oxygen attacks Pb grain boundaries in high purity polycrystalline Pb causing intercrystalline cracking and a decrease in fatigue life. Wild[38] and Ellis[15] also found that oxygen attacks Pb grain boundaries in both Pb-rich and near-eutectic Sn-Pb solders, acting to decrease fatigue life due to intergranular failures.

2.1.4 VOIDS

Some investigators found the presence of voids in the solder joint were deleterious to fatigue life. Blanks[43] found a large distribution of voids in 50Sn-50Pb solder greatly decreased fatigue life. Similar results for 60Sn-40Pb and 5Sn-95Pb soldering silicon power transistors to PWBs were found by Kang et. al.[9]. Here cracks were found to initiate at voids and thereby decrease the fatigue life.

Contrary to the above, Thwaites and McDowall[44] tested solder joints in the ring and plug configuration and state that the presence of voids has no effect on fatigue life. In this scenario the plastic deformation in fatigue causes the voids to disappear and therefore can not act as crack initiation sites.

2.1.5 NO EFFECT OF MICROSTRUCTURE

Solomon[45] performed low cycle isothermal fatigue on single lap shear joints using 60Sn-40Pb solder in isothermal fatigue. Solomon claims the Sn-Pb microstructure has <u>no</u> effect on the fatigue life of solder joints when frequency varied from high to low cycle fatigue.

2.2 FATIGUE LIFE DETERMINATION

Some predictive work on Sn-Pb solder joints in low cycle fatigue has been performed to determine the lifetime of the joints[22,29,45-48]. These formulations are purely empirical, joint microstructure is not accounted for. The basic formulation is the Coffin-Manson[46] equation:

$$N_f = K\left[\frac{1}{\Delta\varepsilon_p}\right]^n$$

The elastic term is ignored for the fatigue of solders as the strains of interest are all in the plastic range.

For the thermal fatigue of solder joints:

$$N_f = K_t\,\gamma_u(\dot{\gamma})\,\phi(T)\left[\frac{2t}{\Delta\alpha\,\Delta T}\right]^n$$

where:

$\gamma_u(\dot{\gamma})$ = Ultimate shear strain, as a function of testing rate

$\phi(T)$ = Empirical term that accounts for testing temperature

K_t = Constant, a function of testing conditions

t = Joint thickness

$\Delta\alpha$ = Difference in coefficients in thermal expansion

n = Empirical power term.

This formulation is purely empirical as evidenced by the constants in the equation. Using this equation it is impossible to determine fatigue life from first principles, tests must be run on each component to determine the constants. Furthermore no account is made for the microstructure of the joint, which will have direct influence on the properties of the joint. A much more efficient means by which solder joint fatigue life may be ascertained would be to understand the basic mechanisms of thermal fatigue and from this modify the microstructure to the desired lifetime. This points to a need to fundamentally understand the microstructure of Sn-Pb solder joints and how they are affected in thermal fatigue.

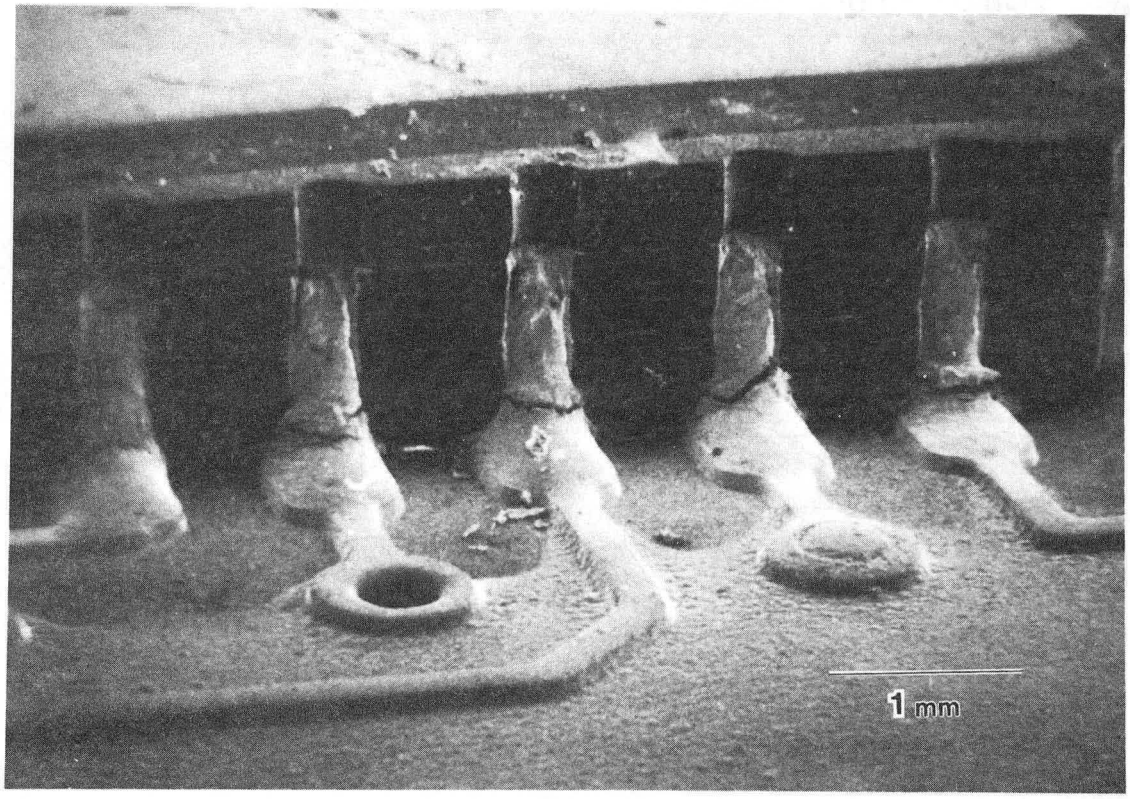

XBB 874-3225

Figure 2.1 SEM micrograph of failed solder joints of a leadless chip carrier after 700 cycles between -55°C and 125°C. Photo courtesy of M. Wolverton of Texas Instruments and is taken from reference 14.

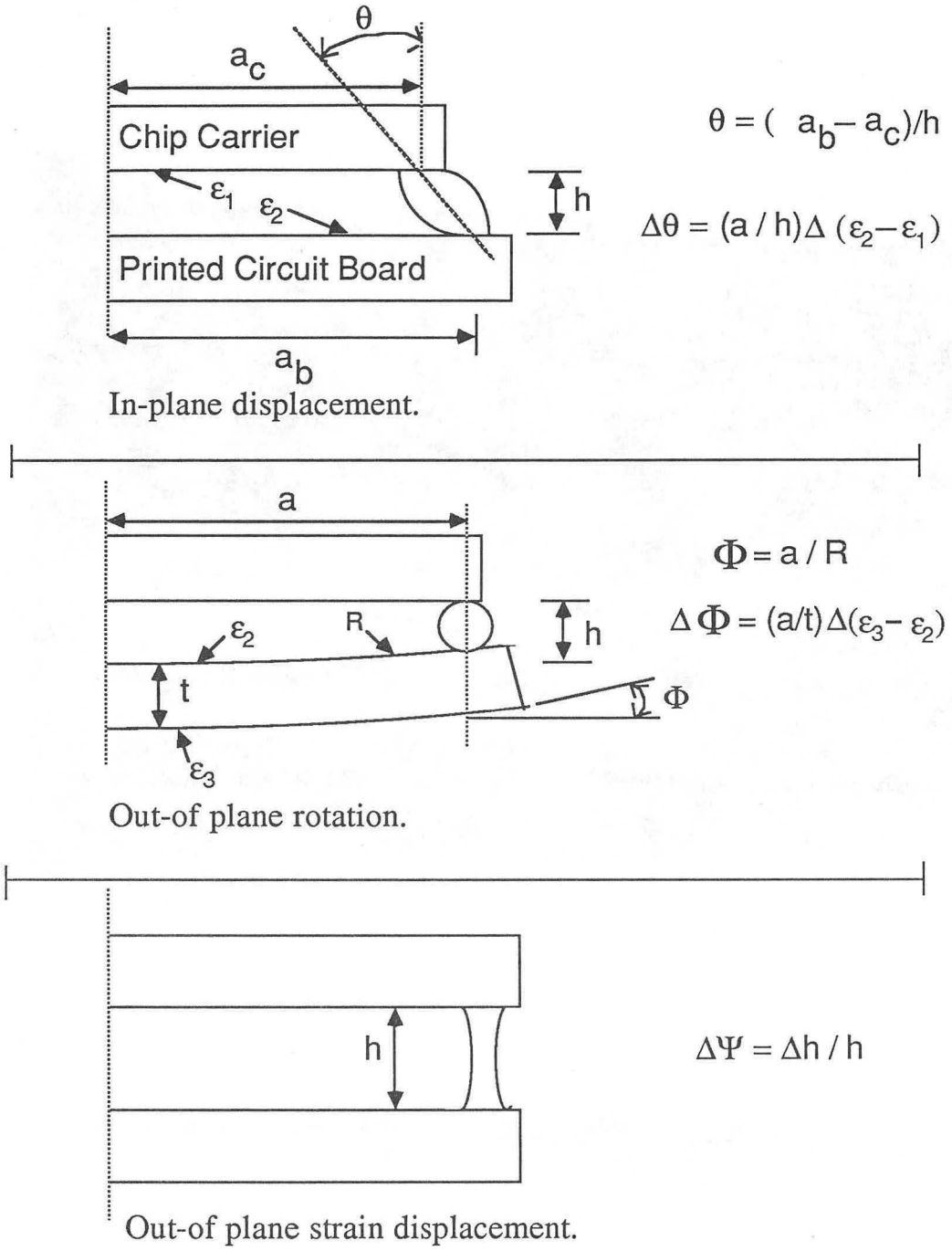

Figure 2.2 Three modes of deformation solder joints can experience in thermal fatigue.

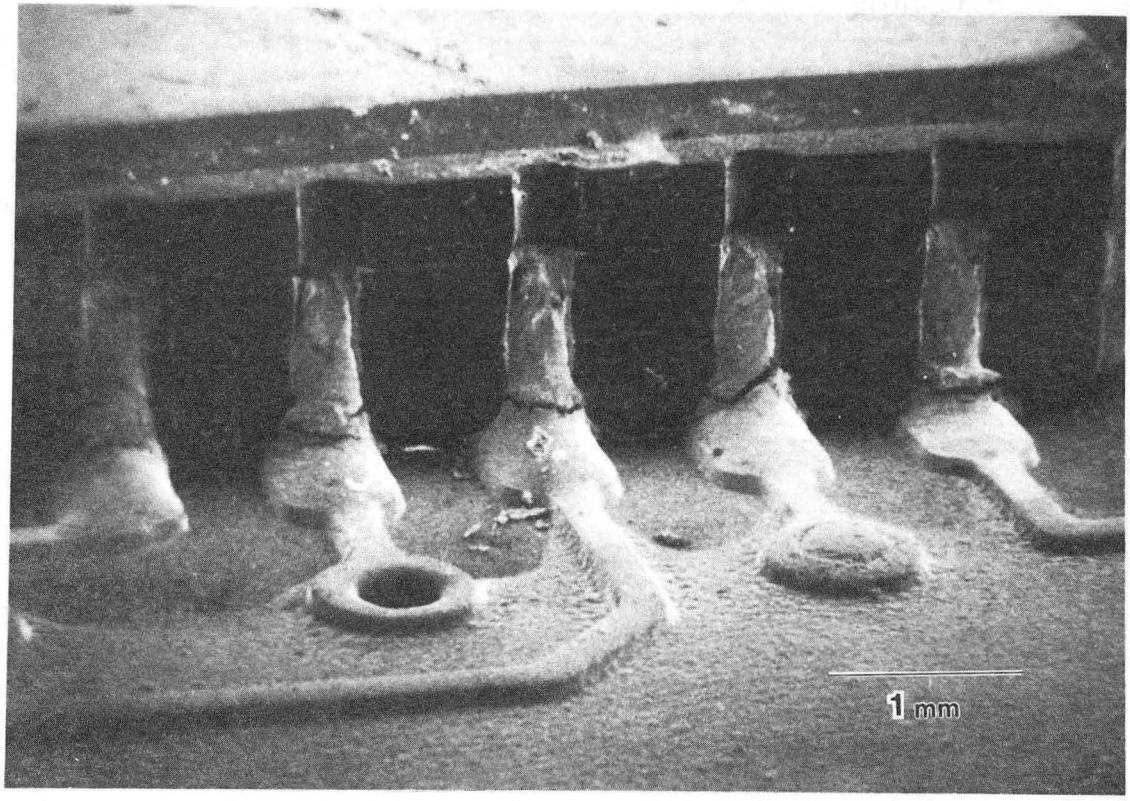

XBB 874-3225

Figure 2.1 SEM micrograph of failed solder joints of a leadless chip carrier after 700 cycles between -55°C and 125°C. Photo courtesy of M. Wolverton of Texas Instruments and is taken from reference 14.

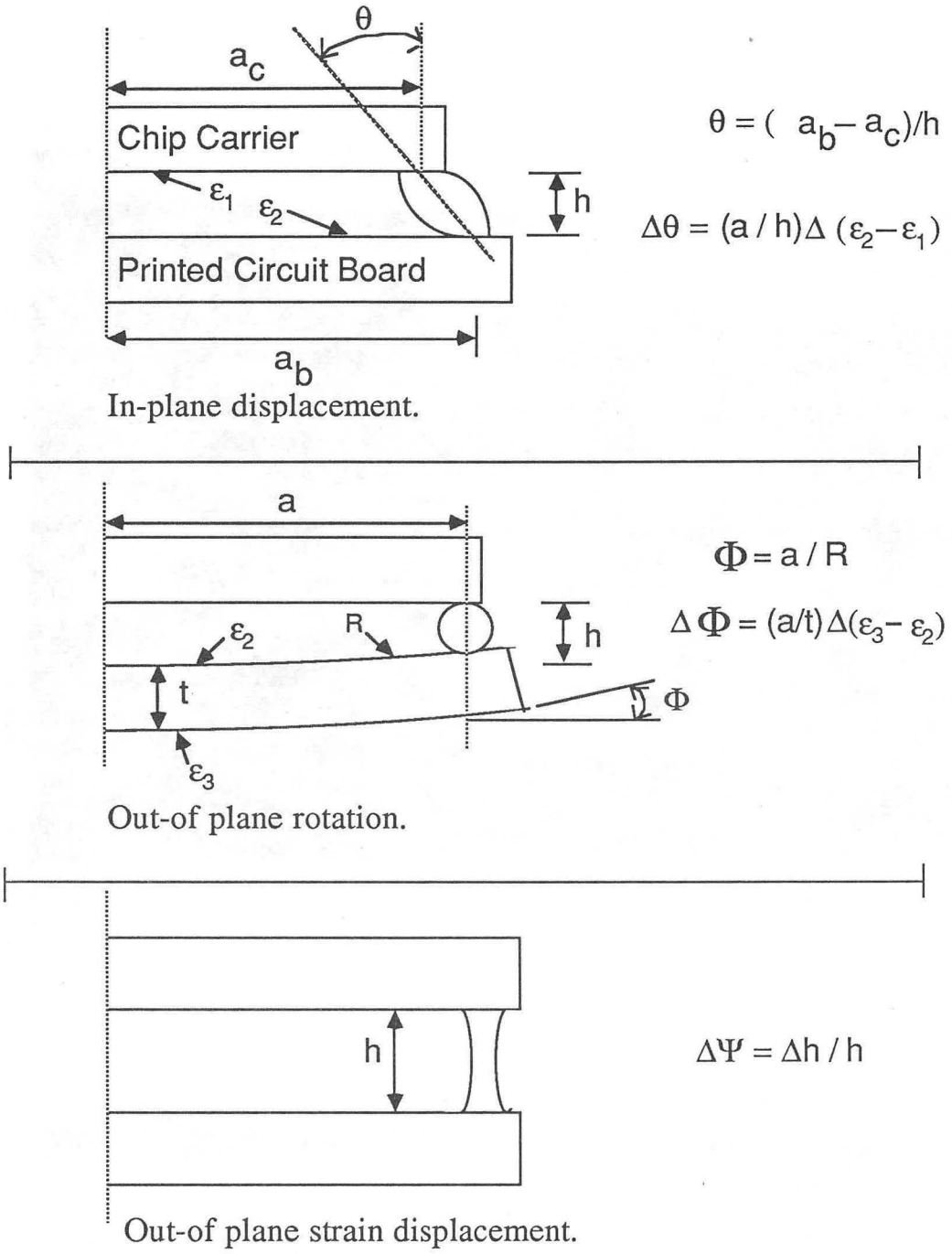

Figure 2.2 Three modes of deformation solder joints can experience in thermal fatigue.

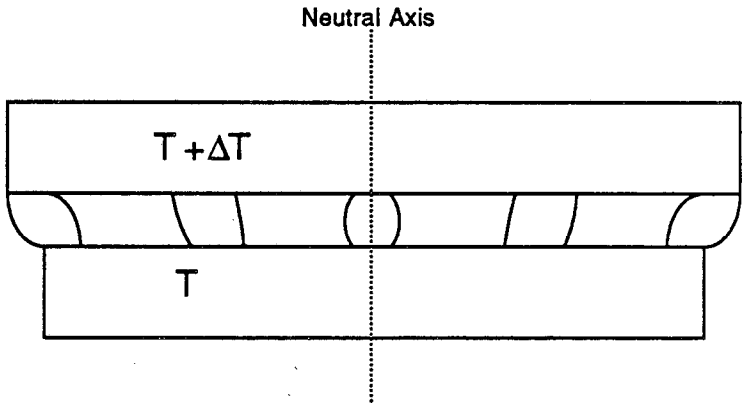

Shear strain in solder joints arising due to non-uniform heating. The upper component heats up and expands before the lower receives the heat.

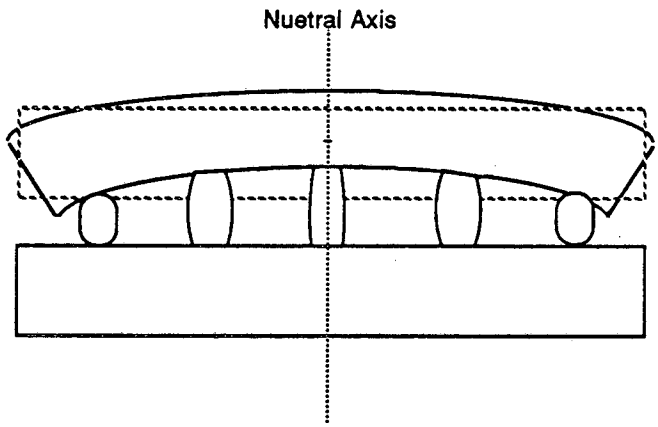

Local heating (hot spots) due to powered chips causes a temperature gradient across the chip carrier, resulting in "oil canning" of the substrate.

Figure 2.3 Illustration of non-uniform heating causing deformation in solder joints.

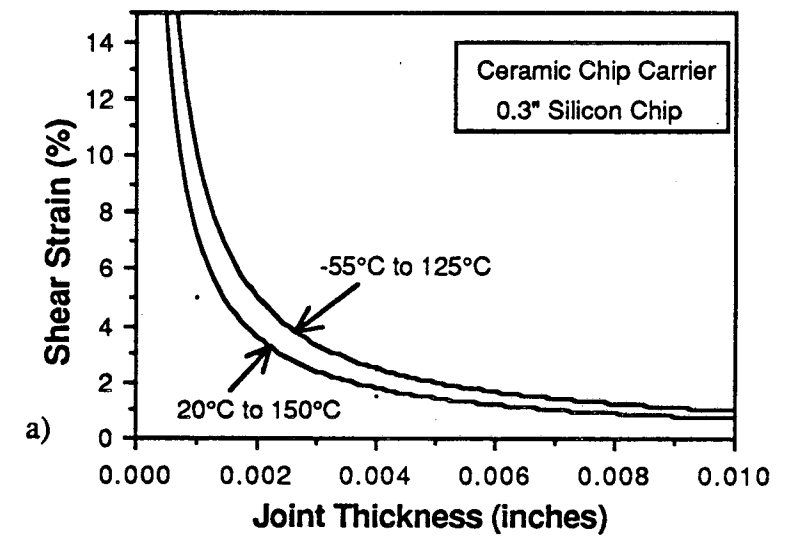

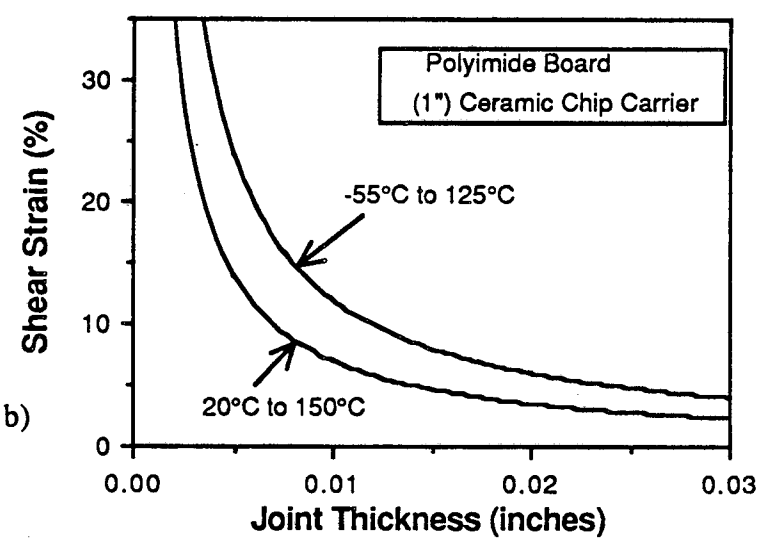

Figure 2.4 Shear strain imposed on a) first level and b) second level solder joints as a function of temperature cycle and solder joint thickness.

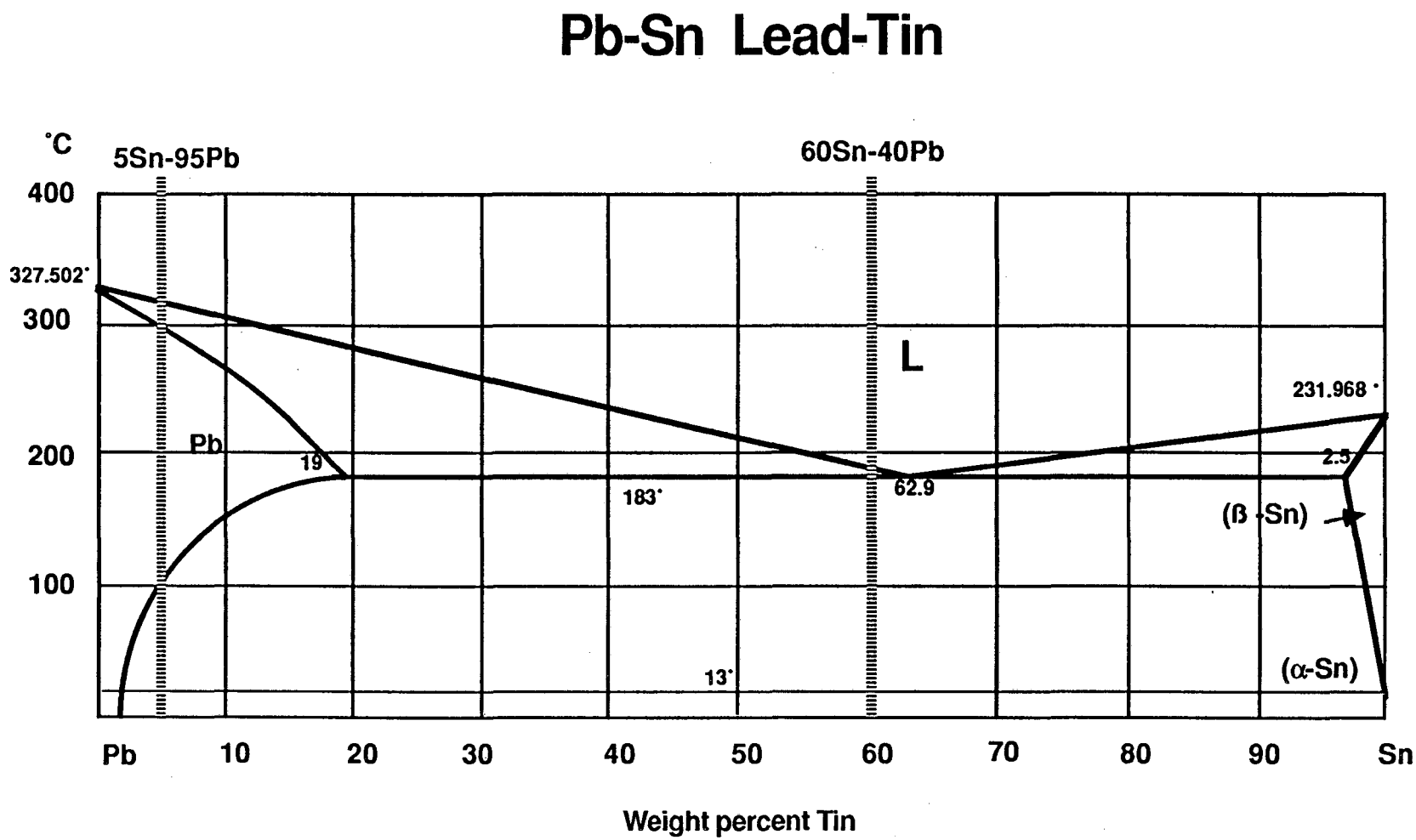

Figure 2.5 Sn-Pb phase diagram.

2.1 PURPOSE

The previous observations on Sn-Pb solder joints, as discussed in section 2.0, show that a clear understanding of how solder joint microstructure influences thermal fatigue behavior is lacking. Extremely varied, and often contradictory, conclusions on the causes of thermal fatigue failures were made in previous studies. These conclusions ranged from interfacial intermetallic failures, to failures in the bulk solder of the joint, to the microstructure having no influence on failure. From these varied positions it is impossible to state conclusively what the cause of thermal fatigue failure is, and furthermore, how to eliminate or delay failures.

Therefore the purpose of this study was to characterize all facets of the solder joint microstructure, from a fundamental perspective, and to relate the microstructure to the thermal fatigue behavior of the joint. The two solder compositions used in this study were 5Sn-95Pb and 60Sn-40Pb soldered to Cu. The compositions and base material are both commonly used in microelectronic packaging. The course of this study is to characterize: A) The microstructure of both solders in bulk, B) The intermetallic that forms when molten solder reacts with Cu, C) The mechanical properties of the solders and solder joints in shear , and finally D) Perform thermal fatigue on solder joints and relate fatigue behavior to the joint microstructure. From these observations it will be possible to recommend fundamental courses of action to alleviate thermal fatigue failures.

3.0 EXPERIMENTAL PROCEDURE

The manufacture, testing, and characterization of solder joints necessitates the design of innovative techniques to generate reliable and reproducible information. The study of solder has not reached the point where techniques are standardized, which explains some of the variances in results between investigators. Therefore the following experimental procedures were developed for this study so as to make this work internally consistent and reproducible.

The solders used in this study were made using 99.9% pure Sn and 99.9% pure Pb. The elemental forms of Pb and Sn were melted into ingots under vacuum for both 60 wt.% Sn - 40 wt.% Pb and 5 wt.% Sn - 95 wt.% Pb. Zone refining was performed three times on each ingot so as to further purify the solder. This involved melting the solder, cooling the molten ingot from the bottom thus segregating the impurities to the top of the ingot. The top of the ingot was then removed and the remaining ingot refined again.

3.1 JOINT MANUFACTURE

To manufacture soldered joints a special specimen assembly and vacuum furnace were designed and built. The specimen assembly consisted of three oxygen free copper (OFC) plates (of dimensions shown in Figure 3.1) that were polished to a 6 μm finish using diamond paste. The plates were then etched for 30 seconds in a 50% H_2O + 50% N_2O_3 solution. The plates were then dried and coated with a thin film of Johnsons Stainless Steel Flux (which consisted of a dilute solution of zinc chloride and hydrochloric acid). The three plates were then bolted together using stainless steel spacers inserted on the edge of the long side of the assembly to form a gap for the solder joint. The assembly and purified solder were then placed in the vacuum furnace shown in Figure 3.2. The furnace has two heating coils. The upper heating coil preheats the assembly and the lower stage heats the graphite crucible containing the solder. Both furnaces were heated simultaneously to a temperature 50°C above the melting point of the solder composition used. Heating was performed under vacuum so as to evaporate the flux off the copper plates, after the surface copper oxide is removed by the flux. Therefore after heating an oxide free surface is created on the copper. When the desired temperature is reached the chamber was backfilled with pure argon gas and the assembly was slowly lowered into the molten solder. The solder is pulled up the gaps between the plates by capillary action. The lower stage furnace was then replaced by an ice water bath to cool the solder and assembly. Cooling time from molten temperature to room temperature averaged 4 minutes. After cooling the excess solder was then machined from the assembly and the edges of the assembly containing the

spacer removed. The specimens described below were then cut from the assembly using a slow speed diamond saw. An average of 8-10 specimens were cut from each assembly. The advantages of this manufacturing technique are: a) the Cu surfaces are oxide free (no wetting problems), b) voids do not form in the joint, and the problems of flux entrapment are eliminated by having the molten solder flow up through the joint, c) and reproducibility is enhanced so comparisons between specimens from the same assembly are possible.

Before testing, the solder joints were aged at room temperature for approximately 1 month to result in an equilibrium microstructure.

3.2 TESTING PROCEDURE

To perform mechanical tests on solder joints in shear the specimen shown in Figure 3.3 was designed. Three holes were machined in the specimen, after cutting the blank from the assembly, to isolate the two solder joints in the center of the specimen. Friction grips were placed on the top and bottom of the specimen. The two solder joints between the holes experience simple shear by loading along the long axis.

The specimen used to test solder joints in thermal fatigue is shown in Figure 3.4. The specimen consists of an aluminum plate (α = 25 μin/in °C) sandwiched between two copper plates (α = 16.6 μin/in °C). The aluminum plate was plated with 0.05 mm (0.002 in.) of Ni to act as a diffusion barrier, and a 0.025 mm (0.001 in.) of Cu to give the solder joint a similar interface on each side. On cycling between different temperatures the solder joints between the Cu and Al plates undergo simple shear deformation. Both Mo ($\alpha = 6 \times 10^{-6}$ in/in°C) and Zn ($\alpha = 25 \times 10^{-6}$ in/in°C) were attempted as souces of thermal strain in the specimen assembly. It was difficult to both cut the Mo and coat it with Cu. The Zn electroplated with Cu well but it did not expand uniformly in thermal cycling. Therefore neither Zn or Mo could be used. The thermal fatigue specimens were manufactured in the same manner as described previously. The shear strain imposed on the specimen follows the relation:

$$\Delta\gamma = \frac{\Delta\alpha \, \Delta T \, a}{h}$$

where:

a = one half the specimen length

h = joint thickness

$\Delta\alpha$ = difference in coefficient in thermal expansion between the two plates

ΔT = difference in temperature in cycling.

Therefore the strain varies from zero at the center of the specimen to a maximum at the ends. The holes drilled in the specimen eliminates the back stress of the solder at the ends caused by the less strained portion of the joint.

To perform thermal cycling the apparatus diagramed in Figure 3.5 was designed and built. The apparatus consists of a crane, controlled by a digital chronometer, that cycles the specimens in the basket between the thermal baths. The high temperature bath was made by resistively heating oil using a temperature controller accurate to ± 2°C. The low temperature bath used ethyl alcohol (200 proof) cooled by a steady flow of liquid nitrogen through a copper tube in the liquid bath. This bath was accurate to ± 5°C. The hold time in each bath was 5 minutes with a transfer time of 30 seconds.

Mechanical tests on solder and solder joints were performed on a screw driven loadframe and on a digitally controlled loadframe. The friction grips used for these tests were made of 316 stainless steel and are shown in Figure 3.6. Tests on bulk solder were performed in tension using the specimen shown in Figure 3.7, using the friction grips and a screw driven loadframe. These specimens were machined from bulk solder castings.

3.3 Optical Polishing Techniques

Special polishing techniques were developed to reveal the microstructure of the solders and solder joints. Special care was taken to polish Sn-Pb solder as the material is very soft and polishing artifacts are easily induced.

Samples were mounted in Koldmount, a low temperature mounting material. The exothermic heat generated in the hardening of Koldmount is low so the microstructure does not change in the solder specimens during the mounting process. Both bulk solder and solder joint specimens were cut on a slow speed diamond saw to minimize excess deformation.

Bulk samples of 5Sn-95Pb were successively ground down to 600 grit silicon carbide paper under a water flood. Samples must be polished using very little pressure. The samples were then polished, by hand, on a piece felt using 1 μm aluminum oxide paste lubricated with kerosene. When polished the surface of the sample appears black, after approximately 1 minute of polishing. The samples were then polished using 0.05 μm aluminum oxide and kerosene, then etched using 5 parts NH_4OH + 5 parts H_2O + 2 parts H_2O_2 (30%) for 10 seconds. A final etch of 20% H_2O_2 + 80% acetic acid glacial selectively removes the Pb-rich phase thus revealing the β-Sn precipitates. For detailed observations of the intermetallic interface of 5Sn-95Pb Cu joints a small amount of the solder was etched away, before polishing, using 30% H_2O_2 + 70% Glacial Acetic acid. The region that contained solder was filled with epoxy and polished. This procedure leaves

the brittle interfacial intermetallic layer intact for observation. To observe the 5Sn-95Pb joint microstructure the samples were polished on 600 grit silicon carbide paper parallel to the joint (else removed Cu and Al become imbedded in the soft solder). The sample was then polished using 0.05 μm Al_2O_3 and kerosene on felt paper, again parallel to the joint. Etching was performed using 20 ml H_2O + 5 ml HNO_3 + 3.5 ml glacial acetic acid for 5 seconds followed by 20 seconds etching in 3 parts glacial acetic acid + 1 part H_2O_2 (30%). This revealed the microstructure of the solder region. The microstructure of the 5Sn-95Pb was very uneven after etching so observations were made in the SEM.

For bulk 60Sn-40Pb solder and 60Sn-40Pb solder joints the same procedure as described above was used, up till the 0.05 μm polishing step. After polishing with the 1 μm aluminum oxide/kerosene mixture the samples were polished on a very slow speed wheel in a slurry of 0.3 μm alumina oxide + 50% H_2O + 50% Mastermet Polishing Solution from Buehler*. The time to polish was between 3 and 15 minutes. Special care must be taken when polishing the thermal fatigue specimens because the aluminum in the sample pits when etched. To prevent the pitting from affecting the joint etching must occur for only a short period of time (approximately 5 minutes). Micrographs were taken using the Nikon Epiphot-TME Inverted optical microscope. Scanning Electron Microscopy (SEM) was performed on the ISI DS-130 Scanning Electron Microscope. Chemical composition measurements were made using the AMR 1000 SEM with Energy Dispersive x-ray analysis capabilities. To reveal additional contrast in the SEM polished 60Sn-40Pb samples were over-etched using 5 parts NH_4OH + 5 parts H_2O + 2 parts H_2O_2 (30%).

3.4 Transmission Electron Microscopy

• Bulk 5Sn-95Pb

After solidification in bulk ingot form the solder was aged at 200°C for 24 hours to homogeneously distribute the Sn in the Pb. The ingot was then quenched and aged at room temperature for 1 month, to allow precipitation to occur. TEM 3 mm foils were cut and mechanically thinned down to 5 mil thickness. Electropolishing to perforation was performed using: 85% Ethyl alcohol (200 proof) + 5% 2-Butoxyethynol + 10% Perchloric acid. Immediately before polishing both sides of the foil were lightly ground using 600 grit silicon carbide paper to remove oxide. Tweezers were then used to lightly scratch both sides of the foil in the center to make the foil polish preferentially in the middle. Polishing was performed at 30-34 volts set at 80 mA of current. Electropolishing was followed by

* The Mastermet solution consists of 0.03 μm Si carbide particles in a slightly acidic solution. This solution simultaneously polishes the sample and etches the Pb-rich phase resulting in an excellent contrast.

35 minutes of cold stage ion milling at 5 KeV at 0.25 mA per gun. This technique results in an almost mirrorlike polish with fairly large thin regions. The foils of 5Sn-95Pb oxidize very rapidly. In fact they oxidize in the high vacuum of the microscope. Therefore after ion milling an absolute minimum of time can be spent in transferring the foil from the ion mill to the microscope.

Standard imaging and diffraction analysis was performed using the Kratos 1.5 MeV High Voltage Electron Microscope (HVEM) at the National Center for Electron Microscopy at Berkeley. A double tilt specimen holder was used in all TEM experiments. A 1.5 MeV accelerating voltage allowed greater penetration depth and large thin areas in the foil were obtainable. High Resolution Electron Microscopy (HREM) was performed using the JEOL 2000CX TEM operated at 200 KeV. The lower accelerating voltage allowed only precipitates near the edge of the foil to be analyzed.

• Bulk 60Sn-40Pb

Foil preparation for bulk 60Sn-40Pb was identical to that for 5Sn-95Pb save two differences. Cold stage ion milling was performed at 5 KeV and 0.2 mA per gun for only 10 minutes. Additionally the oxidation problem is not severe for 60Sn-40Pb. Samples from bulk 60Sn-40Pb solder were taken from the as solidified alloy aged for one month.

• 60Sn-40Pb Joints

Due to electrochemical differences between copper and solder electropolishing is not possible for solder joints. Therefore a mechanical dimpling to perforation technique was employed. Dimpling was performed on a South Bay Technology Model 1500 dimpler using 6 μm and 1 μm diamond paste, successively. Dimpling was followed by cold stage ion milling at 5 KeV and 0.3 mA per gun for 45 minutes. Samples were viewed at 1.5 MeV in TEM.

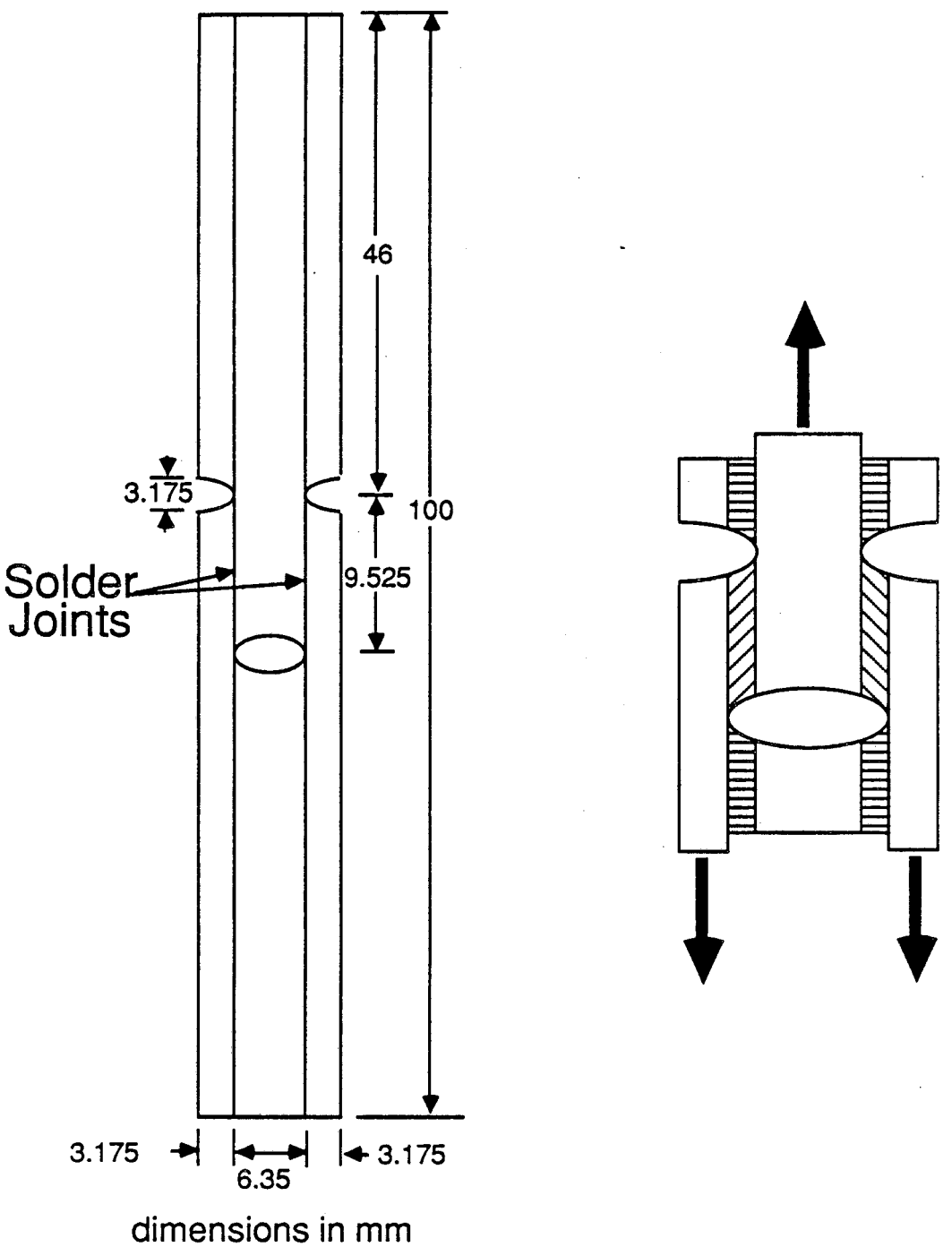

Figure 3.3 Double lap shear specimen used to test solder joints isothermally in a shear configuration. The solder joints between the holes experience shear when the specimen is gripped at the top and bottom and deformed.

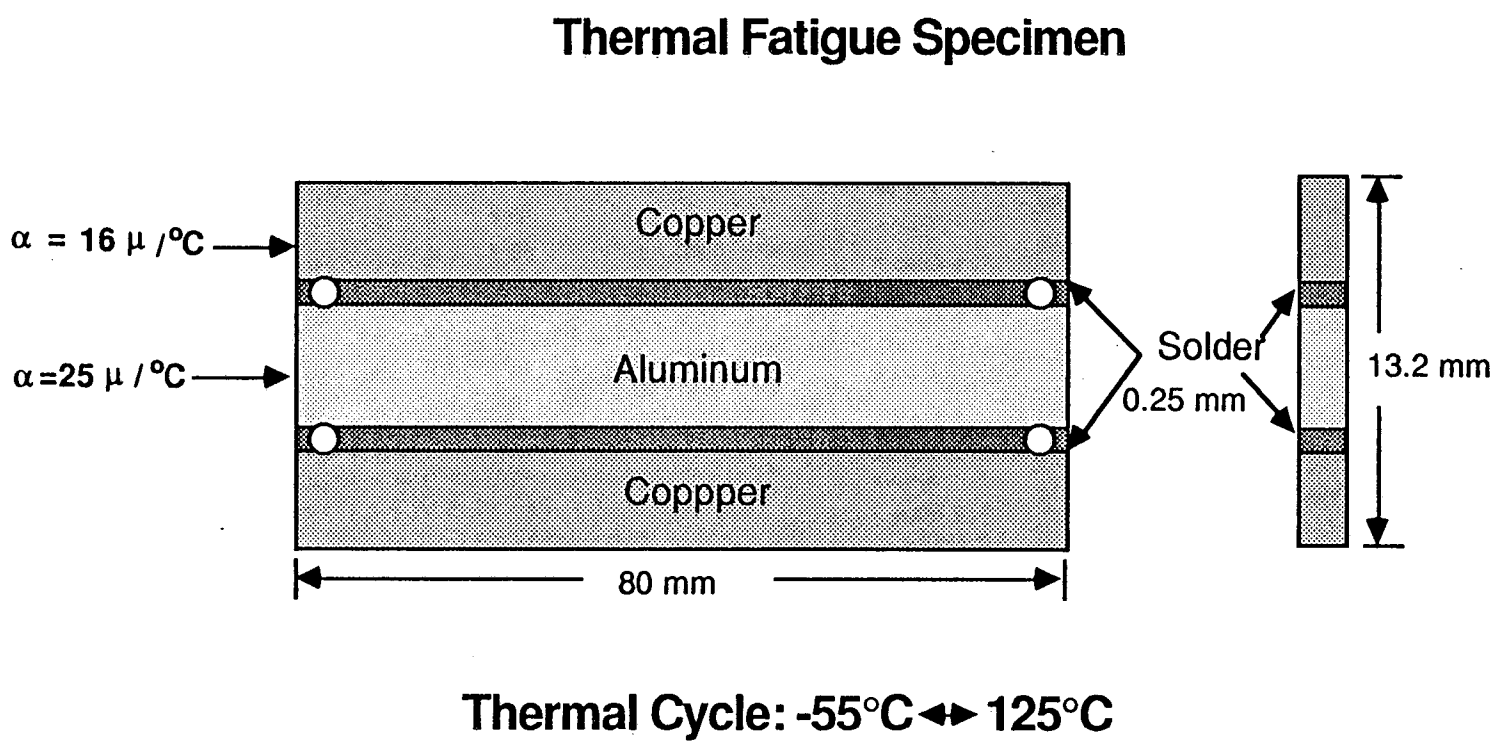

Figure 3.4 Specimen used to test solder joints in thermal fatigue conditions.

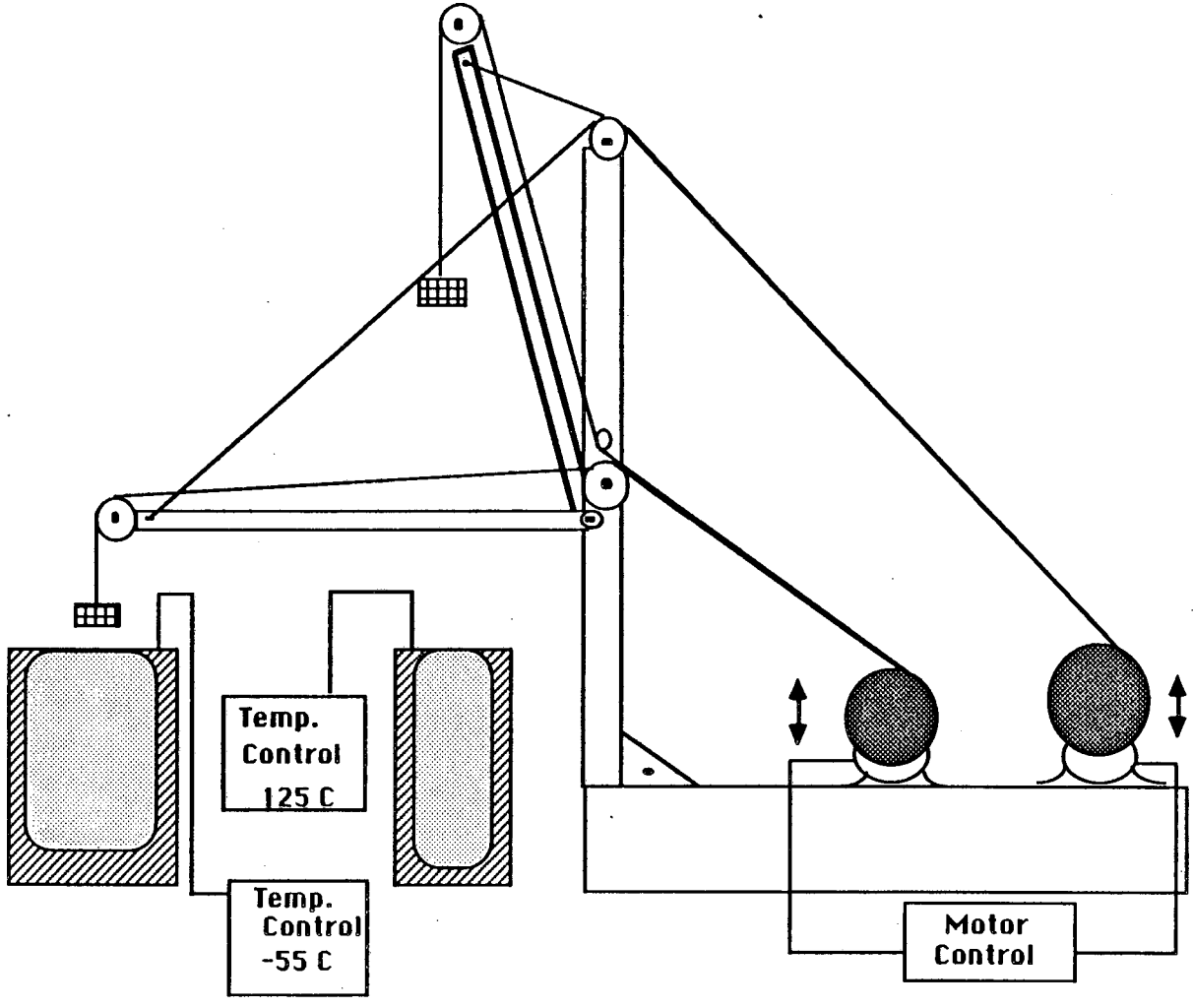

Figure 3.5 Digitally controlled crane used to cycle specimens between thermal baths.

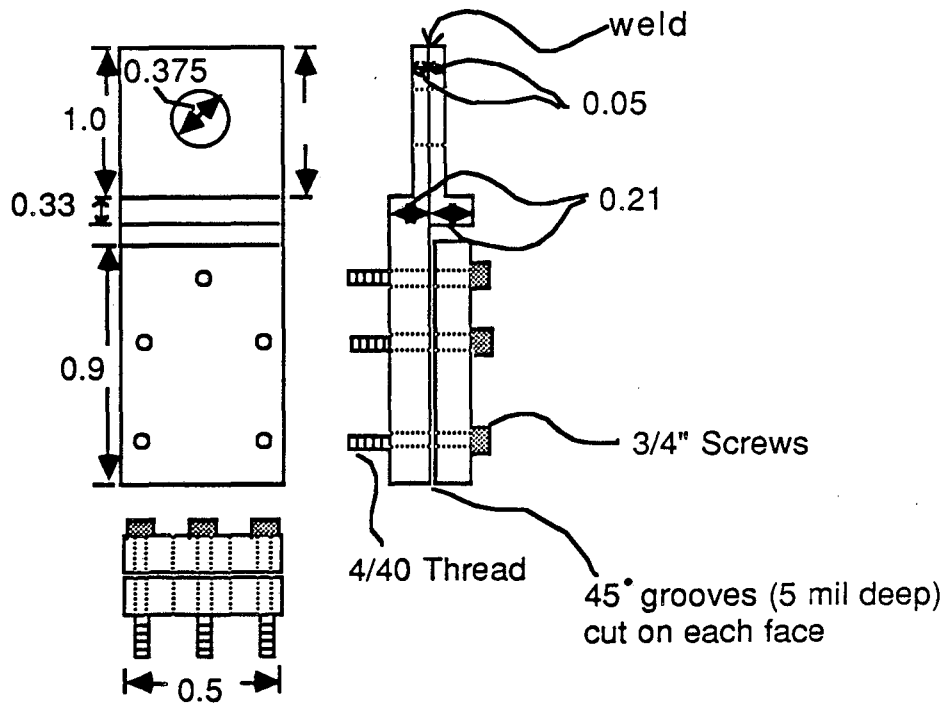

Figure 3.6 Friction grips used to test specimens in isothermal conditions.

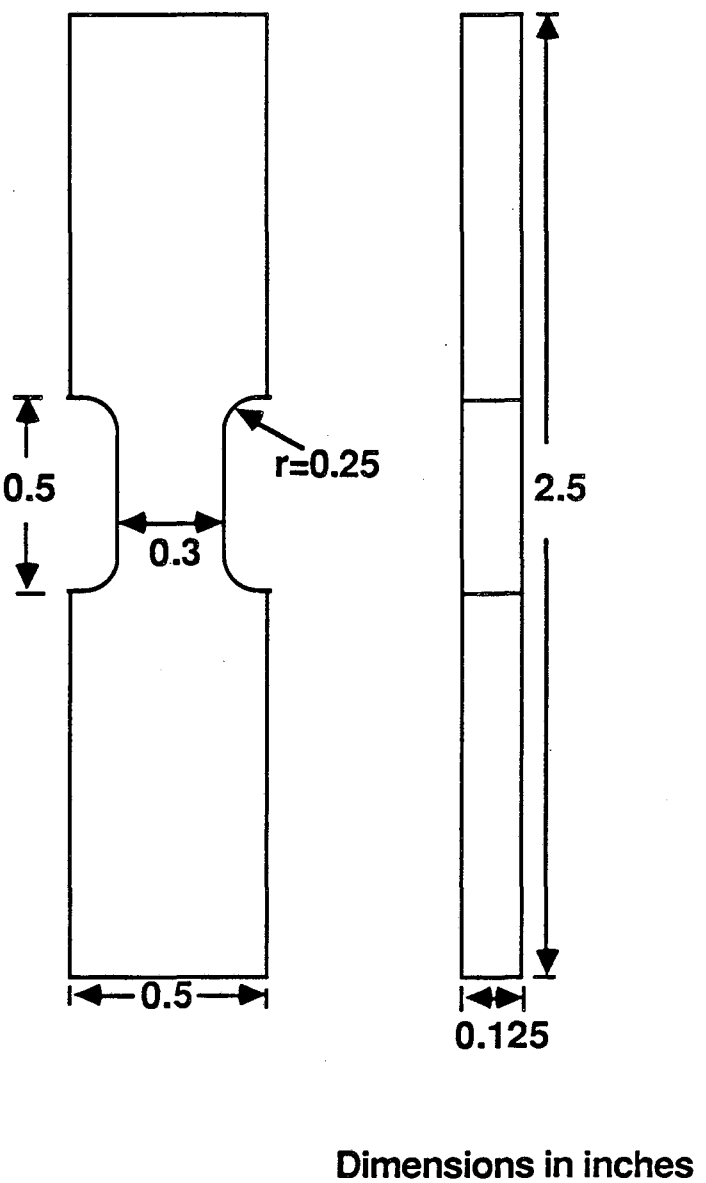

Figure 3.7 Specimen used to perform mechanical tests on bulk solder. The specimen is machined from bulk solder castings.

4.0 RESULTS

The following sections discuss microstructural observations made on 60Sn-40Pb and 5Sn-95Pb solders joined to copper. A possible cause of the variation in observations in previous studies is the processing of joints was not consistent between investigators. To rectify this problem samples in this study were designed to be reproducible, and consistent between tests.

The topics discussed in this section are: Microstructural observations of bulk 5Sn-95Pb and 60Sn-40Pb solders (section 4.1), Solder joint interfacial microstructure (4.2), Intermetallic whisker growth in the 60Sn-40Pb/Cu system (4.3), Solder joint mechanical properties (4.4), and Thermal fatigue of solder joints (4.5).

4.1 BULK SOLDER MICROSTRUCTURE

4.1.1 5SN-95PB SOLDER

4.1.1.1 INTRODUCTION

Solders of Pb-rich compositions, such as 5Sn-95Pb, have found common use as a joining material for relatively high temperature use (< 300°C). A very common application for 5Sn-95Pb is in automotive radiators. A more demanding use for 5Sn-95Pb is in the first level of an electronic package using "flip chip technology". This technology is used, and was developed, by IBM[2] and involves inverting the integrated circuit chip and joining it to a chip carrier package using 5Sn-95Pb solder. In this manner the solder acts as an electrical and mechanical contact in the first level of the electronic package.

The fact that 5Sn-95Pb has a high melting temperature is the main reason it was chosen as the first level solder. Packaging is a two stage soldering process, first the chip is soldered to the package, and secondly the package is joined to the board. The first level joints should not melt during the second level soldering. Therefore a high melting temperature is desired for the first level solder bonds. A secondary reason 5Sn-95Pb is used is that some claims have been made that suggest 5Sn-95Pb is resistant to thermal fatigue. These claims are in dispute and will be discussed in section 4.5.

If 5Sn-95Pb is to be used in conditions of thermal fatigue in electronic packaging it is necessary to understand the solder microstructure. Also the 5Sn-95Pb alloy approximates the composition of the Pb-rich phase in 60Sn-40Pb solder, as shown in the phase diagram shown in Figure 2.5. On cooling 60Sn-40Pb from the melt Sn precipitates out in the Pb-rich phase. It is of fundamental scientific interest to study the precipitation process of Sn from supersaturated Pb in 5Sn-95Pb. Therefore this study was performed to fully characterize the microstructure of 5Sn-95Pb solder. The joint microstructure of 5Sn-95Pb and Cu is discussed later in section 4.2.

4.1.1.2 EXPERIMENTAL PROCEDURE

The alloy was melted in vacuum backfilled with argon gas at 400°C using 99.9% pure Pb and Sn. The ingot was then allowed to cool to room temperature. Samples that were single phase solution treated were placed in a furnace in an air environment. These samples were either quenched in water or furnace cooled. All samples were allowed to age at room temperature for at least one month to reach an equilibrium microstructure.

Specimens for optical microscopy were cut from the bulk material and mounted in Koldmount. The surface was then ground on 600 grit silicon carbide paper. The surface was polished with 6 μm diamond paste, then 1 μm Al_2O_3, by hand, with a kerosene

lubricant. Final polishing was performed using 0.05 μm Al_2O_3 and kerosene. The surface was then etched using: 40 ml. H_2O + 10 ml. HNO_3 + 7.5 ml. Acetic Acid Glacial for 5 seconds. To reveal the Sn precipitates a final etch of 75% Acetic Acid Glacial + 25% H_2O_2 (30%) for 10 seconds was used.

TEM 3mm foils were cut and mechanically thinned down to 5 mil thickness. Electropolishing to perforation was performed using: 85% Ethyl Alcohol (200 proof) + 5% 2-Butoxyethynol + 10% Perchloric Acid. Immediately before polishing both sides of the foil were lightly ground using 600 grit paper to remove the surface oxide that inhibits smooth electropolishing. Tweezers were then used to lightly scratch both sides of the foil, in the center, to create a region for preferential polishing. Polishing was performed at 30-34 volts set at 80 mA current. Electropolishing was followed by 35 minutes of cold stage ion milling at 5 keV at 0.3 mA/gun. The foils oxidize very rapidly. Therefore after ion milling a maximum of 1 minute transfer time between ion mill and microscope was used.

Diffraction and bright field imaging were performed on the Kratos HVEM operated at 1.5 MeV. The 1.5 MeV accelerating voltage was necessary in order to gain sufficient penetration depth so large thin areas could be analyzed. HREM imaging was performed on the JEOL 2000CX microscope operated at 200 keV. In the HREM study only precipitates very close to the foil edge were analyzed because the lower accelerating voltage available for HREM imaging. A discussion of TEM and techniques used to determine crystallographic relationships is found in Appendix II.

4.1.1.3 RESULTS

• Optical Microstructure

The as solidified microstructure of 5Sn-95Pb is shown in Figure 4.1.1.1. The Pb grain boundaries are irregularly shaped and slightly overetched (resulting in the dark contrast at the boundaries). The grain size of the Pb grains is about 40 μm in diameter. The precipitates of β-Sn appear scattered homogeneously throughout the grains and appear as dark spots in the optical micrograph. In Figure 4.1.1.1 a few precipitates appear to be lined up parallel to one another, with a lamellar morphology. A similar microstructure and precipitate distribution develops in specimens that were aged in the single phase region (at 200°C) for 40 hours then quenched in water and aged at room temperature. This quenched microstructure is shown in the optical micrograph in Figure 4.1.1.2.

A different microstructure develops in 5Sn-95Pb that was aged at 200°C for 40 hours then furnace cooled to room temperature, Figure 4.1.1.3. Here the Pb grains are much larger, 150 μm in diameter, and a cellular precipitate morphology is evident. The cells

consist of regions of alternating lamellar β-Sn and α–Pb phases. The lamella of alternating Sn-rich and Pb rich regions are shown in the SEM micrograph of Figure 4.1.1.4.

• TEM Microstructure

A TEM study of 5Sn-95Pb solder was performed to gain insight of the precipitation process of β-Sn in α-Pb. The quenched and aged processing was chosen for this study as it approximates the microstructure found in the rapidly cooled solder joints of an electronic package.

The crystal structures of both Pb and Sn are shown in Figure 4.1.1.5. The Pb has an FCC structure with 4 atoms per unit cell and a_o = 4.9506 Å with a space group of Fm3m. The Sn has two possible phases: gray α-Sn, and white β-Sn. The gray Sn is cubic and was not found in this study. (According to the equilibrium phase diagram α–Sn should form below 13°C in pure Sn but this transformation is greatly inhibited with the presence of Pb or Sb in the Sn alloy.) β-Sn has a tetragonal structure with 4 atoms per unit cell and a_o = 5.81970, c_o = 3.17488 and an I4/lamd space group. Tables I and II show the lattice spacing and indexed planes for α-Pb and β-Sn.

Figure 4.1.1.6 shows a bright field image of the β-Sn precipitates present in 5Sn-95Pb. The precipitates have an even distribution throughout the foil, and a platelike shape. The precipitates have a common crystallography with the matrix, as is is clearly shown in Figure 4.1.1.7 with two variants of the precipitates evident. A face on view of the ß-Sn precipitates is found in Figure 4.1.1.8.

An edge on view of a β-Sn precipitate is shown in Figure 4.1.1.9 with the associated diffraction pattern of the Pb matrix. From this information it was found that the habit plane of the precipitates is $(111)_{Pb}$. Extensive diffraction studies on the precipitates and matrix found the orientation relationship to be $(111)_{Pb}$ // $(010)_{Sn}$ and $[0\bar{1}1]_{Pb}$ // $[001]_{Sn}$. (The methods and procedures for habit plane and orientation relationship determination are found in Appendix II). An indexed diffraction pattern taken at the interface between a β-Sn precipitate and the α-Pb matrix is shown in Figure 4.1.1.10.

In addition to the crystallographic match the precipitates are occasionally found to line up relative to one another, Figure 4.1.1.11. Some precipitates are found have extraordinary lengths, as shown in Figure 4.1.1.12. This is an indication that some vestiges of cellular precipitation and the resultant lamella are still present in rapidly cooled and aged 5Sn-95Pb. Diffraction studies of the cellular regions found the precipitates to have the same crystallographic orientation as described above for the smaller precipitates.

Given this orientation relationship the transformation of α-Pb to β-Sn involves taking the distorted FCC cell found on the $(111)_{Pb}$ and $(110)_{Pb}$ planes and transforming it to a

BCT cell. The $(111)_{Pb}$ goes to $(010)_{Sn}$ and $[0\bar{1}1]_{Pb}$ goes to $[001]_{Sn}$. The strain involved in this transformation is shown in the matrix below:

$$\begin{bmatrix} 0.0383 & -0.17 & 0 \\ 0.17 & 0.0383 & 0 \\ 0 & 0 & 0.091 \end{bmatrix}$$

The transformation involves a 17% strain on the c-axis, a 3.83% strain on the a-axis, and a 9% shear in the basal plane. The strain in transformation must be taken up by the precipitate/matrix interface as few dislocations are found within either the Pb matrix or Sn precipitates. Therefore a High Resolution Electron Microscopy (HREM) study was performed to observe this interface.

A HREM micrograph of the precipitate/matrix interface is shown in Figure 4.1.1.13. The beam direction was $[022]_{Pb}$ which was about 0.5° away from $[001]_{Sn}$ (and, $(111)_{Pb}$ // $(010)_{Sn}$). The β-Sn precipitate is on the right, the α-Pb matrix is on the left side of the micrograph. The regions marked "a" show contrast from dislocation that extend into the Pb matrix. The strain in transformation is at least partially taken up by the dislocation formation in the softer α-Pb matrix. The Moire fringes found in Figure 4.1.1.13 are islands of oxide that have formed in the high vacuum present within the microscope.

Figure 4.1.1.14 is a lower magnification HREM micrograph of the same precipitate shown in Figure 4.1.1.13. Two through-focal-series were taken of the precipitate approximately 15 minutes apart. The photo on the left in Figure 4.1.1.14 is from the first series, and the photo on the right from the second. On the curved irregular surface in Figure 4.1.1.14 ledges are contained in the boundary at ~4 nm in height. After 15 minutes of beam heating, between through-focal-series, the precipitate has dissolved at the curved boundaries by a ledge mechanism, Figure 4.1.1.14[49]. The dissolution has occurred only on the curved boundaries, the planar boundaries have not moved. A higher magnification photo of Figure 4.1.1.14 after dissolution is shown in Figure 4.1.1.15. Here the dislocations in the Pb, at the interface, are marked by arrows. The ledges adjacent to the arrows are ~0.6 nm in height.

An attempt was made to observe precipitate dissolution and reprecipitation *in-situ* using the heating stage on the HVEM. Unfortunately the precipitates are large so that upon heating the precipitates dissolve but the Sn diffused to the surface of the foil and oxidized.

Therefore this experiment could not represent the true precipitation process in the bulk alloy.

An interesting observation on grain boundary motion under beam heating is shown in Figure 4.1.1.16. Figure 4.1.1.16a is before beam heating, 4.1.1.16b after 10 minutes of beam heating. The grain boundary is irregular, made up of steps ~15 nm in height. The arrows indicate the regions where the grain boundary moves via step motion.

A rough estimate of the mechanical properties of 5Sn-95Pb was made using a microhardness vs. aging time after solidification, Figure 4.1.1.17. The hardness was found to decrease immediately after solidification to a steady state after 16 hours for both the rapidly cooled and slow cooled 5Sn-95Pb solders. This indicates the precipitation of β-Sn decreases the strength of the alloy due to precipitate coarsening. A solid solution of Sn in Pb or fine β-Sn precipitates in α-Pb are better strengthening agents. The cellular microstructure that results on slow cooling has a lower hardness at all aging times which is due, in part, to the larger grain size of the Pb in this sample.

4.1.1.4 DISCUSSION

The precipitation process of β-Sn in α-Pb is cooling rate dependant. With a fast cooling rate the precipitate distribution appears to be fairly homogeneous, Figure 4.1.1.1. A slower cooling rate results in a cellular precipitation of Sn from Pb with the resultant lamellar structure, Figure 4.1.1.3. Although the solder that is used in electronic packaging has a fast cooling rate the cellular precipitation process is worthy of discussion from a fundamental point of view.

Cellular precipitation is a discontinuous process where the composition of the matrix changes discontinuously as the solid solution precipitates out a second phase as a cell front passes. The precipitation occurs on boundaries and the boundary moves with the growing tips of the precipitate. The reaction for Sn-Pb is:

$$\alpha' \longrightarrow \alpha + \beta$$

where α' is the supersaturated α matrix, and α and β are the equilibrium phases of the matrix and precipitate, respectively. Cellular precipitation has been observed in previous work on the Pb-rich Sn-Pb alloy[50-56].

Turnbull and Treaftis[52] observed the precipitation reaction in wires varying in Sn content from 7-10%. They claim that cellular precipitation is the only mechanism operative in the Sn-Pb system and that cells nucleate on boundaries, either grain or dendrite. Contrary to Turnbull and Treaftis, Borelius[57] claims precipitates form only homogeneously. Turnbull found in later work[53] that the cellular precipitation process is

very rapid due to "short-circuit" diffusion along defects and boundaries and that the introduction of defects during cold work accelerates the cellular precipitation process.

Tu and Turnbull[50,51] studied the formation of cells in bicrystals of Pb-rich Sn-Pb alloys. The conclusion of this work was that β-Sn lamella form via a "pucker mechanism". This mechanism is illustrated in Figure 4.1.1.18. In the pucker mechanism plates of β-Sn nucleate on a boundary in an orientation such that one side of the β-Sn plate is in the correct orientation relationship with the matrix and the other half has a high energy interface at the boundary. In order to lower the energy the boundary moves (puckers out) to put the entire β-Sn plate into the correct orientation.

The observations presented in this work indicate that the cellular precipitation process proposed by Turnbull et. al.[50,51] is valid for samples that have undergone slow cooling from supersaturated α'-Pb. However, for samples rapidly cooled through the single phase region a more homogeneous distribution of fine precipitates results, although some lamella are occasionally found, Figure 4.1.1.11. This difference in precipitation processes can be explained using a nucleation and growth argument. On slow cooling precipitation is limited by the number of nucleation sites so precipitates form on grain boundaries. Cells grow easily because diffusion of Sn is fast on slow cooling. On fast cooling diffusion is limited but the driving force for precipitation is high so precipitates form in a distributed homogeneous fashion, possibly on vacancy clusters quenched into the microstructure. This is illustrated schematically in the TTT diagram below[58].

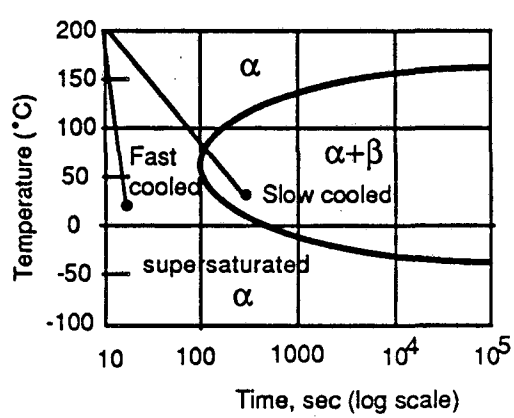

The orientation relationship found by diffraction in TEM shows the best crystallographic fit between β-Sn and α-Pb. The $(111)_{Pb}$ and $(010)_{Sn}$ planes have spacings that closely match ($(111)_{Pb}$ = 2.855 Å and $(010)_{Sn}$ = 2.915 Å) and, as shown in Figure 4.1.1.13, a semi-coherent interface is found between the broad face of the precipitate and the matrix. An orientation relationship with different variants was found by Tu and Turnbull[50] using Laue diffraction information with a $(111)_{Pb}$ habit plane and $[001]_{Sn}$ // $[110]_{Pb}$ and $(310)_{Sn}$

// $(111)_{Pb}$. The stereographic projection illustrating the orientation between β-Sn and α-Pb is shown in Figure 4.1.1.19. This projection shows how Tu and Turnbull found a relationship that was close to the true orientation relationship. The orientation relationship found in this work was also theoretically predicted by Ecob and Ralph[59] based on Bollmans O-lattice theory[60]. Ecob and Ralph compute a factor, R, that is linked to the energy of a two phase semicoherent interface and is essentially a thermodynamic argument that models the energy of arrays of misfit dislocations[61]. Using this argument the same habit plane and orientation relationship as found in this work was determined. The precipitation of Sn in Pb is then determined by the best crystallographic fit in the matrix which lowers interfacial energy.

The precipitate dissolution observation, shown in Figure 4.1.1.14, is relevant to the thermal fatigue behavior of 5Sn-95Pb solder. The observed dissolution occurred under beam heating which roughly corresponds to 100°C. Solder joints in thermal fatigue regularly encounter temperatures that exceed 100°C so the β-Sn precipitates dissolve and reprecipitate on each thermal cycle. This will have an effect on the mechanical properties of the solder and may affect the thermal fatigue life.

Beam heating was also found to move grain boundaries of the Pb, Figure 4.1.1.16. This observation indicates that grain boundaries are very mobile and will move easily under the stress and elevated temperatures in thermal fatigue. The irregular stepped grain boundary interface may also concentrate stress at the grain boundaries in deformation and create initiation sites for failure.

4.1.1.5 SUMMARY AND CONCLUSIONS

The microstructure of 5Sn-95Pb solder in bulk was characterized. In slow cooling from the supersaturated α'-Pb phase β-Sn precipitates out in a cellular precipitation process. When the solder is rapidly cooled through the single phase region (the conditions found in solder joints of electronic packages) the Sn precipitates out with a fairly homogeneous distribution. The precipitation process occurs rapidly. The precipitates have a platelike shape. The precipitates have a $(111)_{Pb}$ habit plane and an orientation relationship of $(111)_{Pb}$ // $(010)_{Sn}$ and $[0\bar{1}1]_{Pb}$ // $[001]_{Sn}$. The strain present on transformation is taken up by dislocations in the Pb that emanate from the precipitate/matrix interface. Regions of precipitates that are curved away from their habit plane form ledges. Upon heating the precipitates dissolve via a ledge mechanism which will have an effect on the properties of the solder during thermal fatigue. Additionally, Pb grain boundaries were found to contain steps that move on beam heating in the microscope which is an indication of easy boundary

motion at elevated temperatures. The solder was found to oxidize very rapidly, even in the high vacuum (10^{-6}torr) of the TEM microscope.

TABLE I

(α Pb)
Face Centered Cubic, 4 atoms/unit cell
$a_o = 4.9506$ O^5_H-Fm3m

d Å	hkl
2.855	111
2.475	200
1.750	220
1.493	311
1.429	222
1.238	400
1.1359	331
1.1069	420
1.0105	422
0.9526	511
0.8752	440
0.8369	531
0.8251	600

TABLE II

(β Sn)
Body Centered Tetragonal, 4 atoms/unit cell
$a_o = 5.831$ $c_o = 3.182$ D^{19}_{4H} - I4/AMD

d Å	hkl	d Å	hkl
2.915	200	1.0252	521
2.793	101	0.9824	213
2.062	220	0.9718	600
2.017	211	0.9310	303
1.695	301	0.9280	512
1.484	112	0.9219	620
1.458	400	0.9178	611
1.442	321	0.8868	323
1.304	420	0.8755	541
1.292	411	0.8485	413
1.205	312	0.8466	532
1.0950	501	0.8386	631
1.0434	103	0.8086	640
1.0401	332	0.8058	701
1.0309	440		

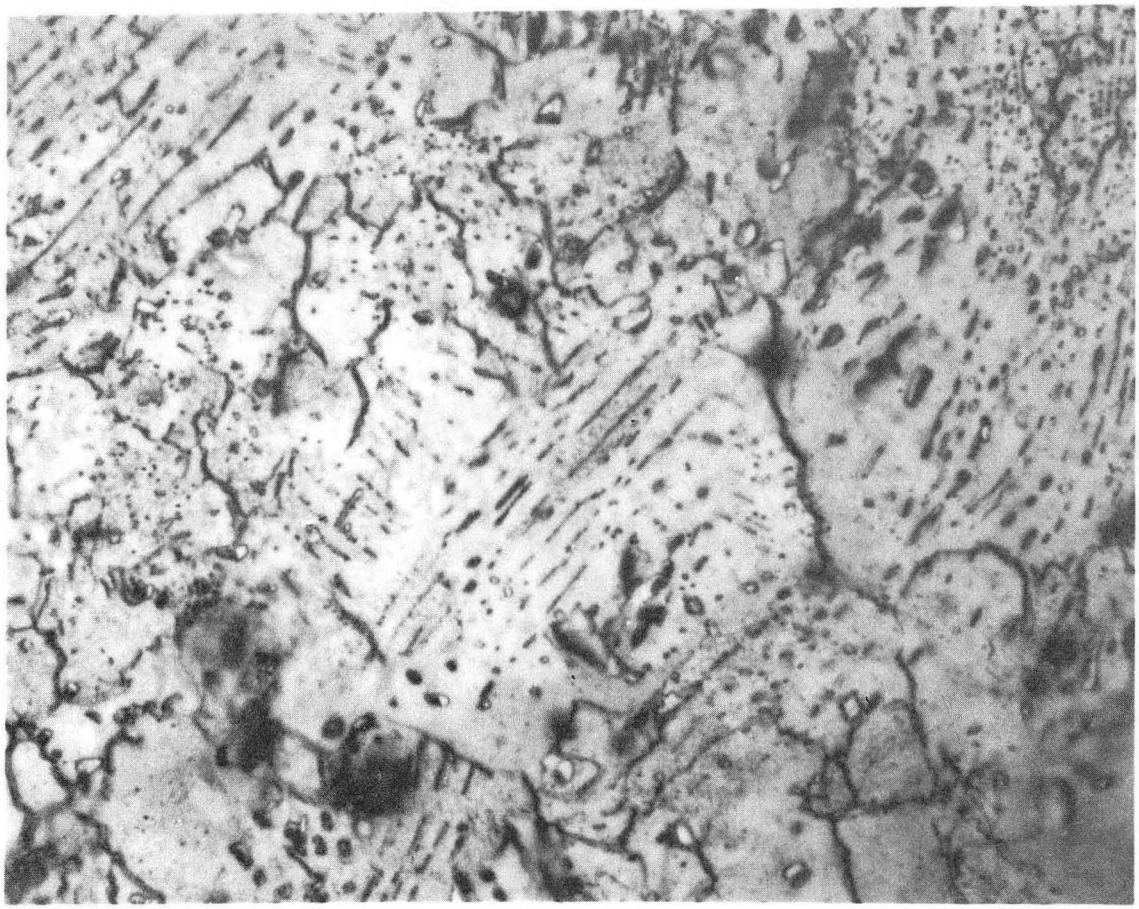

XBB 875-3841

10 μm

Figure 4.1.1.1 Optical microstructure of as-solidified 5Sn-95Pb solder.

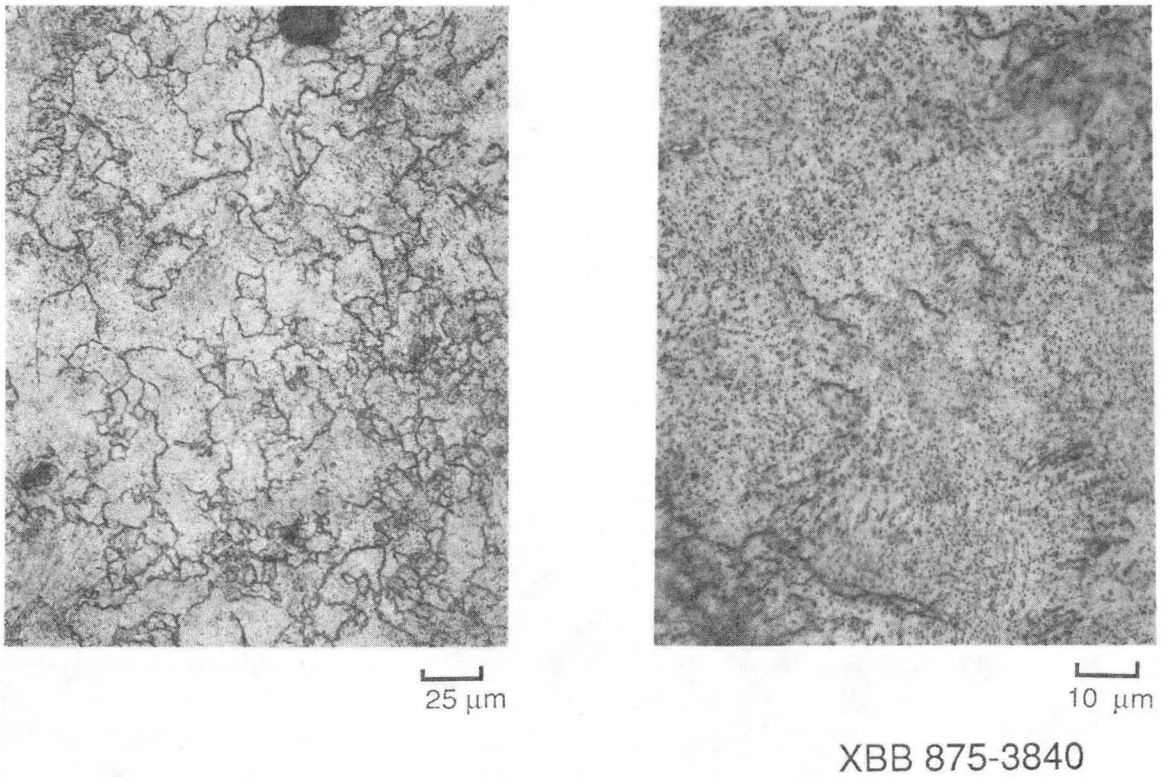

Figure 4.1.1.2 Optical micrograph of solution treated (at 200°C) then rapidly quenched 5Sn-95Pb solder.

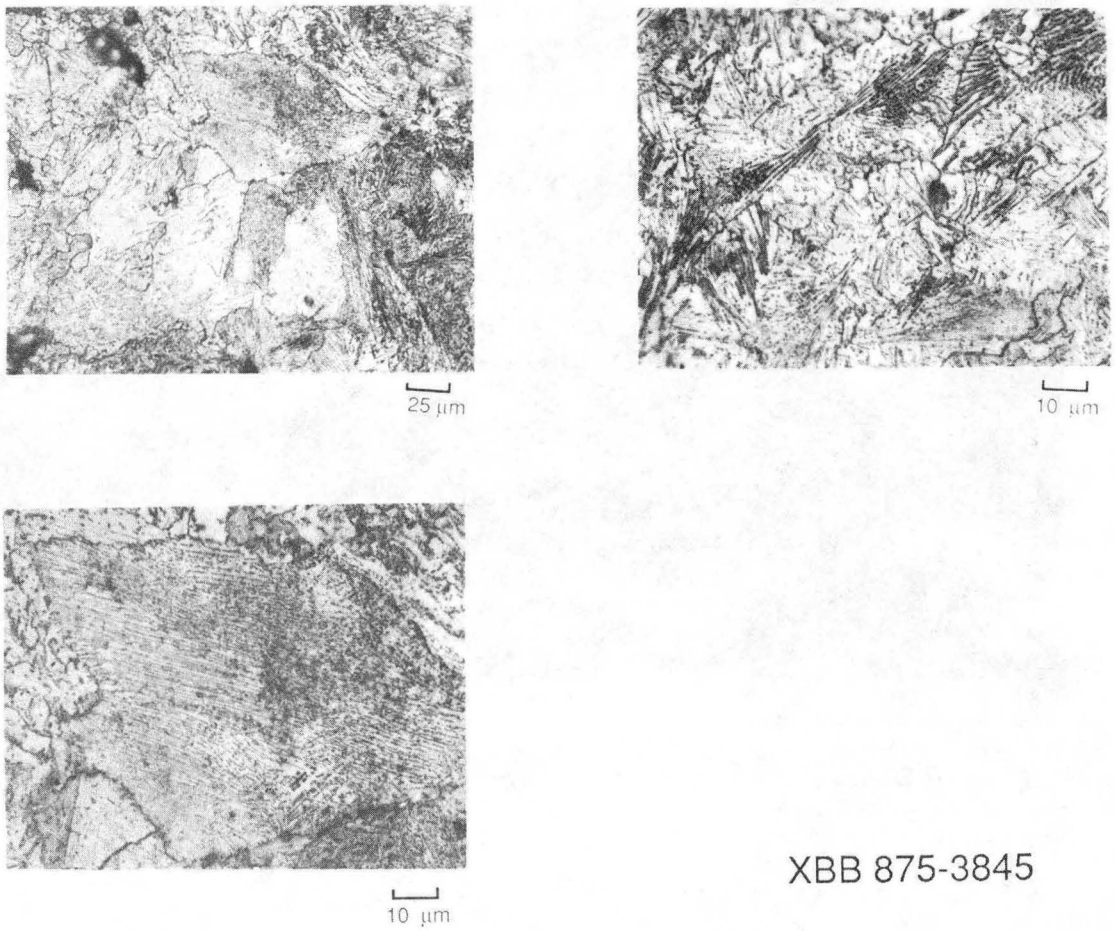

Figure 4.1.1.3 Optical microstructure of solution treated (200°C) then slowly cooled 5Sn-95Pb solder. Three regions from the same sample.

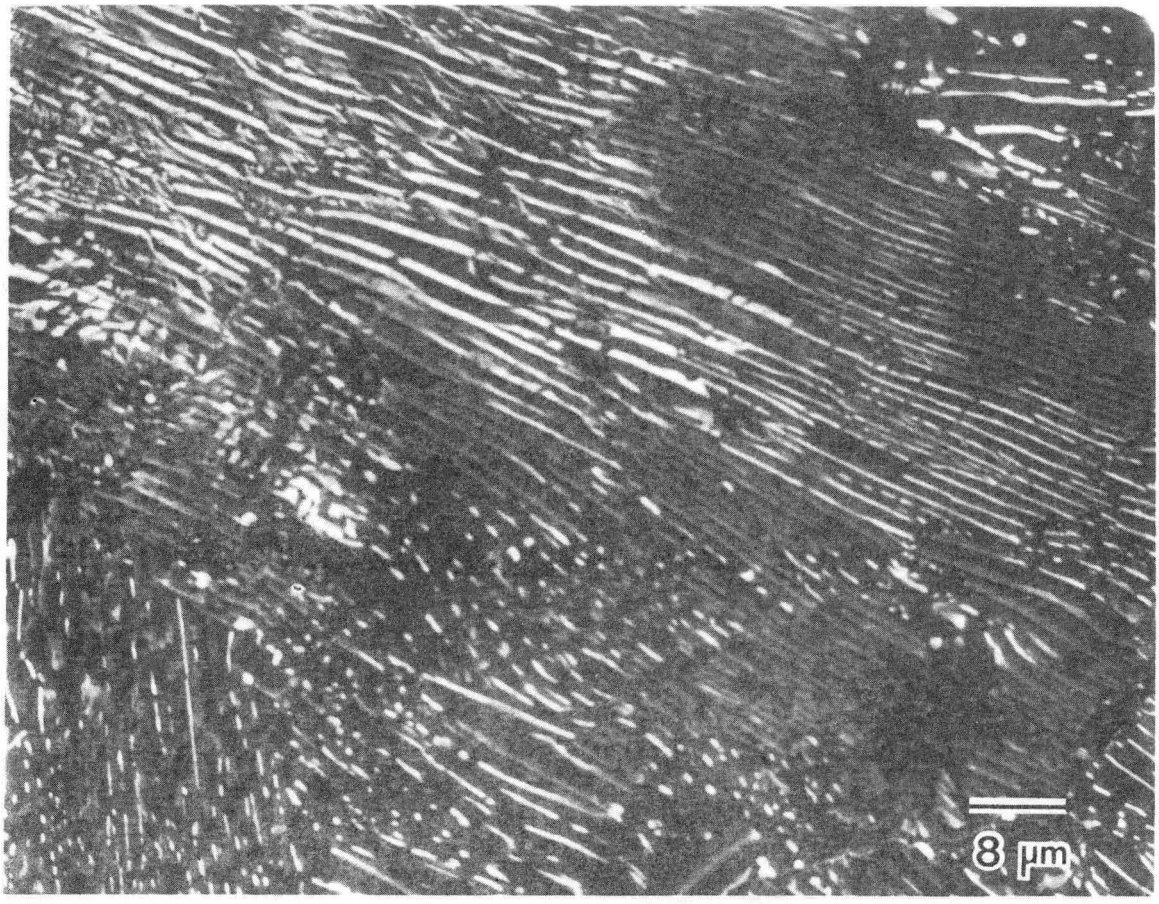

XBB 840-7592

Figure 4.1.1.4 SEM micrograph showing the Sn lamella present in a 5Sn-95Pb sample that was solution treated (200°C) then slow cooled.

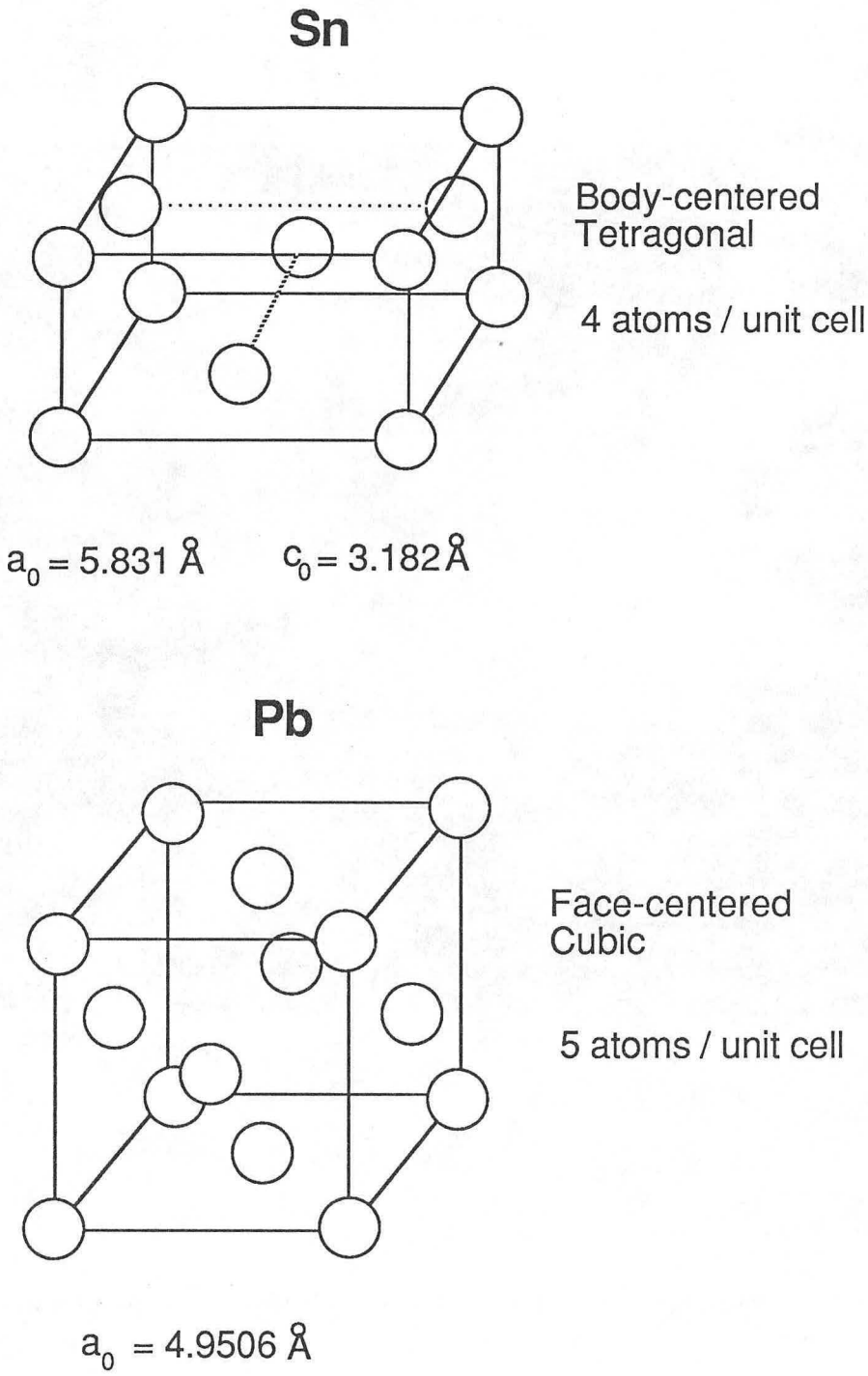

Figure 4.1.1.5 Unit cell diagrams of both α-Pb and β-Sn.

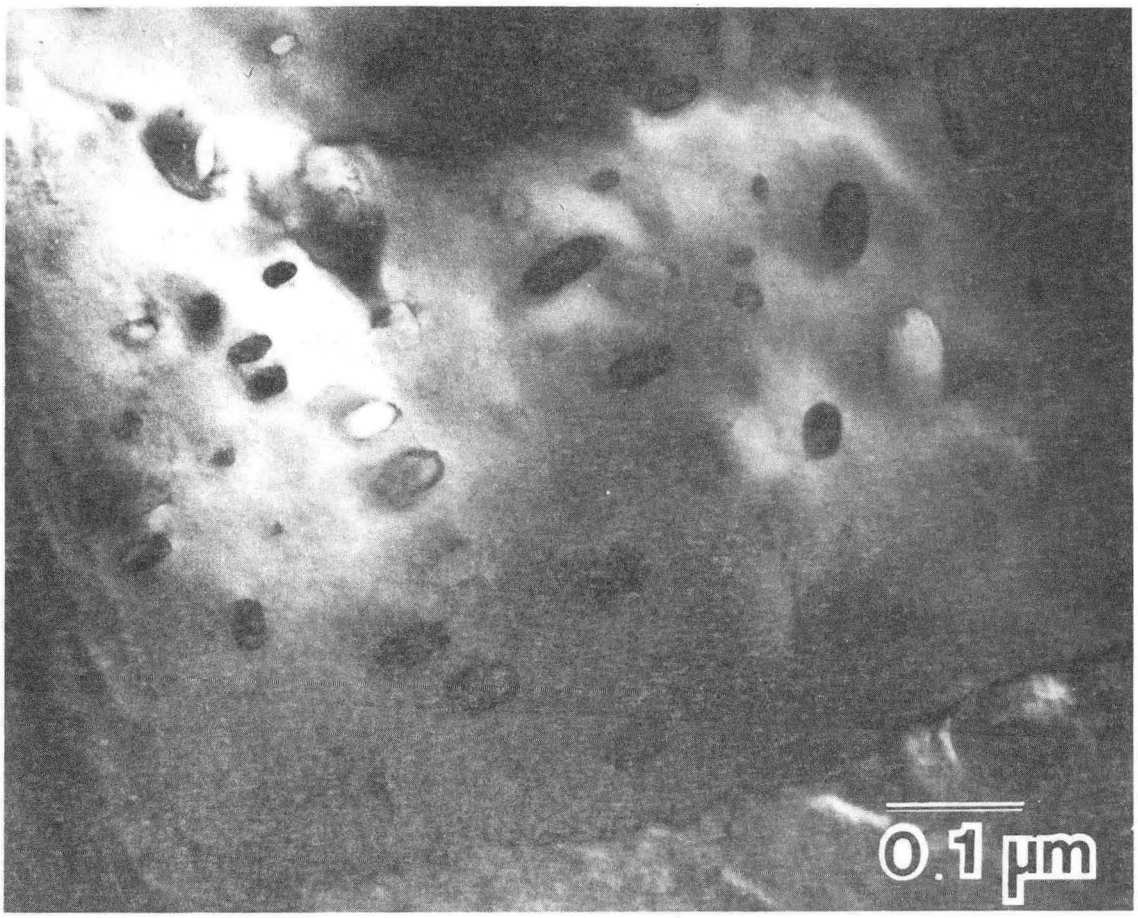

XBB 853-1993A

Figure 4.1.1.6 TEM bright field image of β-Sn precipitates in 5Sn-95Pb solder.

XBB 857-5858

Figure 4.1.1.7 TEM bright field image of β-Sn precipitates in 5Sn-95Pb solder illustrating the common crystallography between the precipitates and the matrix.

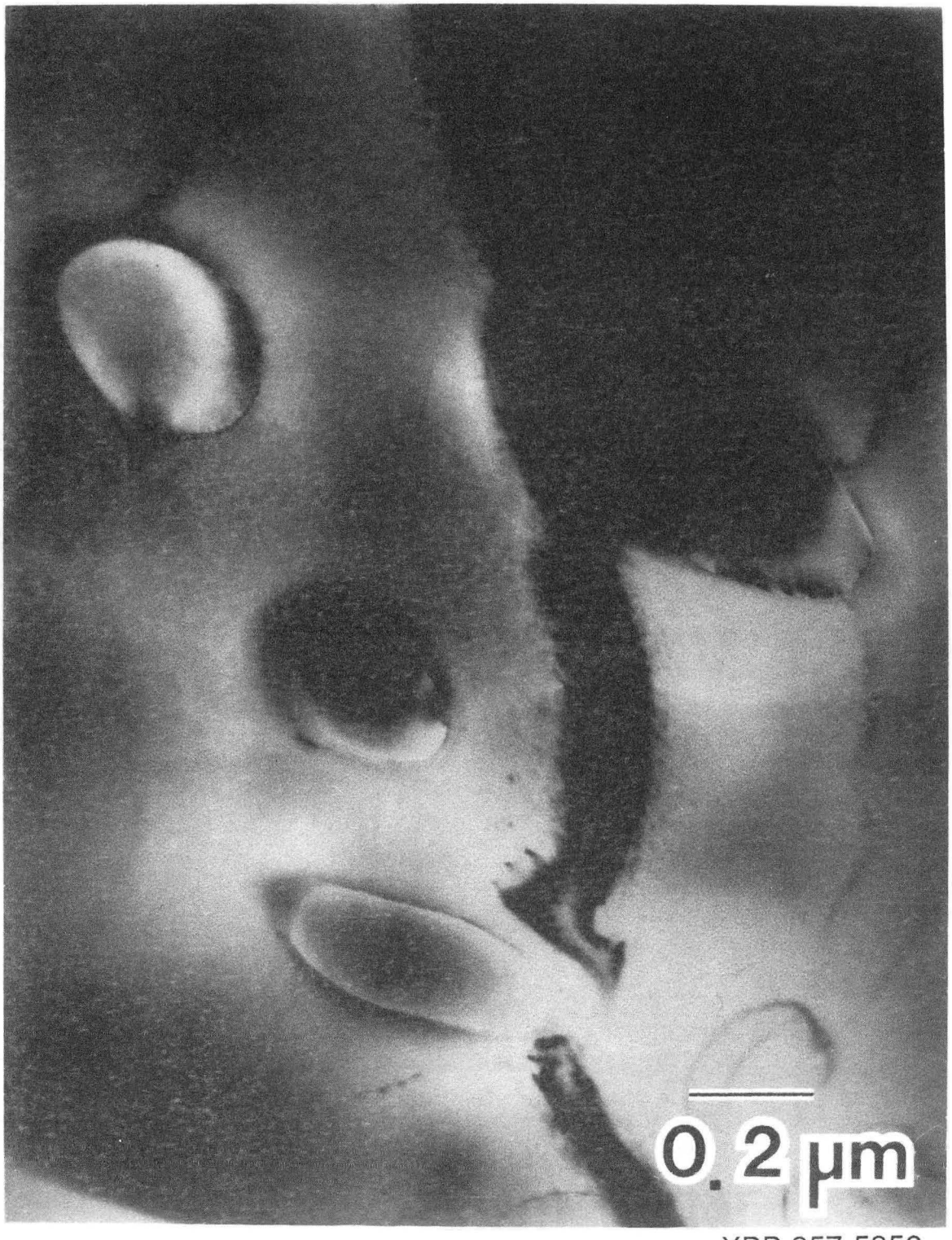

XBB 857-5856

Figure 4.1.1.8 TEM bright field image of platelike β-Sn precipitates viewed face on in 5Sn-95Pb solder.

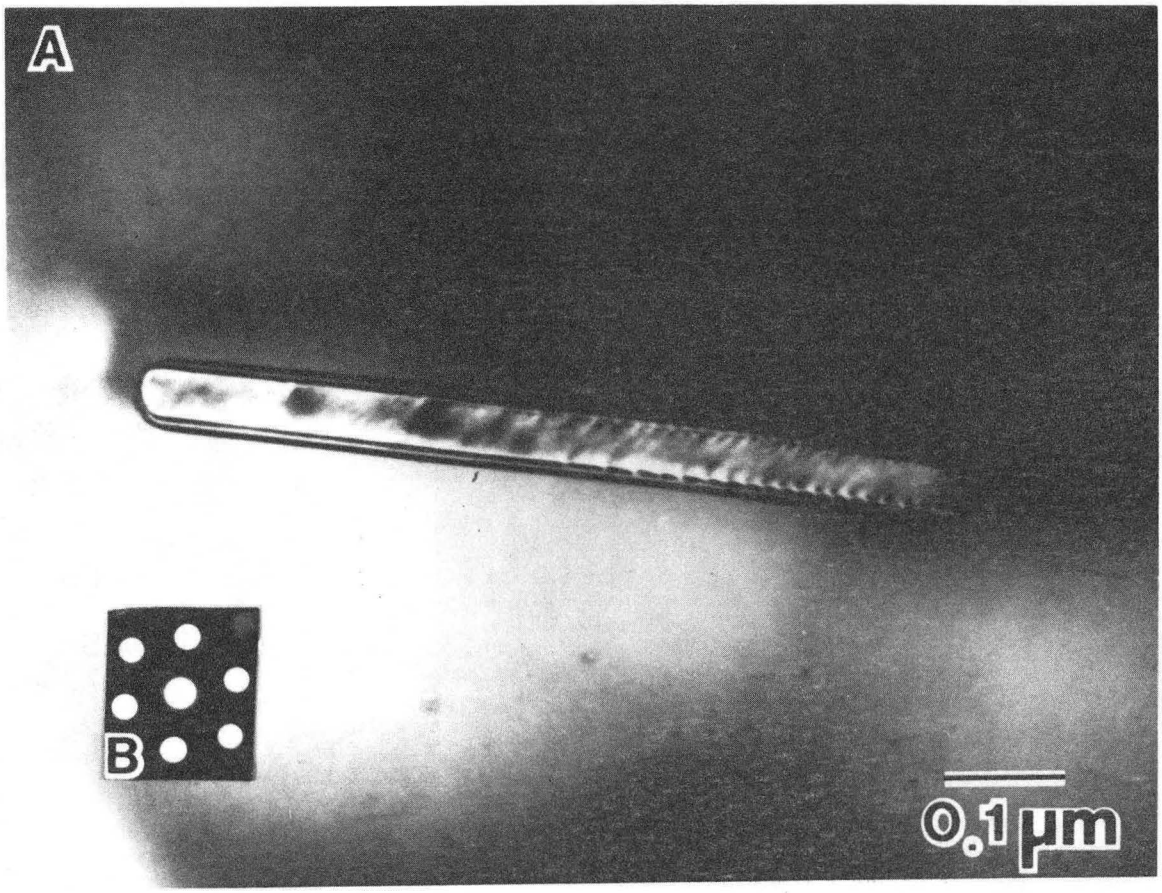

XBB 853-1994

Figure 4.1.1.9 TEM bright field image, with associated $[011]_{Pb}$ matrix diffraction pattern, of a β-Sn precipitate edge on in 5Sn-95Pb illustrating the $(111)_{Pb}$ habit plane.

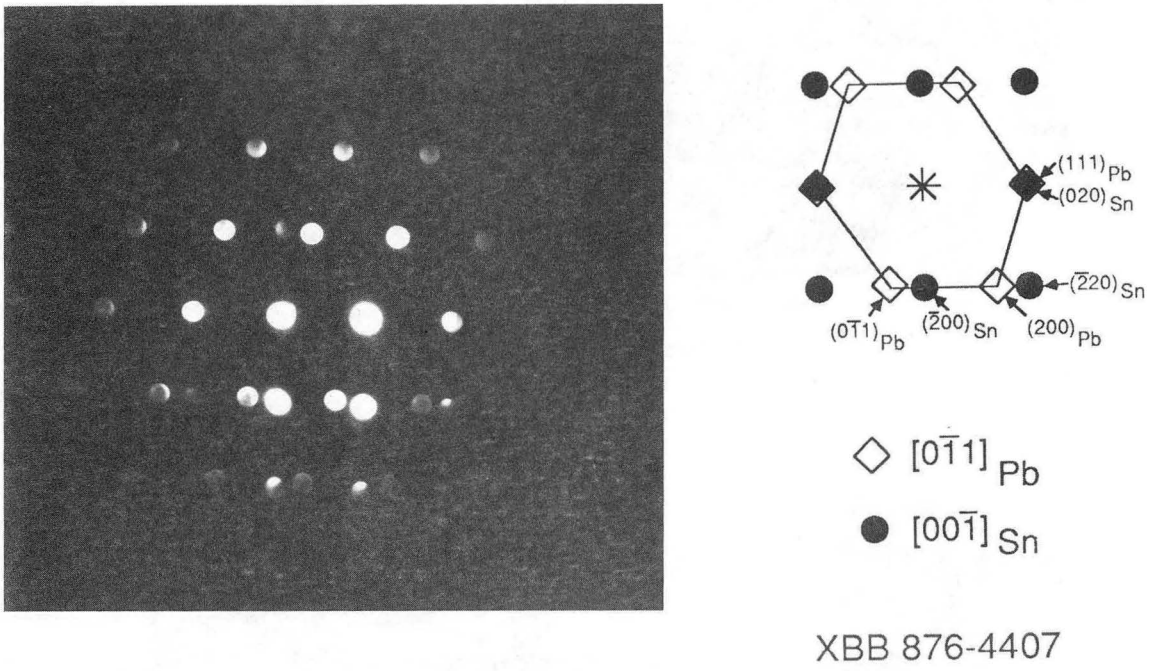

Figure 4.1.1.10 Indexed diffraction pattern of interface between β-Sn precipitate and α-Pb matrix. This shows the orientation relationship $(111)_{Pb}$ // $(010)_{Sn}$ and $[0\bar{1}1]_{Pb}$ // $[001]_{Sn}$.

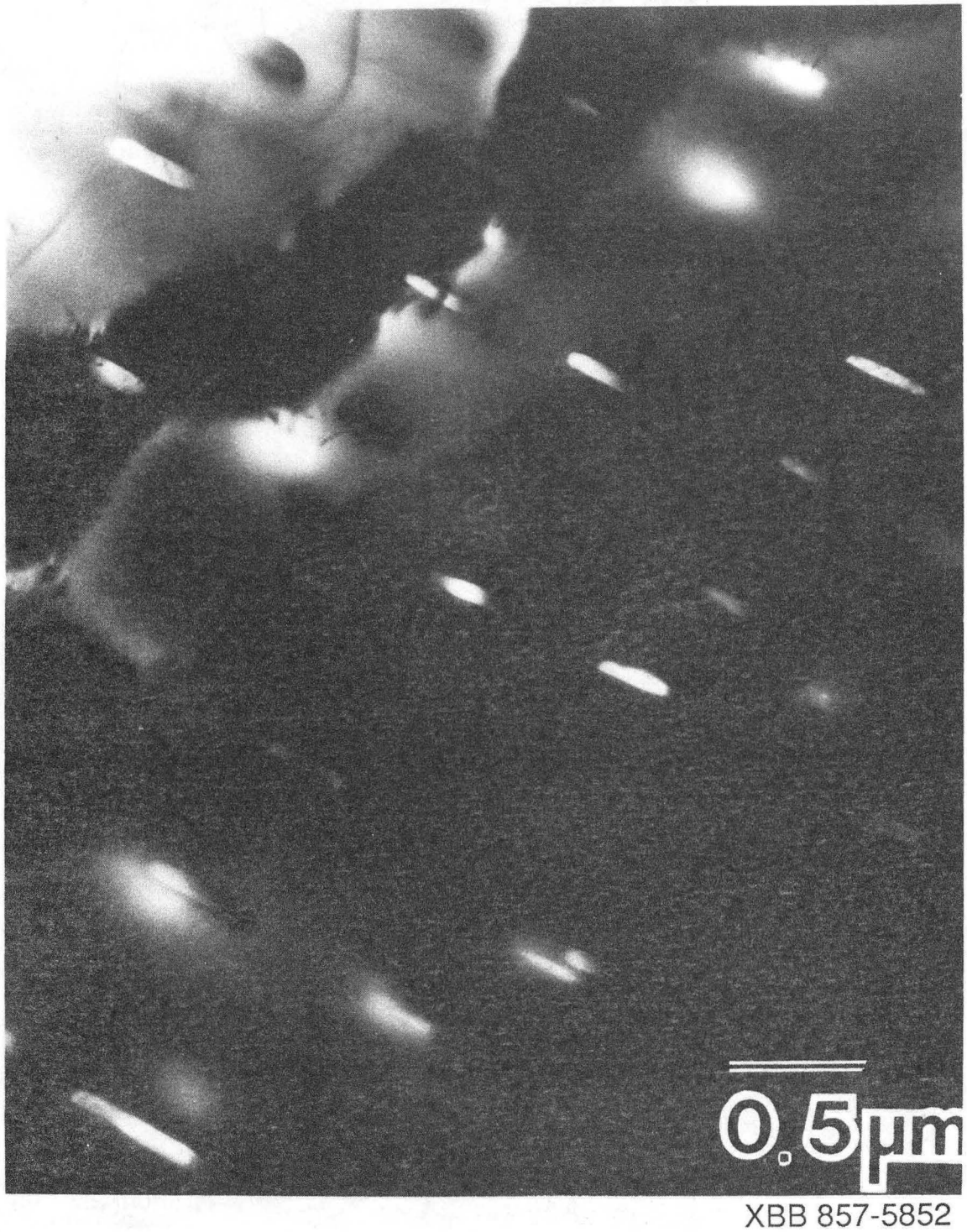

Figure 4.1.1.11 TEM bright field image showing β-Sn precipitates lined up relative to one another.

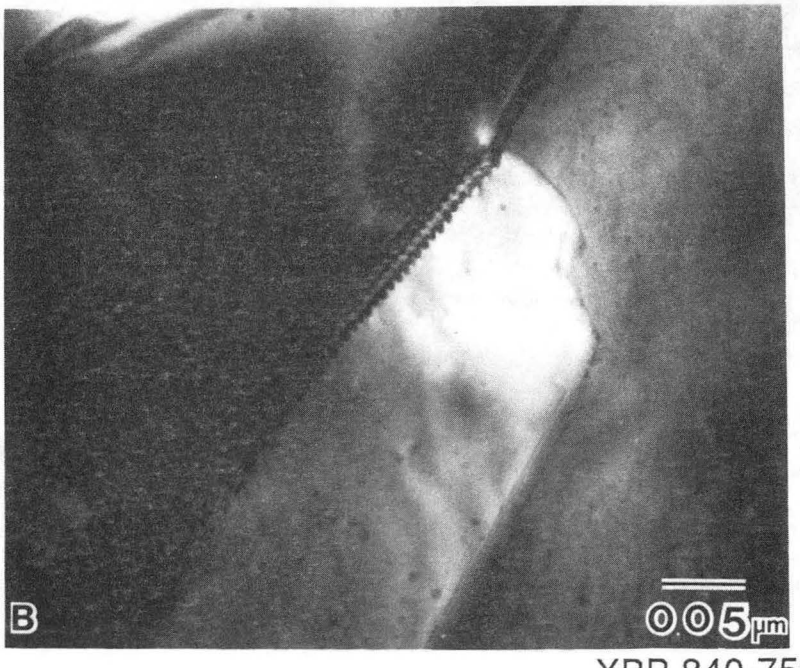

XBB 840-7586

Figure 4.1.1.12 TEM bright field image showing an example of the large size of some of the β-Sn precipitates.

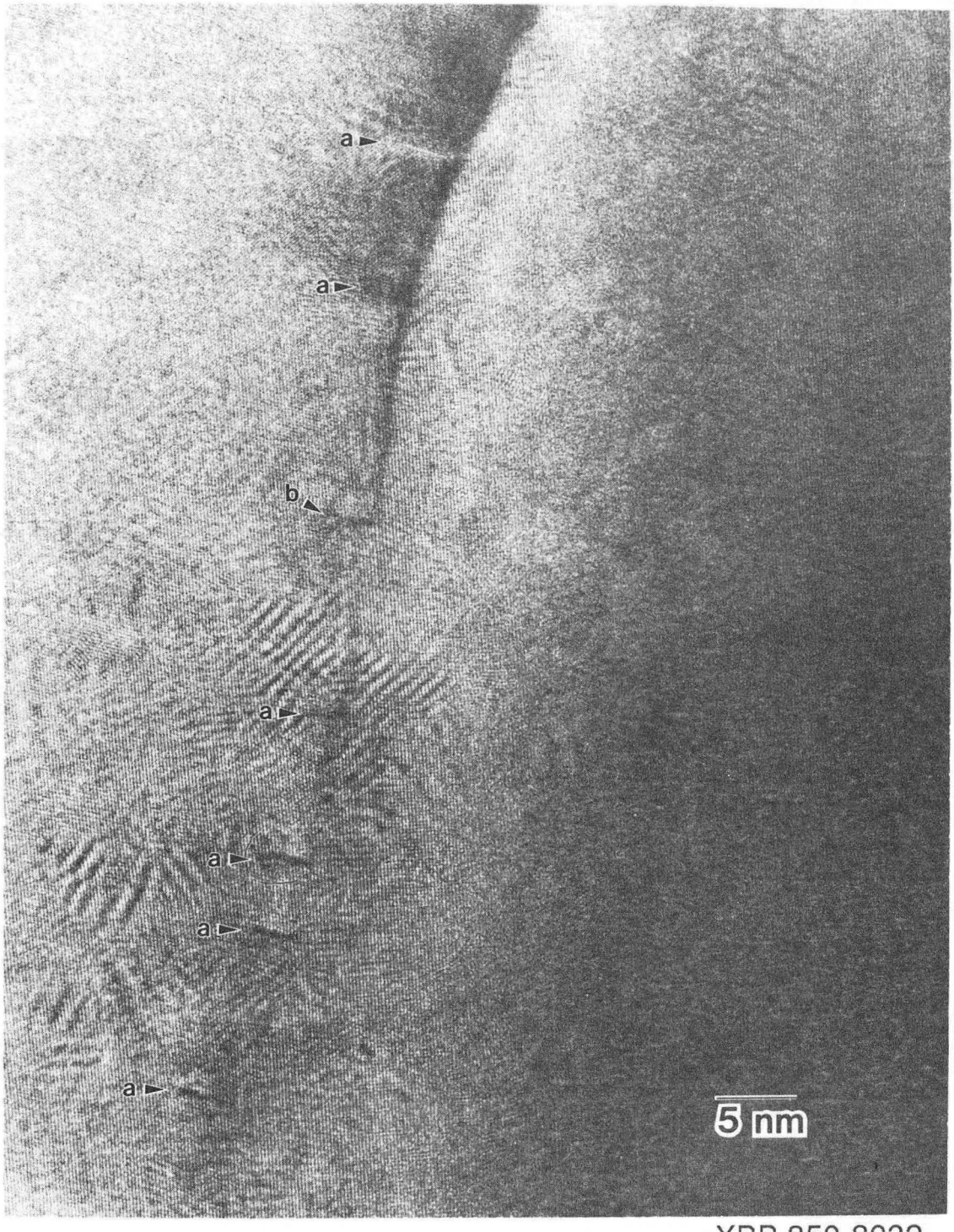

XBB 850-8032

Figure 4.1.1.13 HREM micrograph of the interface between a β-Sn precipitate (on the right in the micrograph) and the α-Pb matrix (on the left). Dislocations are marked by **"a"**. **"b"** denotes a ledge at the interface.

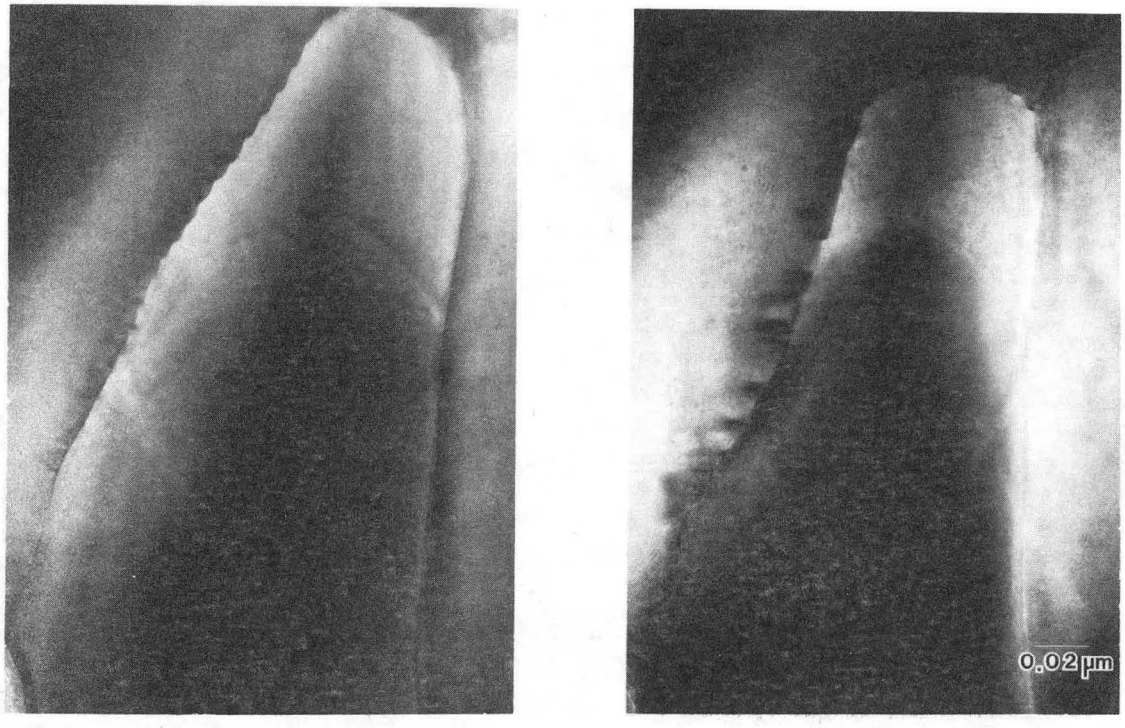

XBB 850-8033

Figure 4.1.1.14 Two HREM micrographs of the same β-Sn precipitate before (left) and after (right) beam heating illustrating precipitate dissolution.

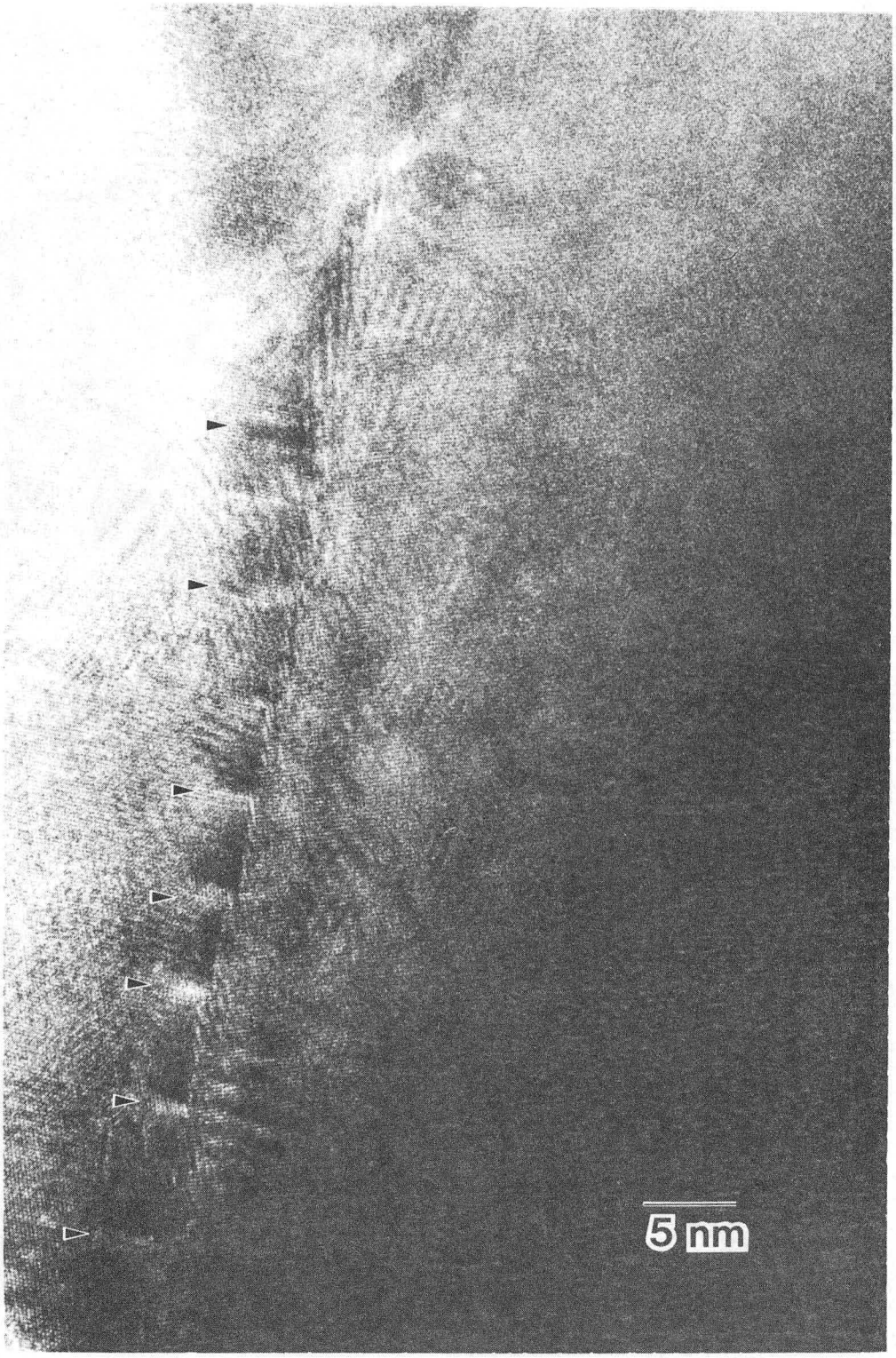

XBB 850-8031

Figure 4.1.1.15 HREM micrograph of the interface between a β–Sn precipitate and the α-Pb matrix after dissolution by beam heating. Interfacial dislocations are marked by arrows.

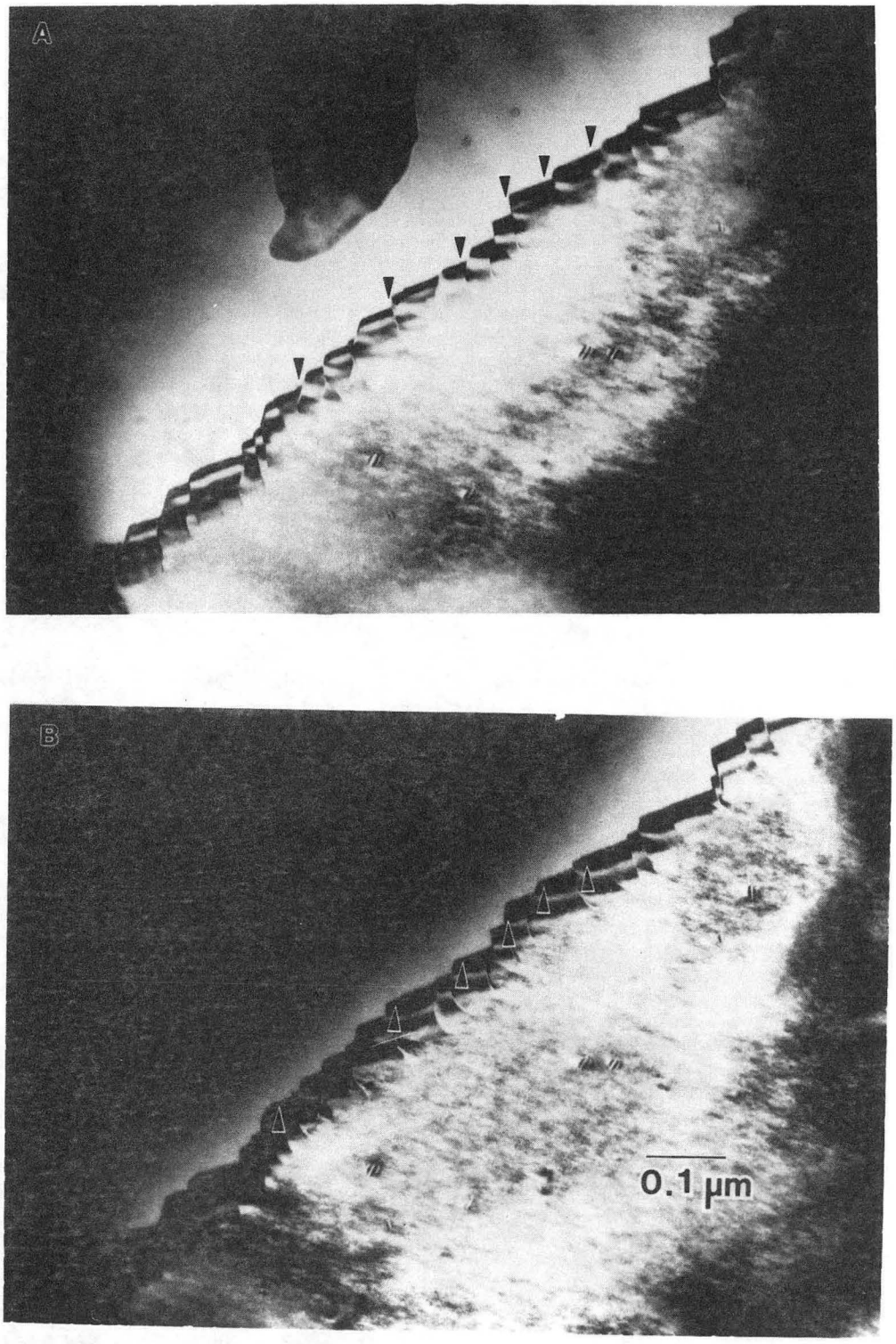

Figure 4.1.1.16 HREM micrographs of a grain boundary in α-Pb. Before beam heating (A), after beam heating (B). The arrows mark regions of boundary motion.

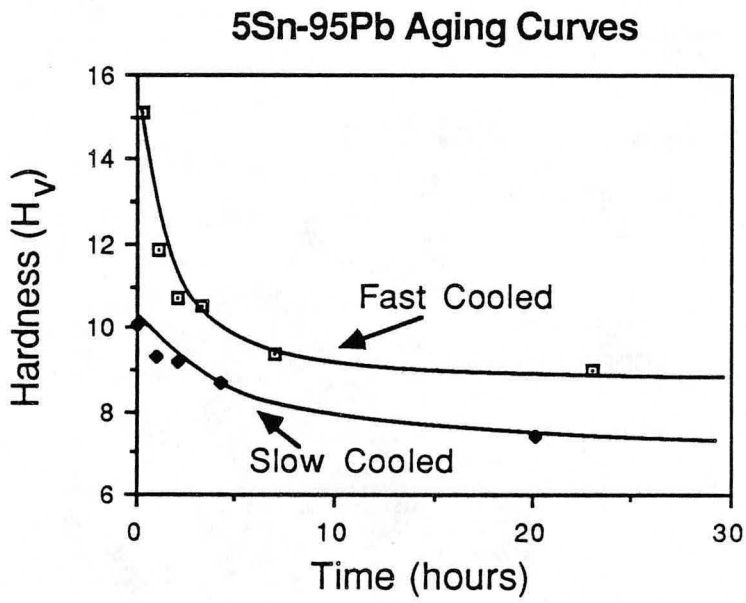

Figure 4.1.1.17 Plot of microhardness (H_V) vs. aging time for homogeneous and cellular precipitate microstructures in 5Sn-95Pb.

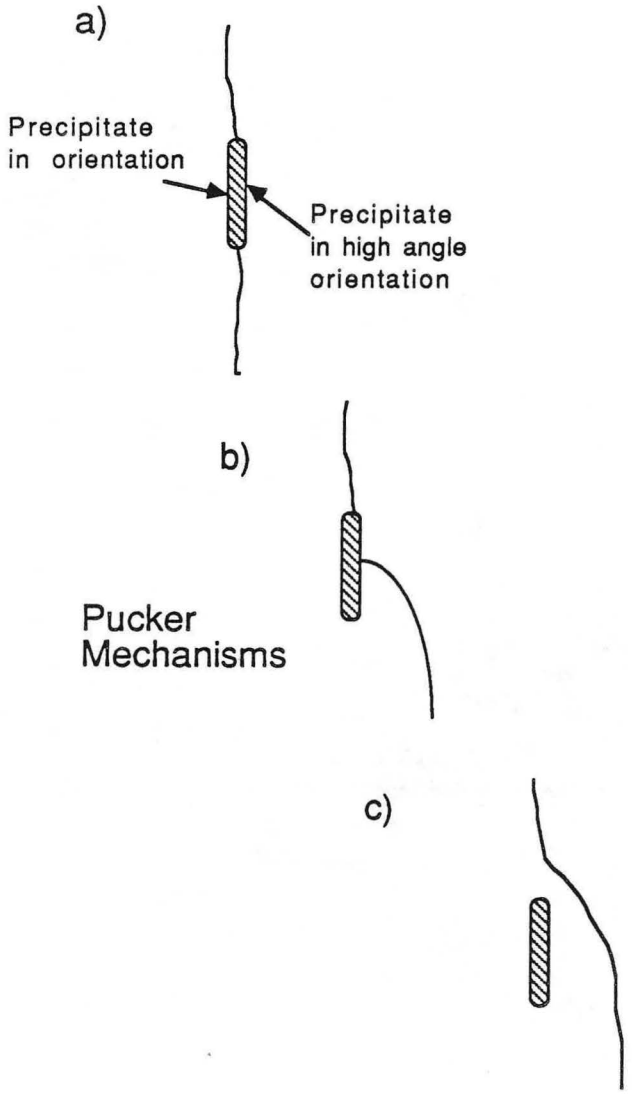

Figure 4.1.1.18 Schematic illustration of the "pucker mechanism" of precipitation. a) Plates of β-Sn nucleate on a boundary that is in an orientation such that one side of the plate is in the correct orientation with the matrix and the other side has a high energy interface. b) The boundary moves (puckers) to lower the energy. c) Finally the entire precipitate is in the correct orientation.

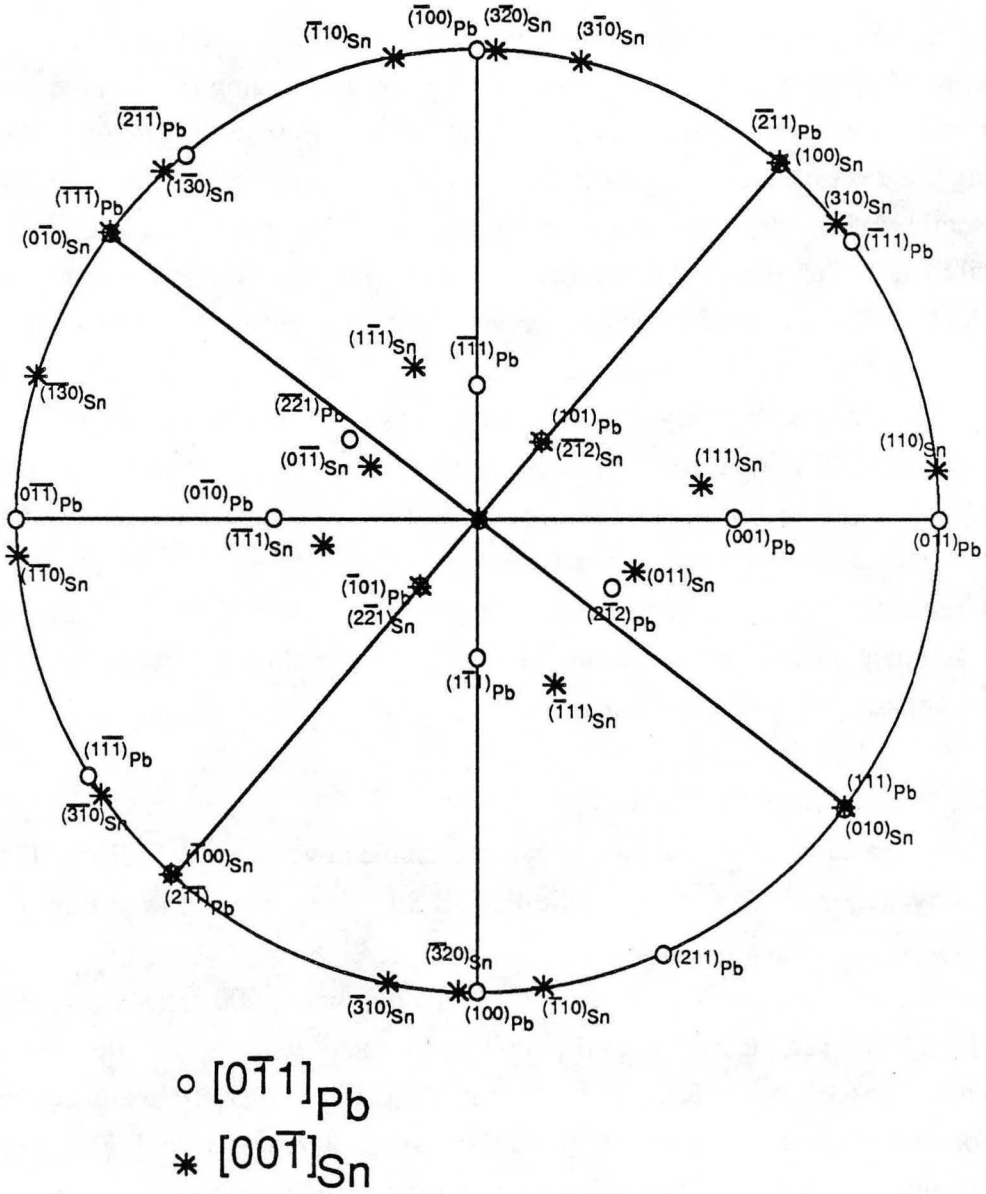

Figure 4.1.1.19 Stereographic projection illustrating the orientation between major poles of Pb and Sn.

4.1.2 60Sn-40Pb Solder

4.1.2.1 Introduction

The 60Sn-40Pb solder is a slightly hypoeutectic Sn-Pb alloy and therefore has a low melting point. This alloy composition finds widespread use ranging from a pipe joiner in plumbing, to second level solder in electronic packaging. The fact that 60Sn-40Pb has a low melting point is especially important in electronic packaging. Soldering is the last step in the assembly of an electronic package so any elevated temperature excursions are detrimental to the diffused device structure on the chip. Therefore the low melting point of 60Sn-40Pb (190°C) is an excellent choice for electronic packaging in so far as to limit heat input.

60Sn-40Pb solder is also very ductile. Ductility is necessary to withstand the large shear strains (up to 20%) that may be imposed on solder joints with thermal fluctuations. Although the joints can withstand a great deal of strain the joints have been found to fail through the bulk 60Sn-40Pb joint after repeated cycles[12,14,38,40,42,44]. It is therefore important to characterize the microstructure of bulk 60Sn-40Pb solder. From this study it is possible to relate the microstructure of 60Sn-40Pb to thermal fatigue properties with the ultimate goal of alleviating fatigue failures.

4.1.2.2 Experimental Procedure

The 60Sn-40Pb alloy was melted in a graphite crucible in vacuum backfilled with argon gas. The alloy was made from 99.9% pure Pb and Sn. The solder was purified by zone melting at 240°C.

Samples were mounted in Koldmount and polished down to 600 grit sandpaper under flood cooling. The samples were then polished, by hand, using 1 μm alumina oxide powder and kerosene on a felt cloth. Final etch and polishing were performed simultaneously with a slurry of 0.3 m alumina powder, 50% water, and 50% Beuhlers Mastermet solution*. The Pb-rich phase etches preferentially, so in a light microscope the Pb-rich appears dark and the Sn-rich phase light, in the SEM this contrast is reversed.

Specimens for TEM were punched into 3 mm disks and hand polished to 2 mil thickness. Electropolishing was performed using 85% Ethyl Alcohol + 5% 2-Butoxyethynol + 10% Perchloric acid at 30-34 volts and 80mA current. Immediately before polishing both sides of the foil were ground with 600 grit paper to remove surface oxide. After electropolishing the foils were cold stage ion milled for 10 minutes at 5 KeV

---

* The Mastermet solution is a colloidal solution of fine (0.06 μm) SiO_2 particles with a high pH aqueous base that etches the surface.

and 0.3 mA per gun and and a tilt of 13°. TEM observations were made using the Kratos HVEM operated at 1.5 MeV.

4.1.2.3 RESULTS AND DISCUSSION

The optical microstructure of 60Sn-40Pb is shown in Figure 4.1.2.1. It has a two phase microstructure consisting of the Pb-rich phase (dark contrast) and a Sn-rich phase (light contrast). Figure 4.1.2.2 shows that β-Sn precipitates form within the Pb-rich phase, as is expected from the Sn-Pb phase diagram, Figure 2.5. Upon solidification, at the eutectic temperature, 19% Sn is soluble in the Pb-rich phase. On cooling to room temperature the solubility drops to about 1% Sn. The microstructure of 60Sn-40Pb solder is highly dependant upon the processing the alloy has received[62]. At moderate cooling rates, such as those found is this work and industrially in solder joints, the microstructure appears as in Figures 4.1.2.1 and 4.1.2.2. There are regions of lamella, Pb-rich and Sn-rich globular regions, and Pb dendrites decorated with Sn precipitates. The Sn-rich phase is interconnected and can be thought of as Swiss cheese, with the Pb-rich phase filling the holes the Sn-rich regions.

When 60Sn-40Pb solder is very rapidly quenched the microstructure changes appearance, Figure 4.1.2.3. The microstructure now consists of fine Pb dendrites in a fine globular Sn-Pb interconnected matrix. When work and recrystallization is imposed on 60Sn-40Pb the microstructure is no longer interconnected[63]. The imposed mechanical work breaks up the interconnectivity and recrystallization creates a fine two phase microstructure. This fine microstructure results in excellent superplastic properties[64]. If the 60Sn-40Pb solder is slowly solidified in a directional manner a lamellar structure results. Verhoeven et. al.[65] varied growth rates of directionally solidified solder and found both degenerate (wavy lamella) and regular lamella form as a function of the growth rate. The difference in lamellar structure was explained as being due to anisotropic thermal conductivity of the Sn influencing the isotherms in front of the soldification causing lamella to degenerate at high growth rates.

The microstructure characterized in depth for this study was processed at a moderate cooling rate, Figure 4.1.2.2. This is the typical microstructure found in the solder joints in an electronic package. The microstructure consists of Pb-rich dendrites, globular Pb-rich and Sn-rich regions, and wavy lamella.

β-Sn precipitates are found in all the Pb-rich phase regions. The TEM micrograph in Figure 4.1.2.4 shows Sn precipitates in globular Pb regions and Figure 4.1.2.5 shows the Sn precipitates in the Pb lamella (precipitates are indicated by arrows). The habit plane of the β-Sn precipitates in the Pb-rich regions is $(111)_{Pb}$ with an orientation relationship of

$(111)_{Pb}$ // $(010)_{Sn}$ and $[0\bar{1}1]_{Pb}$ // $[001]_{Sn}$. This is the same crystallographic relation as found for β-Sn precipitates in 5Sn-95Pb solder, as discussed previously in section 4.1.1. These precipitates have the same platelike morphology as in 5Sn-95Pb solder.

A study of the Sn-rich regions of 60Sn-40Pb was performed using high voltage TEM. Figure 4.1.2.6 shows both lamellar and globular Sn-rich regions. The Sn rich regions are found to be polygranular with an average grain size of 0.44 μm. The Pb grain size was not measured, but is much larger than the Sn grains. The Pb regions shown in Figure 4.1.2.6 are within a single grain of Pb. Verhoven[65] claims the lamella of Sn-rich regions have a large grain size, using an SEM electron channeling method to examine the crystallography. With the assumption that the grain size of the Sn is large, and comparable to that of the Pb, various different orientation relationships have been reported as existing between the Pb-rich and Sn-rich regions in 60Sn-40Pb[66-68]. The most accurate method reported to determine the orientation relationship was the electron channeling method used by Verhoeven. However, the beam size was 2 μm, which is often larger than the width of lamella examined. The scatter in reported orientation relationships could be due to the fine grain size of the Sn. This results in no true crystallographic relationship between the Pb-rich and Sn-rich regions in 60Sn-40Pb.

The microstructure of bulk 60Sn-40Pb was found to slightly coarsen with time at room temperature. Aging at elevated temperatures also produces coarsening, Figure 4.1.2.7, which shows 60Sn-40Pb after 167 hours at 125°C. The microstructure has experienced overall coarsening. High voltage TEM performed on these samples shown in Figure 4.1.2.8 indicates that the grains in the Sn-rich regions have also coarsened and is now 1.31 μm.

4.1.2.4 Summary and Conclusions

The microstructure of 60Sn-40Pb solder was characterized. The resultant microstructure was highly dependant upon processing. The microstructure studied in this work received a moderate cooling rate and consisted of Pb-rich dendrites, Pb and Sn-rich globular regions, and lamella. The Sn-rich phase was interconnected. β-Sn precipitates were found to form within the the Pb-rich regions with a platelike morphology and a crystallographic orientation the same as reported for 5Sn-95Pb (section 4.1.1). The Sn-rich regions were fine grained (an average grain size of 0.44 μm) and the Pb-rich regions had a much larger grain size. For this reason no orientation relationship was found between the Sn-rich and Pb-rich regions. Both phases were found to coarsen with time at elevated temperatures, and the Sn grain size increased to 1.31 μm after 167 hours at 125°C.

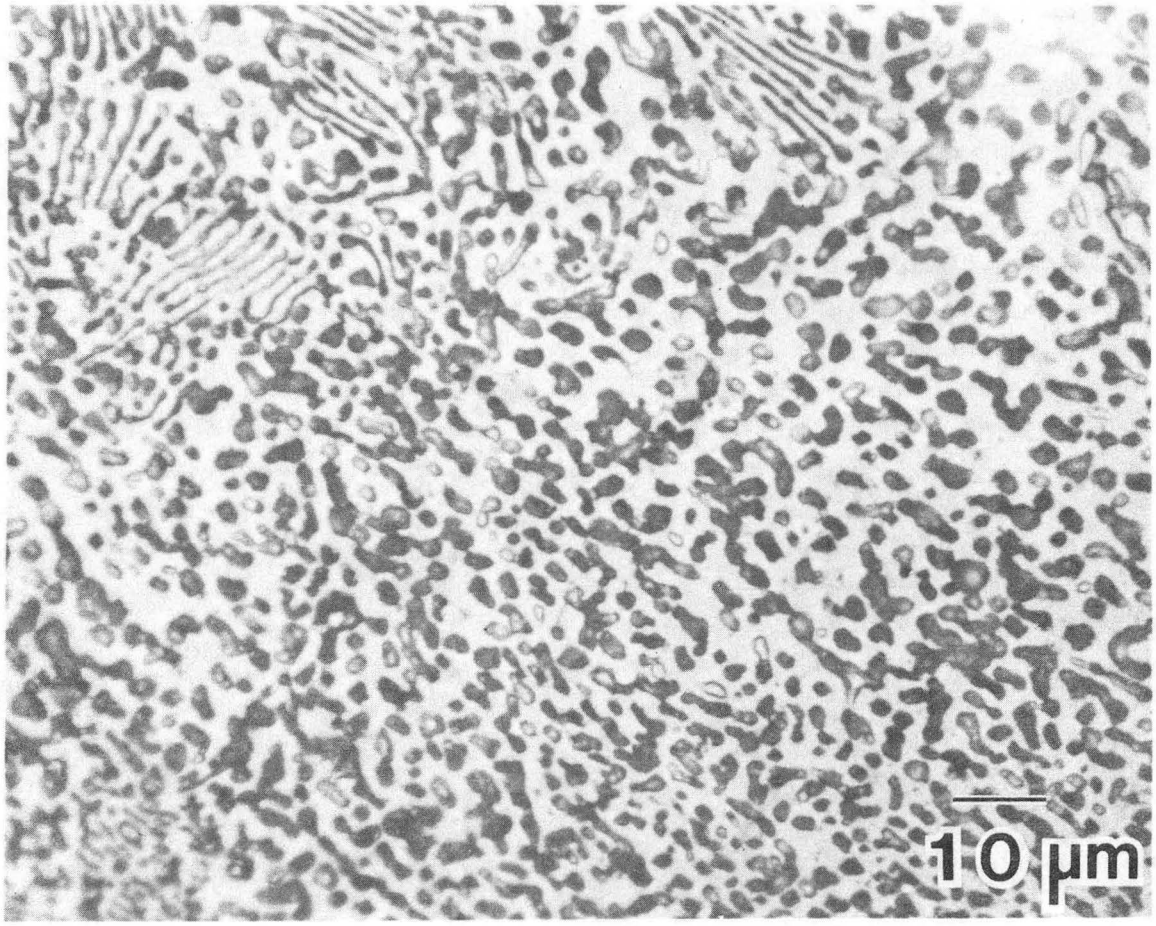

XBB 861-399

Figure 4.1.2.1 Optical micrograph of 60Sn-40Pb microstructure. The Pb-rich phase appears dark and the Sn-rich phase light.

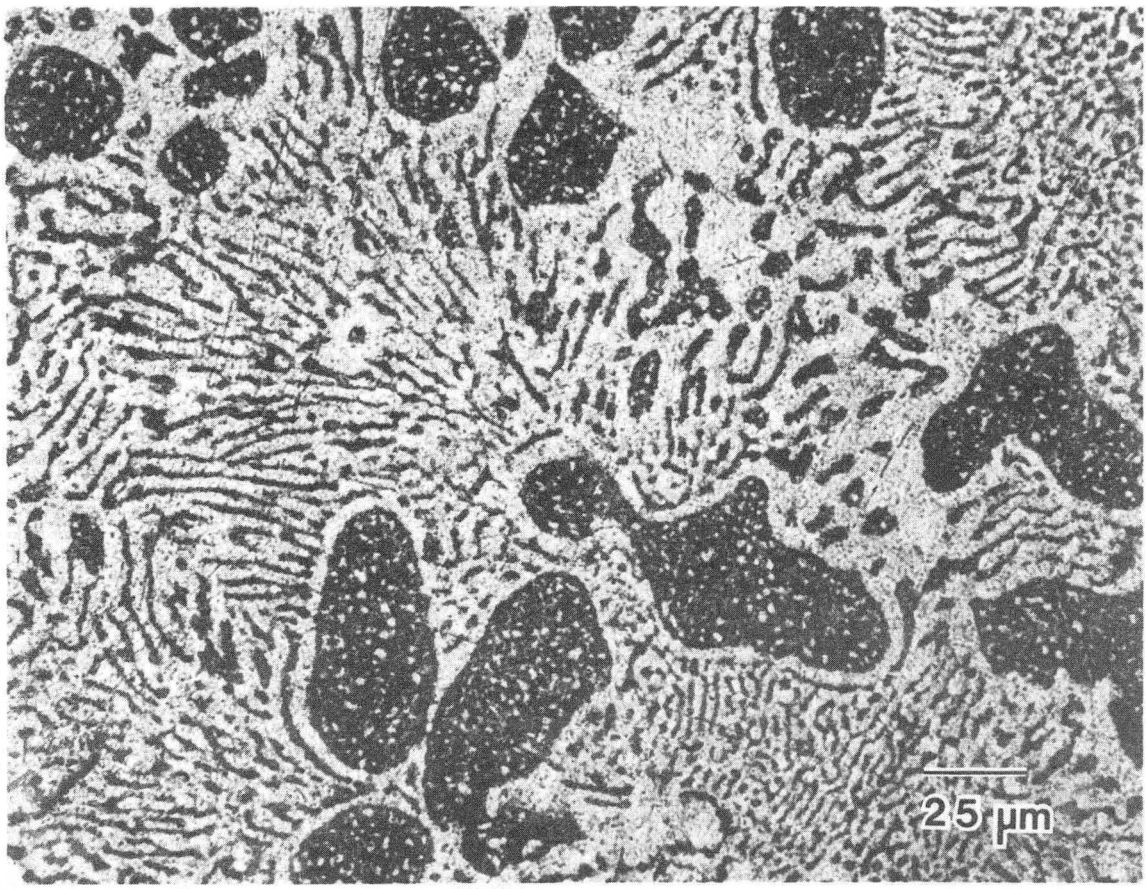

XBB 876-4399

Figure 4.1.2.2 Optical micrograph of 60Sn-40Pb illustrating Sn precipitates in Pb dendritic regions.

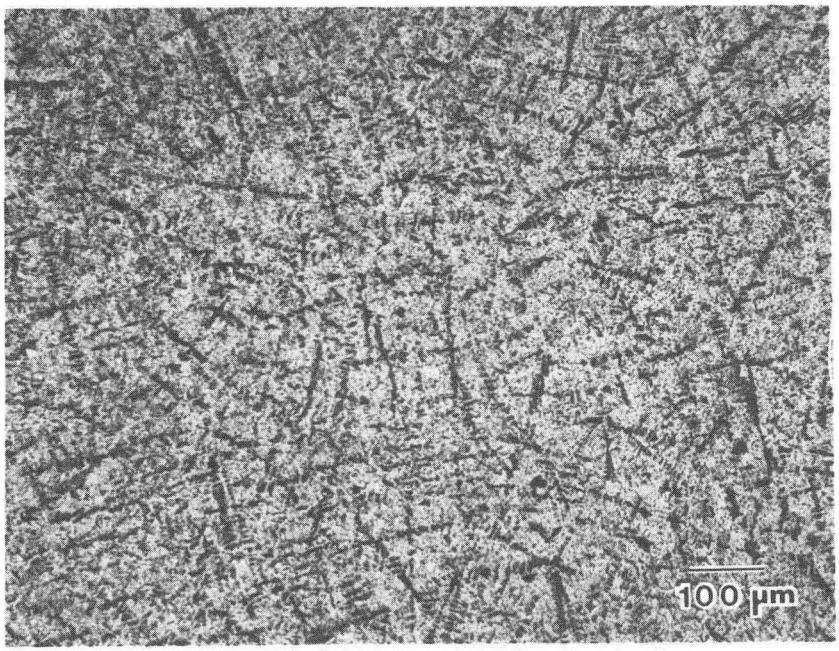

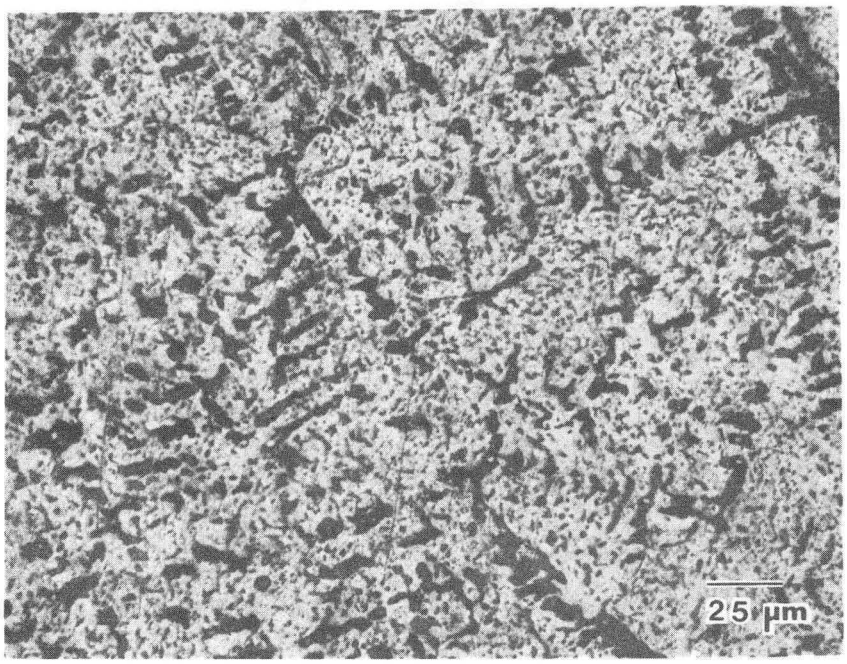

XBB 876-4405

Figure 4.1.2.3 Optical microstructure of rapidly quenched from the melt 60Sn-40Pb.

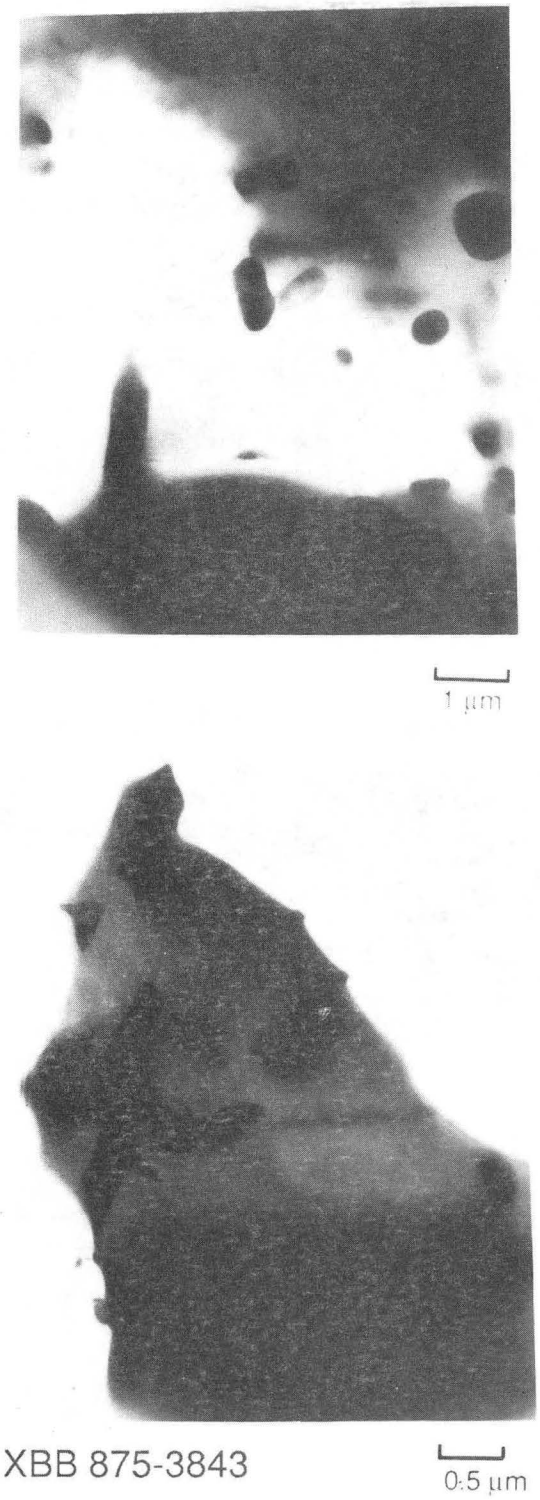

Figure 4.1.2.4 TEM bright field image of β-Sn precipitates in the globular Pb-rich regions in 60Sn-40Pb.

Figure 4.1.2.5 TEM bright field image of β-Sn precipitates in the lamellar Pb-rich regions in 60Sn-40Pb.

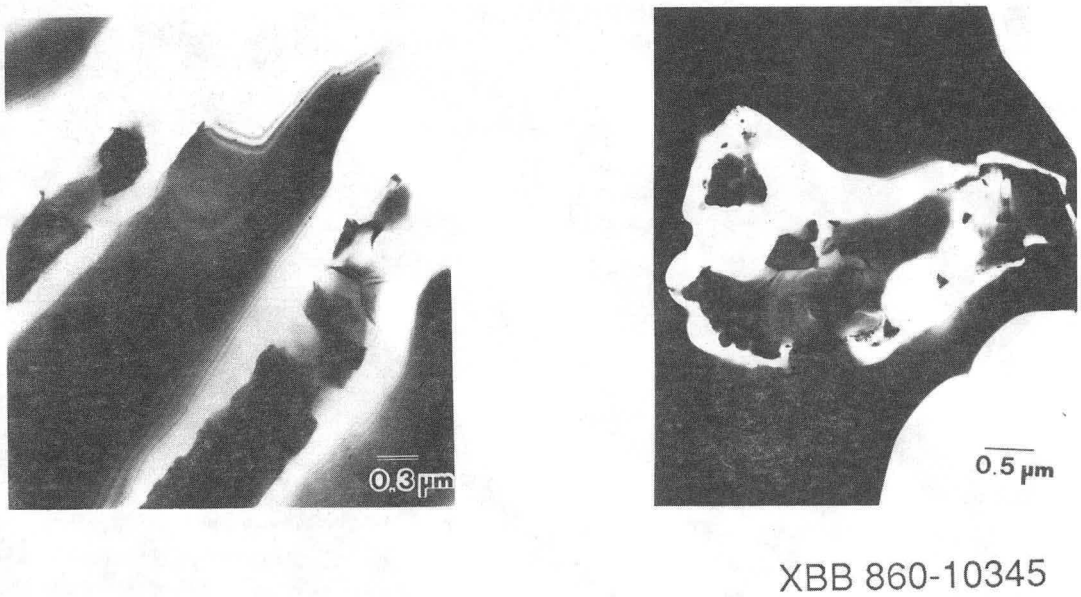

Figure 4.1.2.6 TEM bright field image of polygranular β-Sn in lamellar and globular regions in 60Sn-40Pb.

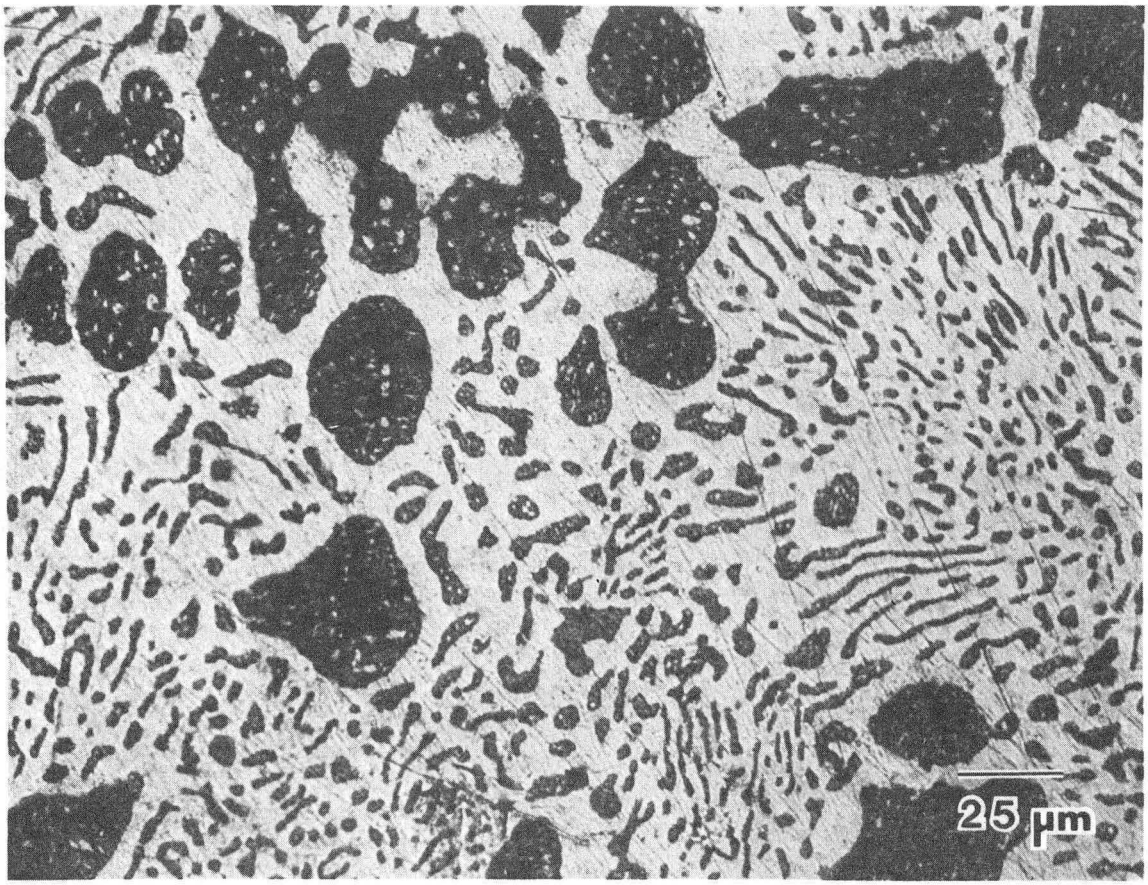

XBB 876-4401

Figure 4.1.2.7 Optical micrograph of 60Sn-40Pb after 167 hours at 125°C illustrating phase growth.

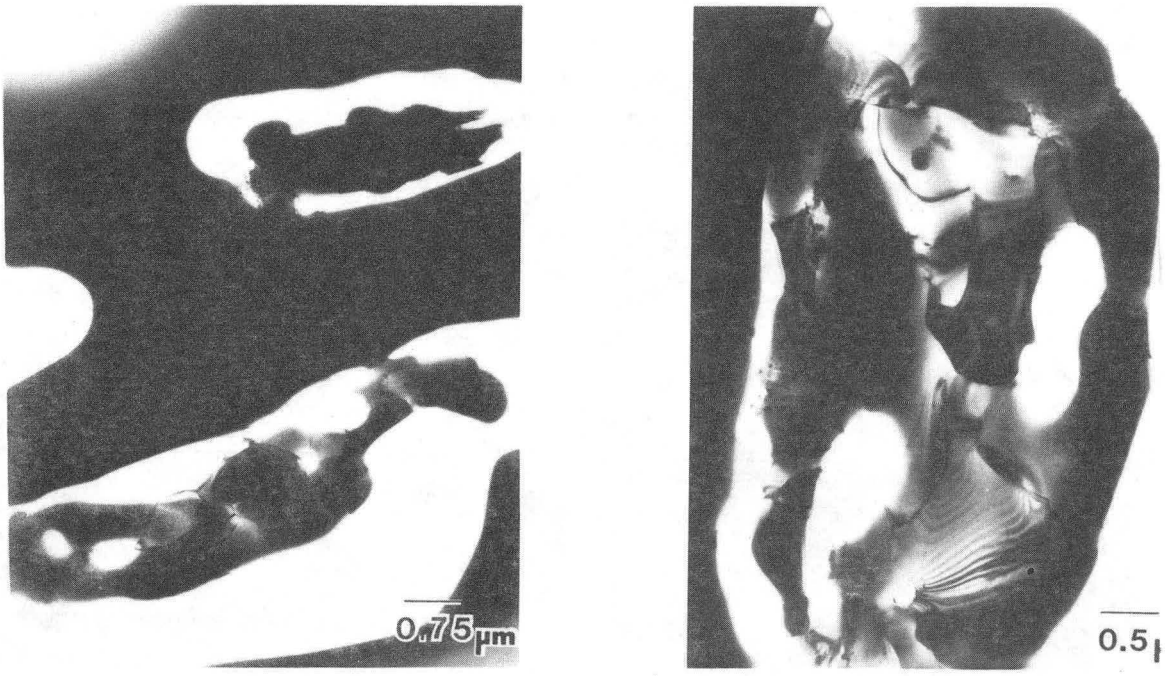

Figure 4.1.2.8 TEM bright field image of polygranular β-Sn after 167 hours at 125°C illustrating Sn grain growth.

4.2 INTERFACIAL INTERMETALLIC MICROSTRUCTURE

4.2.1 INTRODUCTION

The joints in an electronic package are comprised of the solder and the base metal the solder acts to join. A fairly complicated series of metallized layers has been developed to be able to join, say, polyimide to a ceramic chip carrier (and is discussed in Appendix I). The base metal that is soldered is most often made of copper.

When Sn-Pb solder comes in contact with Cu, the Sn and Cu react to form an intermetallic layer at the interface. The presence of this interfacial intermetallic is indicative of good wetting and that a metallurgical bond has formed. However, the presence of interfacial intermetallics is claimed to have a deleterious effect on the fatigue life of solder joints[9,30-35]. These studies claim that failures in joints initiate at the brittle intermetallics. This section presents and discusses the microstructure of the interfacial intermetallics that form when the solders 5Sn-95Pb and 60Sn-40Pb are joined to Cu.

4.2.2 BACKGROUND

There has been some previous work that looked at the reaction of Sn-Pb solder on Cu. The reaction of molten solder and Cu forms intermetallics that are solder composition dependant. For solders under 30% Sn only Cu_3Sn (ε-phase) forms, above 30% Sn both Cu_3Sn and Cu_6Sn_5 (η-phase) form at the interface[69]. These are the only intermetallics that can form at temperatures below 350°C, as shown in the Cu-Sn phase diagram in Figure 4.2.1. However, there is question as to whether Cu_3Sn and Cu_6Sn_5 form in the as- soldered condition with 60Sn-40Pb[70,71], or Cu_3Sn forms after Cu_6Sn_5 upon subsequent aging of the joint[76,82-84].

Research on 5Sn-95Pb solder shows that only ε-phase forms on reaction with Cu[69,72]. Apparently the smaller amount of Sn present in the 5Sn-95Pb solder precludes the formation of the Sn-rich η-phase. Some researchers claim that the Cu_3Sn intermetallics spall off into the molten solder on formation[69,73], and even a model for spallation is proposed[73] that relies on internal stress in the intermetallic layer. The observations presented in this chapter suggest that this spallation is a polishing artifact. The dissolution of Cu into molten solder has been well documented in higher Sn solders, such as 60Sn-40Pb[74-76].

The binary Cu-Sn phase diagram is shown in Figure 4.2.1. Two intermetallic phases can form when Sn is in contact with Cu: ε-phase and η-phase. The ε-phase is ordered and has an orthorhombic long period superlattice with a = 5.514 Å, b = 38.16 Å, and c =

4.329 Å. This long periodicity can be shortened[76a] to a = 5.514 Å, b = 4.7605 Å, and c = 4.329 Å. The η-phase undergoes a transition from η to η' at 170°C which transforms the hexagonal NiAs η-lattice to a long period η'-superlattice. Tables III, IV, and V show the lattice spacing and indexed lattice planes for α-Cu, and the ε and η intermetallics.

This section presents observations of the intermetallic phase Cu_3Sn that forms when 5Sn-95Pb is soldered to Cu. The chemical state and morphology of the intermetallic layer and its growth kinetics are discussed in the context of these observations. Also discussed is the chemical state, morphology, and growth of the two-phase Cu_3Sn and Cu_6Sn_5 intermetallics that form on the reaction of 60Sn-40Pb with Cu.

4.2.3 EXPERIMENTAL PROCEDURE

Three oxygen-free Cu plates were cut to dimensions of 101.6 mm x 31.75 mm, with two plates 0.32 mm thick and one plate 0.64 mm in thickness. These plates were polished down to 1 μm Al_2O_3 powder and were etched with 25% HNO_3 + 75% H_2O to remove the damaged layer of Cu. A light coat of Johnsons Stainless Steel Soft Soldering flux was dried on the interior surface and the plates were assembled as shown in Figure 3.1. A 0.13 mm gap for the solder was created using a this strip of stainless steel.

The assembled sample was then placed in a vacuum furnace, which is illustrated in Figure 3.2. the specimen was held above the molten solder bath for 1/2 hour to burn off the flux and create an oxide free Cu surface for soldering. A pull rod was used to submerge the Cu plates briefly in a molten bath of 5Sn-95Pb solder at 400°C and 240°C for 60Sn-40Pb solder. Capillary action pulls the molten solder between the Cu plates. The furnace was then turned off, the specimen allowed to cool and the excess solder removed from the specimen.

Samples for optical analysis were cut from the soldered specimen. For reflow experiments the samples were placed horizontally in the furnace so that the solder would not squeeze out of the joint. In this orientation the surface tension of the solder was sufficient to keep the molten solder between the Cu plates. Samples were reflowed at 400°C for 5Sn-95Pb and 240°C for 60Sn-40Pb for microstuctural observations. Additional reflows were performed at 350°C and 450°C to determine the diffusion constants for 5Sn-95Pb on Cu.

For optical observations of the 5Sn-95Pb/Cu joint the sample was first mounted in Klarmount. Before polishing a small amount of the solder was etched away using 30% H_2O_2 + 70% glacial acetic acid. A layer of epoxy was then dried into the gap formed. The specimens were then polished to 600 grit on silicon carbide paper. Polishing was

performed using 6 μm diamond paste followed by a 0.6 μm silica suspension. The specimens were etched in 5 parts NH_4OH + 5 parts H_2O + 2 parts H_2O_2 (30%) to reveal the ε-phase intermetallic. The samples were viewed in a Nikon optical microscope. To observe the bulk microstructure of 5Sn-95Pb in solder joint the joints were polished on felt paper using 0.05 μm Al_2O_3 and kerosene. The samples were etched for 5 seconds using 40 ml H_2O + 10 ml HNO_3 + 7.5 ml Glacial Acetic acid and then for 20 seconds using 3 parts Glacial Acetic acid + 1 part H_2O_2 (30%). Due to uneveness of the etched surface observations were performed on the SEM. Optical observations of the 60Sn-40Pb joint were performed on samples mounted in Koldmount. Specimens were polished to 600 grit on silicon carbide paper. Polishing was performed using 1 μm aluminum oxide. Final polishing and etching was performed using the colloidal suspension of Mastermet polishing solution.

Both 5Sn-95Pb/Cu and 60Sn-40Pb/Cu samples were etched with 20% H_2O_2 + 80% glacial acetic acid until the Cu interface was free of solder to reveal the intermetallic for surface examination in the SEM.

4.2.4 Results and Discussion

4.2.4.1 5Sn-95Pb on Cu

• Chemical State of Joint

The as-soldered 5Sn-95Pb solder/Cu joint is shown in Figure 4.2.2. As-soldered signifies that the solder flowed between the Cu plates and then was cooled to room temperature over a total time of approximately four minutes. The joint consists of solder, a thin layer of intermetallic, and the Cu base plate. Energy dispersive x-ray analysis found the joint to be depleted to 3-4%Sn. Thus the formation and growth of the intermetallic also weakens the solder joint by depleting the solder of Sn. The Sn acts as a solid solution and precipitation hardening element in Pb. As the solder is drained of Sn the strength of the solder decreases. No evidence of the Sn rich η phase was found in the as-soldered or reflowed specimens. For η-phase to form a higher content of Sn must be present in the solder[69].

The microstructure of the 5Sn-95Pb solder in the center of the joint is shown in Figure 4.2.3. The microstructure consists of β-Sn precipitates dispersed homogeneously within the Pb grains. This microstructure is the same as that found for bulk as-solidified 5Sn-95Pb solder discussed in section 4.1.1.

• Physical State of Joint

Figure 4.2.4 is a micrograph taken with polarized light of the intermetallic layer after 5 hours reflow at 400°C. This specimen was selected for observation since the morphologies of specimens reflowed for various times were all similar, but the intermetallics are more clearly observable after longer reflow times. As is shown in the Figure 4.2.4, the ε grains are columnar. The Cu/intermetallic and solder/intermetallic interface profiles match closely. The similar contours suggest that Sn diffuses from the molten solder into the Cu allowing the ε to form at the Cu interface. This hypothesis is in accord with results in the literature that Sn is the faster diffusing species in the ε phase and that Sn diffuses into the Cu[75,77-79]. However, the direction of interface motion was not determined directly.

The interface between the intermetallic and Cu is continuous and intact. No spalling of the intermetallic was observed. Previous observations of the intermetallic breaking off during soldering[69,73] are apparently a polishing artifact. The Cu_3Sn intermetallic is brittle so during polishing it may fracture and imbed itself in the soft solder. However, if during polishing the soft solder is reinforced with a layer of epoxy the intermetallic layer remains intact.

Figure 4.2.5 is a micrograph of ε grains after 5 hours of reflow. The joint was sectioned through the intermetallic almost parallel to the Cu surface. Figure 4.2.6 is an SEM micrograph of a similar sample. Here the solder has been completely etched off and the top intermetallics grains are revealed at the solder / Cu_3Sn interface. The number of cracks present in the intermetallic gives an indication of the brittleness of this layer. There is no evidence to suggest that these cracks formed during soldering. However, if the interface was not reinforced with epoxy during mechanical polishing there was a large increase in the number of cracks present in the intermetallic. This observation suggests that the intermetallic cracks formed under the relatively small stresses applied in cutting and polishing. The crack in the center of Figure 4.2.5 runs both transgranularly and intergranularly showing that both the grain boundaries and the grains themselves are susceptible to cracking. This result contrasts with previous work[30] that found cracking in the ε-phase occurs via a cleavage mechanism along particular crystal planes.

• Layer Growth

Reflow experiments were performed to observe changes in the intermetallic that occur when the solder is molten. Reflow was performed at 400°C in an air ambient. Oxidation during heat treatment was not a problem because the oxide formed only on the surface of the specimens. To avoid the surface oxide the specimens were cut in half after reflow and

observations were confined to the central portions of the specimen. Samples were allowed to air cool after the heat treatment. Figure 4.2.7 is a plot of ε-phase layer thickness vs. time at molten temperature, 400°C. In the as-soldered condition the intermetallic is 4 μm thick. A typical micrograph of this joint is shown in Figure 4.2.2. After three hours at 400°C the intermetallic layer is 11 μm thick. The saturation at 11 μm occurs because at this thickness the solder in the joint is almost totally depleted of Sn after which the layer no longer coarsens. An example of the intermetallic after 5 hours of reflow is shown in Figure 4.2.4.

The determination of diffusion constants was performed using three reflow temperatures: 350°C, 400°C, 450°C. No diffusion markers were used so the layer thickness was taken to be the distance between the Cu / Cu_3Sn and Pb-Sn / Cu_3Sn interfaces. A plot of the square of the layer thickness vs. time is shown in Figure 4.2.8. The slope of these lines gives the diffusivity, D. An Arrhenius plot of the natural logarithm of D vs. 1/T, shown in Figure 4.2.9, gives the activation energy for diffusion, -Q/R. From this plot Q was found to be 13 kcal/mol and the pre-exponential constant D_0 to be 2.1×10^{-6} cm^2/sec.

The activation energy of 13 Kcal/mol is consistent with values reported in the literature. Reported values are 11 kcal/mol[75], 14.6 kcal/mol[77], and 21 ± 4.8 kcal/mol[80] for pure Sn reacting with Cu to form Cu_3Sn. One study[81] found the activation energy to be 20.5 kcal/mol for the formation of ε phase on the reaction of 5Sn-95Pb with Cu. The pre-exponential constant $D_0 = 2.1 \times 10^{-6}$ cm^2/sec calculated in this study is also in accord with published values[75,77].

4.2.4.2 60Sn-40Pb on Cu

• Chemical State of Joint

The optical microstructure of as-soldered 60Sn-40Pb on Cu is shown in Figure 4.2.10. Energy dispersive x-ray analysis determined that the light phase adjacent to the Cu is Cu_3Sn. The dark convoluted phase adjacent to the solder was determined to be Cu_6Sn_5. The Cu_3Sn phase forms on soldering, which is in agreement with other work[70,71]. Other observations state that only η-phase forms during the soldering process[76,82-84]. (However, it is generally agreed that, regardless of the initial layers formed on soldering, a two phase Cu_3Sn/Cu_6Sn_5 structure develops on aging.) This discrepancy could be due to the difference in the time the solder is molten on the Cu. For this work the solder was molten for approximately 3 minutes while in the other cases a

shorter time was used. Additionally the ε-phase is very thin and is difficult to observe in the as-soldered condition.

• Physical State of Joint

Figure 4.2.11 is an optical micrograph of 60Sn-40Pb on Cu reflowed for 5 hours at 240°C taken under polarized light, revealing the two phase microstructure. The ε-phase has a fine columnar microstructure. The η-phase is rounded and apparently coarse grained, but the polarized light does not reveal the grain boundaries in η. Figure 4.2.12 shows a joint sectioned through the intermetallic layer almost parallel to the Cu interface. Under this polarized light the ε-phase is shown to be very fine grained, on the order of 0.5 μm in diameter.

The difference in the morphology of the η-phase in the as-solidified and reflowed conditions is shown in Figures 4.2.13 and 4.2.14. In Figure 4.2.13 an as-solidified 60Sn-40Pb/Cu joint was sectioned almost parallel to the Cu surface and the solder was deeply etched with Acetic acid and H_2O_2 to reveal the intermetallic regions. The figure reveals the η-phase intermetallic from an orientation looking down on the intermetallic as it grows out into the solder. The as-solidified η–phase intermetallic has a faceted rod-like morphology, Figure 4.2.13b. As is shown in section 4.3 these rods are each a single crystal of Cu_6Sn_5. The faceted morphology of the η-grains has also been observed by Warwick and Muckett[85].

Figure 4.2.14 shows the morphology of the reflowed joint after 5 hours at 240°C revealing the η-intermetallic. The specimen orientation is similar to that of Figure 4.2.13. Here the η-grains are still somewhat faceted but are much more rounded and larger grained. Apparently the rods of the as-solidified joint have coalesced and coarsened to form the convoluted grains shown in Figure 4.2.14.

• Layer Growth

The thickness of the intermetallic increases with time at reflow temperature as shown in Figure 4.2.11. The η-phase has become more globular and the ε-phase retains a columnar microstructure. Attempts have been made in the literature to calculate the activation energy and diffusivities for two phase intermetallic growth of 60Sn-40Pb on Cu[81]. A theoretical model of layer growth of binary alloys by Kidson[86] has been used to calculate layer thickness[87]. According to this theory the thickness of the alloy layer is a function of the difference of interface separation, the width of the ith layer in a system on n phases and n-1 interfaces:

$$w_j = 2\sqrt{t}\left\{\left[\frac{(DK)_{j+1,j}-(DK)_{j,j+1}}{C_{j,j+1}-C_{j+1,j}}\right]-\left[\frac{(DK)_{j,j-1}-(DK)_{j-j,j}}{C_{j-j,j}-C_{j,j-1}}\right]\right\}$$

where:

w_j = Alloy layer thickness of jth phase
D_{ij} = Diffusion coefficient of i (or j) in a system of i,j
K_{ij} = Constant
C_{ij} = Concentration solute
t = reaction time

With this relationship the intermetallic thickness can be determined as a function of ln(w) α 1/t. It is assumed in this calculation that a planar interface exists between the components of the system. The diffusion relationships were calculated using total intermetallic layer thickness of both η and ε. However, as shown in Figures 4.2.10 and 4.2.11 the intermetallics do no have planar interfaces, in fact the η-phase is quite convoluted. Any diffusion measurements had a large degree of error. Therefore diffusivities for the two phase intermetallics were not calculated in this work.

The formation of the intermetallics can be at least qualitatively discussed from the microstructural observations presented thus far. The reaction to form intermetallics involves the diffusion of Sn into the Cu and Cu out to the Sn. (Gerth[88] analyzed both ε and η-phases and found that Pb was insoluble in both.) Diffusion couple experiments in the literature[75,77,79,89] found that Sn is a fast diffuser through Cu_3Sn indicating that the layer growth of Cu_3Sn is down into the Cu. The morphology of the η-phase indicates that Cu has diffused out to the Cu/molten solder interface and reacted there and thereby forms a very convoluted surface shown in Figures 4.2.10,11,13,14. The initial Cu was very planar, similar to that seen at the interface between Cu/Cu_3Sn and Cu_3Sn/Cu_6Sn_5.

A proposed mechanistic model for the formation of this two phase interfacial intermetallic is the following, and is diagrammed in Figure 4.2.15. Initially upon soldering, Cu and Sn react to form Cu_6Sn_5 at the interface and this transforms to Cu_3Sn at the Cu/η interface. The η-phase has a broken up rod-like morphology so the Sn can diffuse easily to the ε-phase (where it is a fast diffuser) and then react with the Cu to form Cu_3Sn at the ε/Cu interface. Meanwhile Cu reacts with the Sn at the η/ε interface causing the η-rods to grow, from their base, out into the molten solder. For the reflowed intermetallics the η-phase coarsens horizontally as well as the initial vertical growth direction causing the rods to coalesce and coarsen, Figure 4.2.14.

It has been argued that a Pb-rich region forms adjacent to the interfacial intermetallics because the solder has become depleted of Sn[82,84,89,90]. This was not observed in this work even after extensive reflows where an even mixture of Sn and Pb is found adjacent to the solder/intermetallic interface. However, a Pb-rich region may form if the intermetallics develop at temperatures below the melting temperature of the solder.

• Intermetallic Crystallography

An HVEM image of the Cu_3Sn interfacial intermetallic after 5 hours of reflow at 240°C is shown in Figure 4.2.16. In the process of ion milling the η-phase was preferentially milled away. The ε grains are columnar in nature and show a twinned microstructure, with the twins parallel to the columnar c-axis. This twinning phenomenon of the ε-phase has been observed by Kim[91] in a Cu-25%Sn alloy. A possible explanation for twinning is the stresses imposed upon the intermetallic layer on formation. A diffraction study by Tu[83] on thin films of Sn on Cu found that the Cu was in tension, the Sn was in compression and the intermetallic η'-layer was also in compression in the plane of the film. The largest strain was only 0.16% but this would be sufficient to force the ε-phase to twin but not spall or fracture.

A crystallographic relationship between the Cu and ε-phase interfacial intermetallic is shown in the TEM micrograph of Figure 4.2.17. Diffraction patterns from various ε grains are shown, as well as the pattern for the Cu substrate. The Cu in this micrograph has an orientation of $B = [013]_{Cu}$ and the columnar grains of ε phase have formed on this Cu orientation. This is in contrast to work by Tu[83], on thin film Sn on Cu, who found the grain size of ε comparable to the parent Cu and Sn phases. Although there are high angle boundaries between the ε grains there is a common $[002]_\varepsilon$ growth direction for all the columnar ε grains shown. This also indicates that the twinning does not occur on the basal planes of ε but rather on the faces, $(100)_\varepsilon$ planes, of the hexagonal crystal structure. It also appears that the $(002)_{Cu}$ planes are almost parallel to the $(002)_\varepsilon$ planes.

Figure 4.2.18 is a TEM micrograph showing the interface between two ε grains and the Cu substrate. The ε grains appear to be growing into the Cu faster at the ε-grain boundary. This indicates that Sn is diffusing down the ε grain boundaries and reacting with the Cu at the ε/Cu interface. It appears that the ε grows into the Cu by a grain boundary diffusion mechanism.

4.2.5 CONCLUSIONS

• 5Sn-95Pb on Cu

The reaction of 5Sn-95Pb solder with Cu results in the formation of ε-phase Cu_3Sn intermetallic. The size of the intermetallic layer increases with the length of time the solder is molten. The formation of the intermetallic causes a decrease in the Sn concentration of the solder. The Cu_3Sn phase that forms has a fine columnar grain structure and is brittle. Both intergranular and transgranular cracks were found to form in the intermetallic during polishing. The intermetallic did not spall off, as some previous studies have stated. The spalling tendency appears to be a polishing artifact. The activation energy for diffusion was found to be 13 kcal/mol and the pre-exponential diffusion coefficient D_o to be 2.1 x $10^{-6}cm^2/sec$, both of which are consistent with previously published values.

• 60Sn-40Pb on Cu

The reaction of 60Sn-40Pb with Cu results in the formation of two interfacial intermetallics. The η-phase Cu_6Sn_5 forms adjacent to the solder and ε-phase Cu_3Sn adjacent to the Cu. The ε-phase has a columnar morphology while the η-phase has a rod like faceted morphology. Studies of these intermetallic layers in TEM showed that the columnar ε grains have high angle boundaries but a common $(002)_\varepsilon$ growth direction. The internal structure of the ε grains is twinned along the c-axis. The twinning is thought to occur due to compressive stresses in the intermetallic layer that arise on formation of the intermetallic. Both intermetallic phases were found to grow during reflow. However, the diffusion constants were not calculated due to the irregular nature of the η-phase. A model for the formation and growth of the interfacial intermetallics was presented which involves the Cu and Sn reacting to form Cu_6Sn_5 at the interface which transforms to Cu_3Sn at the Cu/η interface. The η-phase has a broken up rod-like morphology. Therefore the Sn can easily diffuse to the ε-phase (where it is a fast diffuser) and reacts with the Cu to form Cu_3Sn at the ε/Cu interface. Meanwhile Cu reacts with the Sn at the η/ε interface causing the η rods to grow, from their base, out into the molten solder.

TABLE III (η phase Cu_6Sn_5)

d(Å)	Indexed as ordered NiAs structure a = 4.19 Å b = 5.09 Å	Indexed as long period superlattice a = 0.85 Å b = 25.10 Å
3.6		501*
3.41		503*
2.95	101	505
2.74		515*
2.55	002	0,0,10
2.45		525*
2.27		535*
2.09	110	550
2.01		554*
1.72	201	10,0,5
1.61	112	5,5,10
1.54	103	5,0,15
1.47	202	10,0,10
1.32	211	10,5,5
1.23	203	10,0,15
1.21	300	15,0,0

* Long period superlattice of η'

TABLE IV (ε phase Cu_3Sn)

d(Å)	Indexed as ordered orthorhombic lattice a = 5.514 Å b = 4.765 Å c = 4.329 Å	Indexed as long period superlattice a = 5.514 Å b = 38.16 Å c = 4.329 Å
3.4	101*	101
3.2	011*	081
2.75	200	181
2.67		191†
2.38	210*	280
2.32		290†
2.23		2,10,0†
2.16	002*	002
1.9	112	182
1.59	022	0,16,2
1.37	230	2,24,0
1.23	213	282
1.16	222	2,16,2
1.15	311	381

* Superlattice line of ε

† Long period superlattice line of ε

Table V

(CU)
Face Centered Cubic, 4 atoms/unit cell
$a_o = 3.615$ O^5_H - Fm3m

d Å	hkl
2.088	111
1.808	200
1.278	220
1.090	311
1.0436	222
0.9038	400
0.8293	331
0.8083	420

Cu-Sn

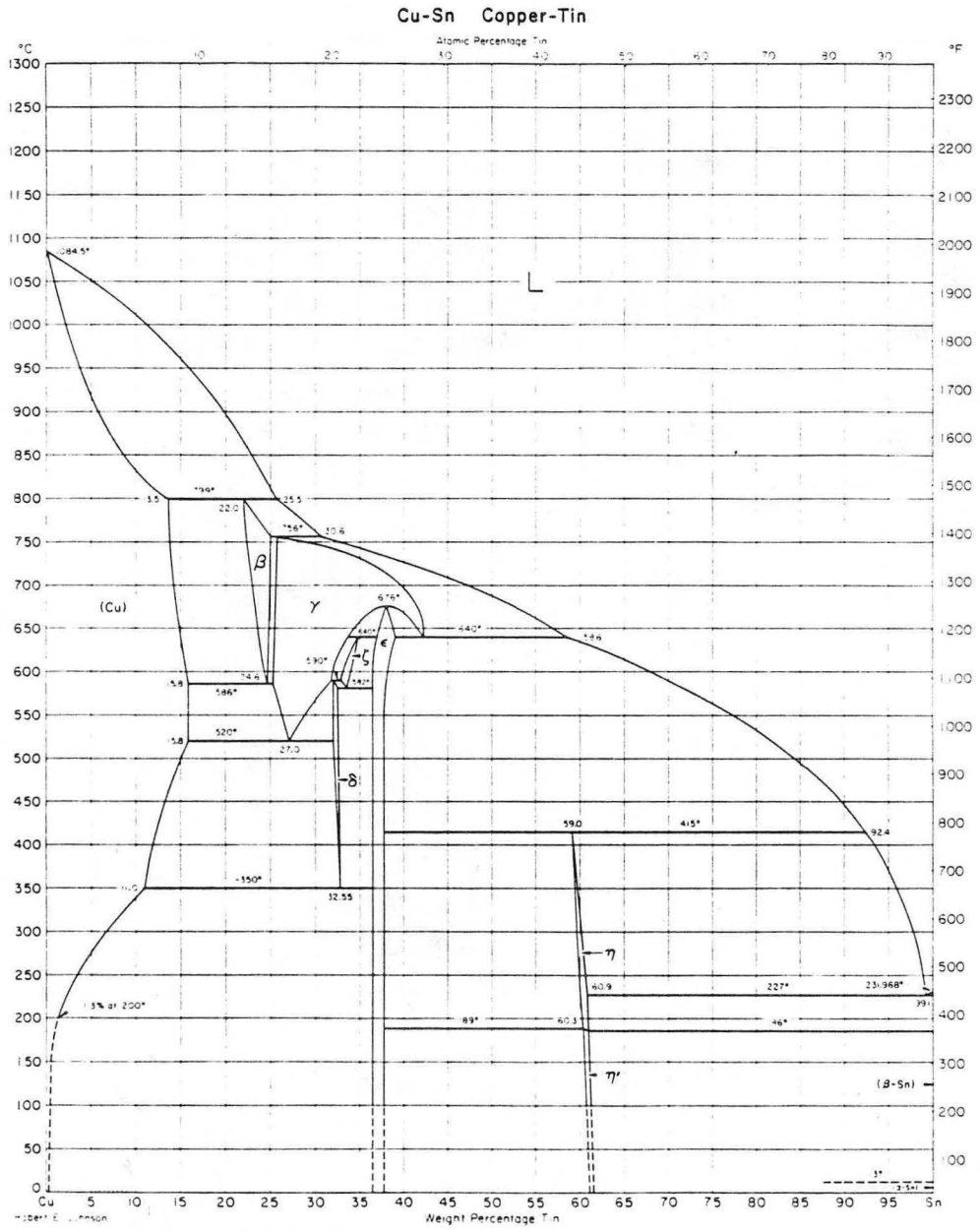

Figure 4.2.1 Cu-Sn phase diagram (taken from ASM Metals Handbook volume 8, pg. 299)

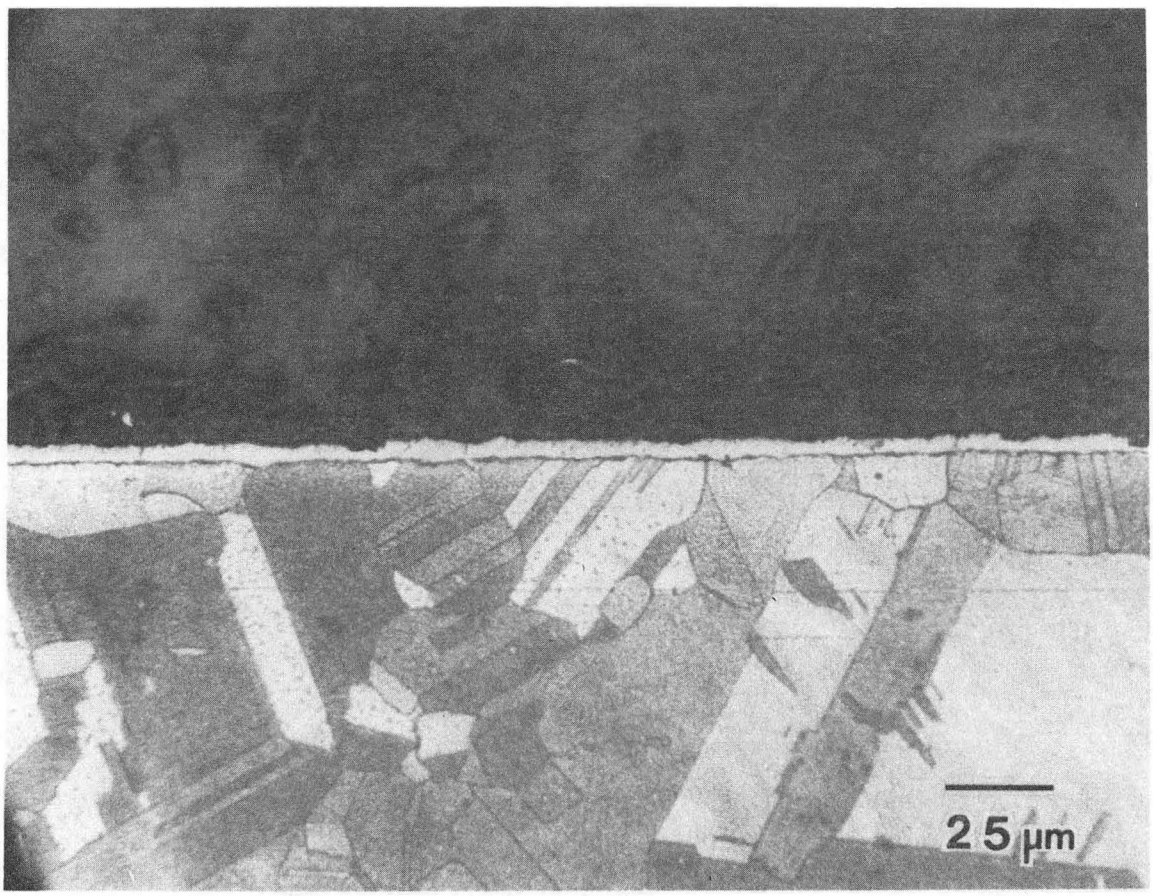

XBB 854-2592

Figure 4.2.2 Optical micrograph of the as-soldered 5Sn-95Pb/Cu interface showing the Cu_3Sn interfacial intermetallic.

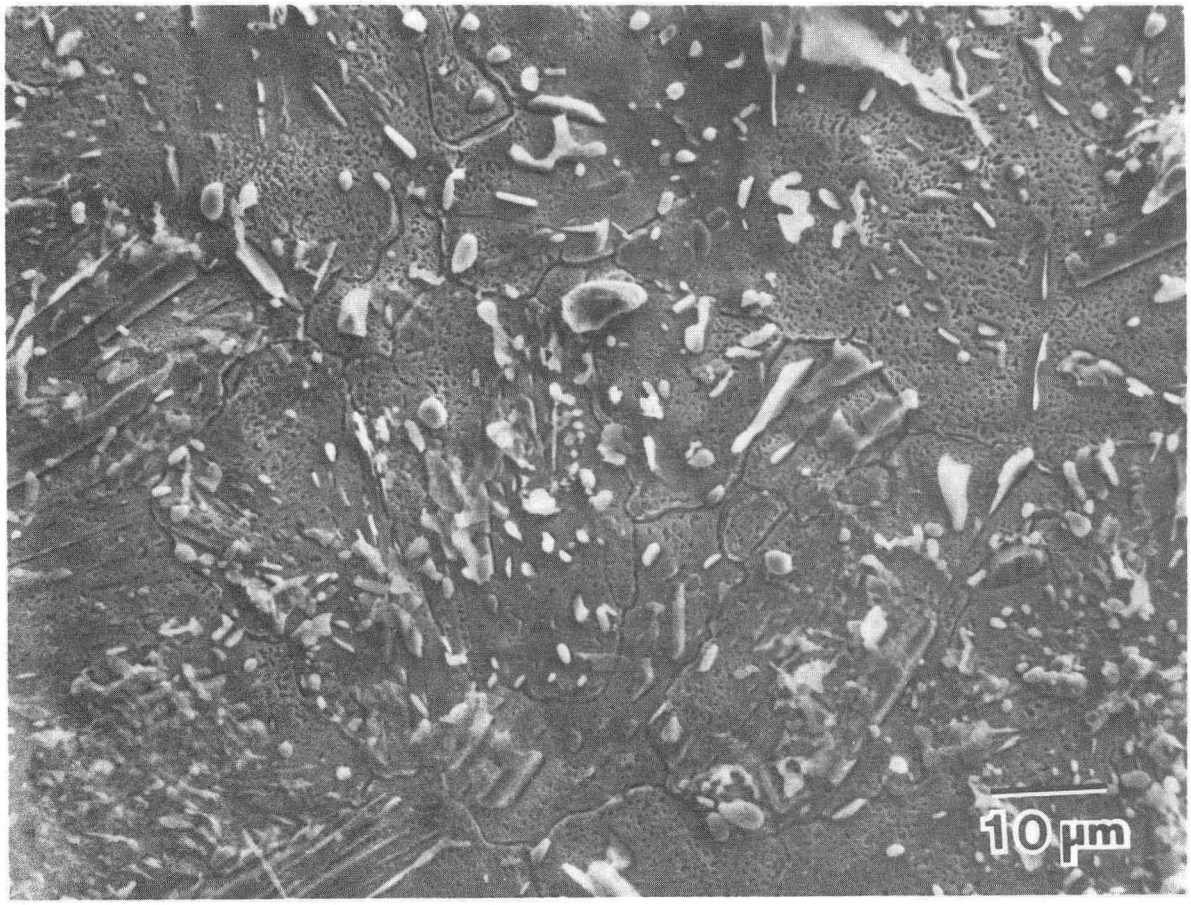

XBB 876-4398

Figure 4.2.3 SEM micrograph showing the microstructure of the 5Sn-95Pb within the as-soldered joint.

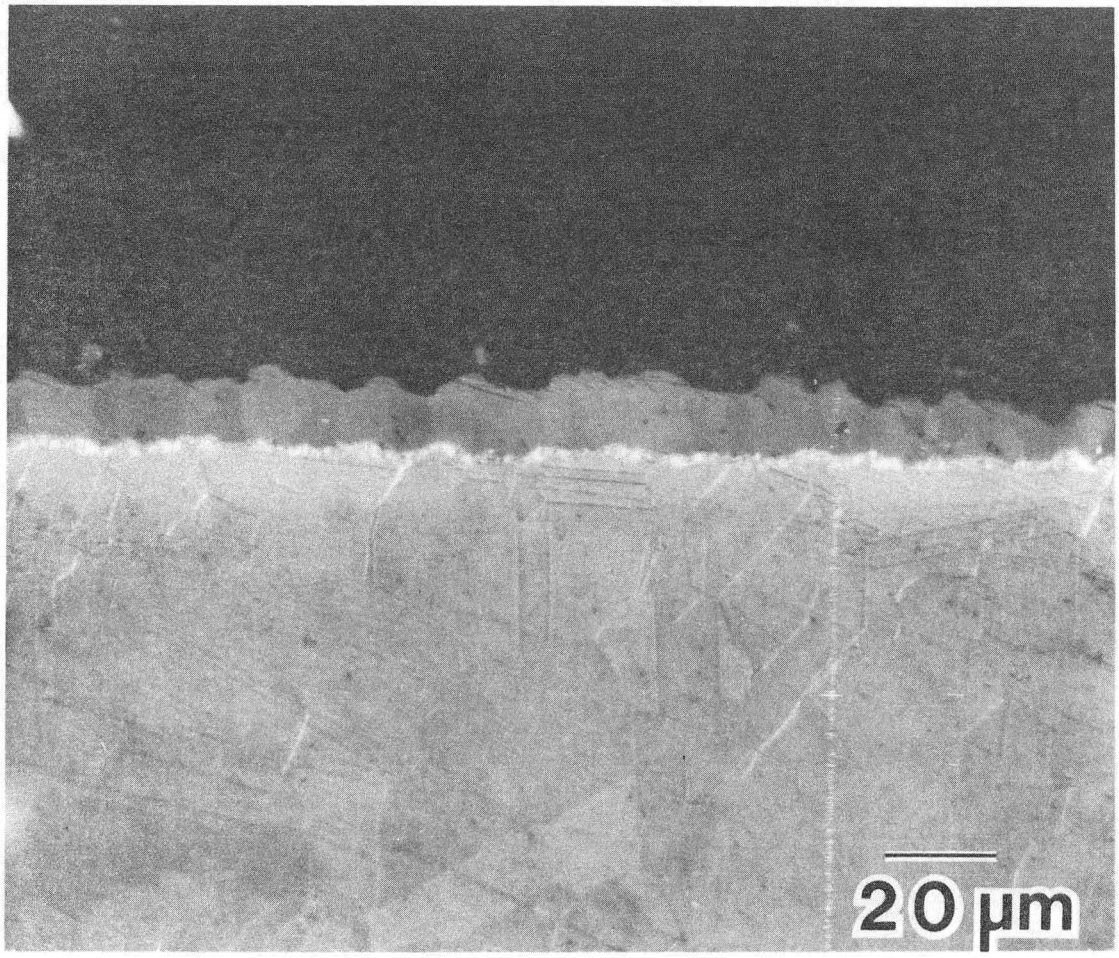

CBB 861-401

Figure 4.2.4 Polarized optical micrograph of the Cu_3Sn intermetallic revealing the columnar microstructure of the intermetallic.

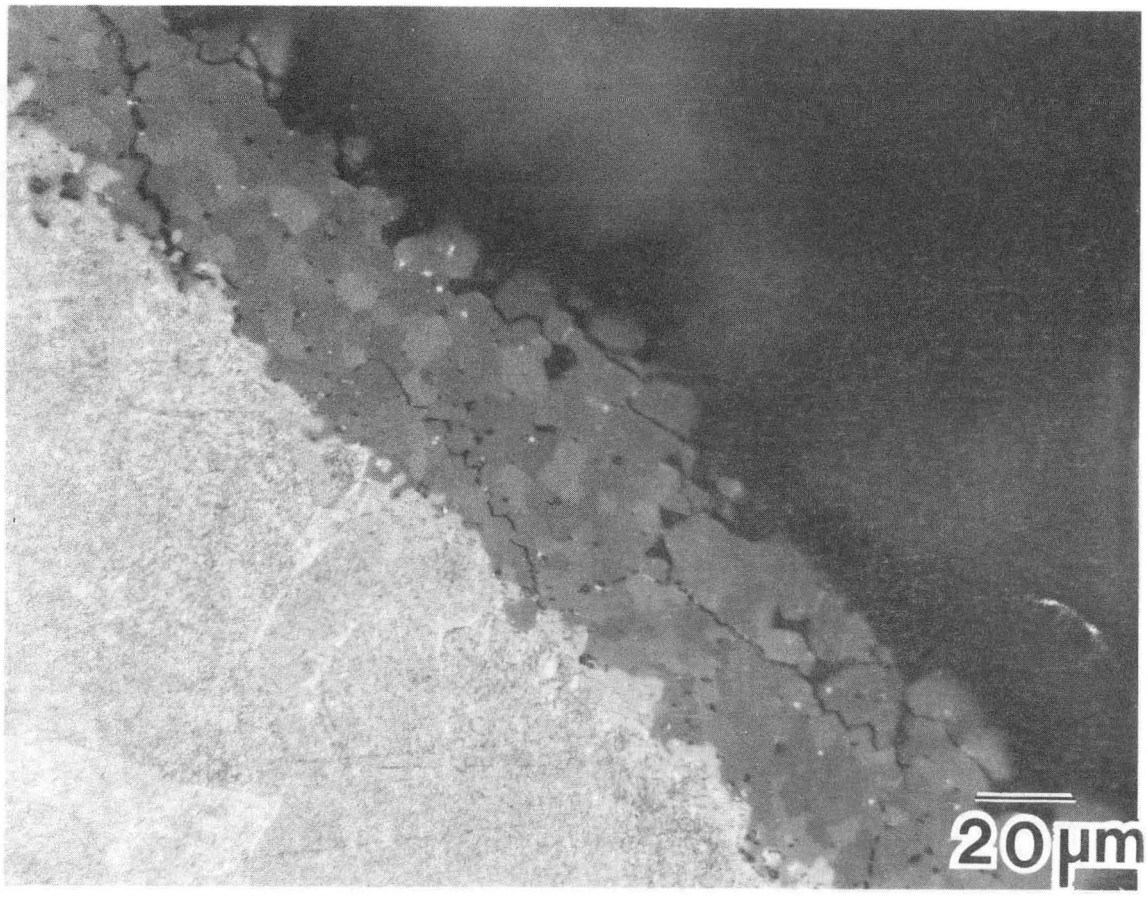

XBB 854-2607A

Figure 4.2.5 Polarized optical micrograph of the Cu_3Sn intermetallic sectioned almost parallel to interface showing the fine grained microstructure of the intermetallic.

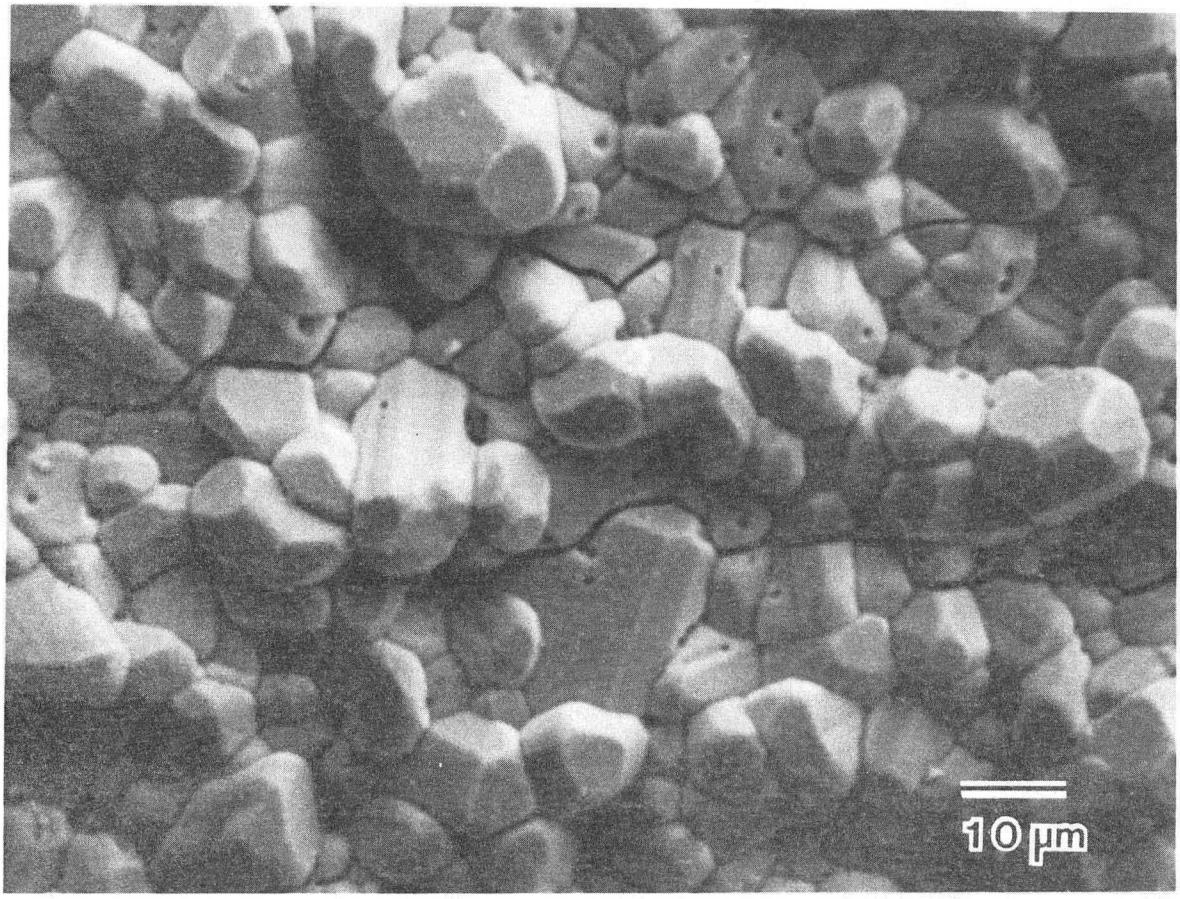

XBB 854-2593

Figure 4.2.6 SEM micrograph of the Cu_3Sn intermetallic after removal of solder by etching.

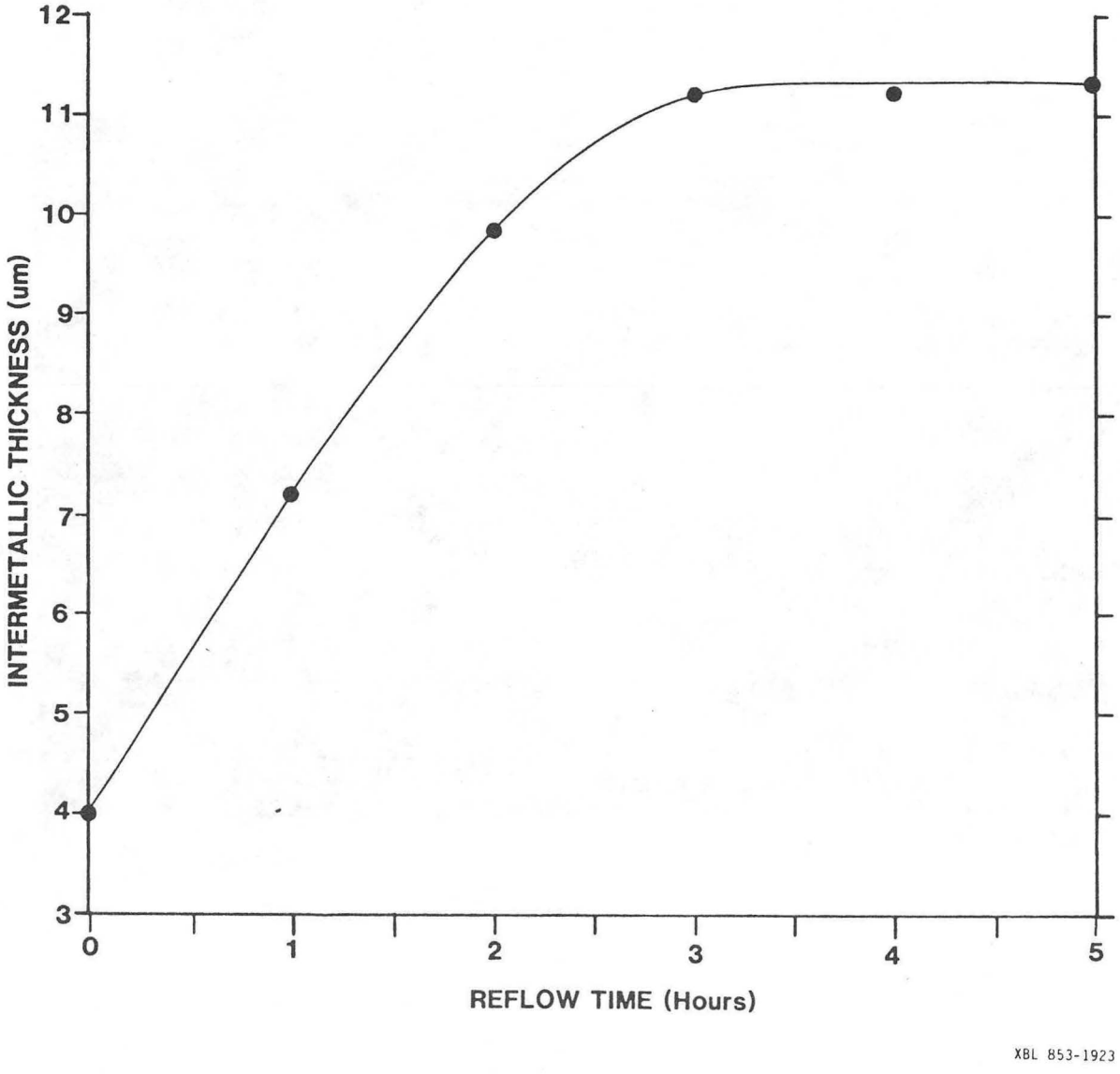

Figure 4.2.7 Plot of Cu_3Sn layer thickness as a function of reflow time at 400°C.

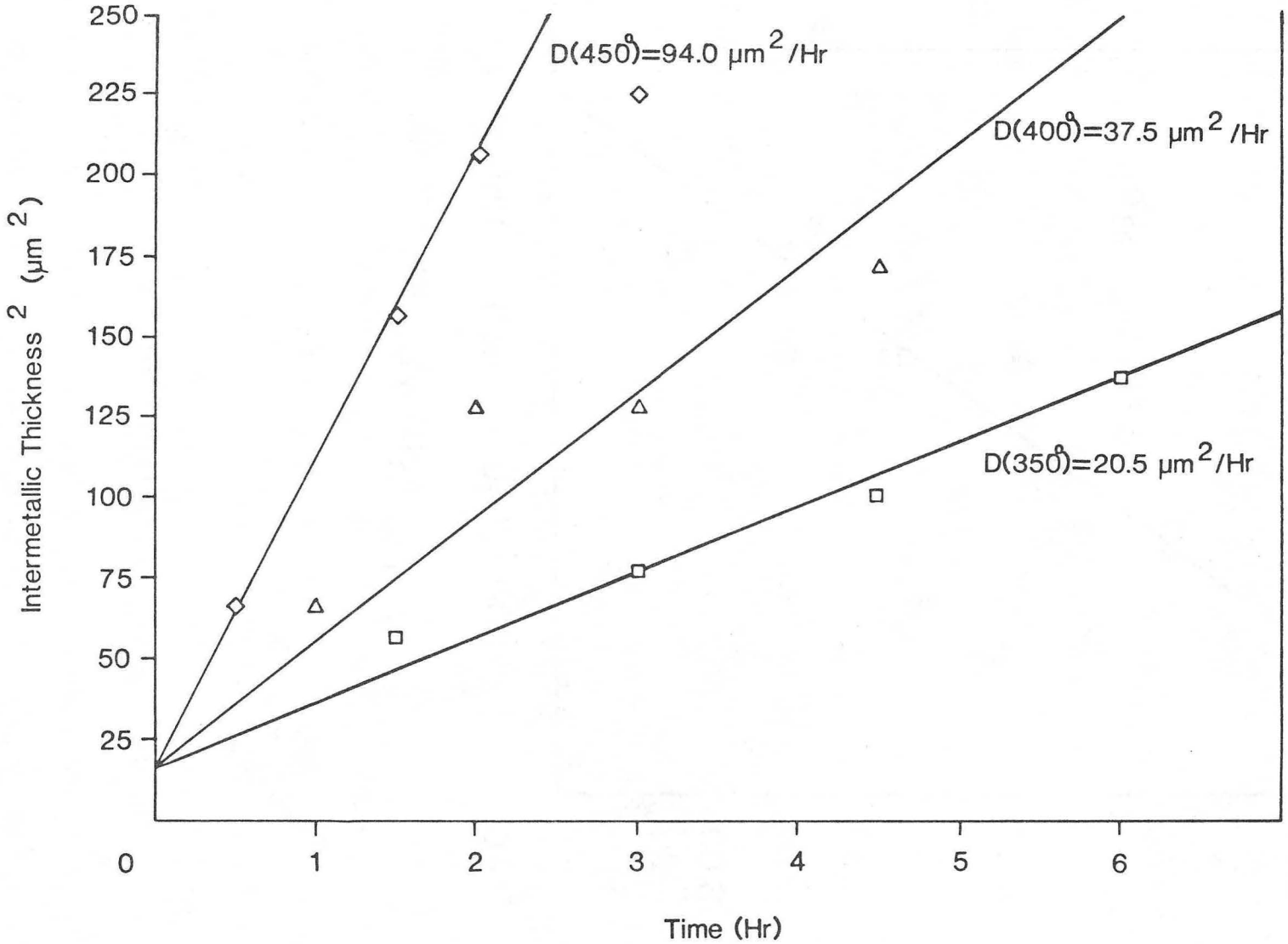

Figure 4.2.8 Plot of the square of layer thickness vs. reflow time for Cu_3Sn.

XBL 857-2956

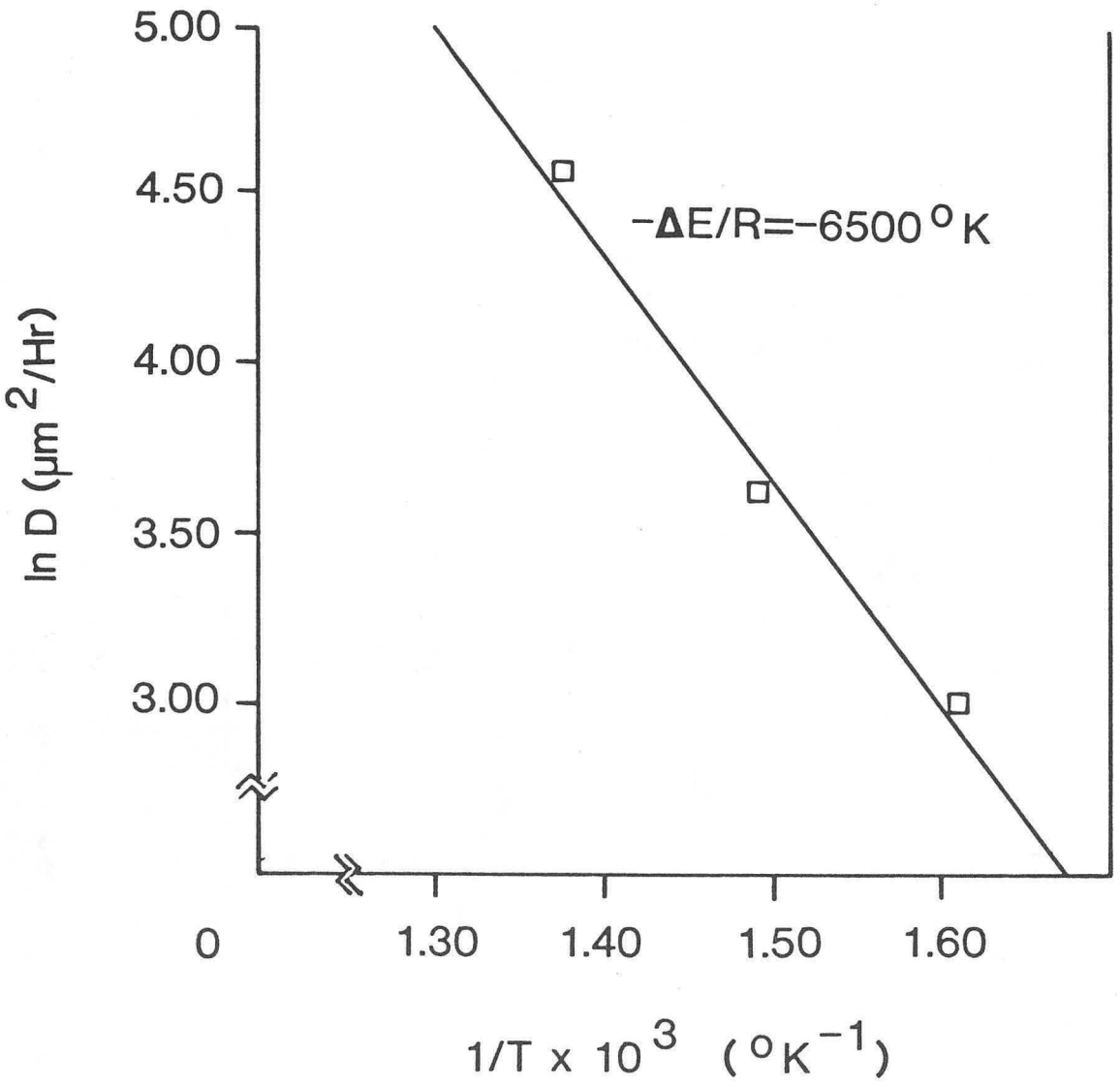

XBL 857-2957

Figure 4.2.9 Arrhenius plot of ln(D) vs. 1/T for Cu_3Sn.

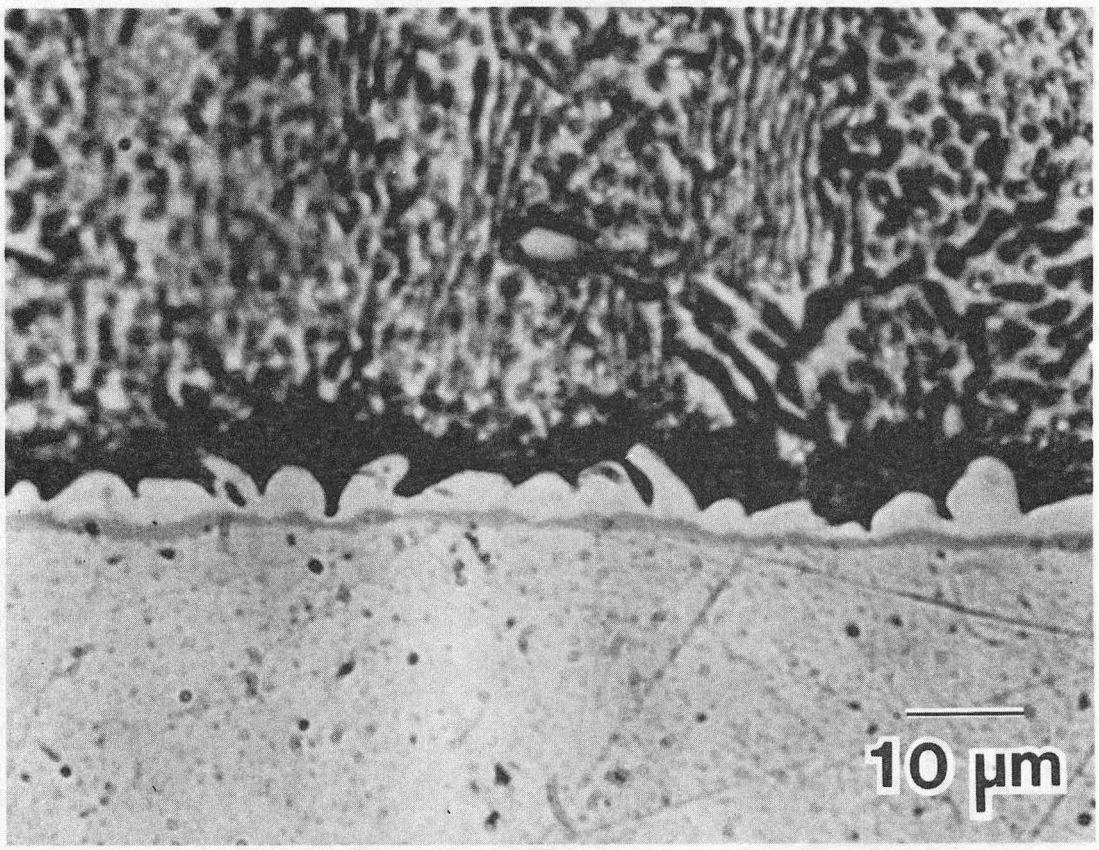

CBB 871-439

Figure 4.2.10 Optical micrograph of as-soldered 60Sn-40Pb/Cu showing the two phase Cu_3Sn (adjacent to Cu) and Cu_6Sn_5 (adjacent to solder) intermetallics.

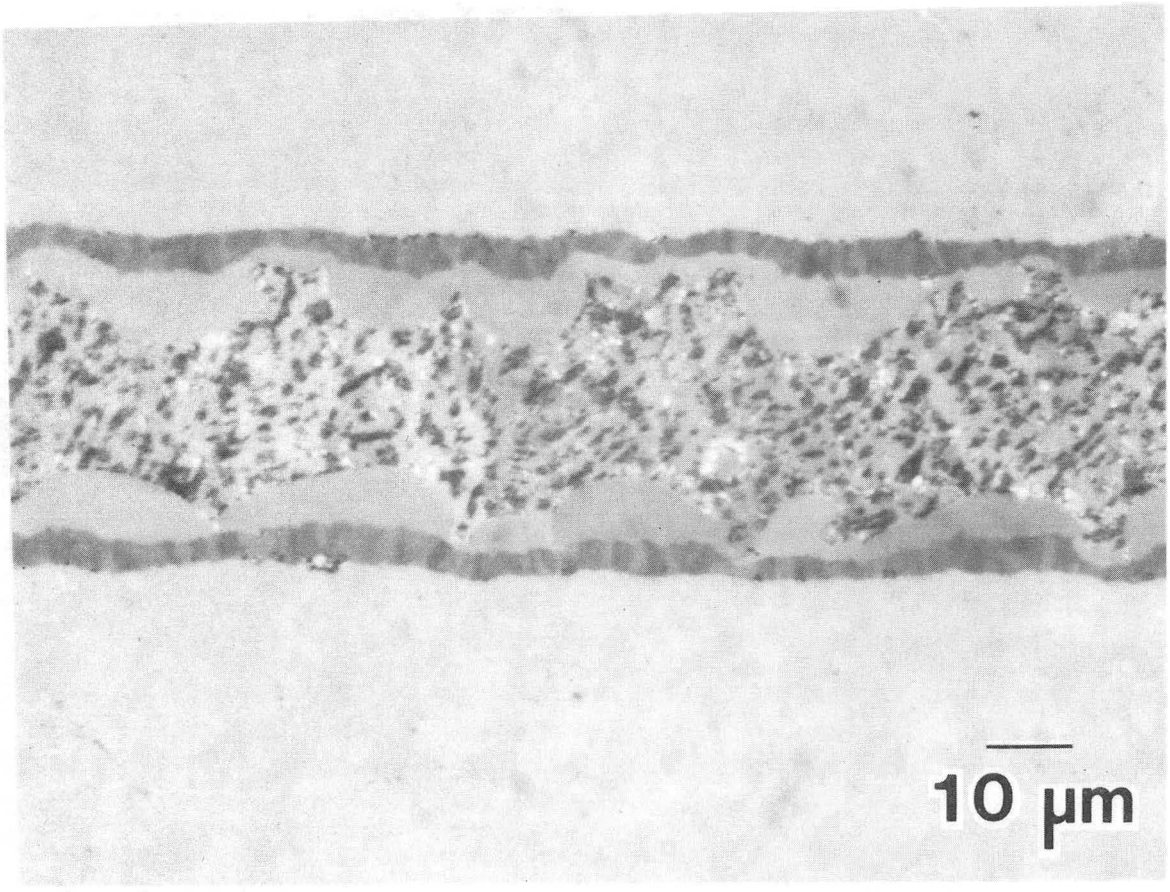

XBB 861-400

Figure 4.2.11 Polarized optical micrograph of 60Sn-40Pb on Cu reflowed for 5 hours at 240°C. The columnar structure of the ε-phase is clearly evident.

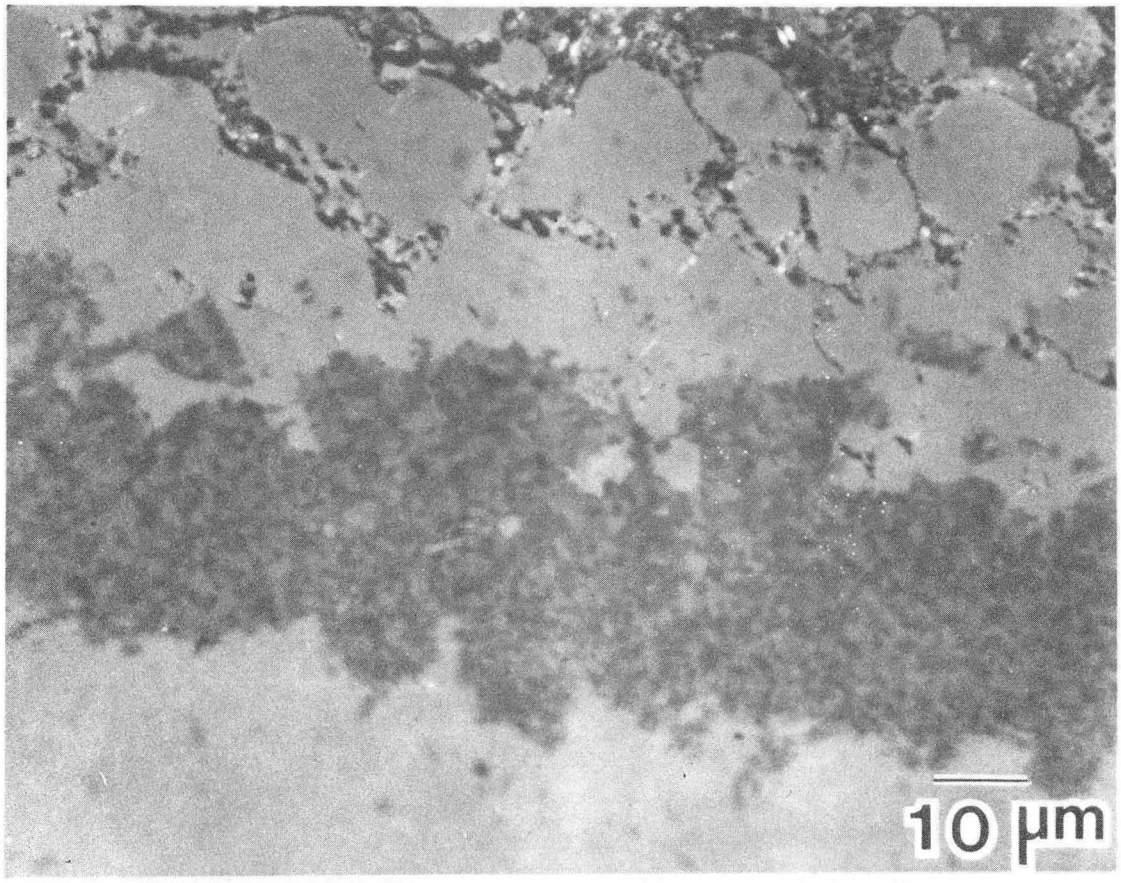

CBB 876-4408

Figure 4.2.12 Polarized optical micrograph of 60Sn-40Pb on Cu reflowed for 5 hours sectioned almost parallel to the joint revealing the fine structure of the ε–phase.

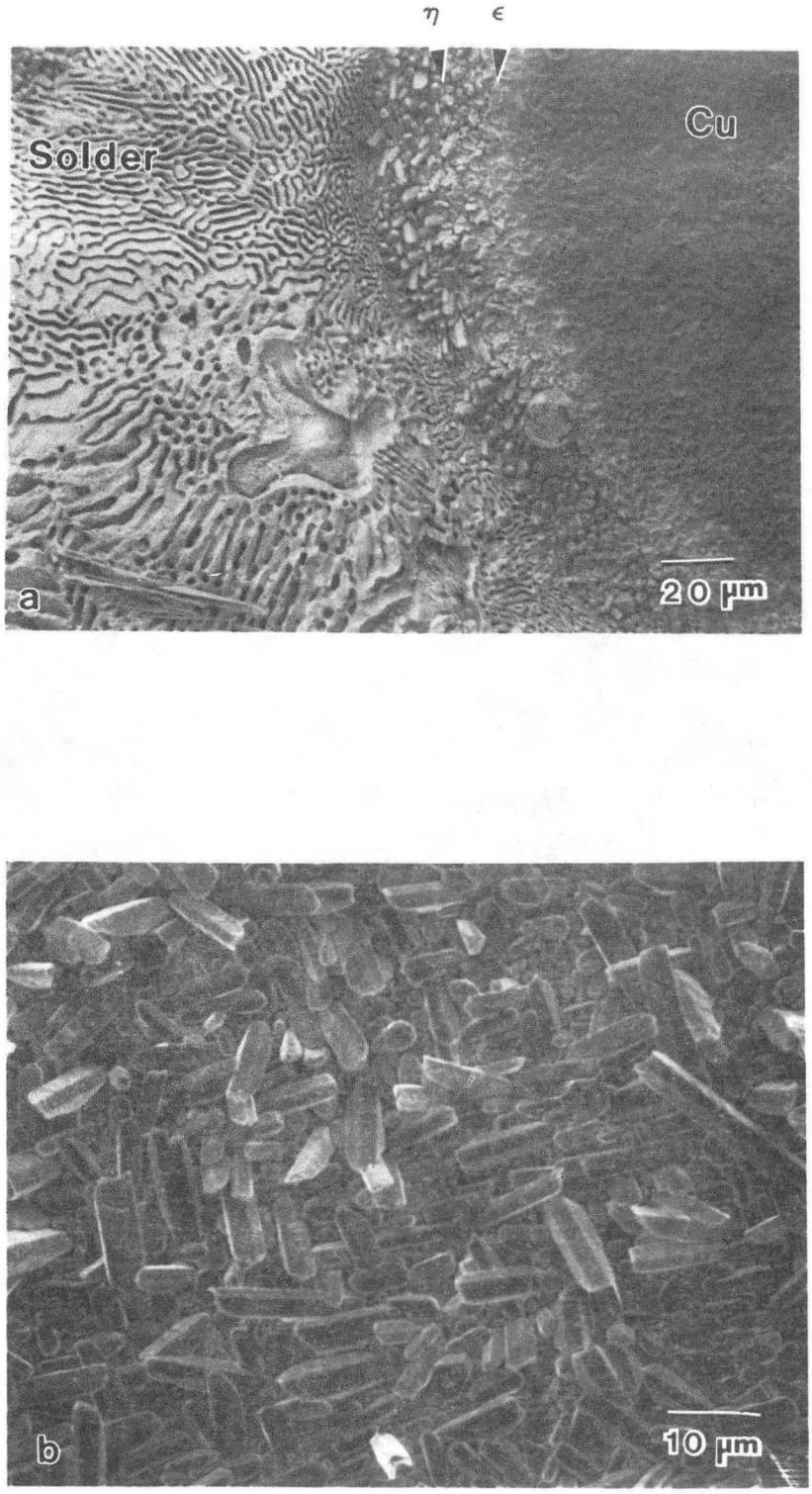

XBB 876-4404

Figure 4.2.13 SEM micrograph of η-phase intermetallic in the as-soldered condition. The faceted rod-like morphology of the intermetallic is evident in (b).

60Sn–40Pb

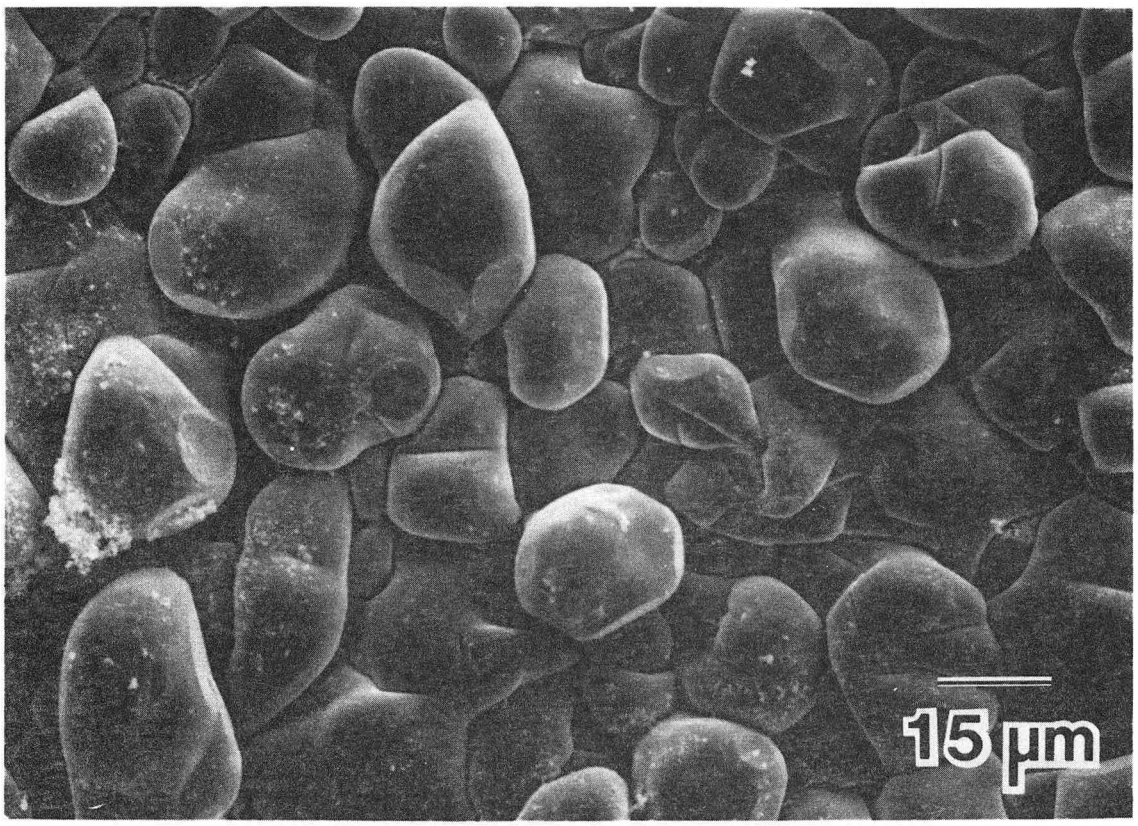

ETA phase (Cu_6Sn_5)

XBB 859-7457

Figure 4.2.14 SEM micrograph of η phase intermetallic after 5 hours at 240°C. The η intermetallic is shown to be more rounded and larger grained than in the as-soldered condition.

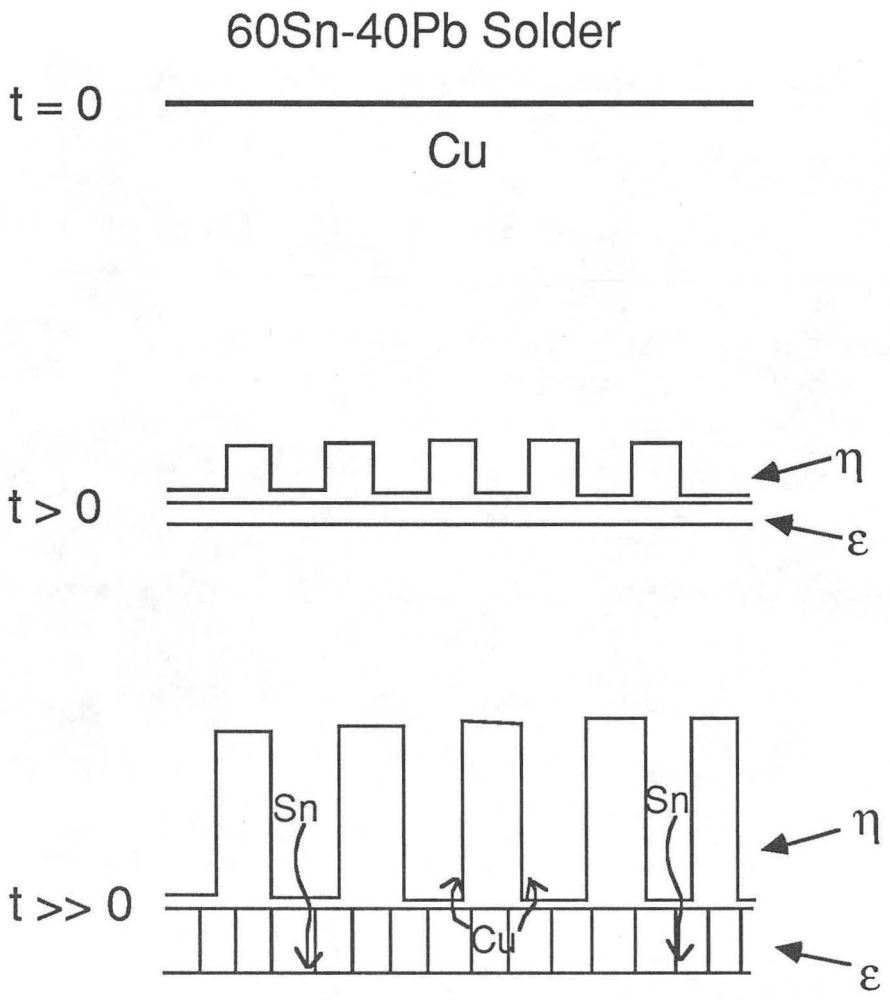

Figure 4.2.15 Model for the growth of the two phase interfacial intermetallics.

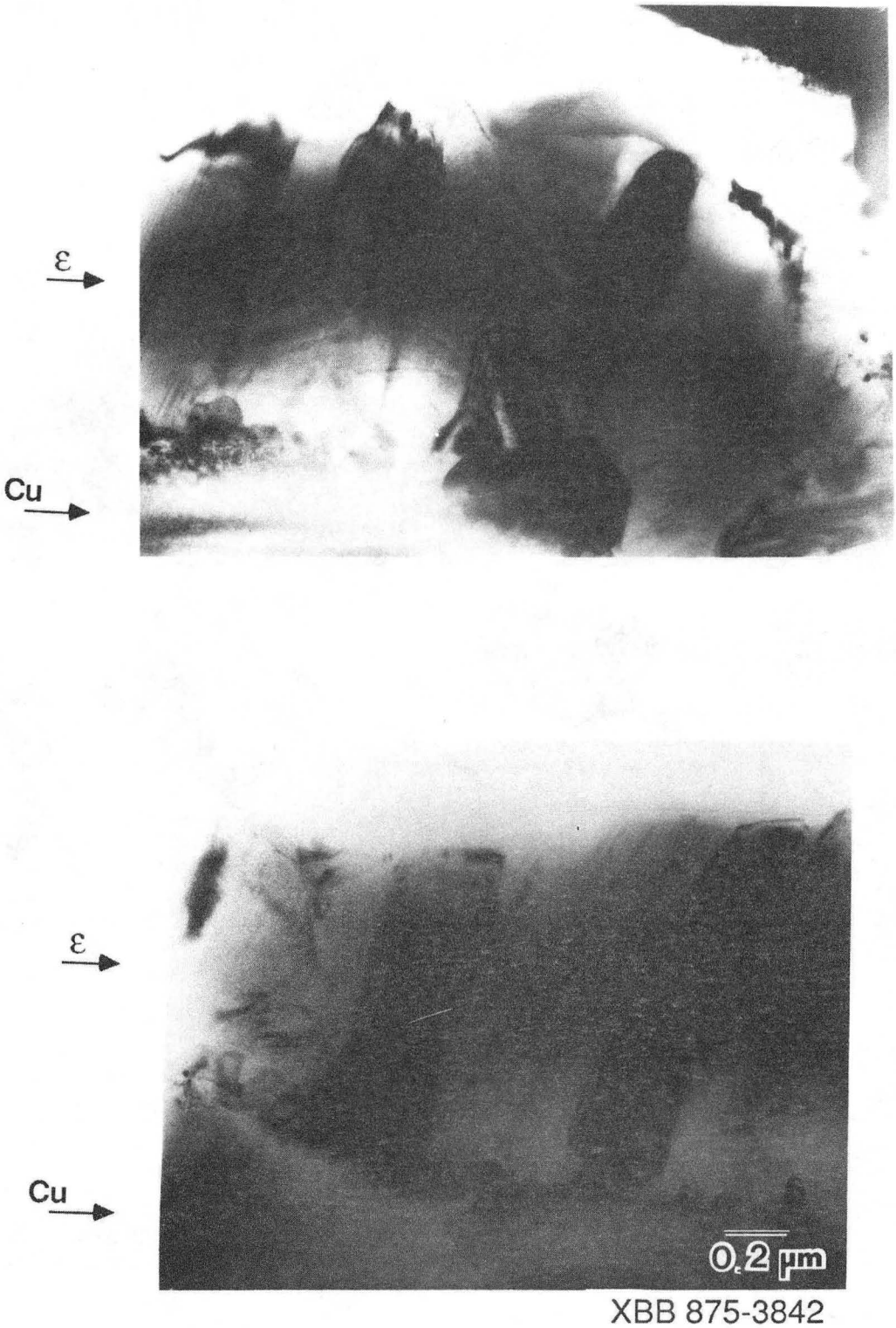

Figure 4.2.16 TEM bright field image of ε-phase intermetallic after 5 hours at 240°C. The columnar twinned structure is clearly shown.

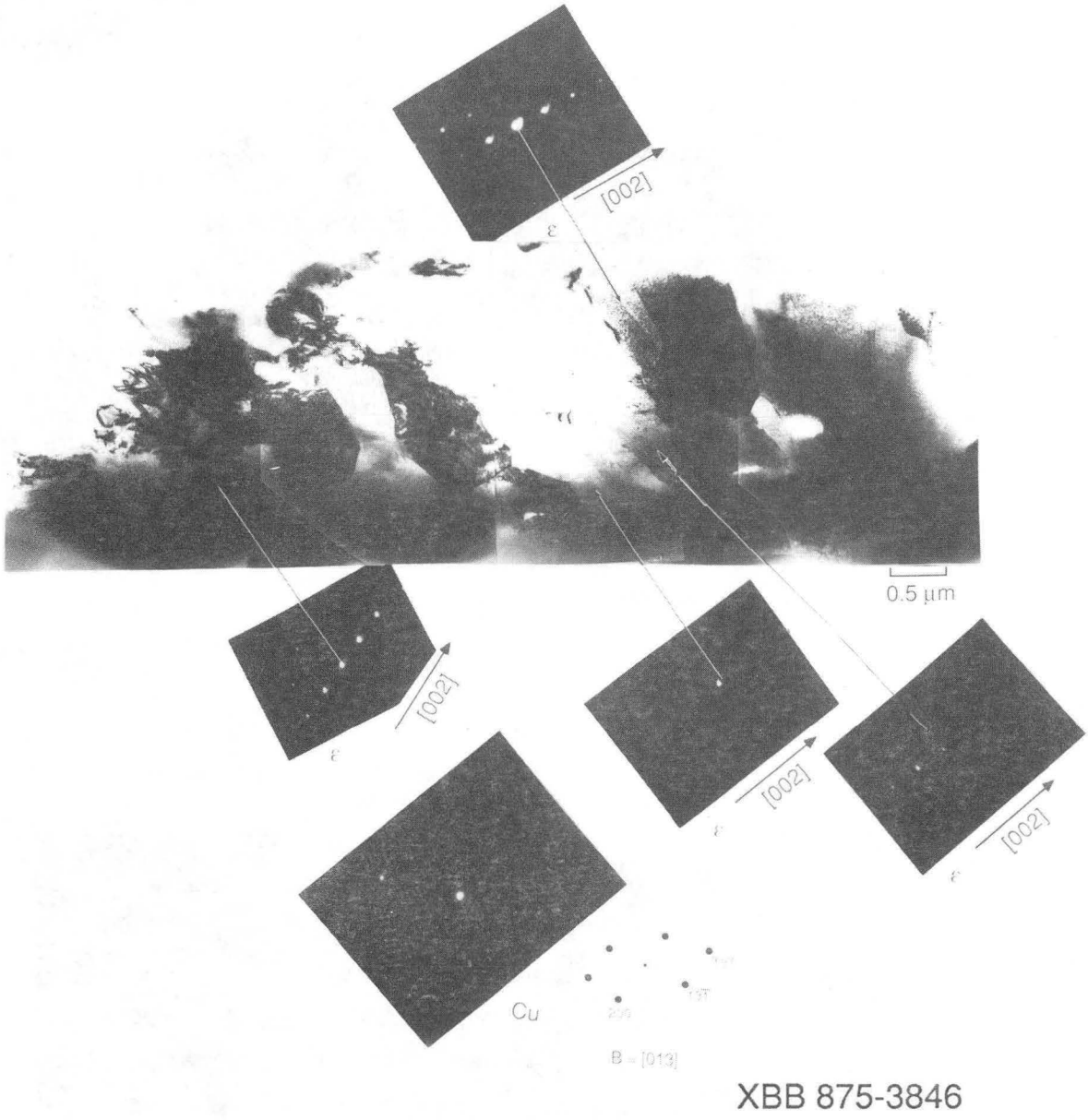

Figure 4.2.17 TEM bright field image with associated diffraction patterns for the Cu and Cu_3Sn interfacial intermetallics. The intermetallics have a similar growth direction of $[002]_\varepsilon$.

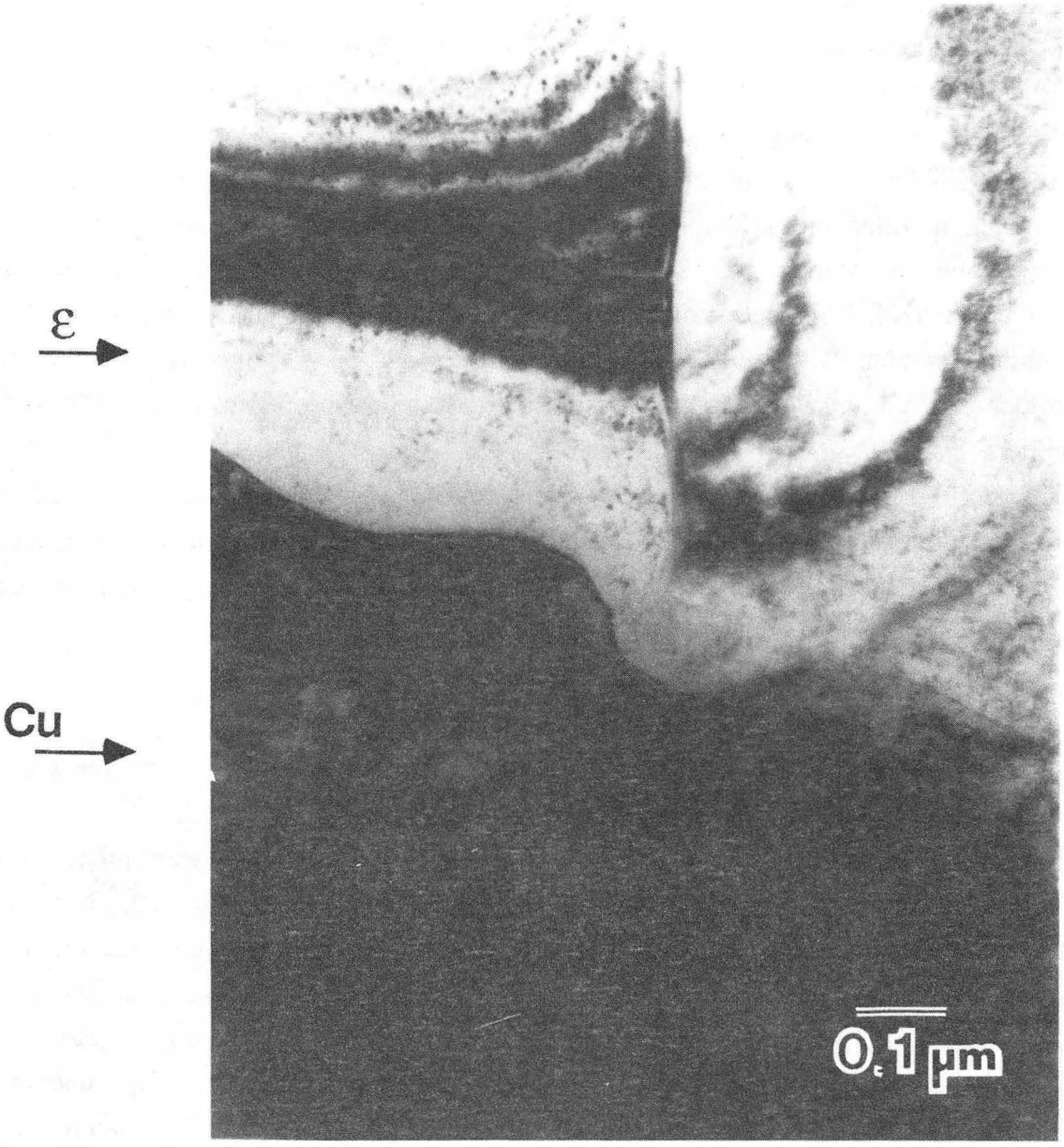

XBB 875-3838

Figure 4.2.18 TEM bright field image of the interface between the Cu_3Sn and Cu at a Cu_3Sn grain boundary showing that the Cu_3Sn grows most rapidly at the grain boundary.

4.3 INTERMETALLIC WHISKERS IN 60Sn-40Pb JOINTS

4.3.1 INTRODUCTION

The soldering of 60Sn-40Pb to Cu produces two phase interfacial intermetallics, as discussed in section 4.2. In addition to these interfacial intermetallics discrete Cu_6Sn_5 intermetallics have been observed in the bulk of the solder joint unattached to the Cu interface[92-94]. (The intermetallics form as whiskers[92] and appear to be tubes of intermetallic filled with solder[92-94].) However, the manner by which these intermetallics come to be present in the bulk solder and their effect on the mechanical properties is not well understood. This section discusses the results of an investigation of the morphology and development of the bulk intermetallic whiskers. Also presented is a study of the influence of the intermetallic whiskers on the mechanical properties of the 60Sn-40Pb solder.

To characterize the intermetallics that form in a Pb-Sn solder/Cu joint a detailed microscopic examination was performed. To determine how bulk solder intermetallics influence mechanical properties the bulk 60Sn-40Pb solder was tested in tension both with and without Cu_6Sn_5 intermetallics.

4.3.2 EXPERIMENTAL PROCEDURE

Samples of Cu/60Sn-40Pb solder joints were prepared to examine the Cu-Sn intermetallics that form on soldering as discussed in section 4.2.3.

Figure 4.3.1 diagrams the method by which ingots of 60Sn-40Pb were processed to include Cu-Sn intermetallics in the bulk solder. A coil of Cu foil was etched, fluxed, and placed in the vacuum furnace described previously in section 3.0. The coil was left in the molten solder for 15 minutes. The Cu foil was then removed and the solder ingot quickly cooled. Tensile specimens were cut and machined from this ingot (and an ingot of pure 60Sn-40Pb, for comparison) to the dimensions shown in Figure 3.7. The specimen was held by friction grips and strained to failure in a screw driven loadframe at a strain rate of 0.51 mm/min (0.02 in/min). Tests at -196°C were performed in a liquid nitrogen bath. Tests at 125°C were performed in an oil bath with a temperature controller accurate to ±1°C. The fracture surfaces were examined in the ISI DS-130 SEM.

4.3.3 RESULTS AND DISCUSSION

• Microstructure

When molten 60Sn-40Pb solder comes in contact with Cu a two layer interfacial intermetallic microstructure develops, Figure 4.2.10. The intermetallic structures are: ε-

phase (Cu3Sn) adjacent to the Cu, and η-phase (Cu_6Sn_5) adjacent to the solder. In addition to the interfacial intermetallics, intermetallic rods are also found in the bulk solder of the joint, Figure 4.3.2. The rods were determined to be η-phase Cu_6Sn_5 by Energy Dispersive x-ray Analysis in the SEM. The Cu_6Sn_5 phase was found by Hansen[95] to be of the hexagonal $B8_1$, NiAs type. The intermetallics have a rod-like hexagonal faceted morphology. It is interesting to note that the rods are often open ended tubes filled with solder. The unusual shapes of the intermetallics shown in Figure 4.3.3 are found when the intermetallic rods are cut through different cross sections. The rods were found to form extremely rapidly. The examples discussed thus far formed in the two to three minutes the solder was molten. The rods form in even less time than this, as is shown in Figure 4.3.4. Here Cu wires were dipped in a molten solder bath for a few seconds, then rapidly quenched in water. Even in this short period of time small rods of intermetallic are found in the bulk solder.

The morphology of these intermetallic rods is shown clearly in Figure 4.3.5 which is an SEM micrograph of a solder tensile fracture surface tested at -196°C. The ductile region in the center of the rods is 60Sn-40Pb solder, and the faceted hexagonal appearance is clearly illustrated in this figure.

The rods grow out from the interface as shown in Figure 4.3.6. In this figure the rod is still attached to the interfacial intermetallics. The rod has the shape of a tube and the center is filled with solder. The rods found in the bulk solder were attached to the interface but broke off while in the molten state.

To investigate the crystallography of these rods high voltage electron microscopy was performed on 60Sn-40Pb foils that contained the intermetallics. The foils were prepared from bulk solder as described previously in section 4.1.2. The rods were found to be single crystalline along their length. An illustration of such a rod is shown in Figure 4.3.7 along with an indexed diffraction pattern. The irregular shape of the rod is due to the thinning process in ion milling. The diffraction pattern has a $[2110]_\eta$ beam orientation with the pattern indexed as hexagonal Cu_6Sn_5. The long axis of the rod is parallel to the $[0002]_\eta$ direction. The rods grow along the c-axis of the hexagonal Cu_6Sn_5 crystal and each of the 6 sides is an {0110} face. This is in accord with work by Mendizza and Arnold[96] who found hexagonal whiskers grow along one of the orthogonal axes, commonly the c-axis.

The even faceted single crystal appearance of these rods suggests that the intermetallics in the bulk formed as whiskers from the interface. By looking at previous studies on whisker formation the mechanism for the whisker formation in the 60Sn-40Pb/Cu system

can be established. A brief survey of information on whisker formation is discussed below.

• Previous Whisker Observations

Doremus[97] is an excellent review of observations and theories of whisker formation. Whiskers form in a variety of metals and compounds, under many conditions. The common basis for whisker growth is a whisker grows out of a polygranular film to lower the internal energy of the film. A variety of mechanisms have been developed to describe whisker growth. The basis of these mechanisms is the whiskers grow via dislocations in the base material[98]. Work by Amelinkx[99], Burton[100], and Frank[101] claim whiskers grow by a screw dislocation at the core of the whisker. Atoms are deposited in this mechanism at the growing tip of the whisker by surface deposition[100,101], or by diffusion through the whisker with resultant vacancies at the base[99]. The most applicable model for growth of η-whiskers is that developed by Ellis[102] and is diagramed in Figure 4.3.8. In this model a screw dislocation is present in the base material terminating on the free surface and an edge dislocation terminates on the grain boundary. Atoms diffuse from the grain boundary and affix themselves to the edge of the extra plane on the edge segment. As the extra plane grows the edge segment rotates and each rotation results in a new plane of atoms added to the base of the whisker. The growth of whiskers from the base has been observed elsewhere as well[103,104]. The rate of growth of whiskers is enhanced by stress in the base layer as found by Fisher et. al.[105] who, by imposing external stress, raised the whisker growth rate from 0.01 Å/sec to 10^{-4} Å/sec.

• Cu_6Sn_5 Whiskers

From this information on whisker formation the following mechanism for η whiskers in the 60Sn-40Pb/Cu system is proposed. On soldering the interfacial η-phase that forms has a faceted morphology, Figure 4.2.13. When a facet is in the correct orientation (long axis on the c-axis of η) and a screw dislocation is present at the core, the mechanism described previously (Ellis[102], Figure 4.3.8) operates. The Sn diffuses to the base of the whisker and reacts with the Cu, coming up from the base metal, at the edge segment of the dislocation. The whiskers grow rapidly from the base which suggests that the driving force for formation is stress[105] in the η-layer. However, this stress was not measured in this work. The whiskers then break off, due to turbulence in the molten solder. In the bulk solder the Cu concentration is relatively low and this causes the intermetallic whiskers to begin to dissolve. The screw dislocation core of the intermetallic whisker, because of its higher energy, is the first portion of the rod to dissolve and is replaced by molten solder. Eventually the entire core of the rod is eliminated and a hollow tube of Cu_6Sn_5 intermetallic remains, filled with solder. Figure 4.3.9 shows an intermetallic rod just after it has broken

off. The core at one end is just beginning to dissolve. This figure also demonstrates the large size of the intermetallic whiskers, in this case a length of 200 μm is found.

• Mechanical Properties

To study the effect that the intermetallic whiskers have on the mechanical properties of 60Sn-40Pb bulk solder, specimens were tested in tension. Samples of both 60Sn-40Pb solder and 60Sn-40Pb solder with intermetallics were tested at -196°C, 20°C, and 125°C. These temperatures were selected to clarify the temperature dependance of the effect. Figure 4.3.10 shows typical stress vs. strain curves for 60Sn-40Pb solder at the various temperatures tested. The ultimate strengths decreased with increasing temperature while elongation increases with increasing temperature.

Figure 4.3.11a-c shows stress vs. strain plots that compare pure 60Sn-40Pb to 60Sn-40Pb with intermetallics at the three temperatures tested. Figure 4.3.11a shows the samples at 125°C. There is little or no difference between the two samples; the ultimate strengths are both about 15 MPa. There is a small increase in total elongation for the pure 60Sn-40Pb sample. Figure 4.3.11b shows the samples tested at 20°C. Again there is very little change in the ultimate strengths, which are about 45 MPa, but the total elongation is greater in the pure 60Sn-40Pb sample. Figure 4.3.11c is a plot of the samples at -196°C. The ultimate strengths are still almost identical at 130 MPa. However, the elongation is substantially greater for the pure 60Sn-40Pb sample. The work hardening rate is increased significantly by the addition of the Cu_6Sn_5 intermetallic whiskers to the solder.

Figure 4.3.12 shows macrographs taken of the solder samples tested in tension as a function of temperature and presence of intermetallics. The amount of plastic deformation also increases with an increase in testing temperature. The pure 60Sn-40Pb sample necked to a point at 125°C. The amount of secondary cracking was extensive in the 60Sn-40Pb with intermetallics tested at 20°C. The amount of visible plastic deformation was smaller in the samples containing the intermetallics. From the above observation the presence of intermetallics in the bulk solder influences the mechanical properties of the solder. To understand the effect of the intermetallics on the fracture mode the fracture surfaces were characterized in the SEM.

Figure 4.3.13 is an SEM fractograph of pure 60Sn-40Pb failed at -196°C. The entire fracture surface is ductile. Figure 4.3.14 is an SEM fractograph of 60Sn-40Pb with intermetallics failed at the same temperature. This figure clearly illustrates the hexagonal shape of the intermetallic rods and that the rods are tubes filled with ductile solder. The failure at -196°C is an interfacial separation between the intermetallic rods and the solder matrix. The temperature is so low that mass flow of the solder is very difficult. Apparently dislocations introduced during deformation pile up at the intermetallic rods

eventually leading up to interfacial separation and failure. This hypothesis is further substantiated by the stress strain curve in Figure 4.3.11c which shows that the work hardening rate increases with the introduction of the intermetallic rods.

Figure 4.3.15 is an SEM micrograph of the 60Sn-40Pb sample with intermetallics that failed at 20°C. This fractograph can be compared to that of the pure solder sample, at the same temperature, which is given in Figure 4.3.16. At room temperature the fracture surface of the sample with intermetallics is composed of a large number of cleaved intermetallic rods. The larger intermetallic rods act as preferential nucleation sites for cracks and therefore the fracture surface is composed of large cleaved rods. The matrix around the intermetallics is ductile. At 20°C the 60Sn-40Pb solder is at 0.63 of its homologous temperature but the temperature is still low enough to make mass flow of the Pb-Sn matrix around the intermetallics difficult at the relatively high strain rate in the tensile test. This puts a stress upon the brittle intermetallic rods which cleave, initiating the failure. The cleavage of the rods during deformation leads to the extensive secondary cracking observed in this sample, as shown in Figure 4.3.12..

Figure 4.3.17 is an SEM micrograph of the 60Sn-40Pb with intermetallics sample fractured at 125°C. The fracture is ductile with very few intermetallics present at the surface. This sample can not be compared with the pure 60Sn-40Pb sample as the pure specimen necked down to a point. At this elevated temperature the intermetallics had little influence on the fracture appearance of the 60Sn-40Pb with intermetallics sample. At 125°C the solder is at 0.86 of its homologous temperature so the Sn-Pb matrix can readily flow around the intermetallics during deformation. In contrast to the specimens fractured at lower temperatures, the intermetallics are not obvious initiations sites for failure at 125°C.

Other work[27] has investigated the room temperature tensile properties of 60Sn-40Pb soldered to Cu plates and found that the hollow intermetallic tubes formed in the joint had a beneficial influence on the fracture strength. This effect is currently under further investigation.

4.3.4 Summary and Conclusions

When molten 60Sn-40Pb solder comes in contact with Cu hexagonal intermetallic whiskers form at the Cu/molten solder interface. The whiskers are single crystalline and form with the long axis parallel to the c-axis of the hexagonal crystal structure. The whiskers form via an edge/screw dislocation mechanism at the base of the whisker. When the whiskers break off into the bulk solder redissolution begins immediately at the high energy screw dislocation core of the intermetallic rod, which is replaced by molten solder.

When the solder is solidified it contains residual hexagonal tubes of Cu_6Sn_5 intermetallic filled with solder.

The effect of the intermetallic whiskers on the mechanical properties of the solder was tested in tension as a function of temperature. The intermetallic whiskers had no effect on the ultimate strength of the specimens tested. The intermetallics did act to decrease the total elongation to failure, especially at 20°C and -196°C. The intermetallics also increased the work hardening rate at -196°C. Decohesive failure occurs between the intermetallic whiskers at the solder matrix at -196°C. At room temperature the solder matrix can flow around the intermetallics during straining but a stress is still present on the intermetallics causing them to cleave. At 125°C the intermetallics have little or no effect on the mechanical properties of the bulk solder.

The presence of the intermetallic whiskers in bulk solder is detrimental to the mechanical properties, especially at low temperatures. The whiskers act as nucleation sites for failure either by cleavage or interfacial separation in bulk solder. This indicates that the intermetallic whiskers would have adverse effects on solder joints that undergo substantial deformation.

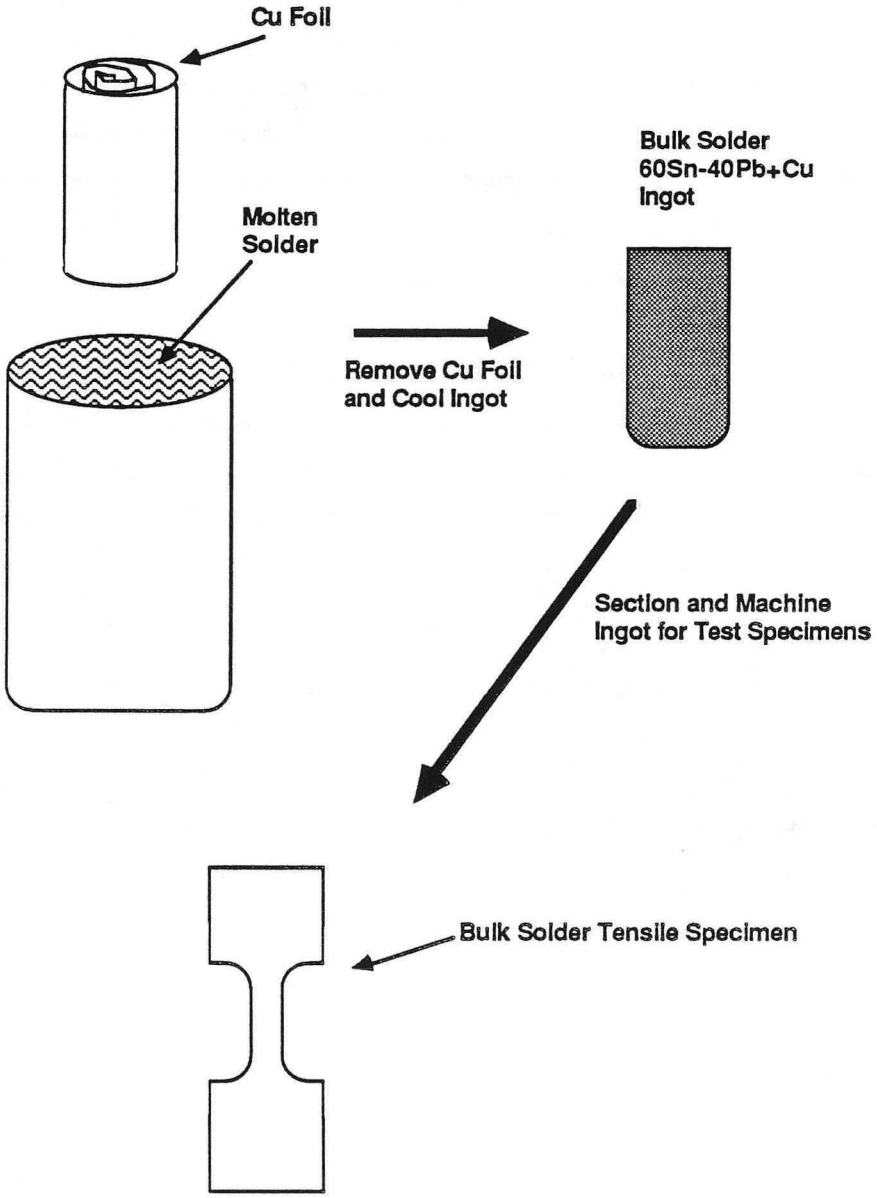

Figure 4.3.1 Procedure for the manufacture of solder ingots that contain Cu_6Sn_5 whiskers. A Cu foil was dipped in molten solder for 15 minutes (under vacuum). The foil was removed and the solidified ingot subsequently machined into tensile specimens.

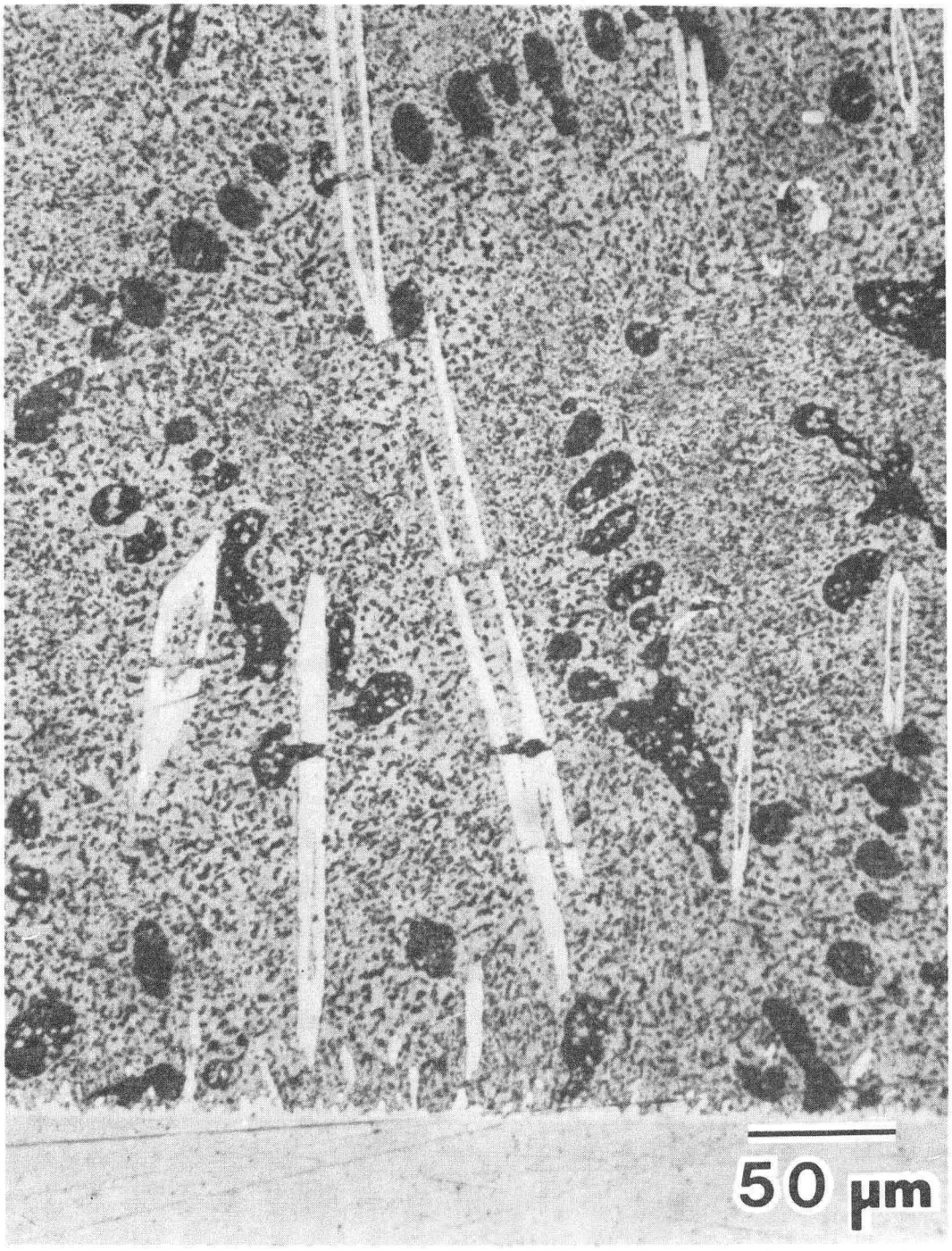

XBB 871-422

Figure 4.3.2 Optical micrograph of rods within the bulk of a solder joint. The rods are Cu_6Sn_5 intermetallics.

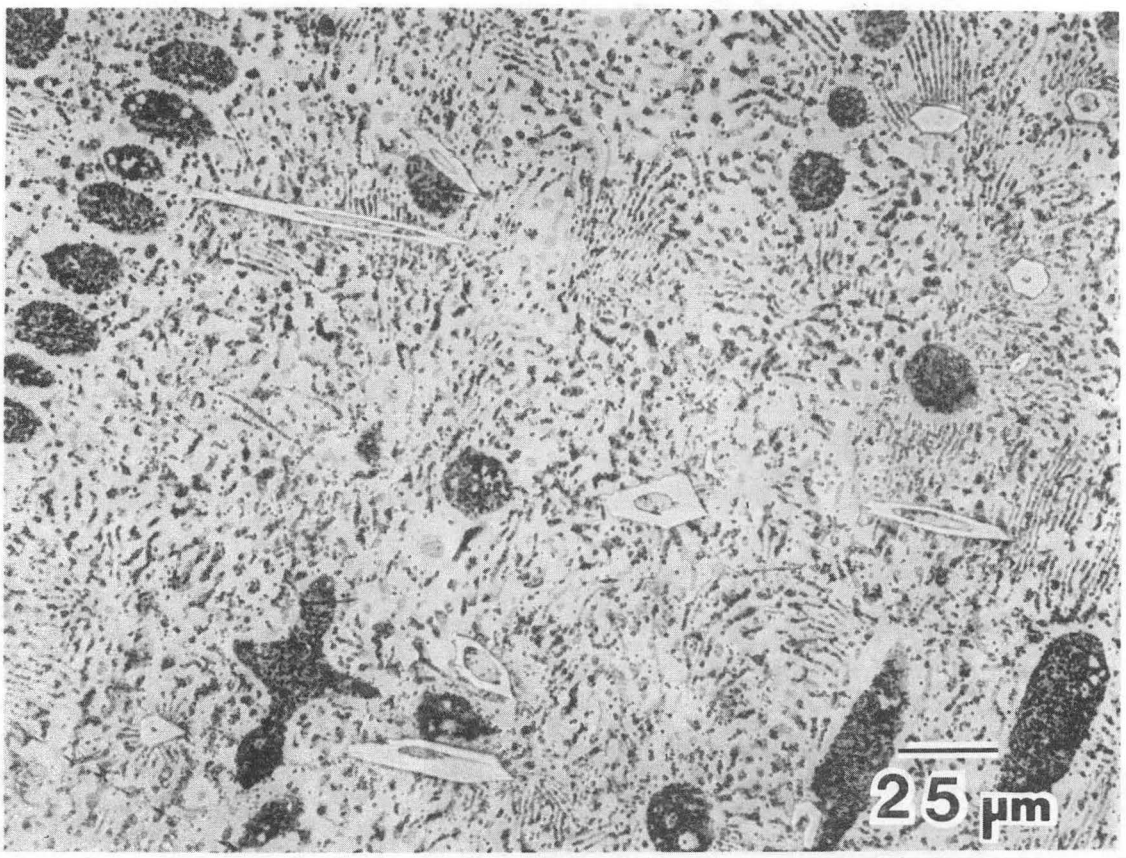

XBB 871-423

Figure 4.3.3 Optical micrograph showing intermetallic rods through various cross sections. The rods are tubes of intermetallic filled with solder.

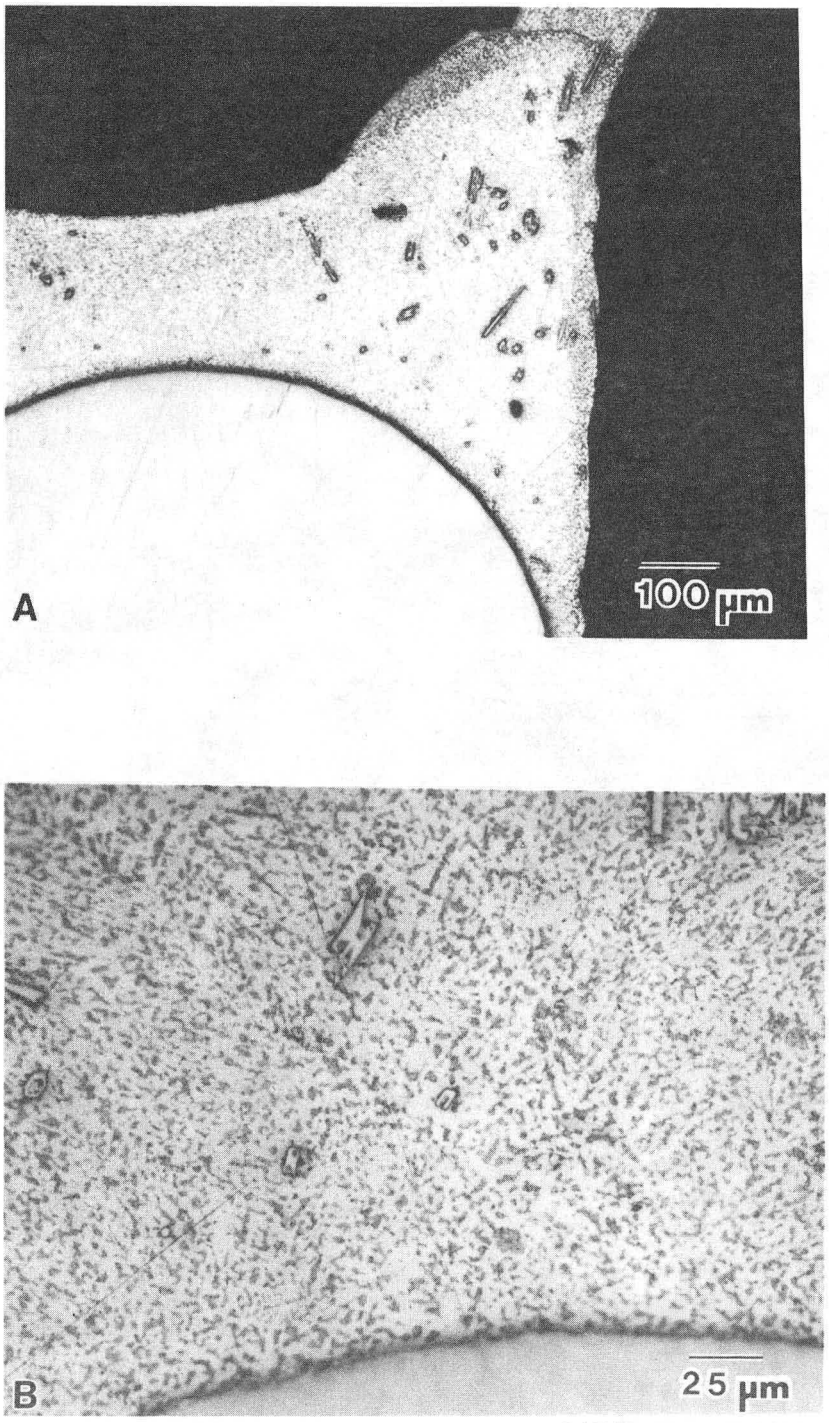

Figure 4.3.4 Optical micrograph showing small intermetallic rods that are present after the few seconds the Cu wires were in the molten solder bath then quenched.

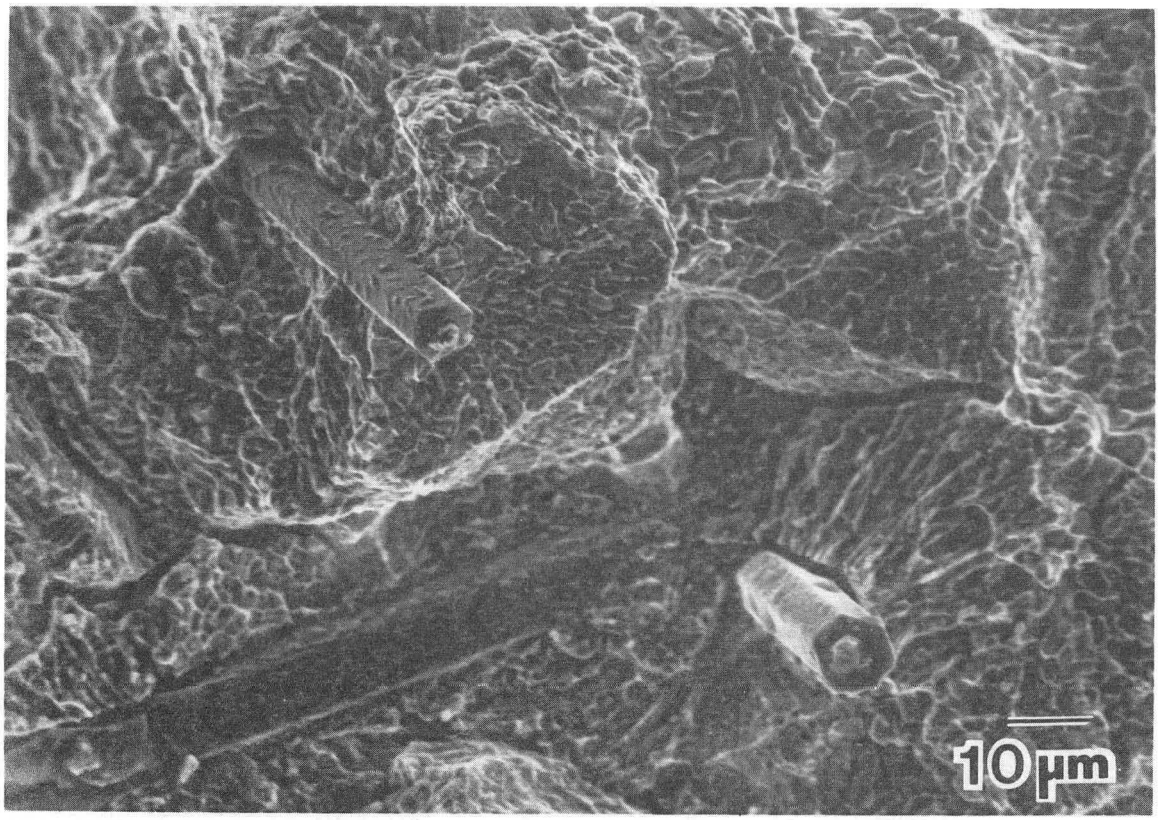

XBB 868-6040

Figure 4.3.5 SEM fractograph of 60Sn-40Pb solder containing intermetallic rods, failed at -196°C. The rods have a hexagonal shape. The ductile center of the rod is due to the solder present within the intermetallic tube.

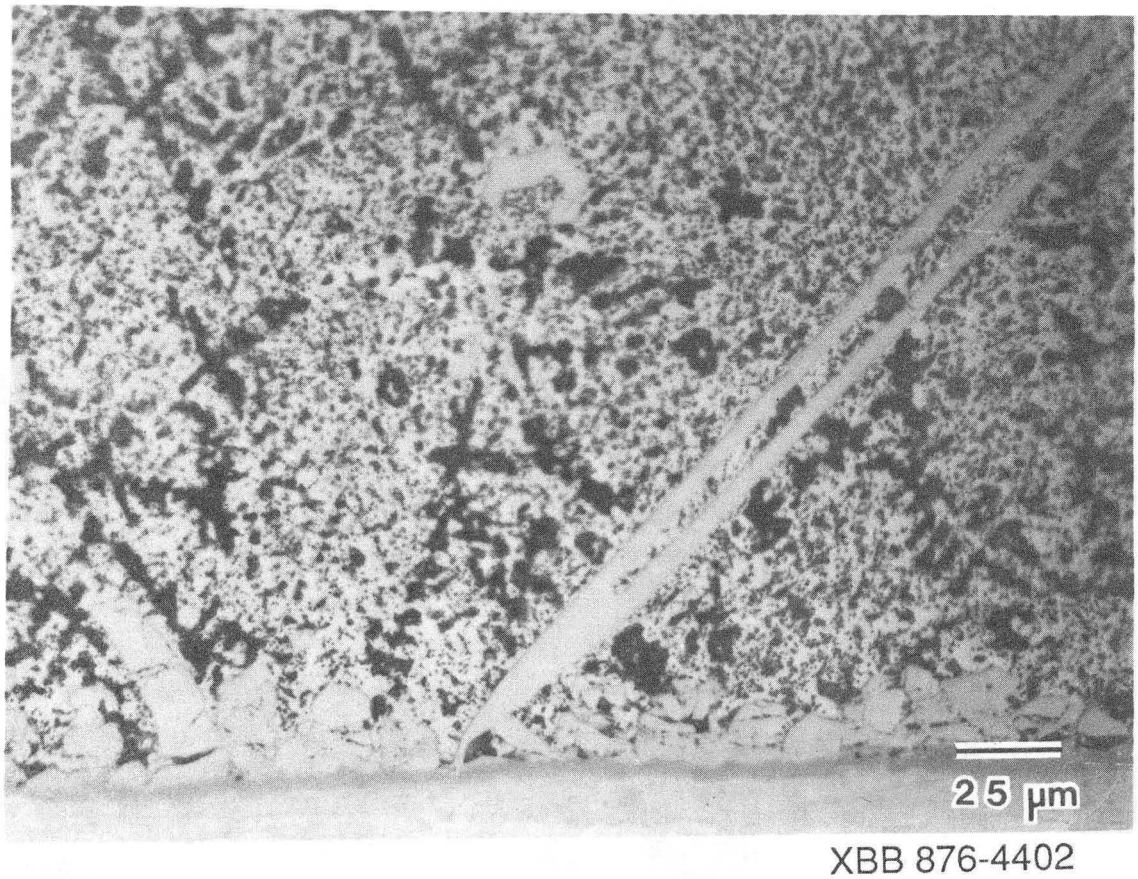

Figure 4.3.6 Optical micrograph showing a Cu_6Sn_5 rod still attached at the interface. The rods grow into the solder from the Cu_6Sn_5 interfacial intermetallic via a whisker mechanism, Figure 4.3.8.

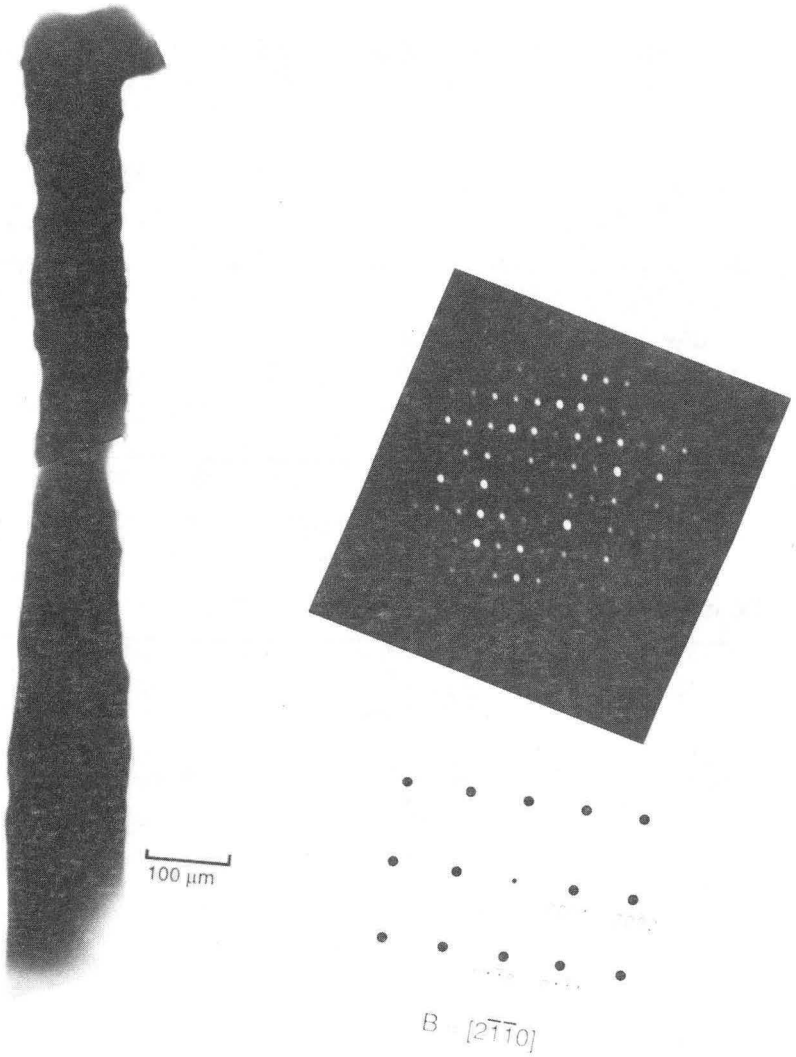

XBB 875-3844

Figure 4.3.7 TEM bright field image of an intermetallic whisker and the corresponding indexed diffraction pattern. The whisker is single crystalline with the long axis of the rod parallel to $[0002]_\eta$.

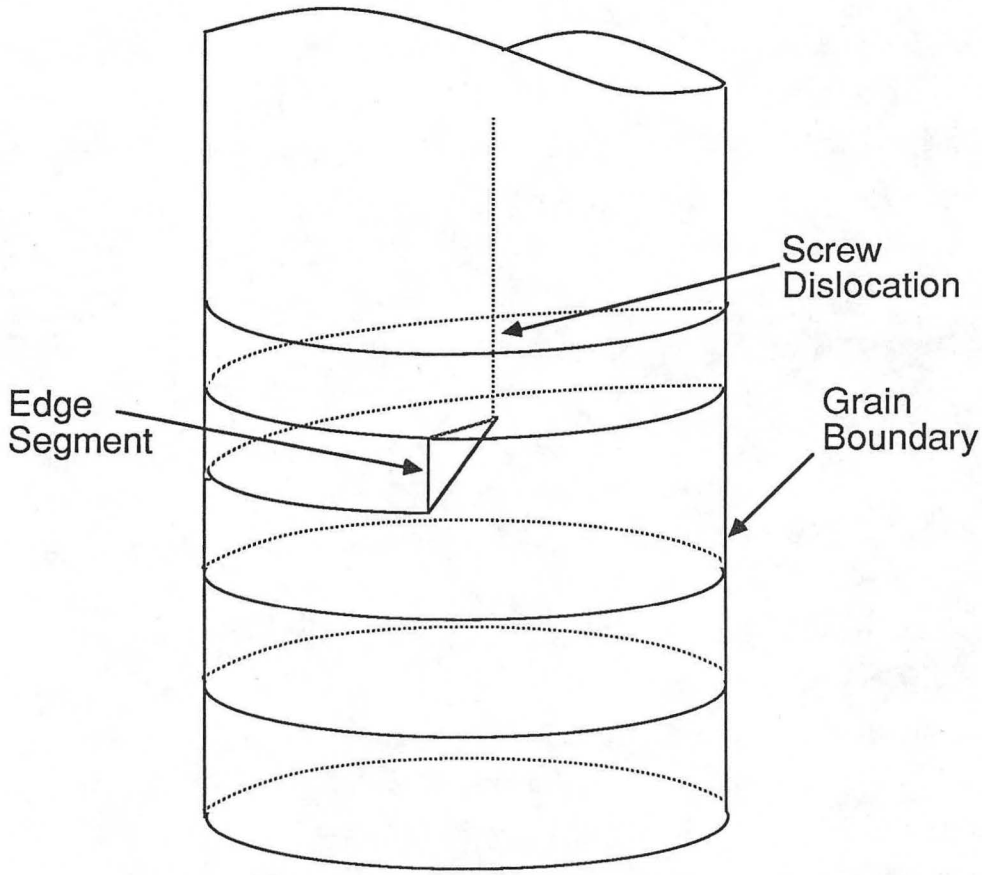

Figure 4.3.8 Model of whisker growth. A screw dislocation is present at the core of the whisker with an edge dislocation terminating at the boundary. The whisker grows as a spiral as atoms diffuse to the extra plane at the edge segment.

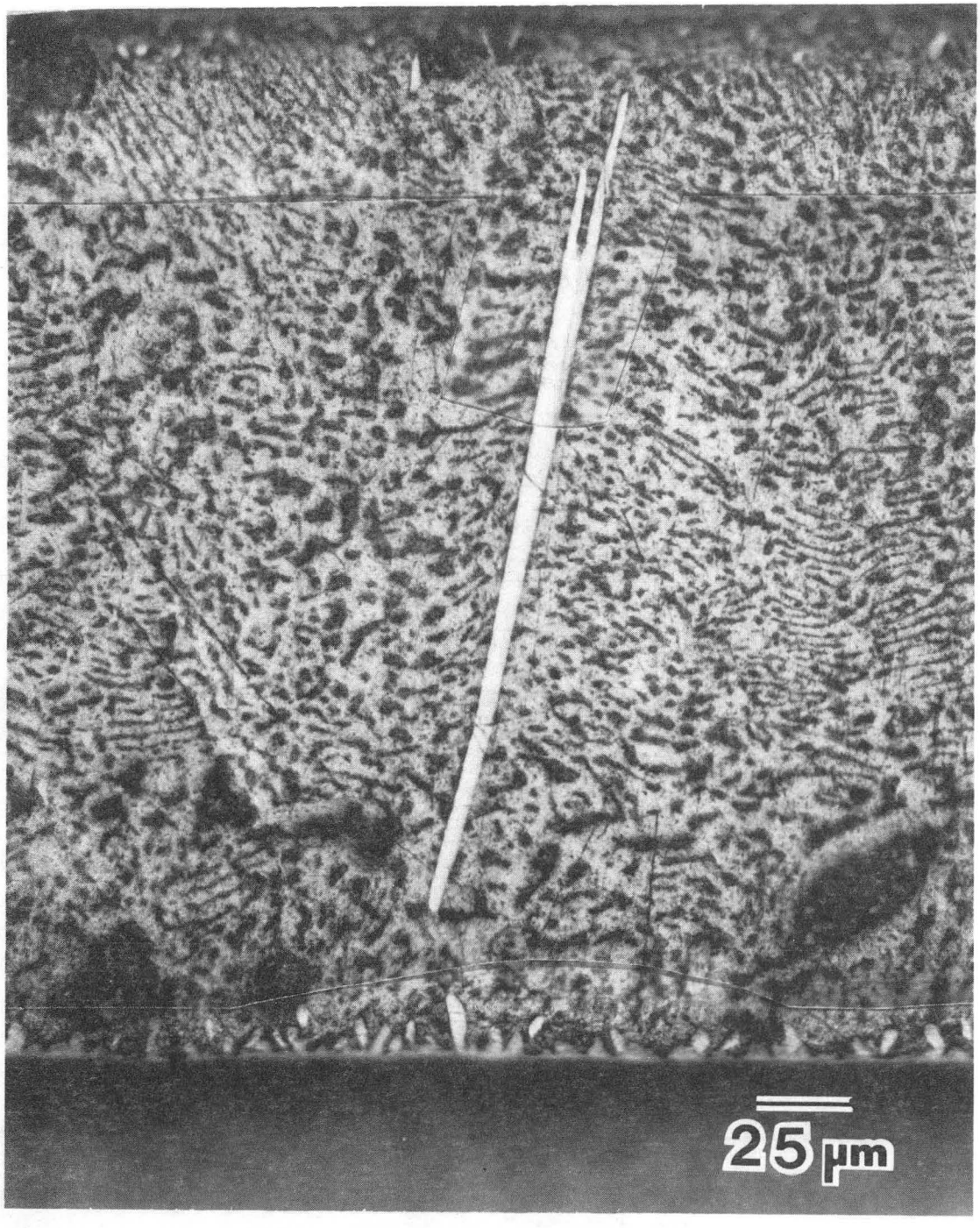

XBB 869-7937

Figure 4.3.9 Optical micrograph showing an intermetallic whisker after it has broken off from the interface. One end of the core is just beginning to dissolve to form the tube.

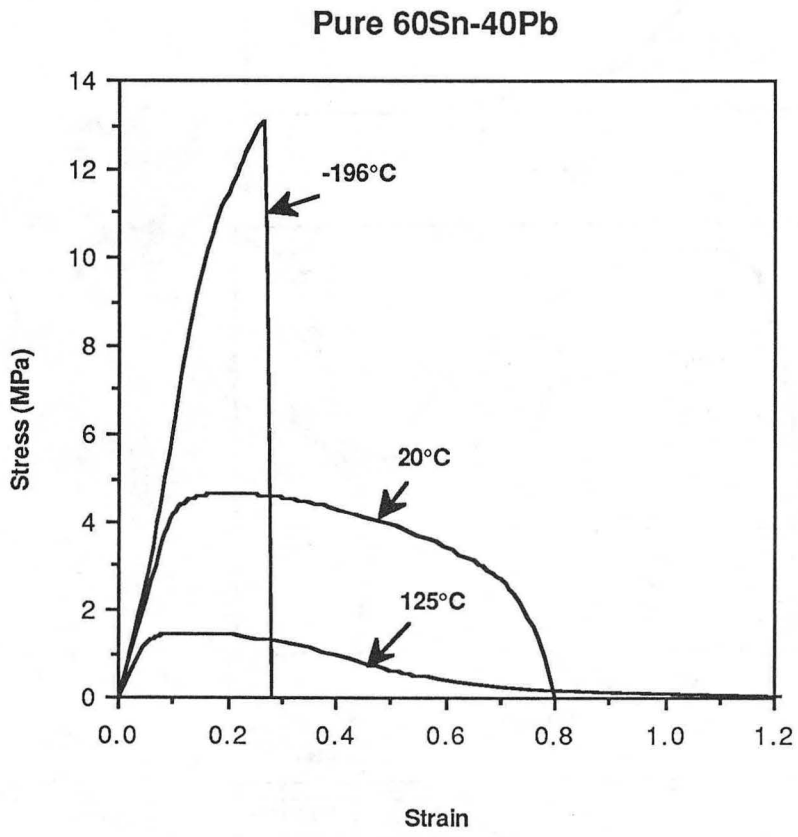

Figure 4.3.10 Plot of stress vs. strain of pure 60Sn-40Pb tested in tension as a function of temperature.

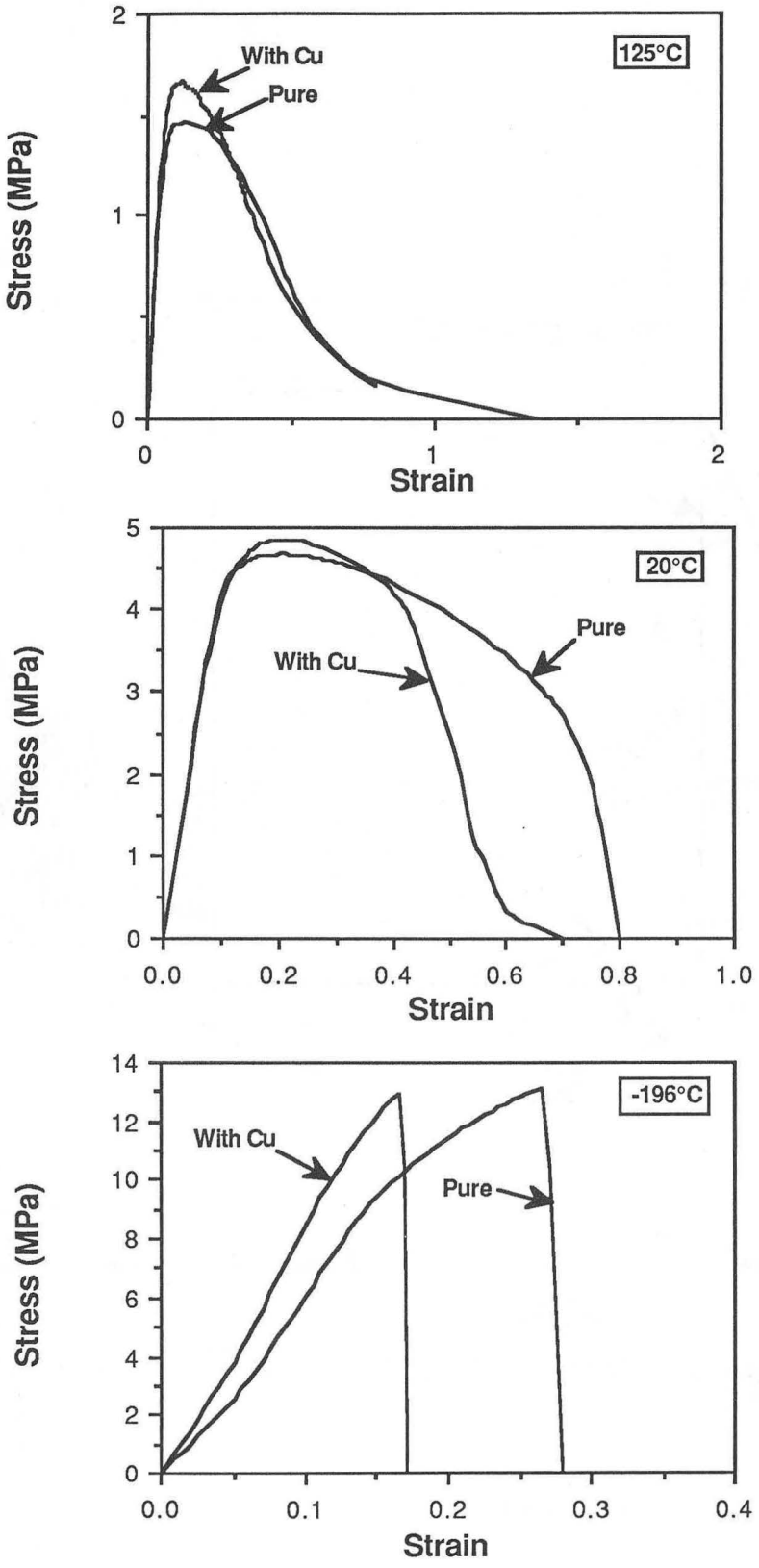

Figure 4.3.11 Plots of stress vs. strain comparing pure 60Sn-40Pb and 60Sn-40Pb with intermetallic whiskers as a function of temperature.

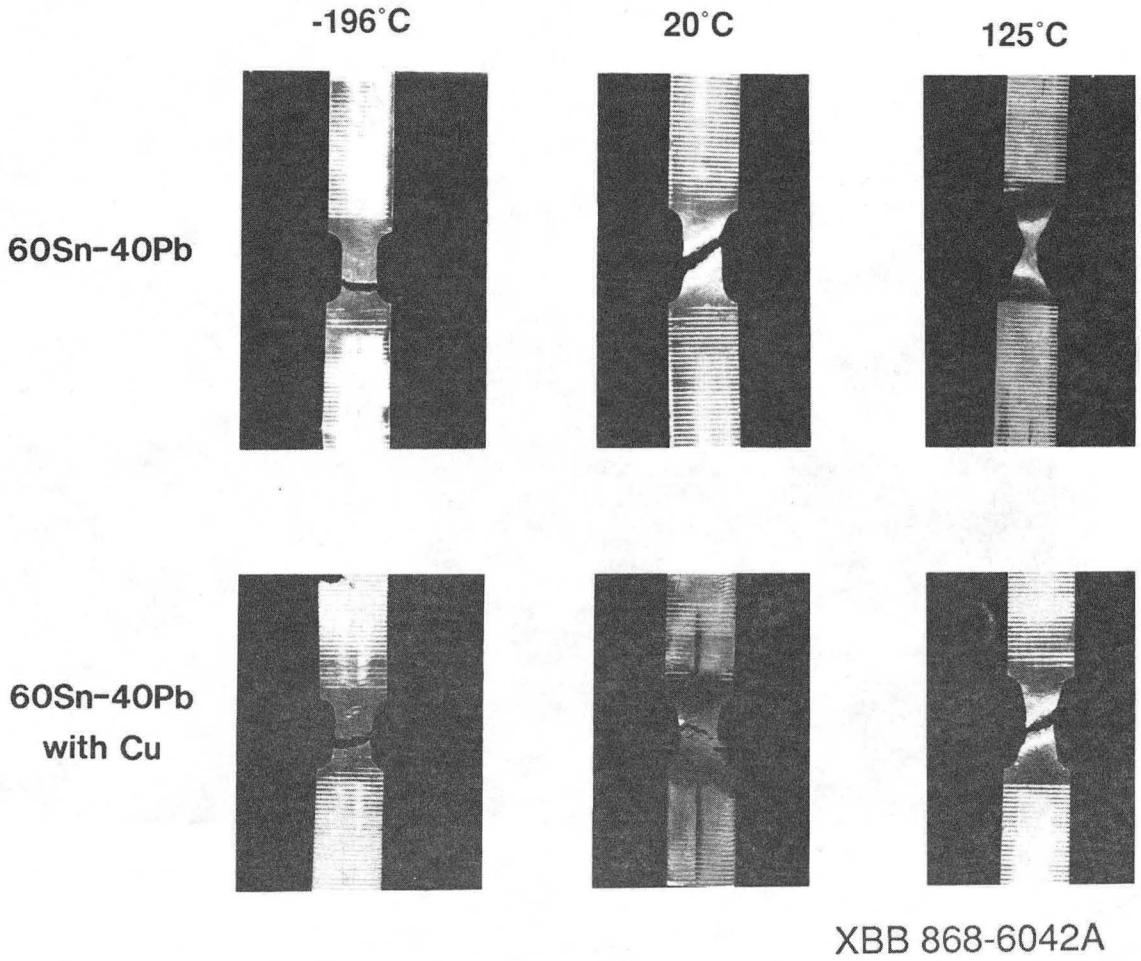

Figure 4.3.12 Macrographs of tensile specimens after failure.

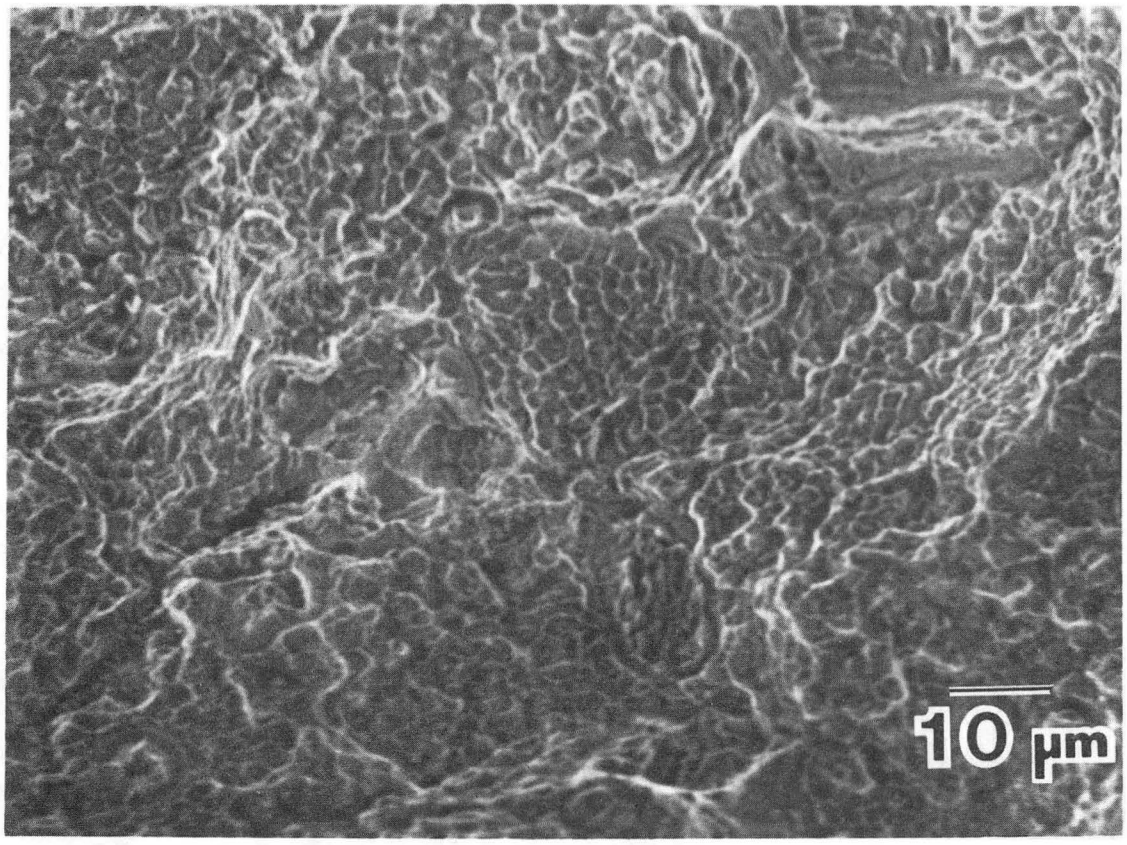

XBB 868-6034

Figure 4.3.13 SEM fractograph of pure 60Sn-40Pb failed at -196°C.

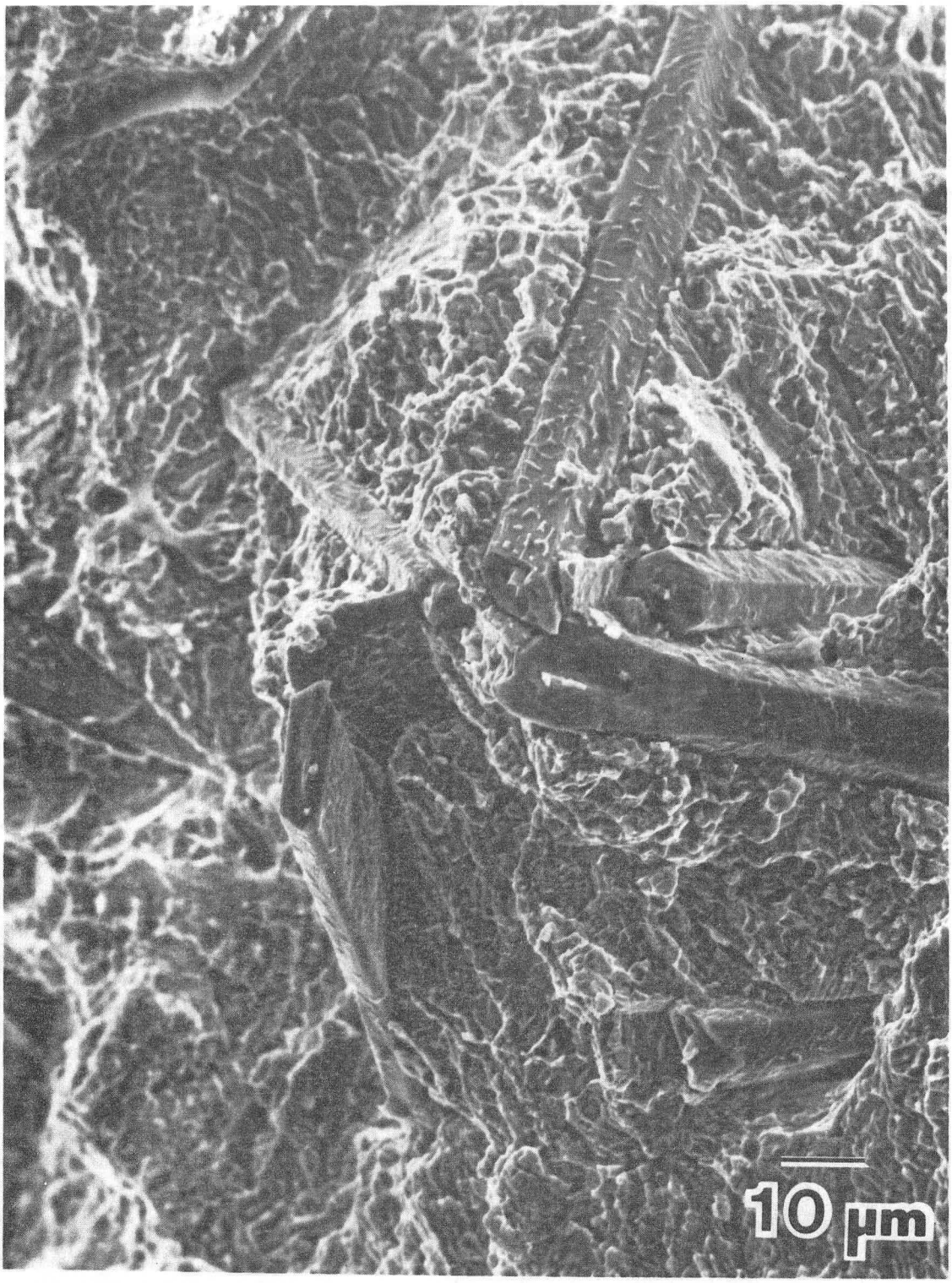

XBB 868-6026

Figure 4.3.14 SEM fractograph of 60Sn-40Pb with intermetallic whiskers failed at -196°C showing interfacial separation at the whisker/solder interface.

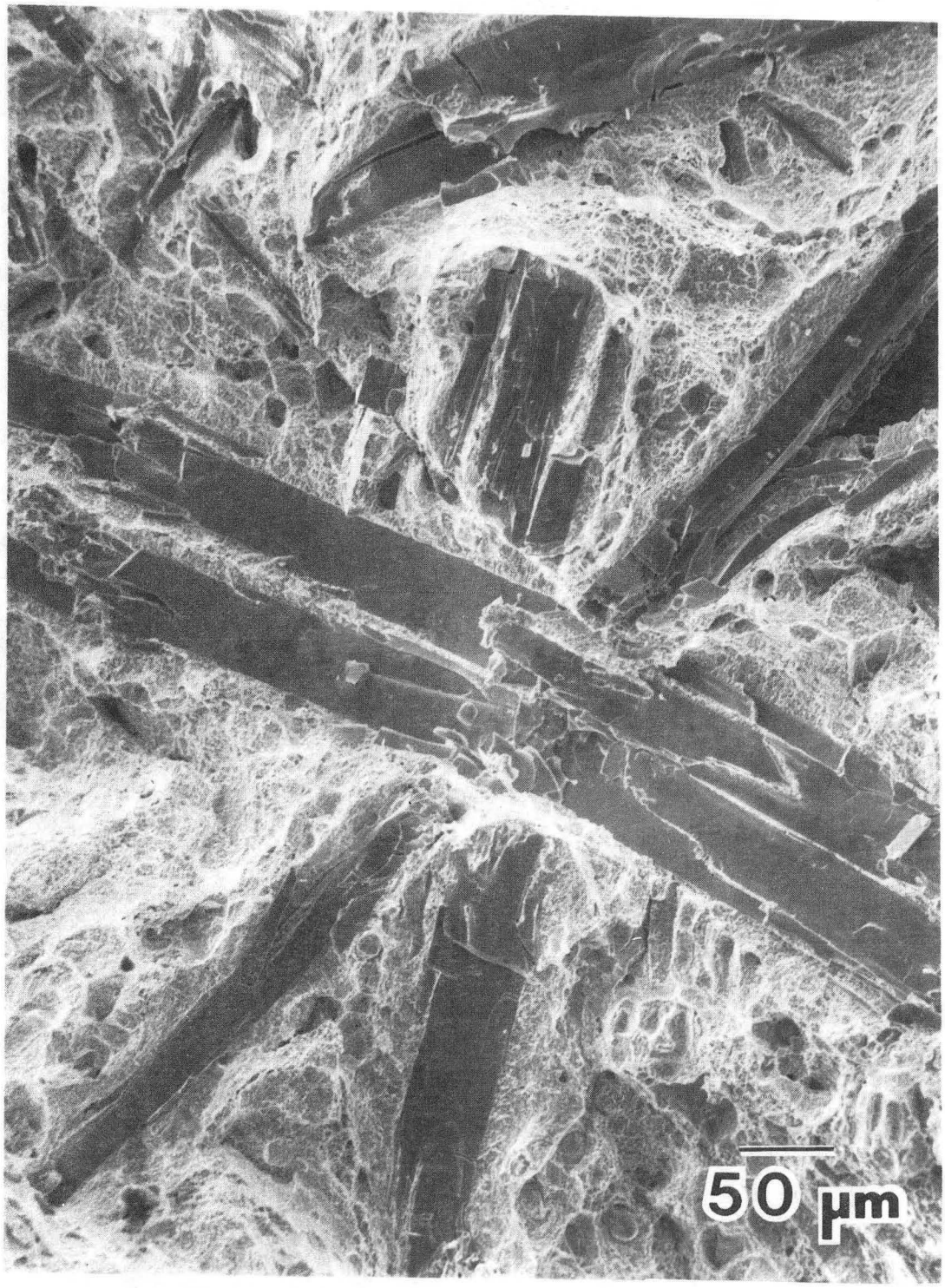

XBB 868-6254

Figure 4.3.15 SEM fractograph of 60Sn-40Pb with intermetallic whiskers failed at 20°C revealing cleaved intermetallics.

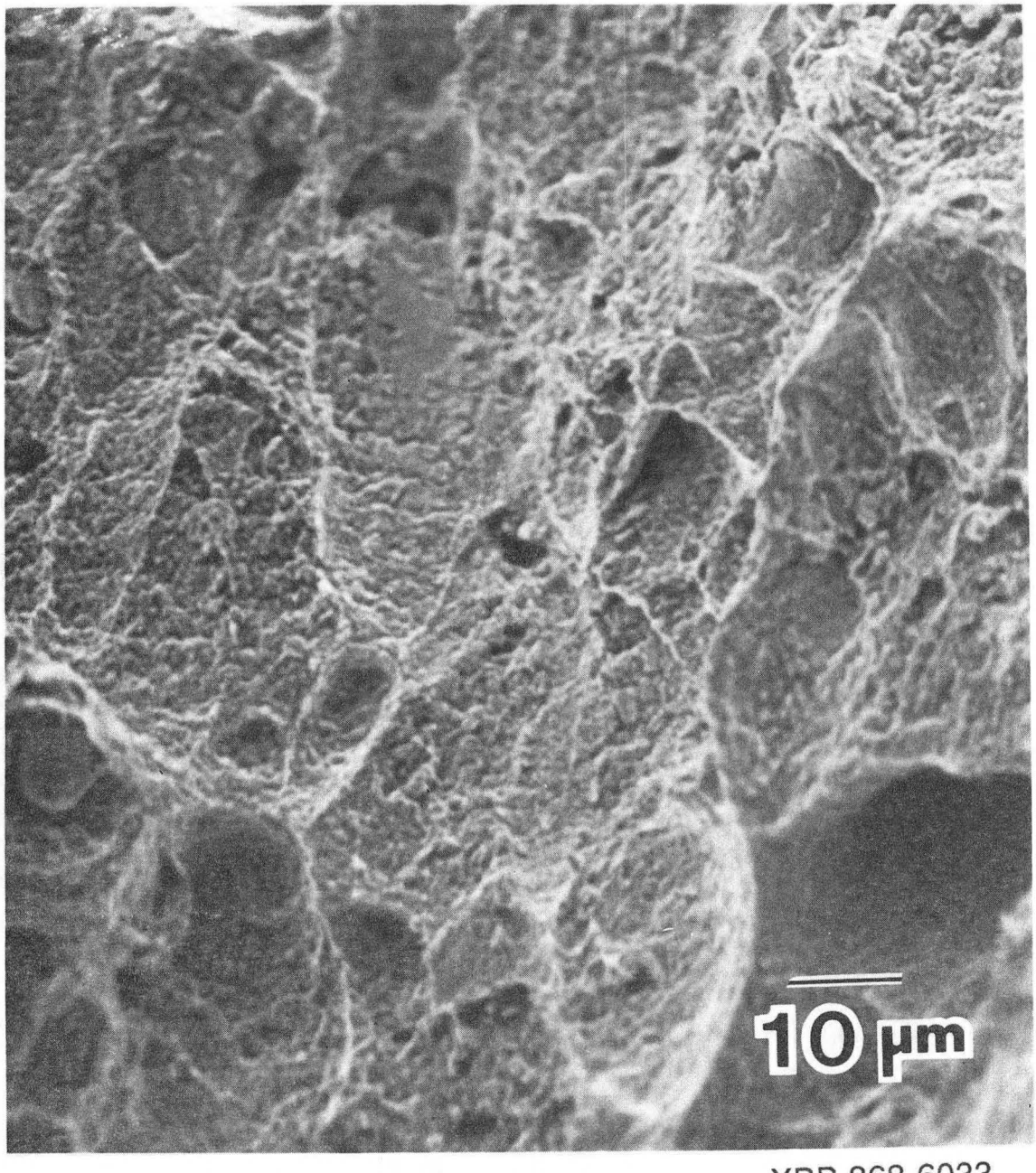

XBB 868-6033

Figure 4.3.16 SEM fractograph of pure 60Sn-40Pb failed at 20°C.

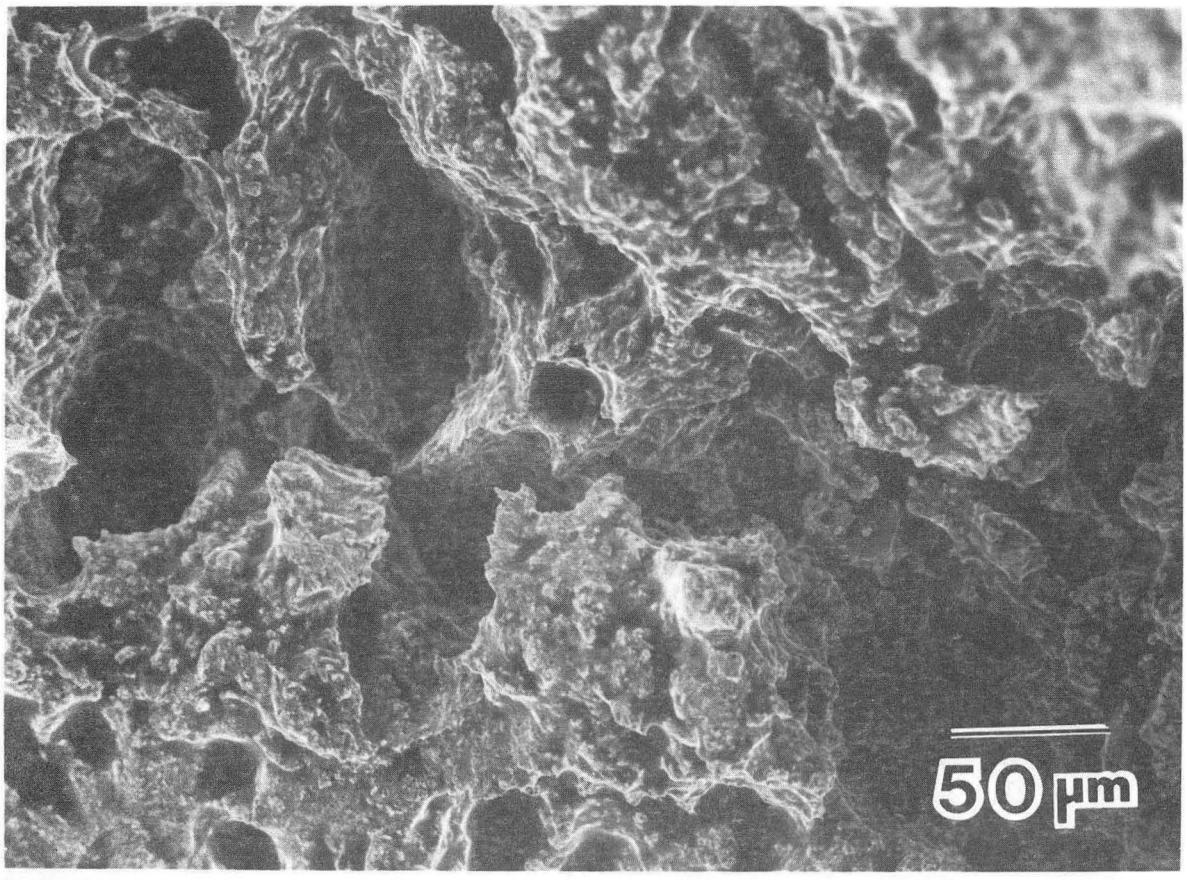

XBB 868-6036

Figure 4.3.17 SEM fractograph of 60Sn-40Pb with intermetallic whiskers failed at 125°C.

4.4 MECHANICAL PROPERTIES OF SOLDER AND SOLDER JOINTS

4.4.1 INTRODUCTION

The mechanical properties of solder joints in electronic packages must be understood to insure reliability in service. However, it is difficult to study the solder joints in packages due to their small size. It is therefore necessary to design mechanical test methods to evaluate solders and solder joints.

There are three factors that directly influence the mechanical properties of solder joints. The first is the geometry of the test specimen. The second is the test conditions (for example: temperature, and strain rate). The third is the microstructure of the specific solder composition.

With regards to the first factor, joint geometry, work has been performed to evaluate an optimum testing geometry[26,33,106]. Most joint designs test solder joints in shear, which is the common deformation mode in electronic packages. However, the designs proposed in the literature are inadequate for reasons discussed later in this section. Therefore a new specimen design to test solder joints in shear, in a variety of test conditions, is presented in this section.

In order to evaluate the microstructure of 60Sn-40Pb and 5Sn-95Pb solders bulk solder specimens were tested with different initial microstructures. These tests are used to evaluate the effect of microstructure on mechanical properties.

4.4.2 SPECIMEN DESIGN

• Shear Specimens

The following designs are commonly used to test solder joints in shear. These specimens are diagrammed in Figure 4.4.1. Each is discussed and shortcomings pointed out.

A) Single Lap Joint

This design consists of two plates soldered together then strained in a direction parallel to the joint. The difficulty with the single lap joint is that it does not test the solder joint in shear. Initially the joint experiences shear but, because the plates do not lie on the same axis during deformation, after a small amount of strain a moment arm develops causing the joint to deform in a condition further and further away from shear. The design is unacceptable.

B) Double Lap Joint

This design eliminates some of the problems associated with the single lap joint by adding a third plate and a second joint to the specimen. Now when the specimen is tested the moment arms balance and thus cancel the rotational forces on the joints. The problem associated with this design is that there are sharp corners present at the solder/plate interface. These corners lead to stress concentrations in these regions causing undesireable crack initiation sites. Furthermore practical difficulties are reported[106] in the manufacture of both the single and double lap joint. Specimens were soldered one at a time causing undesirable variances in microstructure between specimens which influence the mechanical properties of the joint.

C) Ring and Plug Joint

This design consists of a rod soldered into a sleeve. The joint gap is created by the insertion of wires between the rod and sleeve. Friction holds the ring and plug together during the process of soldering by immersion in a solder bath. This design does create a condition of shear in the joint during deformation. This specimen design has been proposed as the best for testing solder joints in shear[106]. However, this design does have shortcomings. First, the presence of the wires in the joint have an effect on joint performance. The wires add a friction force between the ring and plug. Thwaites[106] attempted to test the effect of strength vs. number of wires in the joint and found a weak correlation. The contribution that the wires have on specimen failure has not been determined, but the wires may act an initiation sites for failure. Most importantly this design does not allow for the observation of specimen failure. To observe the microstructure, and failures, cross sections of the specimen must be made. Furthermore the presence of voids in the joint can not be determined as well as overall quality of the joint, without cross sectioning. Similar to the single and double lap specimens, ring and plug specimens are manufactured one at a time causing possible undesirable variations between specimens.

D) Modified Double Lap Joint

To rectify the undesirable elements of the above three designs a specimen was designed to test solder joints in shear. This specimen is diagrammed in Figure 3.3. The specimen consists of three Cu plates soldered together forming two joints. Three rounded holes are machined into the Cu that isolates the joints in the center of specimen. Friction grips can then be affixed to the top and bottom portions of the specimen and vertically displacing the specimen causes the solder joints to experience simple shear deformation.

To manufacture the specimens the initial Cu assembly of Figure 3.1 was used. The assembly consists of three Cu plates bolted together with Cu spacers inserted at the edge of the assembly to form the gap for the solder to flow into. The interior surfaces of the joint were polished and etched with a solution of 50% HNO_3 + 50% H_2O then coated with a light coat of Johnsons Stainless Steel Flux. The assembly was then placed in a two stage vacuum furnace shown in Figure 3.2. In this furnace the Cu plate assembly was heated to 50°C above the melting point of the solder in the upper furnace while simultaneously the solder was heated in a graphite crucible to the same temperature in the lower furnace. This process occurs in vacuum and the flux evaporates from the surface of the Cu plates leaving a clean oxide-free surface to be soldered. The assembly was then submerged into the molten solder and the solder flows into the gaps between the Cu plates by capillary action. The solder bath was then quickly cooled to room temperature. The excess solder was then removed from the Cu plates and the three holes machined into the assembly. Single specimens were then cut from the assembly using a slow speed diamond saw.

The advantage of this specimen design and manufacturing process are the following. The specimen design creates a condition of simple shear in the joint during deformation with rounded corners so stress concentration in the joint is minimized. This configuration also allows for direct *in situ* observation of the deformation process in the joint. Furthermore it is possible to perform low cycle isothermal fatigue tests using this specimen. The manufacturing process introduces reproducibility in testing. From each assembly block 9-10 specimens are cut. Each of these cut specimens therefore have experienced identical processing, so variations between specimens is minimized. In this work only 60Sn-40Pb joints were tested in shear to failure.

• Bulk Solder

The specimen to test bulk solder is shown in Figure 3.7. These specimens were cut and machined from an ingot of solder. Approximately 15 specimens were made from each solder ingot. A strain rate of 0.05 mm/minute was used. Tests were performed in liquid nitrogen at -196°C, in ice water at 0°C, and at room temperature (20°C) to observed temperature effects. Both 60Sn-40Pb and 5Sn-95Pb were tested under different cooling rates and aging times, as described in the results section.

4.4.3 Results and Discussion

4.4.3.1 Solder Joints in Shear

To demonstrate that the double shear specimen does deform in simple shear an *in situ* experiment was performed. Lines were etched in a photolithographic process across the

Cu/solder joint and this specimen was subsequently tested at a slow rate of deformation. Photos were taken at set internals of time, and are shown in Figure 4.4.2. It is apparent from these photos that the lines across the solder joint deform in a linear fashion indicating that the specimen does deform in a state of simple shear.

The 60Sn-40Pb joints were tested at 0.2 mm/min, 0.05 mm/min, and 0.005 mm/min in shear to investigate the effect of deformation rate. These results are plotted in Figure 4.4.3 as a function of shear stress vs. shear strain. The ultimate tensile strength is found to increase and total elongation decreases with increasing strain rate. The effect of strain rate on the fracture surfaces of the joints is shown in Figure 4.4.4. At 0.005 mm/min and 0.05 mm/min the fracture surfaces consist of ductile dimples with the failure through the bulk solder of the joint. However, at the faster deformation rate of 0.2 mm/min the fracture surface consists solely of transgranular and intergranular fracture through the intermetallic. At fast strain rates the solder can not deform as rapidly as a lower strain rates thereby imposing stress upon the brittle intermetallic layers. At lower strain rates the solder takes up all the strain thus relieving any stress from the intermetallics and failure is through the solder. This observation has a strong implication on the testing of solder joints. Too fast a shear testing rate would result in behavior atypical of joints in electronic packages and therefore erroneous conclusions and extrapolations.

4.4.3.2 Bulk Solder

To examine the effect of different microstructures on the mechanical properties of solder bulk tensile tests were performed. For 60Sn-40Pb the effect of phase size coarsening was investigated. For 5Sn-95Pb the effect of cellular vs. homogeneous precipitation was tested.

• 60Sn-40Pb

To create a fine microstructure of 60Sn-40Pb solder the alloy was quenched from the melt in a Cu chill mold. This microstructure is shown in Figure 4.1.2.3 and consists of a fine distribution of globular regions with many small dendrites. The mean phase diameter is 2.5 μm. To create a coarse microstructure the alloy was furnace cooled from the melt and then aged at 150°C for 15 days. The coarse microstructure of globular Pb and Sn phases is shown in Figure 4.4.5. and has a mean phase diameter of 12.5 μm.

The results of the tensile tests on the bulk 60Sn-40Pb solder is shown in Figure 4.4.6 for the temperatures tested (-196°C, 0°C, and 20°C) and a strain rate of 0.05 mm/min. At all temperatures the fine microstructure had greater strength, greater total elongation, and a greater work hardening rate. As the temperature increases the strength decreases, and total

elongation increases for both coarse and fine 60Sn-40Pb microstructures. The implication of this result is that a coarse microstructure in a solder joint is deleterious to the joint behavior. Results, discussed later, in the thermal fatigue of solder joints shows the coarsened regions of the solder are the sites for joint failure.

• 5Sn-95Pb

The two microstructures tested in 5Sn-95Pb were discussed in section 4.1.1, lamellar cellular precipitates and the finely dispersed homogeneous β-Sn precipitates. The microstructures were shown to be cooling rate dependant. Therefore to create cellular precipitates 5Sn-95Pb specimens were solution heat treated at 200°C for 24 hours then furnace cooled to room temperature. To create a fine distribution of precipitates the 5Sn-95Pb specimens were solution treated at 200°C for 24 hours then rapidly quenched to room temperature in water. Both microstructures were aged for 3 days at room temperature to create an equilibrium microstructure.

The results of tensile tests on bulk 5Sn-95Pb solder specimens is shown in Figure 4.4.7 at 20°C and -196°C. The strengths are identical for both microstructures. The total elongation was slightly greater for the lamellar microstructure but this could be due to experimental error.

The tests on 5Sn-95Pb show that the precipitate microstructure has little influence on the mechanical properties of the solder in the equilibrium condition. As discussed previously, in section 4.1.1, the strength of the 5Sn-95Pb alloy decreases with aging time at room temperature, Figure 4.1.1.17. The equilibrium condition is overaged for both the cellular and homogeneous precipitate microstructures and the precipitates have little influence on the deformation behavior of the alloy. Work by Frost[56] also found a decrease in strength with aging time for 5Sn-95Pb and attributes this to a coarsening of the Sn precipitates. Frost also asserts that the precipitate distribution also affects the mechanical behavior, a fine distribution has greater strength. However, the change noted is small and could be within experimental error. The results of the tensile tests shown in Figure 4.4.7 indicate that at room temperature in the equilibrium overaged condition the β–Sn precipitates, regardless of their distribution (cellular vs. homogeneous), are so large as to not be effective dislocation obstacles. Therefore overaged and coarsened precipitates have little influence on strength.

4.4.4 SUMMARY AND CONCLUSIONS

A specimen design and assembly was developed to reproducibly test solder joints in a state of simple shear. This design satisfied the requirements that: a) the solder joints test in simple shear, b) the joints were free of flux entrapment and voids, c) there isreproducibility between tested joints, and d) the deformation process is observable in the joint. Tests using this design found that joint strength is dependant on strain rate. At a fast strain rate (> 0.2 mm/min) the joint failed through the interfacial intermetallics. The interfacial failure is attributable to the fact that fast strains can not be accommodated by the solder and thus imposes strain at the brittle interface.

Tensile tests were performed on bulk 60Sn-40Pb and 5Sn-95Pb solders. The 60Sn-40Pb alloy was tested at -196°C, 0°C, and 20°C for a fine and coarse microstructure. The fine microstructure had greater strength, longer total elongation, and a greater work hardening rate. Therefore the coarsening of the microstructure of 60Sn-40Pb is deleterious to the mechanical behavior of the solder. Bulk 5Sn-95Pb samples were also tested in tension at -196°C and 20°C for both homogeneous and cellular precipitate microstructures. For this solder the tensile behavior was found to be independent of microstructure. The reason for this behavior is attributed to the equilibrium microstructure of 5Sn-95Pb solder has an overaged coarse precipitate morphology and therefore the precipitates are ineffective as dislocation obstacles, regardless of distribution.

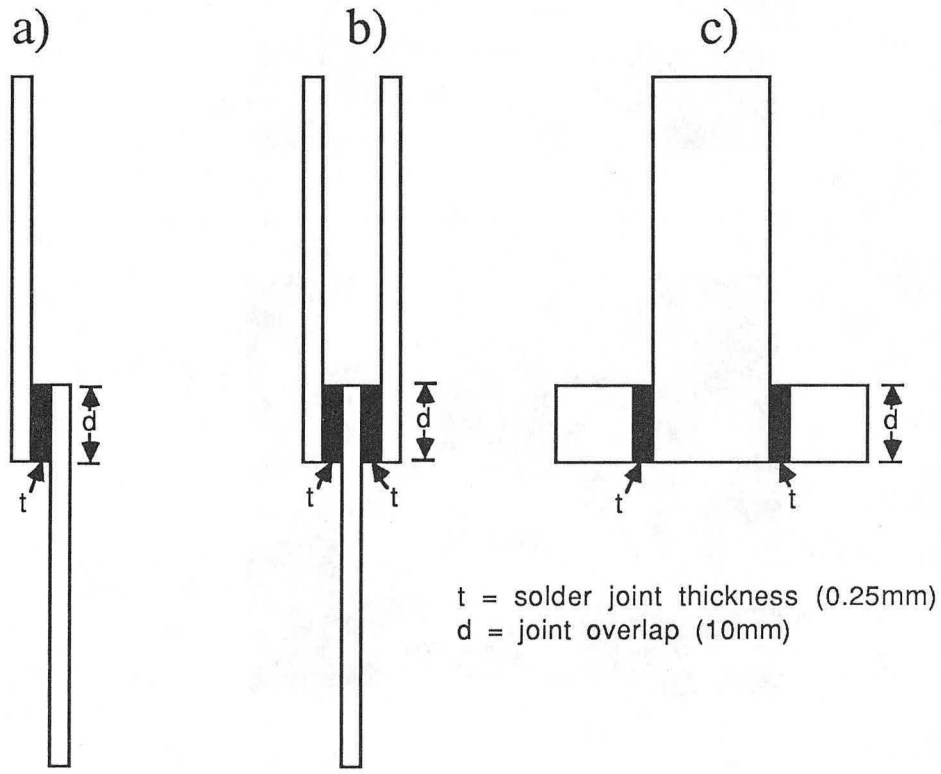

Figure 4.4.1 Specimen designs commonly used to test solder joints in shear. a) single lap, b) double lap, and c) rod and sleeve.

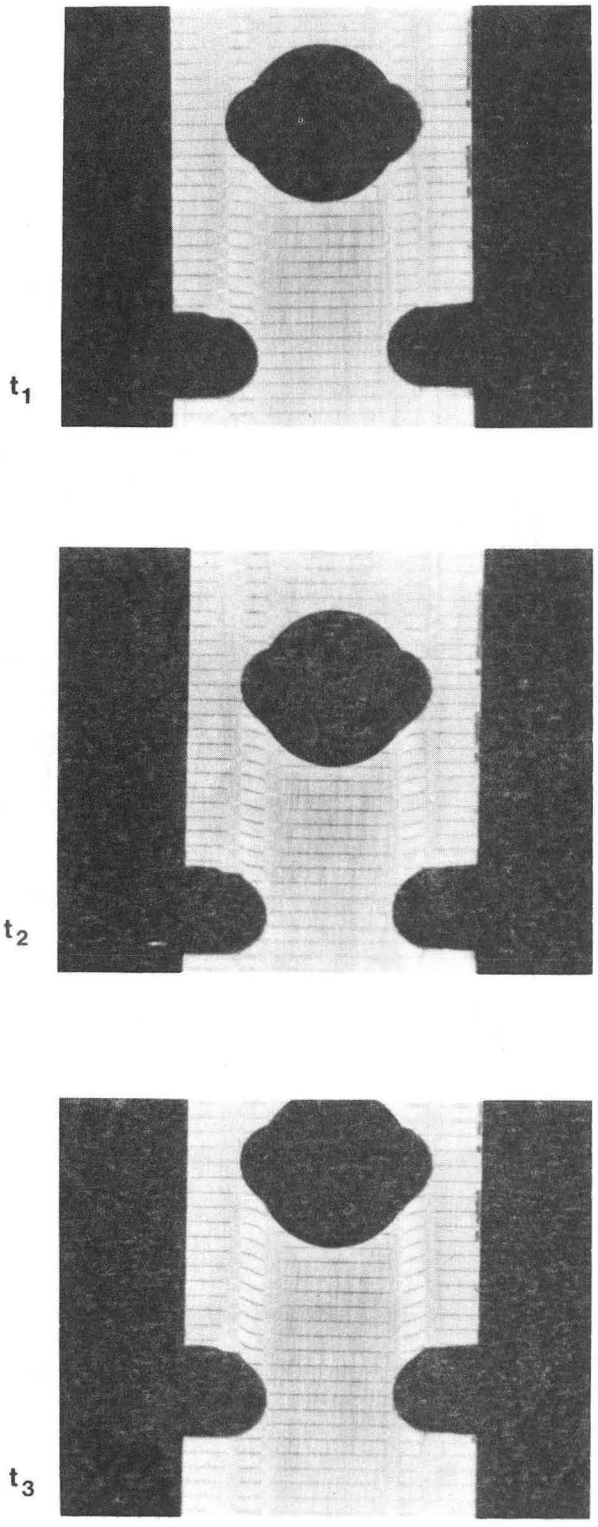

XBB 863-1818

Figure 4.4.2 Optical photograph showing deformation of double lap shear specimen.

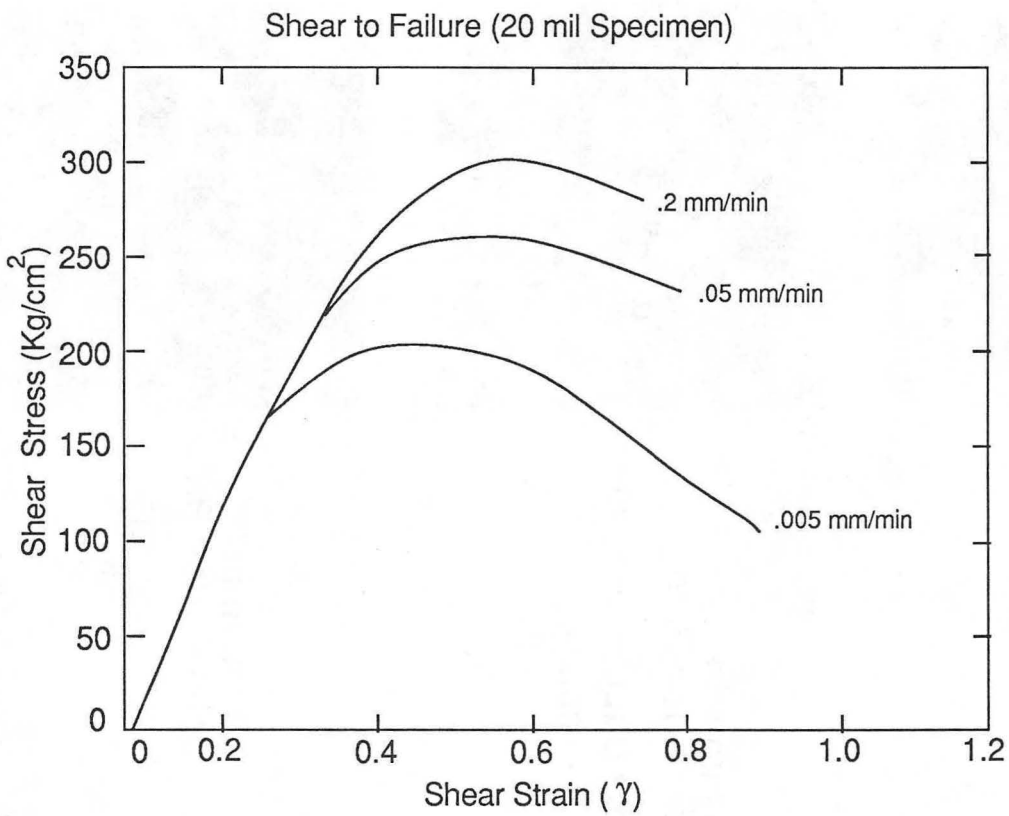

Figure 4.4.3 Plot of shear stress vs. shear strain for a 20 mil thick solder joint as a function of deformation rate.

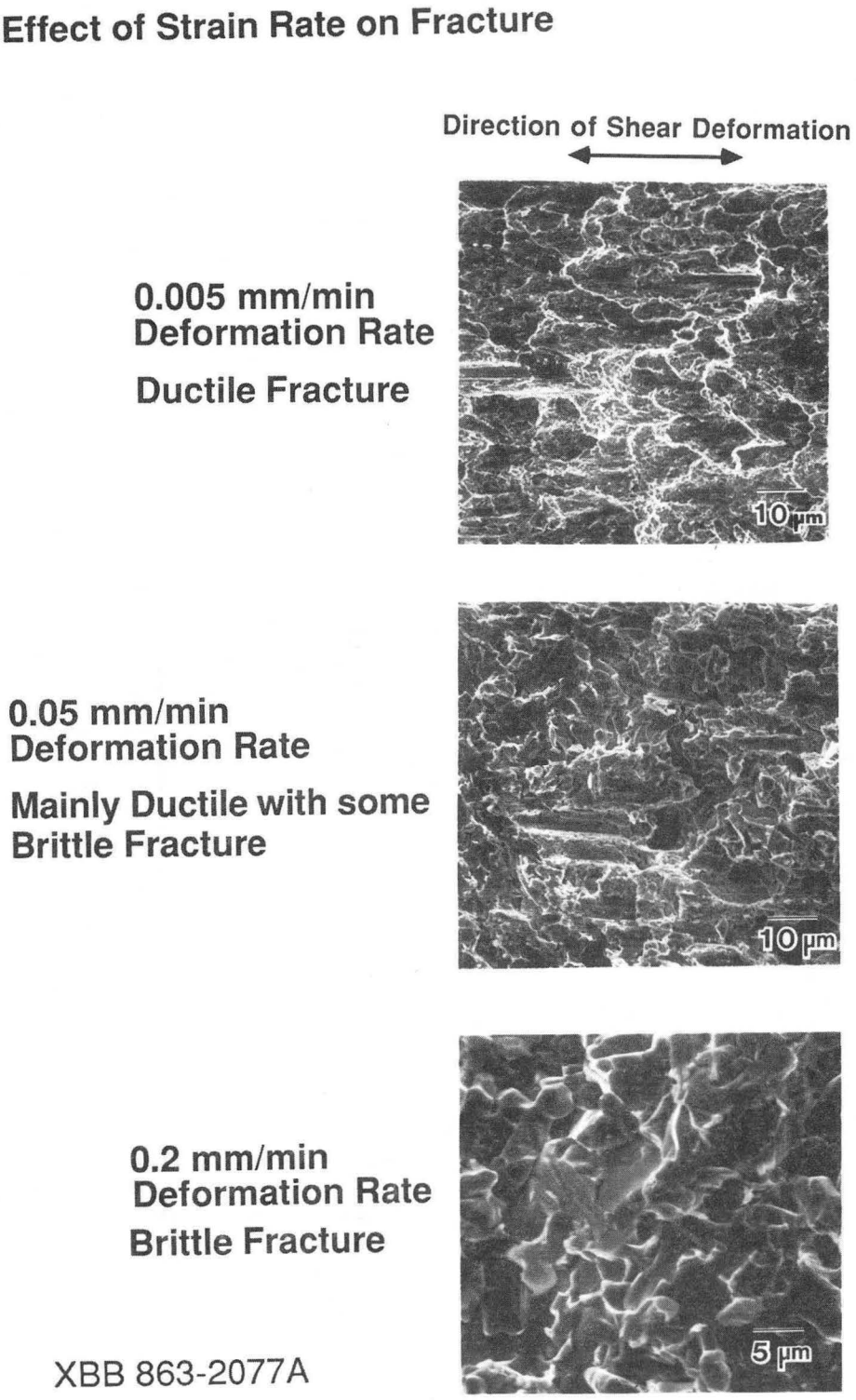

Figure 4.4.4 SEM fractographs showing the effect of deformation rate on the failed 60Sn-40Pb/Cu joints.

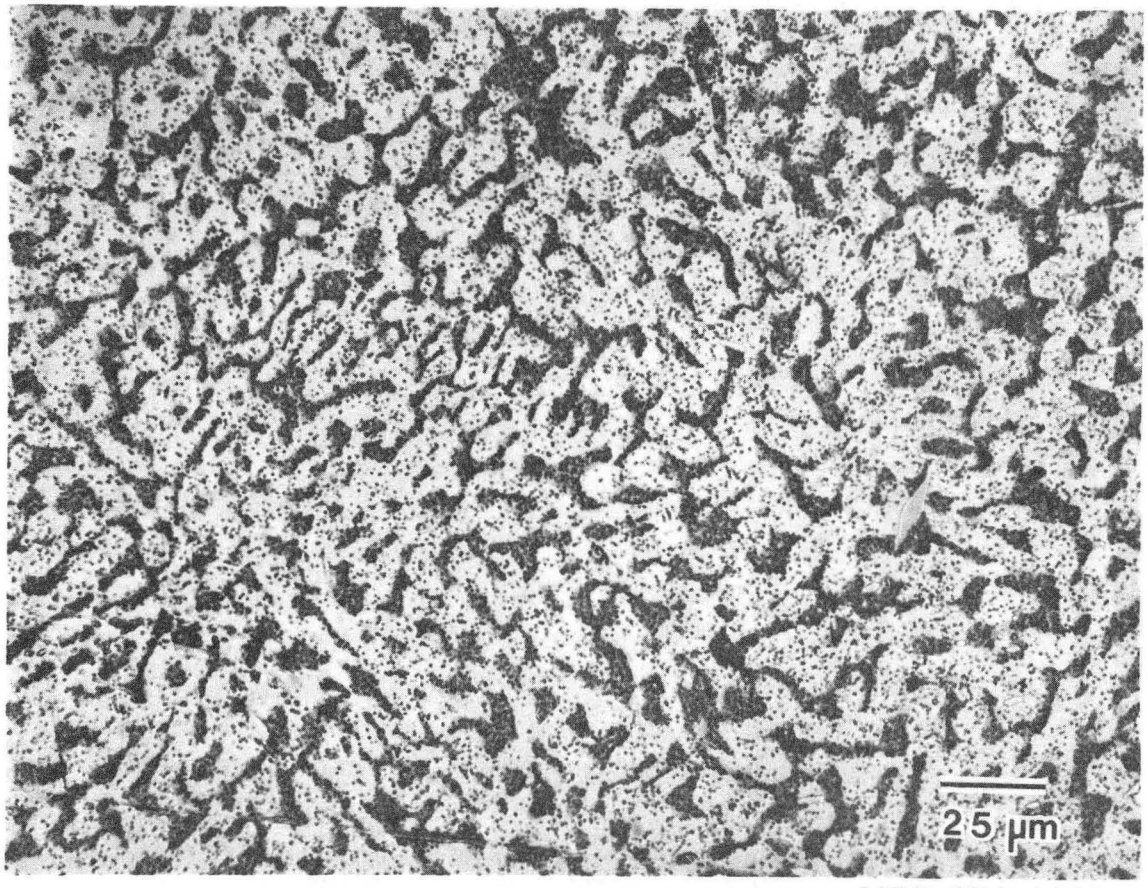

XBB 876-4400

Figure 4.4.5 Optical micrograph of coarse 60Sn-40Pb microstructure (slow cooled from the melt and aged for 15 days at 150°C).

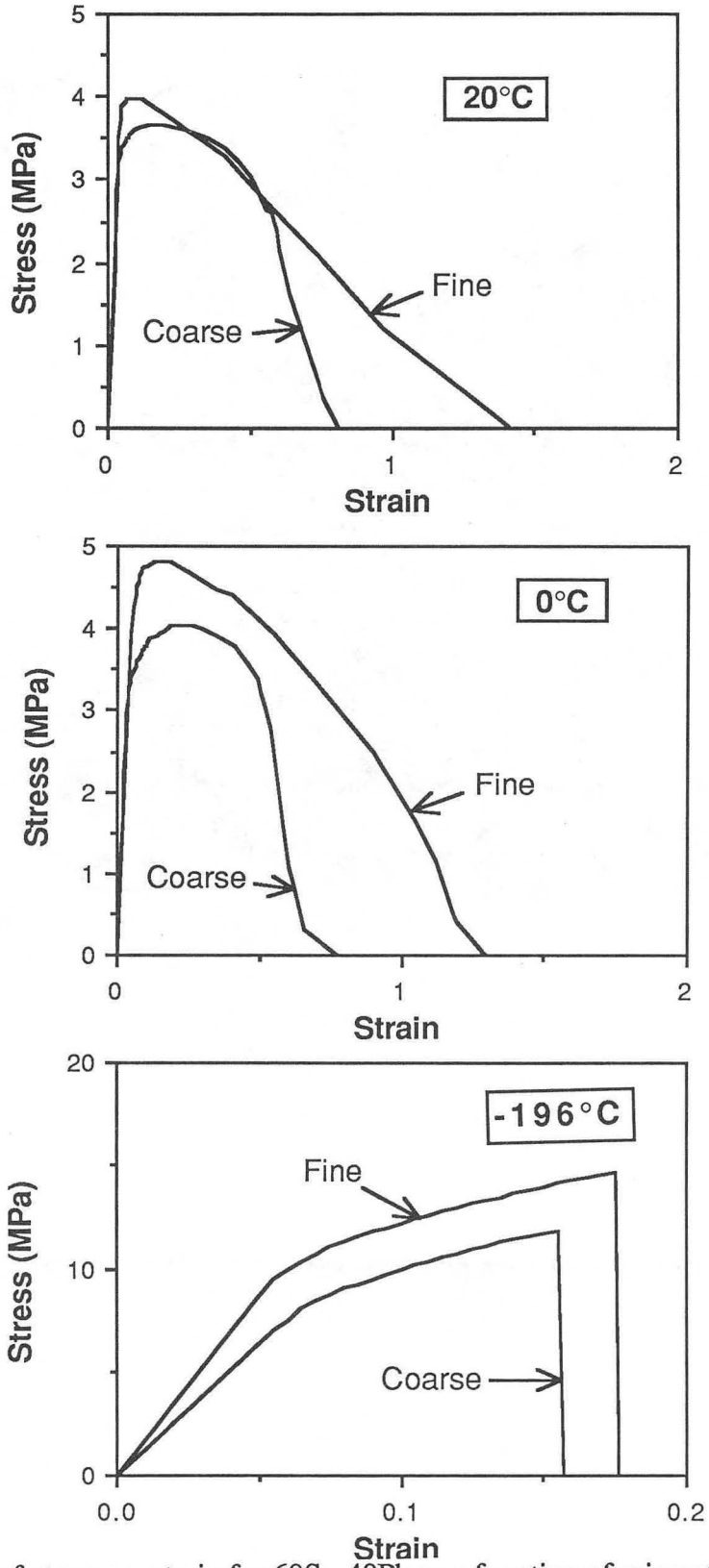

Figure 4.4.6 Plots of stress vs. strain for 60Sn-40Pb as a function of microstructure and temperature.

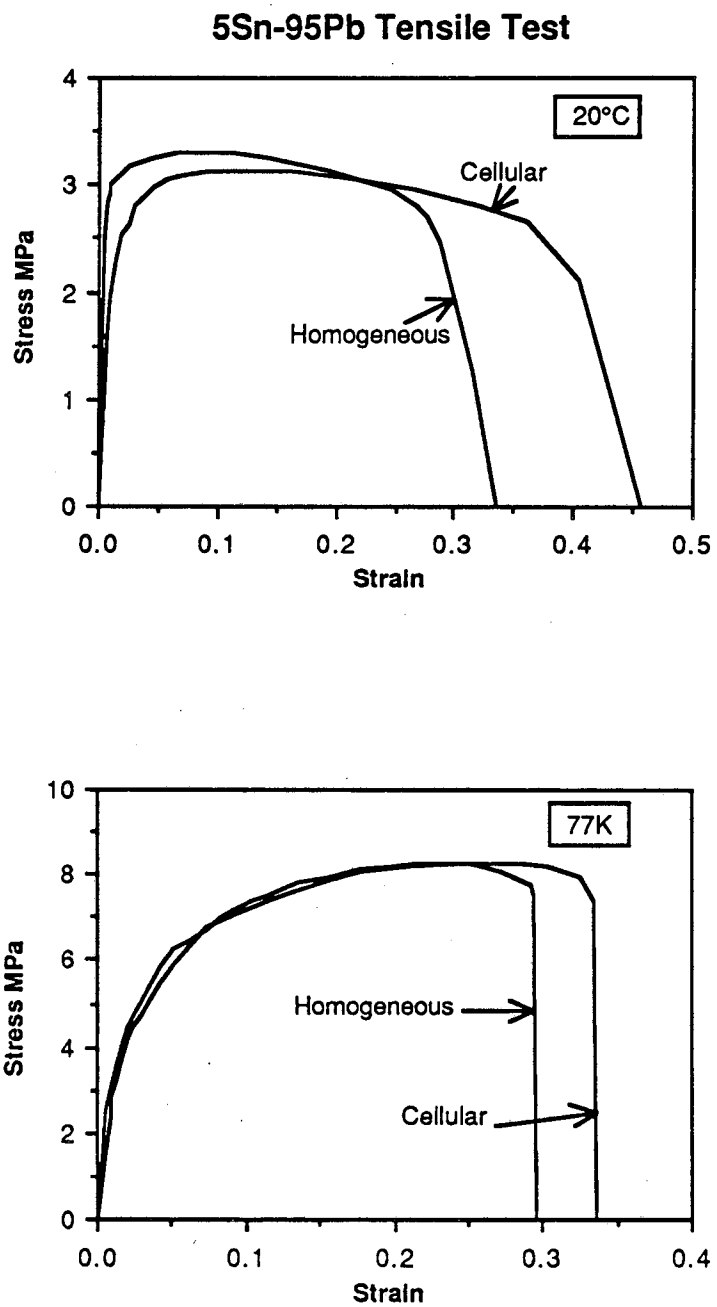

Figure 4.4.7 Plots of stress vs. strain for 5Sn-95Pb as a function of microstructure and temperature.

4.5 THERMAL FATIGUE

4.5.1 INTRODUCTION

Thermal fatigue failures of solder joints in electronic packages is of critical concern in the microelectronics industry. The cause of these failures is a combination of thermal fluctuations experienced by the package and the materials of differing thermal expansion coefficients used in the package. When an electronic package encounters thermal fluctuations cyclical strain is imposed upon the solder joints which eventually leads to joint failure. The failure of solder joints of electronic components due to thermal fatigue is well documented[8-15,22,24,36,37,47,107,108]. An example of one such failure is shown in Figure 2.1 (and is courtesy of M. Wolverton of Texas Instruments). The solder joints failed in this surface mount package after 700 cycles between -55°C and 125°C. To further complicate the thermal fatigue problem the trend in microelectronic packaging is towards larger integrated chips (and therefore larger chip carriers) surface mounted on circuit boards. As carriers become larger the strains imposed upon solder joints also increases thereby exacerbating the thermal fatigue problem. Therefore the thermal fatigue behavior of solder joints must be better understood to alleviate the problem of thermal fatigue. A microstructural analysis of solder joints in thermal fatigue is the most appropriate method to perform this study.

The solder joints in an electronic package encounter a complicated state of strain in thermal cycling[16], although the primary strain state is in shear[16]. This would make a fundamental study of the microstructural evolution in thermal fatigue difficult to interpret on actual joints in an electronic package. Therefore for the work in this study a simplified solder joint was designed that experiences simple shear on thermal cycling[109,110].

The purpose of this study is to document, and understand, the microstructural development of two solders (60Sn-40Pb and 5Sn-95Pb) in a joint configuration, in thermal fatigue. These observations make it possible to characterize the microstructural causes of failures in thermal fatigue. Furthermore it is possible to compare these thermal fatigue results with isothermal fatigue tests[109-111] (fatigue of solder joints in shear with cyclical strain at constant temperature) and evaluate whether isothermal fatigue tests represent true thermal fatigue.

4.5.2 EXPERIMENTAL PROCEDURE

To perform thermal fatigue tests a specimen was designed that would impose strains on a solder joint under thermal cycling conditions. This design is shown in Figure 3.4. The design consists of an aluminum plate sandwiched between two copper plates. The

aluminum plate was plated with 0.05 mm (0.002 in) of Ni to act as a diffusion barrier, and a 0.025 mm (0.001 in) of Cu to give the solder joint a similar interface on each side. The specimens were manufactured using the techniques described previously for the wholly Cu assembly, section 3.0. The holes drilled at the ends of the specimen were made so that the solder joints at the ends of the specimen imitate the small surface mount joints in an electronic package. The Al has a thermal expansion coefficient of 25 μin/in°C while that of Cu is 16.6 μin/in°C so upon thermal cycling a maximum strain is imposed upon the ends of the specimen and decreasing linearly to zero in the center. The magnitude of strain imposed is increased by either lengthening the specimen or by decreasing the solder joint thickness. For the experiments in this study a maximum 19% shear strain was imposed on the solder joints.

Thermal cycling was performed using the apparatus shown schematically in Figure 3.5. The device consists of a digitally controlled crane that automatically cycles specimens between two thermal baths. The high temperature bath consists of resistively heated oil. The low temperature bath was made using ethyl alcohol cooled by a liquid nitrogen through a Cu coil. The low temperature was controlled by varying the liquid nitrogen flow rate. The use of liquid baths had a two fold purpose. First, using a liquid medium reduces the oxidation specimens would receive in air, and thus eliminates a complication to the results. Secondly, the liquid gives a rapid heat transfer, allowing for an accelerated fatigue test.

The hold time in each bath was 5 minutes with a transfer time of 30 seconds. The short hold time was based on stress relaxation data obtained by Tribula et. al.[112]. They found for a 20% imposed shear strain on 60Sn-40Pb solder joints 50% of the initial strain is relaxed in a few minutes after which the stress remains relatively constant (on the order of days) at 50%. Therefore a hold time of 5 minutes imitates the field conditions of a solder joint, but at an accelerated rate. Microstructural evolution versus the number of thermal cycles was evaluated by placing a number of specimens in the cycling device and removing individual specimens after a number of cycles.

Specimens of 60Sn-40Pb and 5Sn-95Pb joints were prepolished down to 1 μm Al_2O_3 before thermal cycling so that observations on surface joint deformation could be obtained. The 60Sn-40Pb joint specimens were also polished for optical observations using the technique described in section 3.0. Special care was necessary in the polishing of these specimens because the Cu and Al became galvanically coupled causing the Al to severely pit and interfere with the joint interface. This problem was solved by polishing the specimen for only short times in the Mastermet colloidal solution.

To observe the 5Sn-95Pb joint microstructure, after cycling, samples were polished on 600 grit silicon carbide paper parallel to the joint (else removed Cu and Al become imbedded

in the soft solder). The sample was then polished using 0.05 μm Al_2O_3 and kerosene on felt paper, again parallel to the joint. Etching was performed using 20 ml H_2O + 5 ml HNO_3 + 3.5 ml glacial acetic acid for 5 seconds followed by 20 seconds etching in 3 parts glacial acetic acid + 1 part H_2O_2 (30%). This revealed the microstructure of the solder region. The microstructure of the 5Sn-95Pb was very uneven after etching so observations were made in the SEM.

4.5.3 RESULTS

4.5.3.1 5Sn-95Pb Joints

The 5Sn-95Pb joints after thermal cycling between -55°C and 125°C is shown in cross section in the SEM micrograph of Figure 4.5.1 for various numbers of cycles. These joints were not polished after cycling. The strain imposed on these specimens was 19%. Cracks form through the bulk of the solder after 120 cycles and become more severe as the number of cycles increases. A more magnified view of the 5Sn-95Pb joint after 120 cycles is shown in Figure 4.5.2. The direction of shear is horizontal across the page in this micrograph. The cracks run both parallel and perpendicular to the joint and the cracks have a homogeneous distribution throughout the joint. The 5Sn-95Pb cycled specimens were polished and etched to determine where these cracks occur in the microstructure. A typical example is shown in Figure 4.5.4 after 250 cycles. The cracks are intergranular at the Pb grain boundaries. (The raised regions adjacent to the cracks is an etching artifact where etched material from the cracked region redeposited at the crack.) The cracks appear to not be influenced by the presence, or absence, of β−Sn precipitates. After cycling the precipitation pattern has not changed. Discrete precipitates are found throughout the joint with some cellular precipitates in localized regions. The microstructure has not significantly changed from the initial 5Sn-95Pb microstructure shown in Figure 4.2.3. The thermal cycling does not appear to influence the precipitation of the Sn, even though the precipitates dissolve and reprecipitate on each thermal cycle.

The failure pattern observed in this work is very similar to that found by Levine and Ordenez[8] who thermally cycled 5Sn-95Pb joints in the first level of flip chip carrier package. They found that the 5Sn-95Pb joints cracked in the bulk solder both parallel and perpendicular to the direction of shear. Although the microstructure was not analyzed in depth the mechanism for failure was thought to be grain boundary sliding. SEM micrographs of the failed solder balls appeared the same as the joints in Figure 4.5.2.

Isothermal fatigue has also been performed on 5Sn-95Pb joints[109-111] using the double lap shear specimen described in section 2.0. The purpose of performing isothermal fatigue tests is to simulate the strain induced in thermal fatigue without the necessity of cycling the

temperature. Isothermal fatigue tests are much simpler to perform and would be useful if the results could be applied to thermal fatigue. The isothermal fatigue tests were performed at shear strains ranging from 20% to 35%, at strain rates varying from 8.4 cycles/hour to 14.8 cycles/hour. Failures typically occurred in these joints after 100 cycles regardless of imposed strain. A typical example of a failed 5Sn-95Pb joint in isothermal fatigue is shown in figure 4.5.4. Note that the joint has failed in the solder again both parallel and perpendicular to the direction of shear. The etched microstructure of an isothermally fatigued joint is shown in Figure 4.5.5. The cracks occur at Pb grain boundaries independent of precipitate location or morphology. The failures in isothermal fatigue are very similar both in appearance and number of cycles to failure to those in thermal fatigue.

4.5.3.2 60Sn-40Pb Joints

4.5.3.2.1 -55°C to 125°C Thermal Cycle

Thermal fatigue specimens, shown in Figure 3.4 with 10 mil (0.254 mm) 60Sn-40Pb joints were thermally cycled between -55°C and 125°C up to 2000 cycles with a 5 minute hold time at each temperature. The optical microstructure of these joints as a function of number of cycles is shown in Figure 4.5.6. An interesting development in the microstructure is found to occur after 625 cycles, the microstructure in the bulk solder heterogeneously coarsens parallel to the direction of shear in the regions of high shear strain. This is shown clearly in Figure 4.5.7 which is a specimen after 684 thermal cycles. Both the Pb and Sn-rich phases coarsen. The coarsened Pb-rich phase is devoid of Sn precipitates. The coarsening is not associated with the interface, heterogeneous coarsened regions occur anywhere from near the interface to the center of the joint. The coarsened regions show no preference to form either on the Cu or Al side of the joint. The coarsened regions initially are very thin but gradually increase in width as the number of cycles increases.

After 1000 cycles cracks develop in the heterogeneous coarsened region of the solder, Figure 4.5.6. These cracks are found to occur only within the heterogeneously coarsened regions of the solder joint, as shown in Figure 4.5.8. The crack follows the coarsened region as it tails down from right to left across the joint. The cracks occur through the Sn-rich regions or at the interface between the Sn-rich and Pb-rich regions. This is clearly shown in the polarized optical micrographs in Figure 4.5.9 of the specimen after 1300 cycles. The cracks occur though the Sn-rich regions at Sn-Sn grain boundaries. In polarized light different Sn grains show variations in contrast and cracks are observed between these variations in contrast. The cracks propagate through Pb-rich regions so as to join failed Sn-rich regions. The Sn grains observed in the polarized micrographs are about

3 μm in diameter. The Sn grain size previously observed for bulk solder aged at 125°C for 167 hours (which is equivalent to 2000 cycles with a 5 minute hold time) was 1.3 μm, as described in section 4.1.2. The Sn grains in the highly strained coarsened regions therefore grow larger than expected for thermal aging alone.

To determine the effect of joint thickness 60Sn-40Pb solder joint specimens of 20 mil (0.51 mm) thickness were also thermally cycled between -55°C and 125°C. By doubling joint thickness the shear strain was halved to 10%. The results of this experiment are shown in Figure 4.5.10. Again heterogeneous coarsened regions develop throughout the solder. After 1000 cycles multiple coarsened regions occur parallel to the shear direction. More than one heterogeneous region was observed in each sample. Despite the halved strain the joints fail, through the coarsened region, after 1000 cycles. This is the same as for the 19% shear strained samples. The failures again occur through the Sn-rich regions in an intergranular fashion.

Besides the heterogeneous coarsening, a columnar microstructure develops in the 60Sn-40Pb joints with thermal cycling. These columns consist of similar Sn-Pb colonies that run perpendicular to the direction of shear. The most clear evidence of these columns are shown in Figure 4.5.10 after 1300 cycles (and Figure 4.5.14). A transition from a globular column to a lamellar column is shown in Figure 4.5.7, and the abruptness of the transition is evident. The cause of the development of these columns is not understood but their creation may act to relieve the shear strain imposed on the joint. This can be thought of being similar to the way a deck of cards respond to a shear strain. This point is not fully understood and is worthy of further investigation.

4.5.3.2.2 High and Low Temperature Thermal Cycling

In an effort to determine the effect of high and low portion of the thermal cycle the following experiments were performed. The full -55°C to 125°C cycle was split into two equal cycles of -55°C to 35°C and 35°C to 125°C. The specimen length was increased to induce a 19% shear strain on cycling. A 10 mil (0.254 mm) 60Sn-40Pb solder joint thickness was used in these experiments.

• 35°C to 125°C

The 35°C to 125°C cycle shows the effect of the high temperature portion of the thermal cycle. Furthermore this thermal fluctuation is representative of the temperatures encountered in power cycling an electronic package.

The optical microstructure of the 60Sn-40Pb joints as a function of the number of cycles between 35°C and 125°C is shown in Figure 4.5.11. After 500 cycles the heterogeneous

coarsened region develops in the center of the solder joint, in a fashion identical to that found for the full -55°C to 125°C thermal cycle.

Cracks develop in the coarsened regions after 1500 cycles. A higher magnification of these cracks is shown in Figure 4.5.12. The cracks preferentially occur through the Sn-rich phase or at the interphase boundaries. Cracking occurs in the Pb-rich phase only when a path through the Sn is not available. The similarities between the full thermal cycle and the high temperature cycle indicate that coarsening and cracking is dependant on strain at elevated temperatures.

• -55°C to 35°C.

Cycling between -55°C and 35°C examines the behavior of the solder joint at the low temperature portion of the thermal cycle. Figure 4.5.13 shows the optical microstructure of the joint as a function of cycles between -55°C and 35°C. Heterogeneous coarsening is not extensive for this low temperature cycling. However, a very thin heterogeneously coarsened region in the solder does develop after 1500 cycles. This coarsening is shown clearly in Figure 4.5.14 for the sample after 1500 thermal cycles. A coarsened region develops both parallel to the shear direction and between columnar cells of the solder. Cracks develop in the thin coarsened regions, after 1500 cycles, and the cracks run through the Sn-rich regions or at interphase boundaries. Cracks were only observed within the coarsened regions.

Coarsening can occur at these low cycling temperatures because even at 35°C the solder is at 0.67 of its homologous temperature. With strain and temperature present at 35°C heterogeneous coarsening can occur but not to the same extent as at higher temperatures in the thermal cycle.

4.5.3.3 Thermal Cycling (-55°C to 125°C) of Unconstrained Bulk Solder

Unconstrained bulk 60Sn-40Pb solder was cycled between -55°C and 125°C to observe coarsening behavior as a function of temperature alone. Optical micrographs of the solder are shown in Figure 4.5.15 as a function of the number of cycles. Coarsening is observed to develop as the number of cycles increase. The coarsening was homogeneous in nature, both the Pb and Sn regions coarsened throughout the solder. The Sn grain size was found to be 1.31 μm, section 4.1.2. The Pb-rich regions remain heavily decorated with Sn precipitates ranging from 0 cycles to 2000 cycles. In heterogeneous coarsening, described previously, the Pb-rich regions were denuded of precipitates. No cracking was observed to occur anywhere within the solder for any number of cycles. The heterogeneous coarsening and cracking is therefore a function of temperature and applied strain.

4.5.3.4 Thermal Cycling of Cu/Solder/Cu Joints (-55°C to 125°C)

There exists a difference in the coefficients of thermal expansion between Cu (16.6 μin/in°C) and 60Sn-40Pb solder (24..7 μin/in°C). It has been suggested[13,14] that failures of solder joints occur, in part, due to these differences. To examine this postulate specimens of Cu/Solder/Cu joints were manufactured and thermally cycled from -55°C to 125°C. The only strain imposed in these specimens was due to the thermal expansion difference between the solder and the Cu.

Optical micrographs of the Cu/Solder/Cu joints as a function of the number of thermal cycles is shown in Figure 4.5.16. Heterogeneous coarsening does occur but only begins after 2000 cycles. The experiment ended after 2000 cycles and no cracks were observed anywhere within the joint. (The dark interfacial regions in the sample after 1000 cycles is a polishing artifact of the height difference between the solder and Cu.) It is expected that cracking would eventually occur in the coarsened region given enough thermal cycles. This indicates that the difference in expansion between solder and Cu is significant to the thermal fatigue failure of solder joints. However, this effect is not as prevalent as when an externally applied strain is present (i.e. when the joint is constrained between Cu and Al).

4.5.4 DISCUSSION

• 5Sn-95Pb Joints

The results of this work suggests that cracks form in 5Sn-95Pb joints in thermal fatigue throughout the solder, parallel and perpendicular to the direction of shear. In the shear configuration used in this study cracks are on planes of maximum shear stress. Furthermore the cracks in the solder are intergranular in nature. Results from other work[109-111] on isothermal fatigue, in similar strain conditions, show an identical failure pattern. The following discusses possible metallurgical causes for this behavior.

There are three possible means by which 5Sn-95Pb solder joints can take on the intergranular failure pattern observed. These are: grain boundary sliding, hard particle/matrix cracking, and cracking at grain triple points. The most plausible explanation is grain boundary sliding as it is a high temperature deformation process. At room temperature 5Sn-95Pb is at 0.51 of its homologous temperature.

As the solder joint is deformed in shear the Pb grains deform to accommodate the strain. A mechanism for this process is diagramed in Figure 4.5.17. Under shear strain the grains slide relative to one another, 4.5.17b. In so doing voids open up at the boundaries which fill by diffusional flow, 4.5.17c. Two mechanisms by which cracks could form are as follows. If diffusional flow is limited (by, say, the low temperature portion of the thermal cycle) the voids would remain present at the grain boundaries which could eventually lead to

intergranular cracks upon repeated cycling. The second possible means of intergranular cracking is tied to the irregular morphology of the Pb grains. The Pb grains have been observed to have very irregular boundaries, section 4.1. When strain is imposed the grains can not slide relative to one another, to accommodate the strain, due to the rough irregular boundaries. Eventually cracks must then form at the grain boundaries to accommodate the strain.

The two mechanisms discussed above are related to grain boundary sliding, and indirectly, to triple point cracking. The third possible cause of failures is hard particle/matrix cracking. This mechanism was not observed. The Sn precipitates did not act as initiation sites for cracks. Cracks were found to form intergranularly and the Sn was found to precipitate within the grains and not preferentially at the boundaries. It may be that the Sn precipitates have no influence whatsoever in the thermal fatigue failures of 5Sn-95Pb and cracks form at grain boundaries solely because the grain boundaries are the weak link in the microstructure. This is supported by isothermal fatigue results[109-111] that showed 5Sn-95Pb joints failed in a similar pattern at low and high temperatures. However, the Sn precipitates may influence the behavior of the joints in thermal fatigue. As discussed in section 4.1.1 the precipitation of Sn in Pb lowers the strength of solder parabolically with time, Figure 4.1.17. In thermal fatigue, Sn dissolves into solid solution on each thermal cycle, at the high temperature, and reprecipitates out at the low temperature. At the initial point of the low temperature cycle the interior of the Pb grains are at their strongest due to the Sn being in solid solution in the Pb, and the precipitates are small. Therefore deformation within the Pb grains is difficult causing the strain accommodation to move to the grain boundary. Cracks formed in 5Sn-95Pb joints after approximately 100 cycles both in thermal and isothermal fatigue (and at temperatures varying from -55°C to 125°C in isothermal fatigue). It would then appear that failures in 5Sn-95Pb are not a thermally activated process but are caused by imposition of strain.

The strain imposed on 5Sn-95Pb joints (19%) is large. Some studies on bulk fatigue of 5Sn-95Pb[113] argue that only 0.1% to 0.4% strain should be imposed on the joint and that the failure mode should be transgranular. This may be important for small amounts of strain imposed in small thermal cycles. However, for large strains imposed in the C-4 first level electronic packaging scheme result in an intergranular failure pattern[8] identical to that reported in this study.

• 60Sn-40Pb Joints

Heterogeneous coarsening was found to be the precursor to failure in 60Sn-40Pb joints at all temperature ranges tested in this work. Observations presented in the literature also show heterogeneous coarsening in solder joints in thermal fatigue. Wild has published[12] optical micrographs of 60Sn-40Pb joints that show a coarsened region in the solder joint with a crack running through this region. However, no comment was made on the phenomenon. Also Wild incorrectly attributes the failure to slip across multiple Pb and Sn-rich phases. Multiple phase slip would be difficult as the phases are polygranular at a fine scale, as described in section 4.1.2, and contiguous slip planes are unlikely. Bangs and Beal[37] also observed coarsening but they do not attribute failures to the coarsened region. They claim failures to be due to interphase separation, and that the Sn-phase does not fail. Lynch et. al.[18] appreciated that coarsening is detrimental to fatigue life and did attribute failures as being due to the presence of coarsening of the solder. However, they performed no optical microscopy so their assumption was that the solder coarsens homogeneously due to aging at the high temperature side of the thermal cycle. Yenawine et. al.[14] directly observed heterogeneous coarsening of the solder microstructure in electronic packages during thermal fatigue. They also state that the cracks run solely through the coarsened region. The coarsening in the Yenowine study was complicated as the solder joints do not experience simple shear deformation. However, the most extensive coarsening was found to occur in regions of the joint that encountered the highest shear strains.

Almost all observations in the literature of solder joint failures due to thermal fatigue state that the cracks run through the Pb-rich phase[12,14,37,38]. Results of this current work, however, show that it is the Sn-rich phase that fails, Figure 4.5.11. The reason for this discrepancy could be that observations made in the literature were made well after final joint failure. The polishing of these joints could then cause the solder material adjacent to the crack to fall out. On subsequent observations it would then appear that the joint failed through the Pb-rich phase when the actual failure pattern was lost during polishing.

Heterogeneous coarsening was found in this study to occur in regions of high shear strain more or less parallel to the direction of shear. The mechanism for the formation of a heterogeneous coarse band is not fully understood but a qualitative explanation is as follows. The shear strain across the solder joint is uniform in deformation but becomes concentrated due to some heterogeneity in the solder. All the shear deformation in the joint then becomes localized at the heterogeneity inducing dislocations and vacancies into the solder at this location. Upon thermal cycling the region adjacent to the heterogeneity undergoes recrystallization and phase growth. The dislocations and vacancies assist in diffusion causing this region to coarsen as the thermal cycling proceeds. The coarsened

region is weaker then the rest of the solder in the joint[26] so subsequent deformation will further concentrate at the coarsened region. Multiple coarsened regions are found in thick solder joints, Figure 4.5.12, because the possibility of heterogeneities in the initial joint are higher. The initial heterogeneity is not necessarily associated with the interface between the solder and Cu as coarsening occurs both at the interface and in the center of the joint. The cause of the initial heterogeneity is not known at this time but may be associated with the boundaries between Sn-Pb colonies within the solder joint.

The failure of 60Sn-40Pb joints was found to initiate in the Sn-rich phase, within the coarsened region. The cracks propagated intergranularly through the Sn-Sn grain boundaries. A possible mechanism for these failures is related to the mode of deformation utilized by near-eutectic Sn-Pb alloys. Fine grained near-eutectic Sn-Pb alloys are superplastic[63] and deform by grain rotation and grain boundary sliding. The initial microstructure of the 60Sn-40Pb joint consists of an interconnected Sn-rich phase. The initial Sn grain size was found in section 4.1.2 to be 0.44 μm. The Sn grain size after thermal cycling in the heterogeneously coarsened region increases to about 3 μm. At this large grain size the Sn grains can no longer easily rotate and slide to accommodate the imposed strain so intergranular cracks develop at the Sn-Sn grain boundaries. Once the interconnected Sn phase fails cracks form across the Pb-rich regions.

Isothermal fatigue tests have also been performed on 60Sn-40Pb joints[109-111]. Isothermal fatigue is a much simpler method to determine the thermal fatigue life of a solder joint if the fatigue mechanisms are similar in both processes. A summary of isothermal fatigue results are plotted in Figure 4.5.18 as a function of cycles to failure vs. strain induced. The number of cycles to failure increases with decreasing strain and temperature. The failure mode in isothermal fatigue is shown in Figure 4.5.19 and is intergranular through the Sn-rich phase. Heterogeneous coarsening was found to occur only in tests performed at 100°C and above. Even this coarsening at elevated temperatures is limited, Figure 4.5.20. Here the coarsened region is very thin, 25 μm across. At low temperatures heterogeneous coarsening was not observed, Figure 4.5.21 (isothermal fatigue at 0°C). Therefore heterogenous coarsening is associated with high temperature deformation both in thermal and isothermal fatigue. However, the coarsening is much more extensive in the cyclical temperatures in thermal fatigue.

If isothermal fatigue is similar to thermal fatigue a Miners Rule of cumulative damage could be applied to determine fatigue life. This rule is diagrammed in Figure 4.5.22. The rule states that the number of cycles to failure at each temperature may be added to determine the thermal fatigue life of the solder joint. From the isothermal fatigue results this indicates that the maximum possible number of cycles to failure is at the low temperature and the

minimum number of cycles to failure is at the elevated temperature. The extrapolated number of cycles to failure at 19% shear strain and 125°C in isothermal fatigue are somewhat similar to that for thermal fatigue. At lower temperatures isothermal fatigue predicts lifetimes that are much longer than found in thermal fatigue. This discrepancy is due to the metallurgical changes (i.e. the heterogeneous coarsening) that occurs in thermal fatigue but occurs to a much lesser extent in isothermal fatigue. Therefore isothermal fatigue is not a useful means to relate the thermal fatigue life of 60Sn-40Pb joints. However, as discussed earlier, isothermal fatigue does work in 5Sn-95Pb solder because no microstructural changes occur during thermal fatigue in 5Sn-95Pb.

Some claims have been made that 5Sn-95Pb is a much better solder in thermal fatigue than 60Sn-40Pb[9,38,40]. This reasoning is based on the fact that the Pb-rich solder has a higher melting point than 60Sn-40Pb and should be therefore more fatigue resistant. This current work has definitively shown that 60Sn-40Pb is more thermally fatigue resistant solder than is 5Sn-95Pb. The 5Sn-95Pb is sensitive to grain boundary cracking very early in the thermal cycle (~100 cycles between -55°C and 125°C) whereas 60Sn-40Pb does not fail until the Sn grains have coarsened enough to fail intergranularly.

One suggestion for eliminating thermal fatigue failures in 60Sn-40Pb joints is to match the thermal expansion coefficients of the materials joined by the solder. Besides being an expensive proposition, matching the materials only slightly delays failures. The optical micrographs in Figure 4.5.16 show that even the difference in thermal expansion between Cu and 60Sn-40Pb solder causes heterogeneous coarsening to occur. Eventually cracks will form in the coarsened region leading ultimately to failure.

Both high (35°C to 125°C) and low (-55°C to 35°C) temperature thermal cycles were detrimental to the fatigue life of 60Sn-40Pb solder joints. The high temperature cycling coarsened and failed in a manner identical to that for the full -55°C to 125°C cycle, Figure 4.5.11. This indicates that the coarsening and failure is temperature dependant and occurs at the high temperature portion of the thermal cycle. However, the solder does coarsen and fail even in low temperature cycling. Even in low temperature cycling the high portion of the cycle, 35°C, is still 0.69 of the homologous temperature and high temperature deformation occurs (recrystallization and growth and eventual grain boundary failures).

The thermal fatigue problem in 60Sn-40Pb solder is that heterogeneous coarsening occurs in the solder and cracks form within the coarsened regions. The obvious solution to the problem would be to add a grain boundary surfactant that inhibits coarsening and Sn grain growth. The surfactant would pin the grain boundaries to keep them from growing with the imposition of strain and temperature on thermal cycling. The actual solution may be difficult in that the surfactants can embrittle the grain boundaries thus enhancing the

problem. Possible ternary additions are Bi, B, and Mg. The Bi is soluble in both Sn and Pb and may segregate to the grain boundaries. Unfortunately Bi tends to make the 60Sn-40Pb solder gritty and difficult to flow. Boron is an obvious choice in that it is extensively used, in small amounts, in Al-Ni alloys and Fe-Mn steels[114] as a grain boundary "glue" to inhibit intergranular failures. The Mg is suggested by work by Lashko et. al.[28] who added 0.1% Mg to 60Sn-40Pb and greatly increased shear strength. This small amount of Mg probably did not precipitation harden or solid solution strengthen the solder but possibly did affect the grain boundaries making it an interesting addition for future studies.

4.5.5 Summary and Conclusions

Thermal fatigue tests were performed using a specimen designed to impose simple shear strain on solder joints in thermal cycling. Both 5Sn-95Pb and 60Sn-40Pb joints were tested with a maximum shear strain of 19% imposed. The nominal thermal cycle was -55°C to 125°C.

• 5Sn-95Pb Joints

The 5Sn-95Pb joints were observed to fail after 120 thermal cycles. The cracks formed at the Pb grain boundaries on planes of maximum shear stress in the joint (parallel and perpendicular to the imposed shear). The precipitation of β-Sn had no effect on crack initiation or propagation in 5Sn-95Pb. Failures occurred because the Pb grains were unable to accommodate the imposed shear by sliding respective to one another. This resulted in the formation of cracks on the grain boundaries.

Thermal fatigue observations were related to isothermal fatigue results[109-111]. The 5Sn-95Pb joints in isothermal fatigue also failed after approximately 100 cycles at Pb grain boundaries. The isothermal fatigue cycles to failure and fracture mode were relatively independent of temperature. Therefore isothermal fatigue tests can be used as a good representation of the thermal fatigue 5Sn-95Pb joint characteristics.

• 60Sn-40Pb

The failures in 60Sn-40Pb joints were preceded by heterogeneous coarsening of the solder. Both the Pb and Sn-rich phase were found to coarsen. The Pb-rich phase was found to be denuded of precipitates. The heterogeneous coarsening was due to strain imposed in thermal cycling by the thermal expansion differences between joined materials. Only homogeneous coarsening was observed in unconstrained bulk solder specimens. Heterogeneous coarsening was also observed when the only strain imposed was due to the difference in thermal expansion between the solder and the joined material. This indicates that by designing a joint to have matched expansion coefficients only delays thermal fatigue failures, it does not eliminate them.

The heterogeneous coarsening arises at some heterogeneity in the solder that concentrates the shear strain at one point in the joint. The concentrated strain results in recrystallization and phase growth at the heterogeneity. The coarsened region is the weakest point of the joint leading to further coarsening on continued thermal cycling.

The 60Sn-40Pb joints crack through the heterogeneous coarsened regions. The cracks are intergranular through the interconnected Sn-rich phase at Sn-Sn grain boundaries. The Sn grains are large in the coarsened region so that they can no longer rotate and slide to accommodate the strain. This results in cracks at Sn grain boundaries.

Experiments were performed at low (-55°C to 35°C) and high (35°C to 125°C) thermal cycles. The elevated temperature portion of the cycle was found to be the source of coarsening and failure. The 35°C to 125°C cycled specimens failed in a fashion identical to the -55°C to 125°C cycle. The low temperature cycle also failed, after a larger number of cycles, through a thin heterogeneous coarsened region. Low temperature failures occurred because even at 35°C the solder is at 0.69 of the homologous temperature and there is enough thermal energy for coarsening to occur.

Thermal fatigue results on 60Sn-40Pb joints were compared to isothermal fatigue tests[109-111]. The thermal fatigue life was found to be shorter than the isothermal fatigue results predict. The reason for this poor correlation is that a metallurgical change occurs in the joint in thermal cycling (heterogeneous coarsening) that is not found in isothermal fatigue. Therefore one can not use isothermal fatigue results to accurately predict thermal fatigue behavior in 60Sn-40Pb joints.

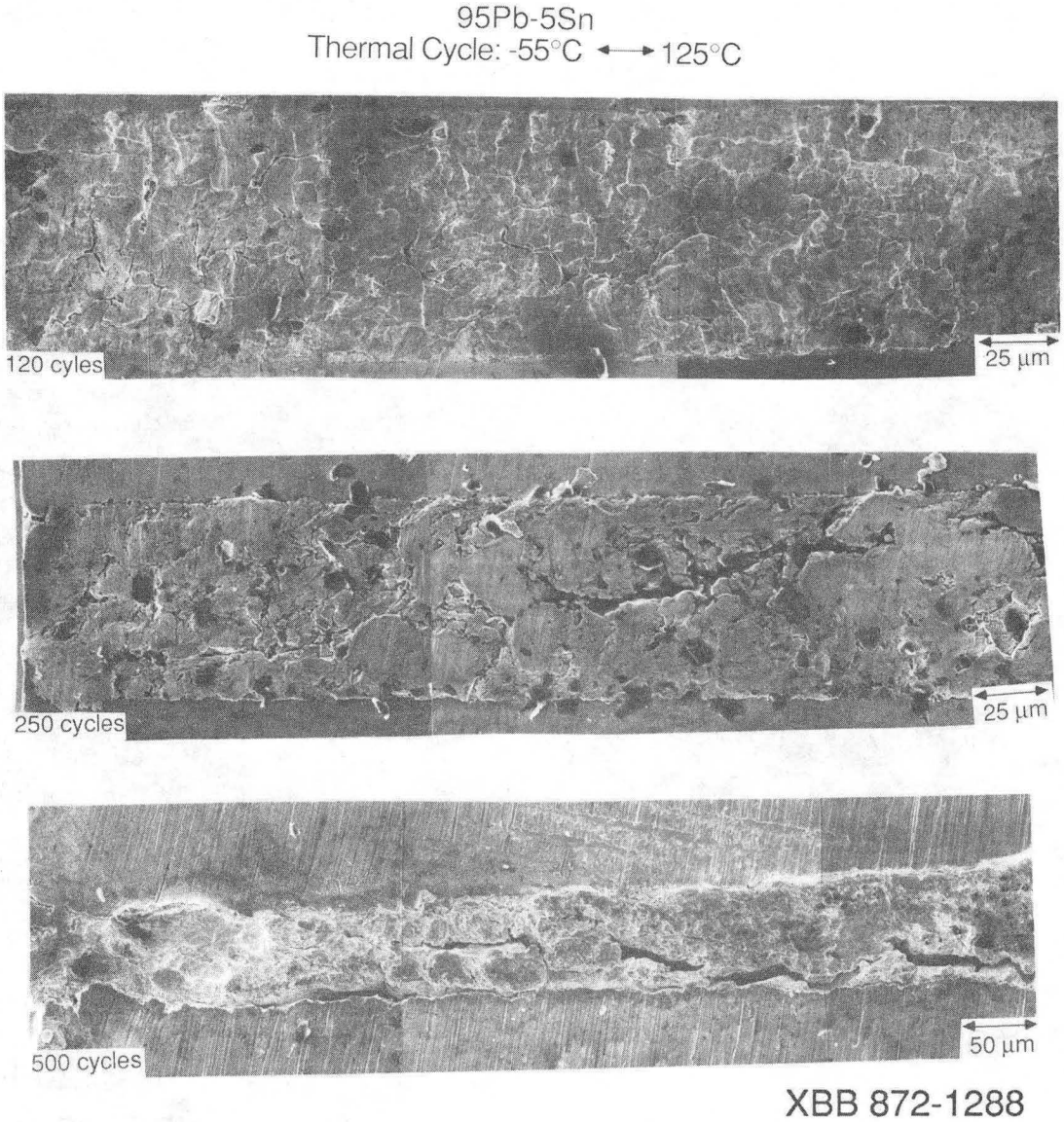

Figure 4.5.1 SEM unpolished cross section of 5Sn-95Pb/Cu joints as a function of number of cycles between -55°C and 125°C.

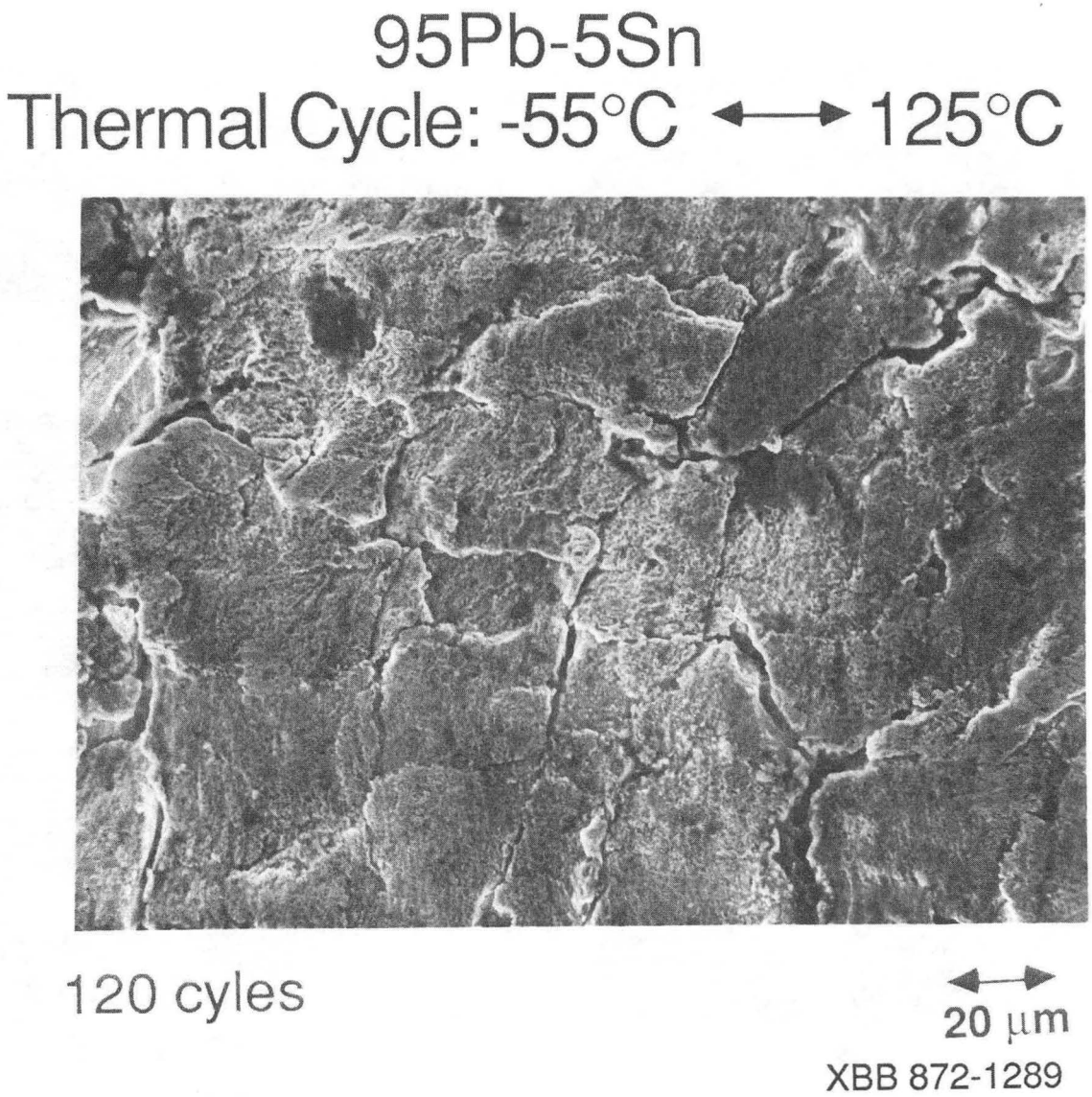

Figure 4.5.2 SEM unpolished cross section of 5Sn-95Pb/Cu joints after 120 cycles between -55°C and 125°C.

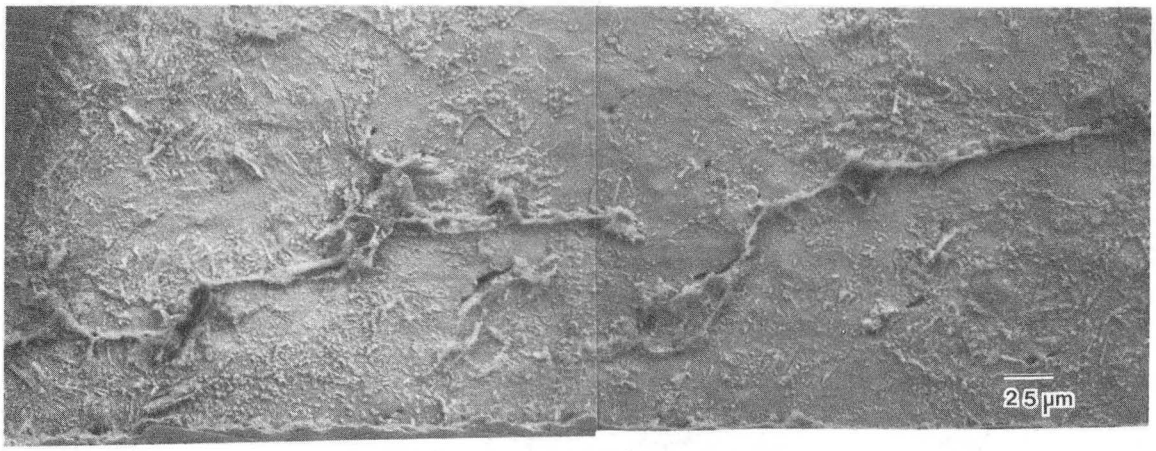

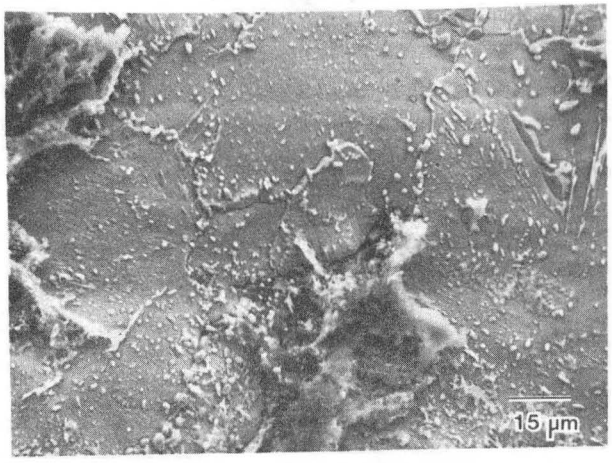

XBB 876-4403

Figure 4.5.3 SEM polished cross section of 5Sn-95Pb/Cu joints after 250 cycles between -55˚C and 125˚C. Cracks are found along Pb grain boundaries.

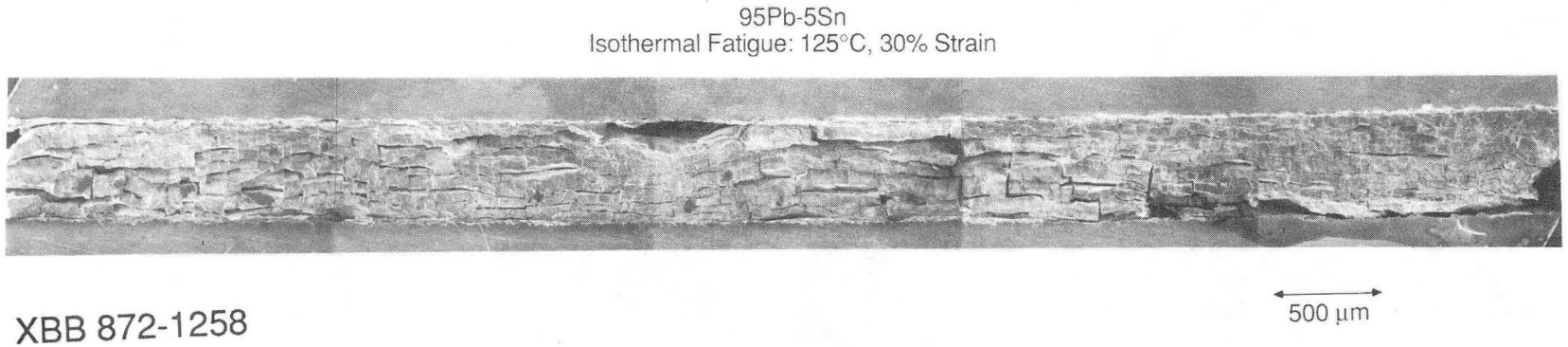

Figure 4.5.4 Unpolished SEM cross section of a 5Sn-95Pb/Cu joint after isothermal fatigue at 125°C.

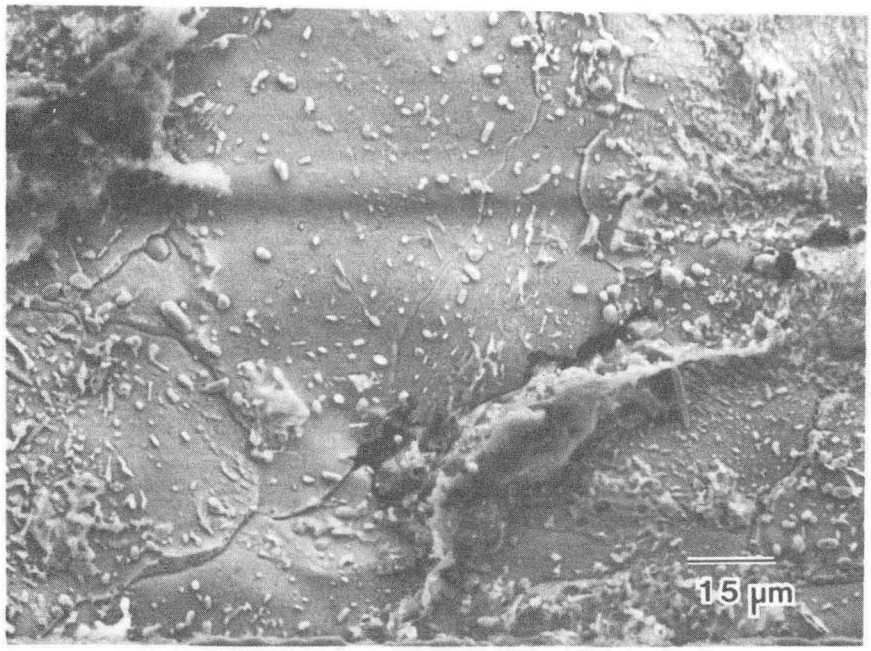

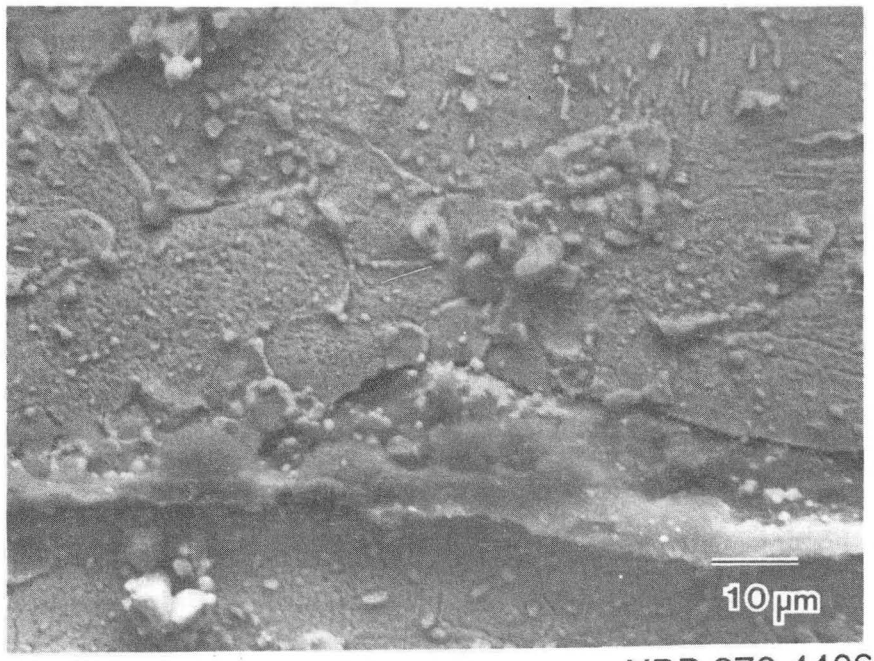

XBB 876-4406

Figure 4.5.5 SEM polished cross section of a 5Sn-95Pb/Cu joint after isothermal fatigue at 20°C.

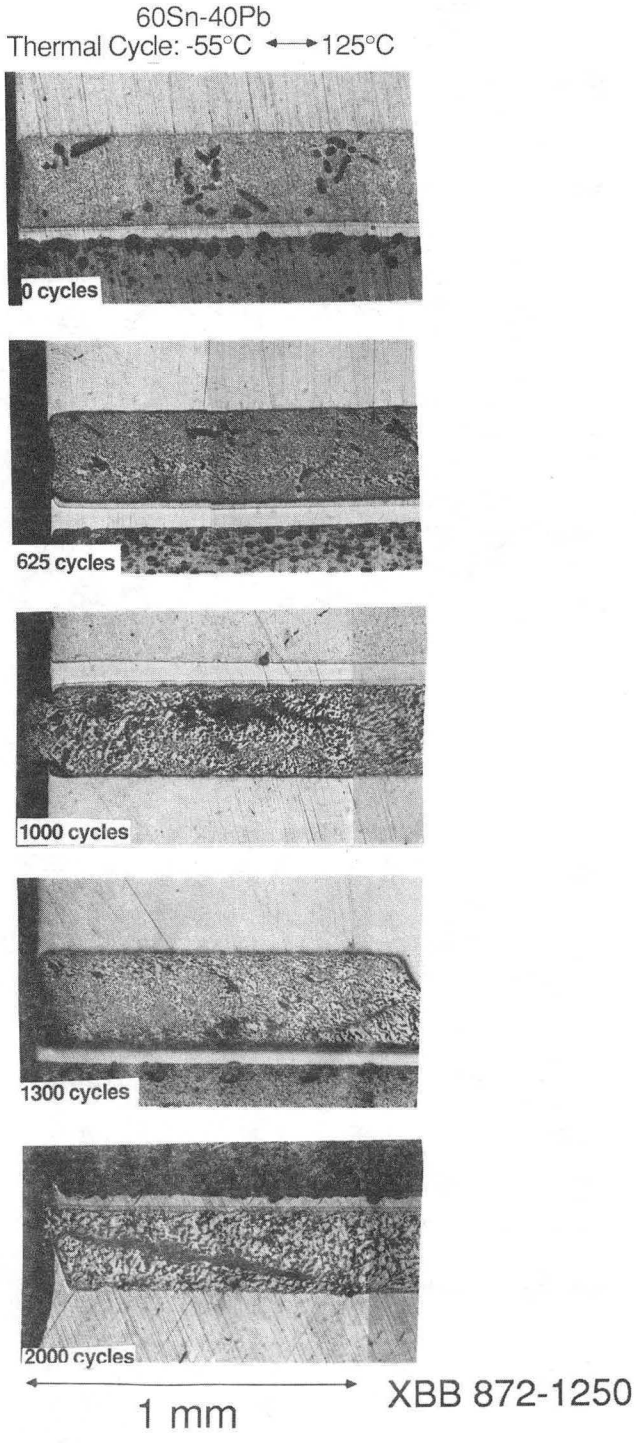

Figure 4.5.6 Optical microstructure cross sections of 60Sn-40Pb/Cu joints as a function of the number of cycles between -55°C and 125°C.

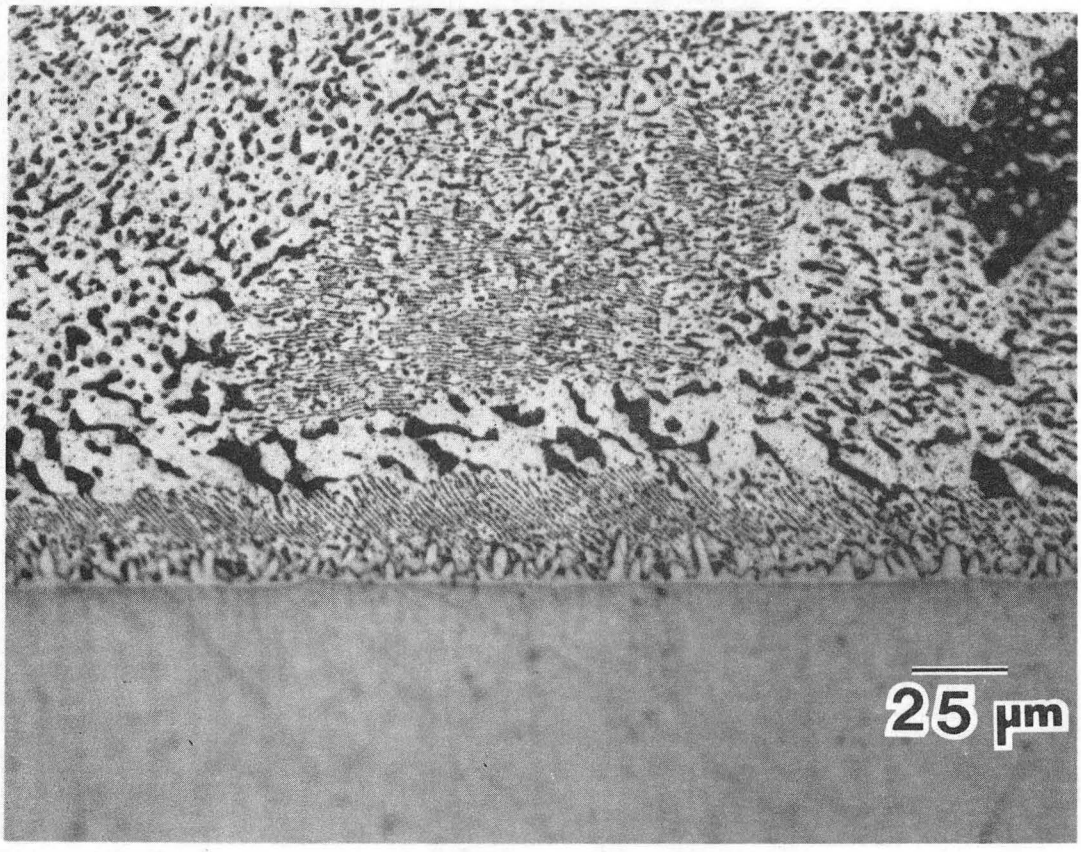

XBB 869-7138

Figure 4.5.7 Optical microstructure cross section of a 60Sn-40Pb/Cu joint after 684 cycles between -55°C and 125°C revealing the heterogeneous coarsened region.

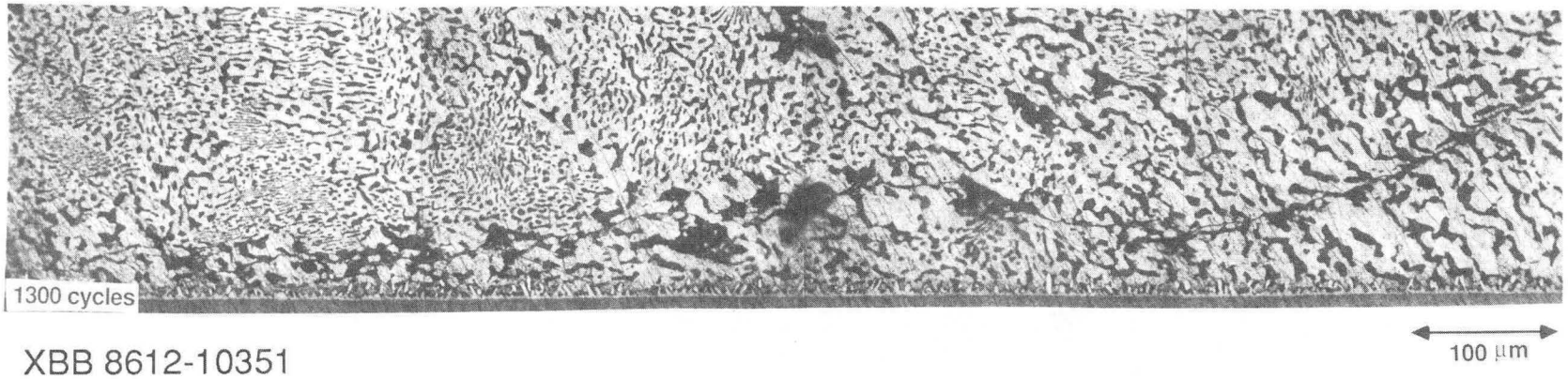

XBB 8612-10351

Figure 4.5.8 Optical microstructure cross section of a 60Sn-40Pb/Cu joint after 1300 cycles between -55°C and 125°C showing a crack in the coarsened region.

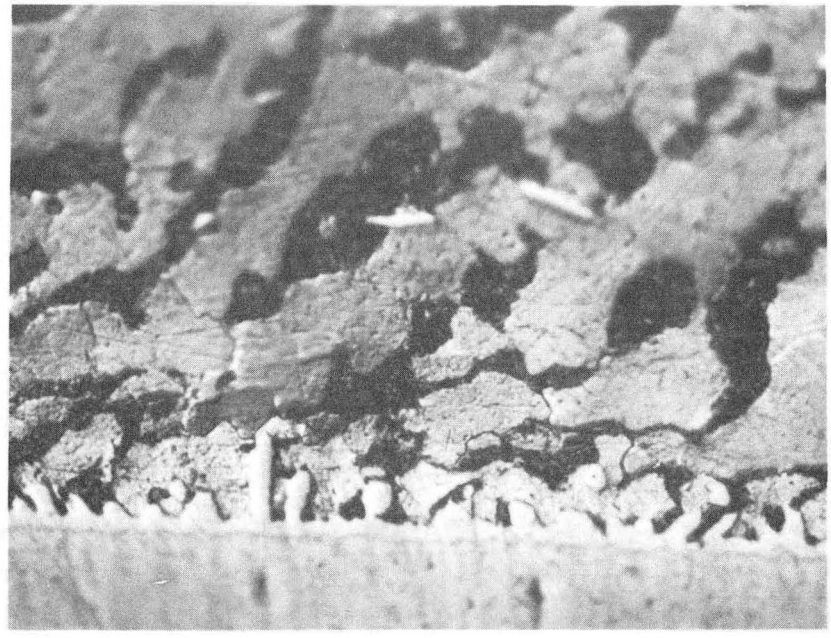

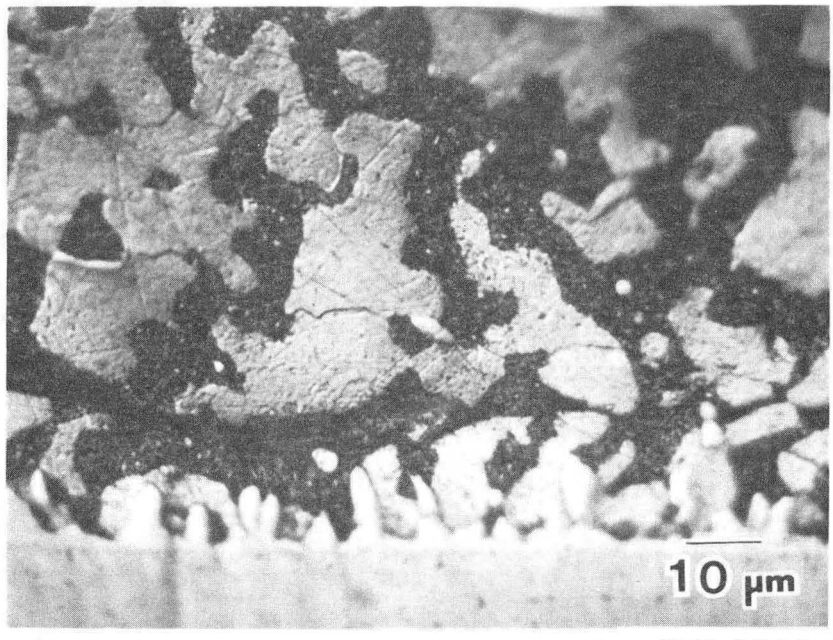

XBB 8612-10349

Figure 4.5.9 Polarized optical microstructure cross section of a 60Sn-40Pb/Cu joint after 1300 cycles. Intergranular cracks through the Sn rich phase are shown.

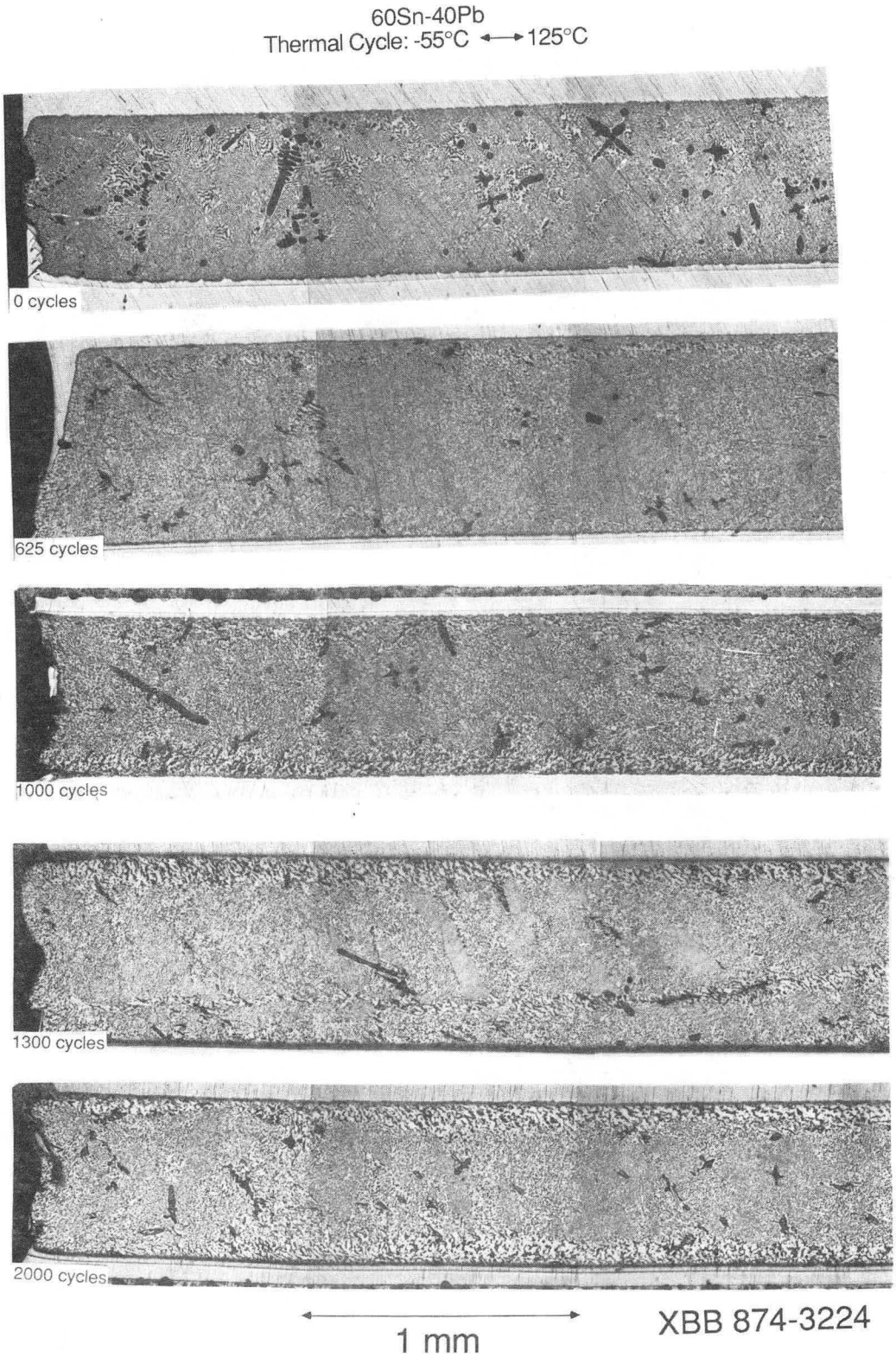

Figure 4.5.10 Optical microstructure cross section of a 20 mil (0.51 mm) thick 60Sn-40Pb/Cu joint as a function of the number of thermal cycles between-55°C and 125°C.

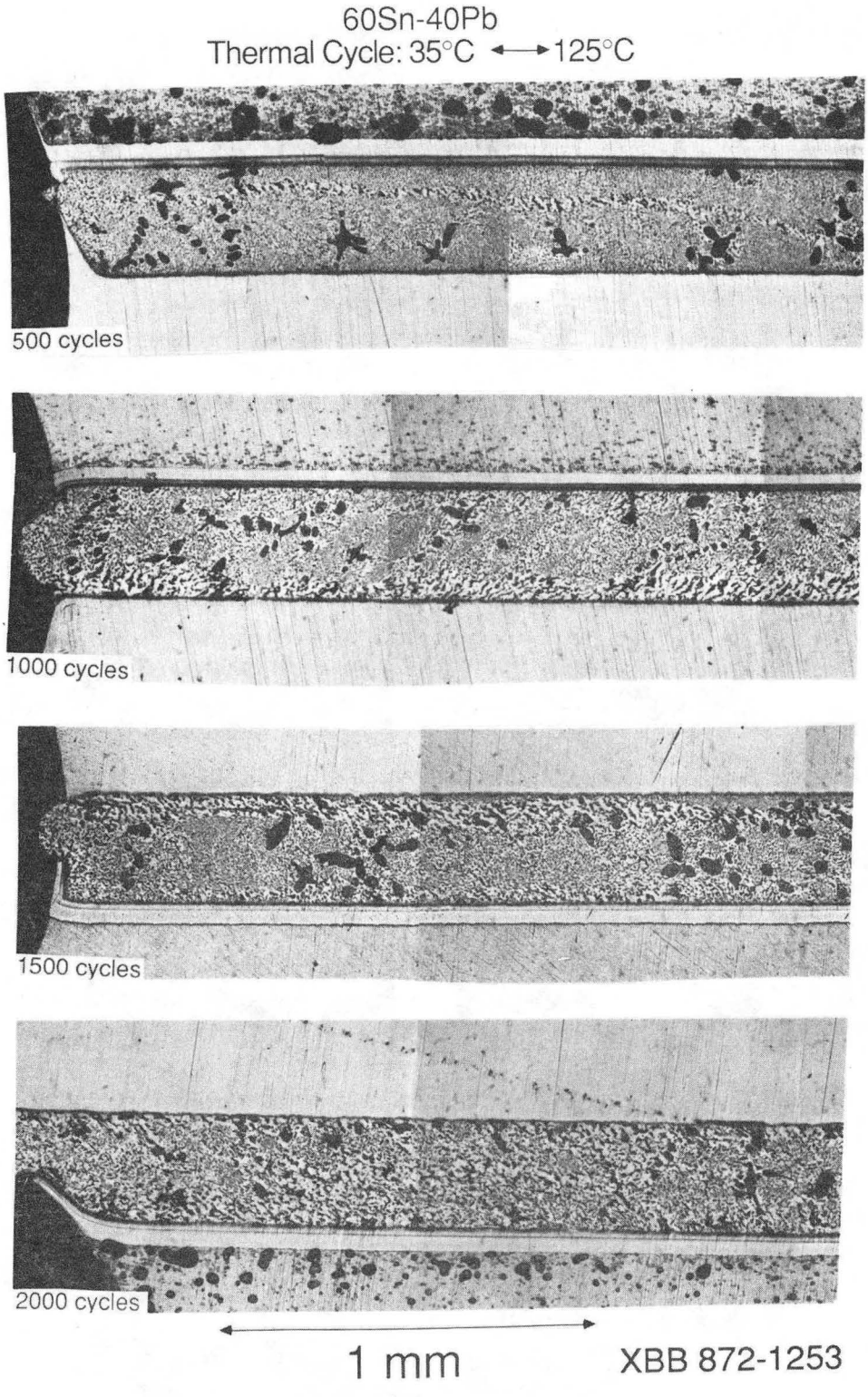

Figure 4.5.11 Optical microstructure cross sections of 60Sn-40Pb/Cu joints as a function of the number of cycles between 35°C and 125°C.

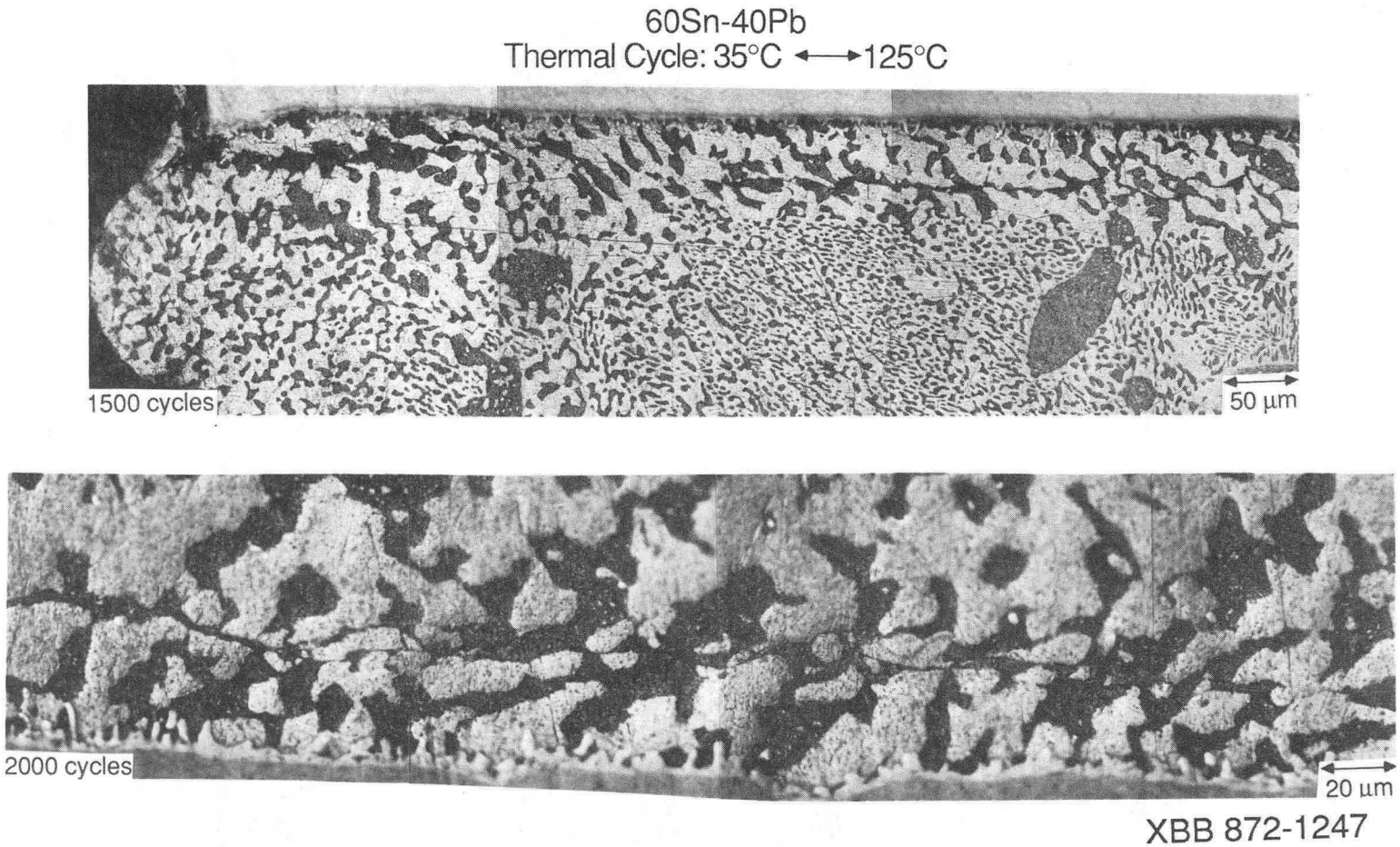

Figure 4.5.12 Optical microstructure cross sections of 60Sn-40Pb/Cu joints after 1500 and 2000 cycles between 35°C and 125°C revealing cracks through the coarsened regions.

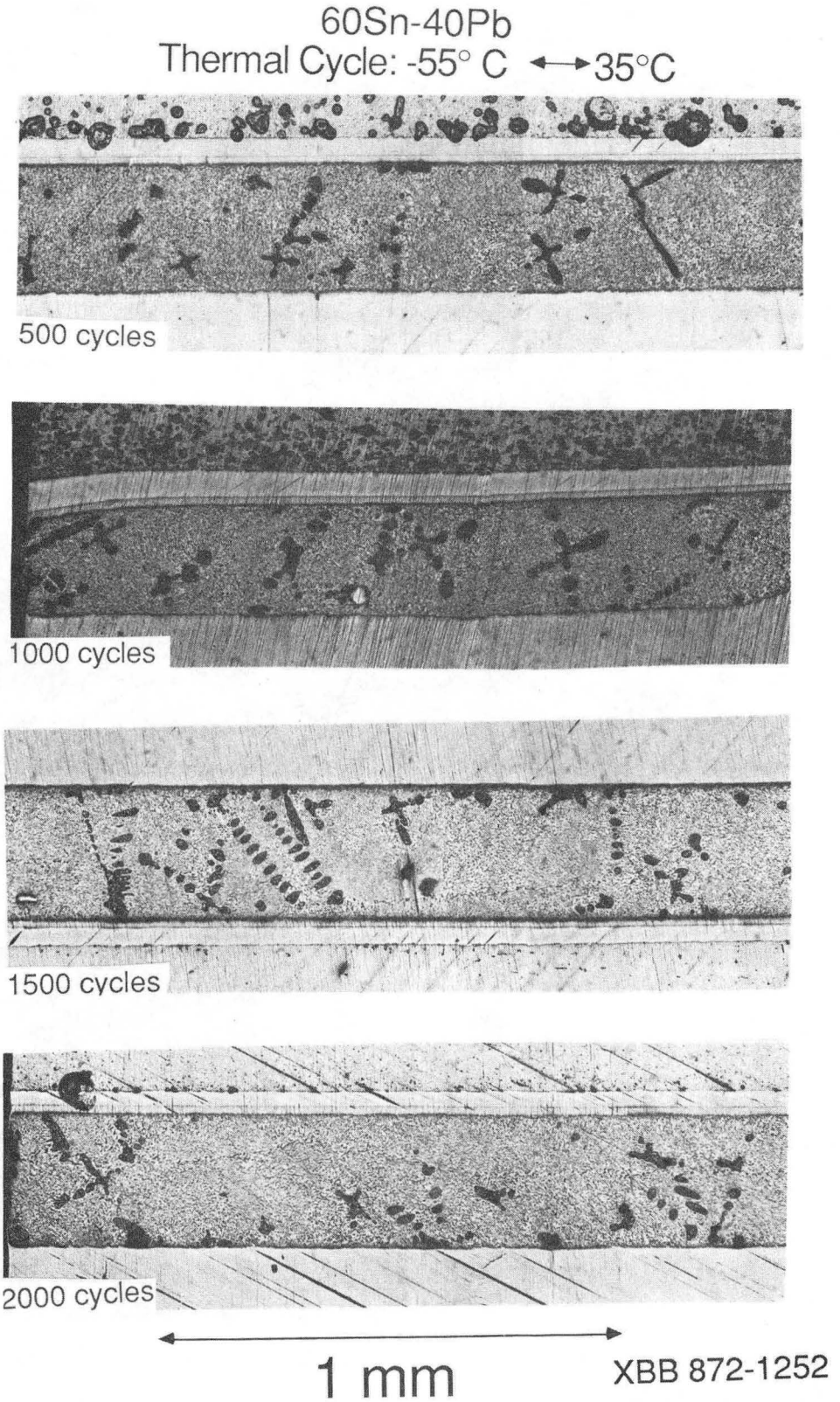

Figure 4.5.13 Optical microstructure cross sections of 60Sn-40Pb/Cu joints as a function of the number of cycles between -55°C and 35°C.

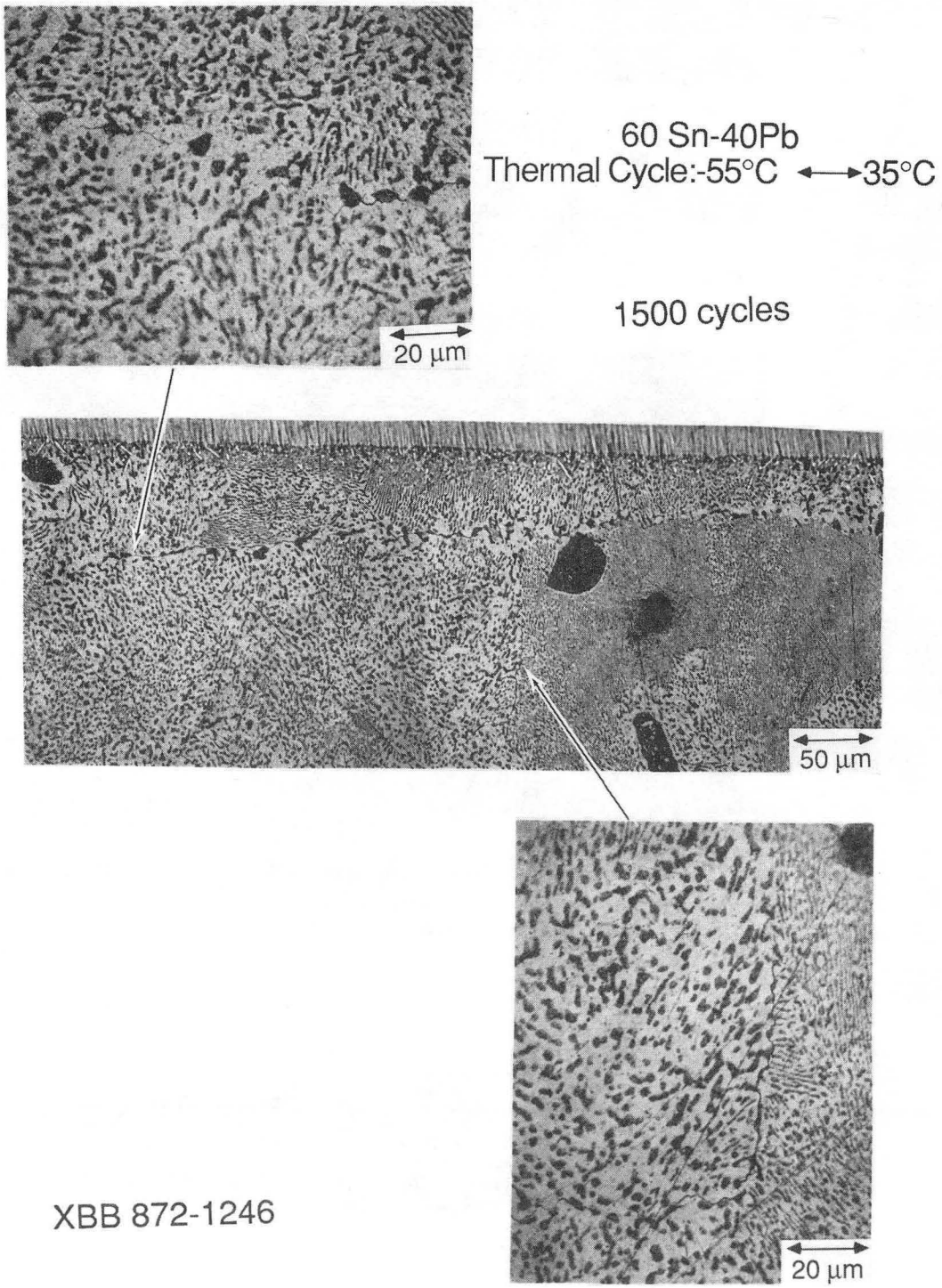

Figure 4.5.14 Optical microstructure cross section of a 60Sn-40Pb/Cu joint after 1500 cycles between -55°C and 35°C revealing a thin coarsened region and cracks propagating through the Sn-rich phase in this region.

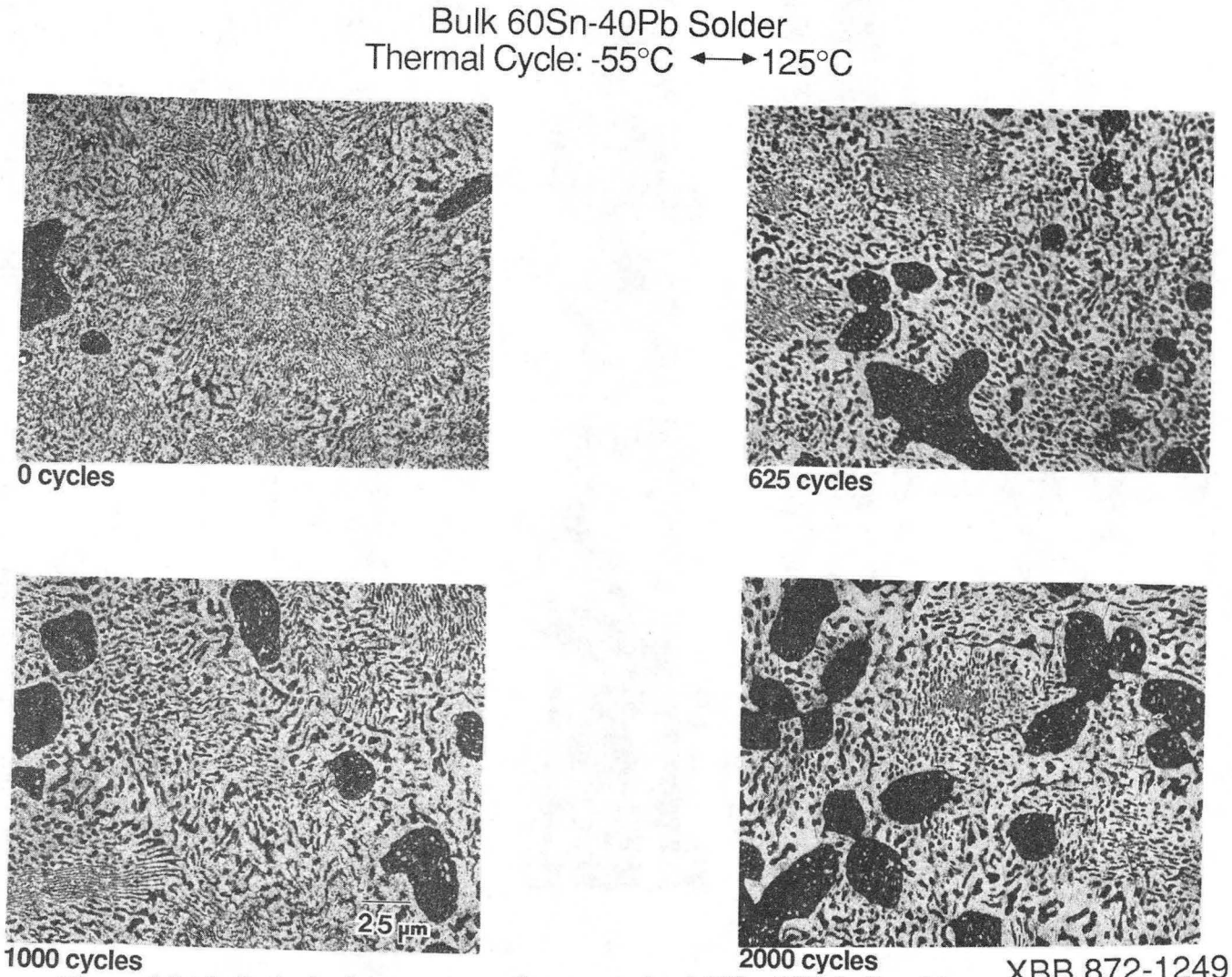

XBB 872-1249

Figure 4.5.15 Optical microstructure of unconstrained 60Sn-40Pb bulk solder as a function of the number of cycles between -55°C and 125°C.

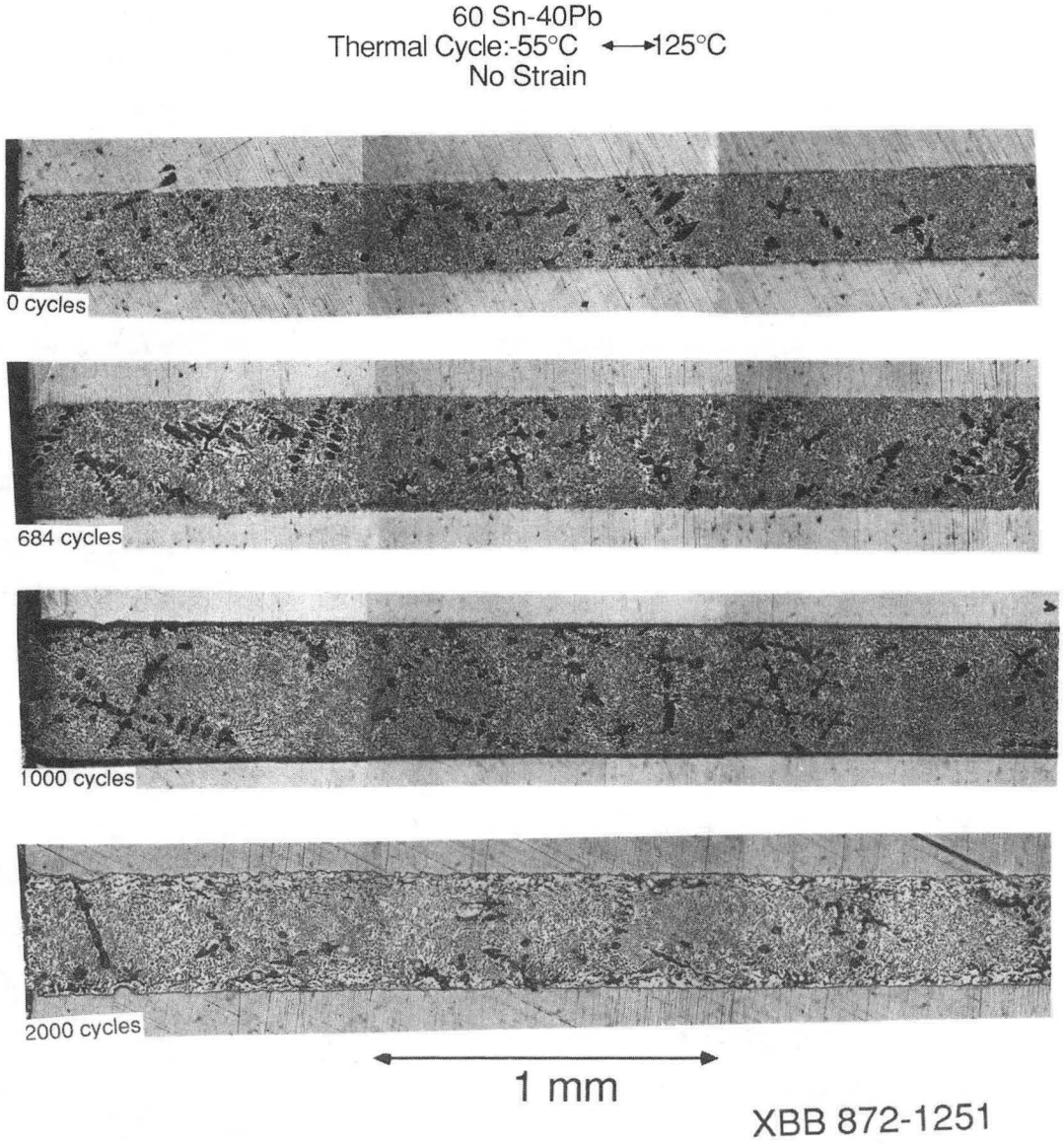

Figure 4.5.16 Optical microstructure cross sections of Cu/60Sn-40Pb/Cu specimens as a function of the number of cycles between -55°C and 125°C. Heterogeneous coarsening is found at 2000 thermal cycles.

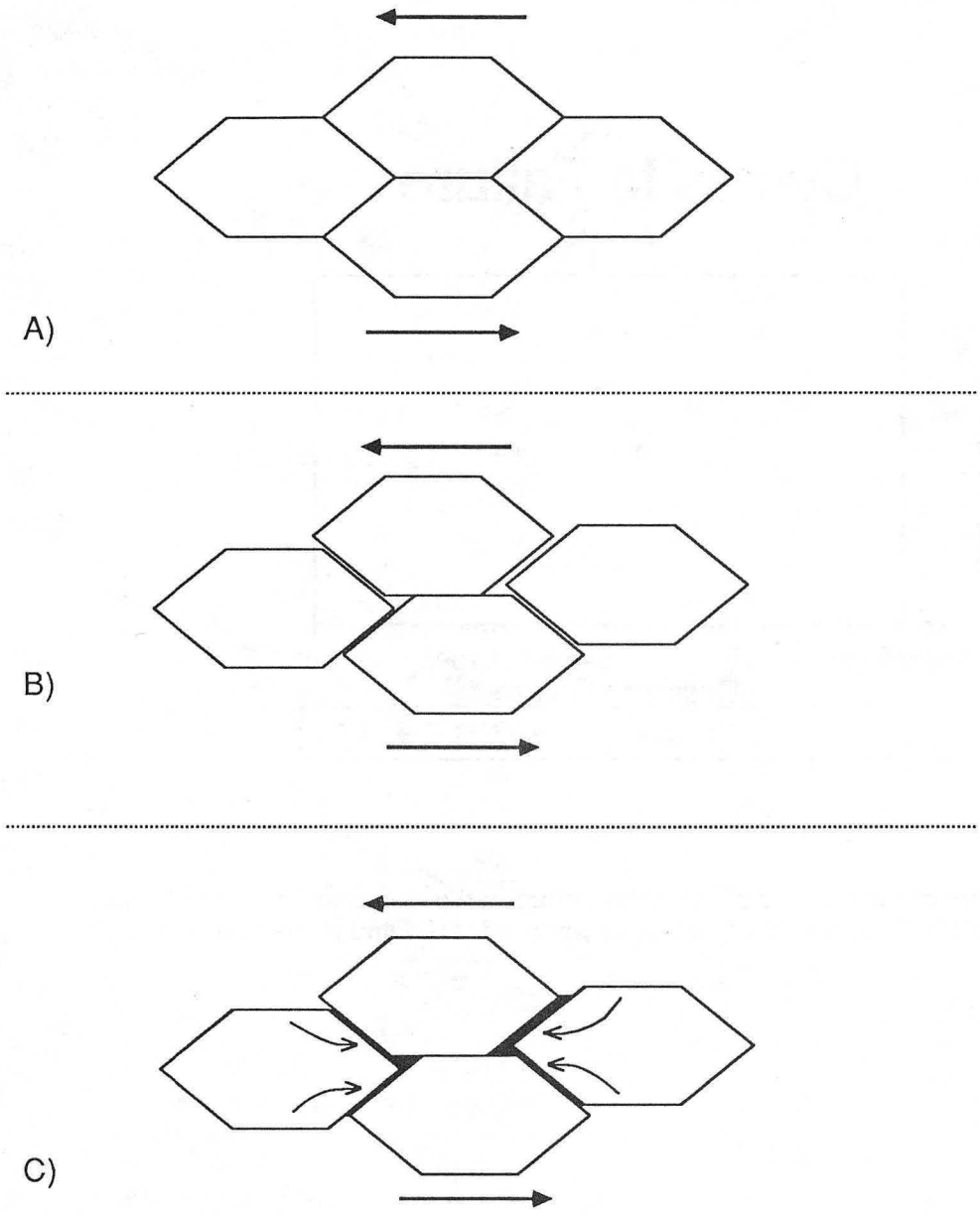

Figure 4.5.17 Schematic illustration of grain boundary deformation in shear.

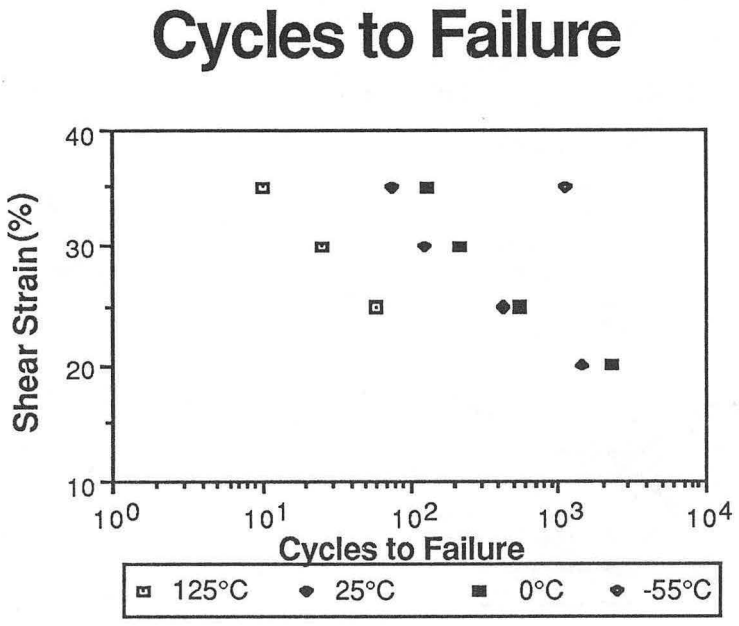

Figure 4.5.18 Plot of the number of cycles to failure in the isothermal fatigue of 60Sn-40Pb/Cu joints as a function of imposed strain and temperature.

7.0 μm

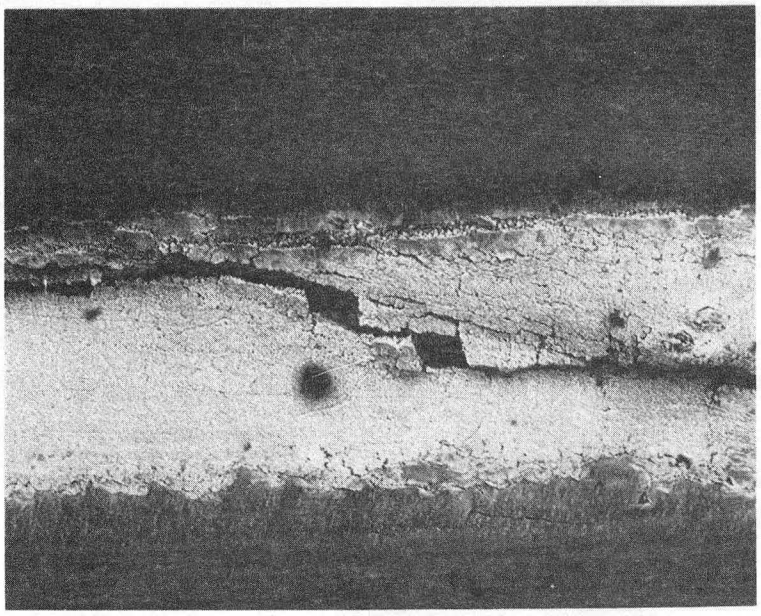

90 μm

XBB 871-655

Figure 4.5.19 SEM cross section of an isothermally fatigued 60Sn-40Pb/Cu joint revealing cracks through the Sn-rich phase (regions of dark contrast in the SEM).

Isothermal Fatigue
100°C 30% Strain

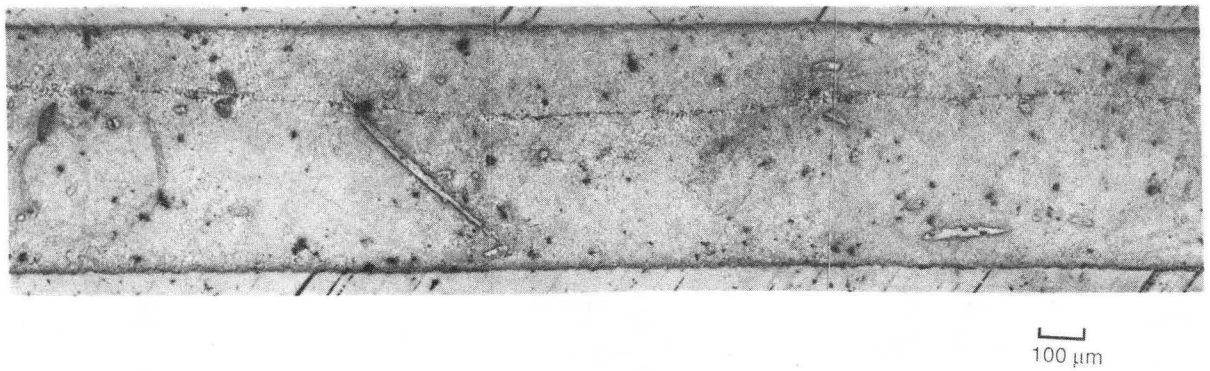

Figure 4.5.20 Optical microstructure cross section of a 60Sn-40Pb/Cu joint isothermally fatigued at 100°C and 30% shear strain.

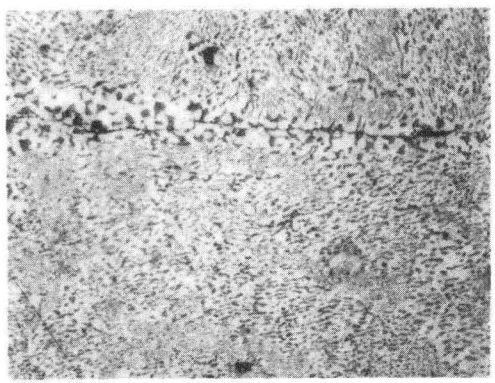

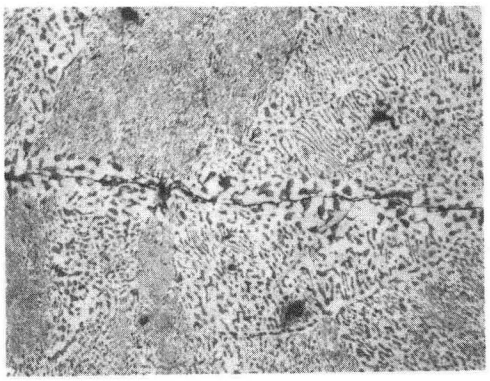

Isothermal Fatigue
0°C 20% Strain

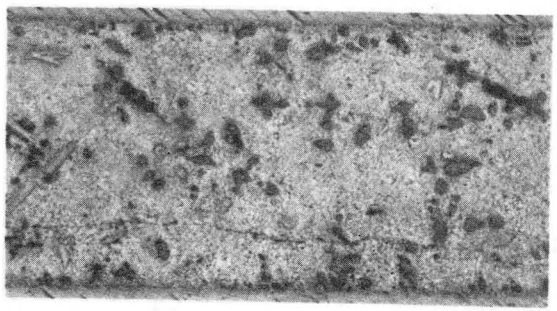

100 μm

Figure 4.5.21 Optical microstructure cross section of a 60Sn-40Pb/Cu joint isothermally fatigued at 0°C and 20% shear strain.

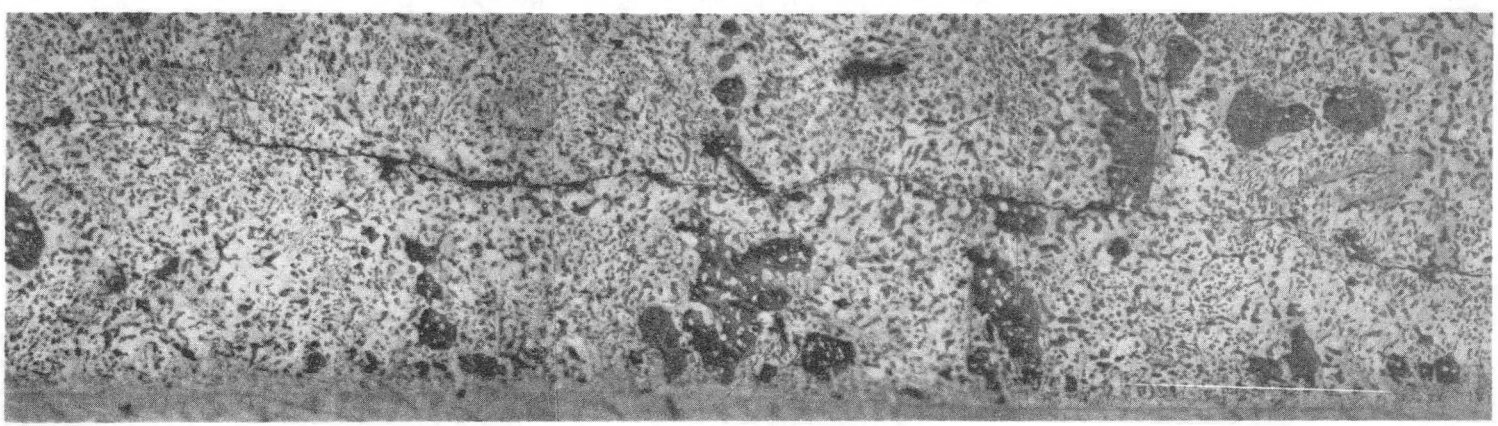

25 μm XBB 876-4487

Fatigue Life Approximation

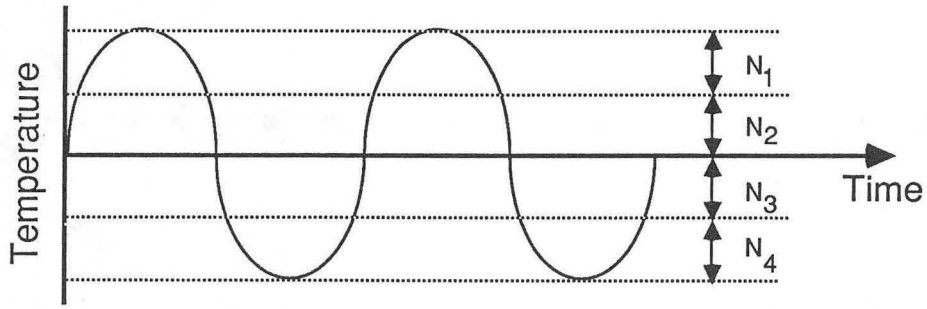

Miners Rule $\sum_i \frac{N_i}{N_f} = 1 \longrightarrow$ Failure

$$N \left\{ \frac{1}{N_{f_1}} + \frac{1}{N_{f_2}} + \frac{1}{N_{f_3}} + \frac{1}{N_{f_4}} \right\} = 1$$

If : $N_{f_1} < N_{f_i}$

$$\longrightarrow \boxed{N = N_{f_1}}$$

Figure 4.5.22 Miners rule applied to fatigue life.

5.0 DISCUSSION SUMMARY

The problems associated with the joining technology in electronic packaging range from wetting characteristics to joint corrosion. Thermal fatigue failures of Sn-Pb solder joints are a small, but very important, aspect of the packaging problem. Therefore the purpose of this work was to characterize the microstructure of Sn-Pb solder joints and relate the thermal fatigue behavior to these microstructural observations. This section discusses and relates microstructural observations made in this study to the thermal fatigue behavior of Sn-Pb solder joints.

• Interfacial Intermetallics

There have been suggestions in the literature[9,31-35] that thermal fatigue failures initiate and propagate through the brittle interfacial intermetallic layer. Interfacial failures are proposed based on the fact that Cu-Sn intermetallics are inherently brittle. Furthermore crystallographic observations, section 4.2, indicate that the basal planes of both ε and η-phases are parallel to the shear direction which could provide an ideal location for crack initiation. The isothermal shear tests on solder joints indicated that at fast deformation rates (0.2 mm/min) failures do occur through the intermetallics. At slower deformation rates failures were through the bulk solder alone. The thermal fatigue tests on both 5Sn-95Pb and 60Sn-95Pb show that all failures occurred through the bulk solder. Therefore thermal fatigue failures occur occur independent of interfacial intermetallics, even under the thermal shock testing used in this study. The temperature ramp conditions encountered by an electronic package are much less severe than those in this study. The deformation rates in an electronic package are slower than the thermal fatigue tests used here so failures through the intermetallic are even less likely.

The strain imposed upon the solder deforms the solder but does not concentrate at the interface. The presence of interfacial intermetallics is not detrimental to the thermal fatigue behavior of Sn-Pb solder joints. However, interfacial intermetallic layers coarsen, especially with time at molten temperature. It is possible that with a thicker intermetallic the interface would become more likely to fail. This was not investigated in this study but is of interest.

Tests, performed at slow strain rates on solder butt joints, by Quan et. al.[27] show that solder joints fail at the interface when strained in tension. When in tension a solder joints is a "series" of composite materials (Cu/Intermetallics/Solder) with the solder constrained at the edges (due to the constrained nature of a butt tensile joint). The intermetallic is the weakest link in this series and fails the joint. In shear the composite materials are tested in

"parallel". In this case the strain is taken up by the most deformable material, the solder. This leads to an eventual failure in the bulk of the solder. Therefore to inhibit interfacial intermetallic failures in electronic packages it is necessary to eliminate tensile forces on the joints.

• Intermetallic Whiskers (60Sn-40Pb η-phase whiskers)

The formation of η-phase whiskers in a solder joints was found to have a striking effect on the low temperature mechanical properties of solder, section 4.3. At low temperatures the whiskers act as initiation sites for brittle cracks or decohesive failures. However, the whiskers had little or no effect on the thermal fatigue behavior of Sn-Pb solder joints. The heterogenious coarsened regions, and cracks, appeared to form independently of the intermetallic whiskers in the bulk solder. In isothermal mechanical tests[27] on solder joints in tension intermetallic whiskers did act as initiation sites for failure.

The explanation for the absence of an effect of intermetallic whiskers has to deal with the thermal cycling the solder joint experiences. At the low temperature portion of the cycle some interfacial separation may occur at the whisker interface. However, the strain imposed (9% strain from room temperature to -55°C) is not sufficient to create a failure (18% strain is required at -196°C). Upon cycling to the elevated temperature diffusion and creep are enhance and the interfacial separation is eliminated. In effect the high temperature portion of the cycle "heals" the low temperature deformation due to the intermetallic whiskers. The whiskers may act as the initial heterogeneities upon which coarsened regions form, but there is no direct evidence of this.

• Bulk Solder

The effect of bulk microstructure in thermal fatigue has been discussed in depth in section 4.5. The salient points of this discussion were that cyclical thermal fluctuations influence the microstructure of both 5Sn-95Pb and 60Sn-40Pb with resultant failures. To avoid complete repetition between section 4.5 and this section only the major points of discussion on this topic are presented here.

The failure in 5Sn-95Pb joints was intergranular both in thermal and isothermal fatigue. The large irregular Pb grains can not slide and rotate to accommodate the imposed shear so intergranular cracks form. The β-Sn precipitates do not act as initiation sites for cracks but by dissolving and reprecipitating the Sn solid solution strengthens the grain interiors so the grains are less able to deform to accommodate the strain.

Pb-rich Pb-In solders have been suggested[24] as being a more thermally fatigue resistant than 5Sn-95Pb. Both In and Sn form intermetallics with Cu (Pb does not). However, the In does not strengthen the Pb to the same extent that Sn does and this may make the Pb-In

solders fatigue resistant because the Pb-In grains can easily deform under the imposed strain. The 5Sn-95Pb solder is very poor in thermal fatigue and replacement should be considered in large strain conditions, possibly with a Pb-In alloy. However, fundamental work needs to be performed on the Pb-In alloy to quantify its fatigue resistance.

The heterogenious coarsening and failure of 60Sn-40Pb solder is attributed to be due to the localization of strain within the bulk solder. The localized strain promotes phase and grain growth. The Sn grains in the Sn-rich phase grow to size where they can no longer slide and rotate to accommodate the strain. Failure then occurs intergranularly through the Sn-rich phase. The heterogenious coarsening only occurs with imposed strain due to different thermal expansion coefficients and thermal cycling. Therefore isothermal fatigue tests can not be used to imitate thermal fatigue properties. The lack of thermal cycling in isothermal fatigue does not allow the microstructure of the solder to change as it does in thermal fatigue.

• Oxidation

The problem of oxidation in thermal fatigue may be an acute one. Snowden[42] found PbO forms when the oxygen pressure is only 3×10^{-2} mm of Hg. The TEM study of 5Sn-95Pb found Pb oxide to form in the high vacuum (10^{-6} torr) of the microscope. The free energy of formation of PbO at 125°C is 92 kcal. Similarly SnO has a free energy of formation of -108 kcal. Therfore both Pb and Sn oxidize very rapidly.

The oxidation of samples in this study was limited by the use of liquid baths, but was still present. Pb oxide tends to form on grain boundaries and could explain the intergranular failure of 5Sn-95Pb. However, 60Sn-40Pb failed through the Sn in thermal fatigue in this study. Wild[38] attributed the failure of 60Sn-40Pb joints in his study to be due to oxidation and cracking of the Pb-rich phase. Whether Wild observed a polishing artifact or that Pb oxide is a major contributor to failure remains to be seen. It is possible the intergranular failure of the Sn-rich phase in this study was due to Sn oxide formation. The Sn oxide could embrittle the grain boundaries and on straining cracks form. However, one would expect that this would occur uniformly throughout the joint and not just where the phases and Sn grains have coarsened. This point is in need of more study.

• Recommendations to the Electronics Industry

This study provides no absolute answers to the problem of thermal fatigue in Sn-Pb solder joints of electronic packages. However, some recommendations can be made.

First of all, 5Sn-95Pb is not a suitable solder alloy for large strains in thermal fatigue and should not be used for this purpose.

To increase lifetimes it is obvious that the joint should be exposed to a minimum of imposed strain. This is not the complete answer as this delays, but does not eliminate fatigue failures. As pointed out in section 4.5 even the difference in thermal expansion between the solder and base material (60Sn-40Pb and Cu in this study) results in coarsening and eventual failure of the solder joints.

Concerns about the interfacial intermetallics should be limited to wetting, and not include thermal fatigue behavior (unless the intermetallics have excessively grown). The major concern should be about the bulk of the solder. To eliminate solder failures in thermal fatigue, in 60Sn-40Pb, heterogeneous phase growth and intergranular cracking through the Sn-rich phase must be eliminated. Further study is needed in this area in the form of ternary alloy additions that pin grain boundaries and strengthen boundaries while at the same time inhibit growth.

6.0 FUTURE WORK

The results presented in this work represent only a foundation for the study of thermal fatigue of solder joints. Other facets of the thermal fatigue problem need to be considered to gain deeper understanding of the fundamental causes of thermal fatigue failures. With the background of microstructural observations presented in this work the following studies are appropriate to better understand thermal fatigue in Sn-Pb solder joints.

• Effect of Hold Time at Temperature Extremes in Thermal Fatigue

The 5 minute hold times used in the thermal cycling experiments were selected as the times when the samples had completely reached thermal equilibrium so as to accelerate the fatigue process. It would be of interest to vary the length of the hold times to examine the effects of extended aging. Work by Tribula et. al.[112] on the stress relaxation of solder joints showed that stress relaxation below 50% of the initial stress took on the order of days at room temperature. This data was used as the base assumption that short hold times can be used to model extended hold times. However, this point should be proven experimentally in thermal cycle testing.

• Effect of Cycling Frequency

Solomon[45] isothermally fatigued 60Sn-40Pb solder joints and found a strong cycling frequency dependance. Solomon found that the slower the frequency the shorter the lifetime of the joint. If this result is valid, slow temperature ramping in thermal fatigue would be more deleterious than the thermal shock testing method used in this study. This study has shown that there is a poor correlation between thermal and isothermal fatigue and frequency dependance may only occur in isothermal fatigue. However, this point should be studied.

• Study the Effect of Small Strains

Using the thermal fatigue specimen it would be possible to study small strains in thermal fatigue. Small strains are of interest for leaded solder joints in electronic packages and surface mount joints that encounter little strain. The lifetime of joint under small strain amplitudes does increase thus increasing the time for each test. It would be expected that under small strains the expansion difference between the solder and the Cu becomes more prominent and may dominate failures.

• Effect of Different Strain Orientations

The only orientation used in this study was shear. However, the strains encountered by solder joints in electronic packages are a complicated mixture of various modes of deformation[16], Figure 2.2. It would be of great interest to study the thermal fatigue behavior of 60Sn-40Pb joints in tension or mode III deformation. These tests would shed more light on the heterogeneous coarsening that occurs in 60Sn-40Pb joints. A new specimen design would need to be developed for these tests.

• Effect of Oxidation in Thermal Fatigue

The oxidation of Sn and Pb in thermal fatigue in these experiments was minimized by using liquid media thermal baths. However, the solder joints in electronic packages are exposed to an oxidizing environment in service. To study this effect thermal cycling tests should be performed in air. To perform these tests a different thermal cycling device would be designed that uses cooled and heated air as thermal environments.

• Effect of Coarsened Interfacial Intermetallics

As pointed out in section 5.0, the interfacial intermetallics had no effect on the behavior of solder joints in thermal fatigue. However, the thick interfacial intermetallics that form on reflow, or extended aging at elevated temperatures, may influence joint behavior in thermal fatigue. By reflowing thermal fatigue specimens before testing this effect would be easily investigated.

• Solder Alloy Modification

The end objective of this study is to alleviate the problem of thermal fatigue. As processing modification on the solder would be extremely difficult the only other alternative is alloy additions. By itself 5Sn-95Pb is a poor alloy for large strain thermal fatigue. Possibly a ternary addition that will either strengthen the Pb grain boundaries or make the grains slide around each other would work. Even an addition that minimizes the Pb grain size would be beneficial for thermal fatigue behavior. For 60Sn-40Pb a ternary addition must be found that will slow or eliminate the heterogeneous coarsening process. Ideally the addition would pin the phase and grain boundaries in Sn and Pb to slow growth while at the same time strengthen the boundaries to eliminate intergranular failures. Additionally the addition must not hinder the wetting process. Possible addition include:

- Bi: This element does not form intermetallics with Sn or Pb and is small enough to sit on grain boundaries, possibly as a surfactant. Unfortunately Bi does increase the "grittyness" of solder and decreases the wetability.

- Ag: Forms intermetallics with Sn. This has been suggested[23,115] as an element that increases fatigue life in solder joints by refining the solder microstructure. The means by which this occurs was not explained but the addition is worthy of study.
- B: Boron is extensively used as a grain boundary "glue" in superalloys and is well known as an inhibitor to intergranular cracking.
- Mg: This element has shown promise in a study by Lashko et. al.[28] who showed that Mg containing solders had better strength and ductility in very small amounts (0.1%) which is too small for solution strengthening but is sufficient as a grain boundary surfactant.

The above are only a short list of possible elements, only extensive testing in thermal fatigue can determine the effectiveness of ternary additions.

7.0 SUMMARY AND CONCLUSIONS

The purpose of this study was to fully characterize solder joint microstructure. With this understanding a relationship between microstructure, mechanical properties, and thermal fatigue behavior was derived. The two solder alloys tested in this study were 5Sn-95Pb and 60Sn-40Pb joined to Cu. The topics covered in this work were: bulk solder microstructure, interfacial Cu/solder intermetallics, intermetallic whisker formation, isothermal solder joint mechanical properties, and thermal fatigue observations on solder joints.

5SN-95PB BULK SOLDER

The precipitation process of β-Sn from Pb was fully characterized. On slow cooling from the single phase region a cellular precipitation process results. On fast cooling an even homogeneous distribution of β-Sn precipitates forms. In both cases the precipitates have a platelike morphology and a definite crystallographic relationship ($(111)_{Pb}$ habit plane with $(111)_{Pb}$ // $(010)_{Sn}$ and $[0\bar{1}1]_{Pb}$ // $[001]_{Sn}$). The β-Sn precipitates were found to dissolve an heating into the single phase α-Pb region. The precipitates dissolved via a ledge mechanism.

The 5Sn-95Pb alloy overages rapidly, the strength was found to decrease immediately upon solidification. A solid solution of Sn in Pb has greater strength than the alloy has after precipitation. In thermal fatigue precipitates dissolve and reprecipitate during thermal cycling so the Pb grains often contain a solid solution of Sn in the thermal cycle. This strengthens the grain interiors so the Pb grains can not deform as easily under applied strain. The result is intergranular cracking in thermal fatigue for 5Sn-95Pb joints. The fatigue cracks initiate and propagate independently of the Sn precipitates.

60SN-40PB BULK SOLDER

The 60Sn-40Pb solder is a two phase alloy consisting of an interconnected Sn-rich phase and globular, dendritic, and lamellar Pb-rich regions. The Sn was found to precipitate out in the Pb-rich regions with the same morphology and crystallography as found for β-Sn precipitates in 5Sn-95Pb. The Sn-rich phase is fine grained on solidification (with a grain size of 0.44 μm) which coarsens with time at elevated temperature (1.3 μm after 167 hours at 125°C). In heterogeneous coarsened regions in thermal fatigue the Sn grains coarsen further (3 μm after 2000 cycles between -55°C and 125°C). In thermal fatigue eventual failures occur at Sn-Sn grain boundaries in the coarsened regions due to the inability of the large Sn grains to slide and rotate to accommodate the strains.

INTERFACIAL INTERMETALLIC MICROSTRUCTURE

Single phase Cu_3Sn (ε-phase) forms on the reaction of 5Sn-95Pb with Cu. The ε- phase is columnar and does not spall off into the solder when the solder is molten. The activation energy of formation of Cu_3Sn was found to be 13 Kcal/mol and the pre-exponential constant $D_0 = 2.1 \times 10^{-6}$ cm^2/sec.

The reaction of 60Sn-40Pb with Cu resulted in Cu_3Sn ε-phase forming adjacent to the Cu and Cu_6Sn_5 η-phase adjacent to the solder. The ε-phase was columnar and the η-phase was faceted and had a rod-like morphology. The ε-phase grows into the Cu on the $[0002]_\varepsilon$ direction. Twinning was also found to occur along $[0002]_\varepsilon$ due to compressive stresses present on layer formation. A model for the formation and growth of the interfacial intermetallics was presented which involves the Cu and Sn reacting to form Cu_6Sn_5 at the interface which transforms to Cu_3Sn at the Cu/η interface. The η-phase has a broken up rod-like morphology so Sn can diffuse easily to the ε phase (where it is a fast diffuser) and reacts with the Cu to form Cu_3Sn at the ε/Cu interface. Meanwhile Cu reacts with the Sn at the η/ε interface causing the η rods to grow, from their base, out into the molten solder. The irregularity in morphology made it impossible to determine diffusion coefficients for 60Sn-40Pb solder on Cu.

Although interfacial intermetallics were brittle the thermal fatigue failures were independent of the interface. Only under rapid deformation rates do failures occur through the interfacial intermetallics in either 5Sn-95Pb or 60Sn-40Pb solder joints.

INTERMETALLIC WHISKERS

When molten 60Sn-40Pb comes in contact with Cu hexagonal intermetallic whickers of Cu_6Sn_5 form at the Cu/solder interface. The whiskers grow via a screw dislocation mechanism from the base of the whisker along the c-axis of the η-phase. The whiskers break off into the molten solder and the high energy core of the whisker dissolves and is replaced with molten solder. On solidification hexagonal tubes of the whiskers remain filled with solder.

The mechanical properties of solder containing whiskers were determined as a function of temperature (-196°C, 20°C, and 125°C) and were compared with pure 60Sn-40Pb solder. The presence of whiskers had no effect on strength. At -196°C decohesive failure at the whisker/solder interface increases the work hardening rate and decreases elongation. At 20°C the failures occurred via cleavage of whiskers and the total elongation decreased. At 125°C the whiskers had no effect.

Although the whiskers had a strong effect on the isothermal mechanical properties of the solder the whiskers had little or no effect on the thermal fatigue behavior. The damage

incurred at low temperature in thermal fatigue, due to the whiskers, is "healed" at the high temperature via creep or diffusion of the solder. The strains induced in thermal fatigue are not sufficient to cause failures due to decohesion or cleavage.

ISOTHERMAL MECHANICAL PROPERTIES

A specimen design and assembly were developed to reproducibly test solder joints in simple shear. Isothermal shear to failure tests with these specimens found that 60Sn-40Pb joint behavior was dependant on deformation rate. At fast deformation rates (> 0.2 mm/min) interfacial failures occur through the intermetallics. At slower rates failures occurred through the solder. In thermal fatigue the deformation rate, even in thermal shock testing, is slow enough that the deformation is taken up by the solder rather than the interface.

Tensile tests on bulk 60Sn-40Pb and 5Sn-95Pb solder were performed to gain understanding of the effect of microstructural extremes on mechanical properties. For 60Sn-40Pb coarse and fine microstructures were tested. The coarsened 60Sn-40Pb microstructure was found to be deleterious to the mechanical behavior. The coarse microstructure had lower strength, less total elongation, and a lower work hardening rate. The 5Sn-95Pb samples were tested in tension to examine homogeneous vs. cellular precipitate microstructures. For 5Sn-95Pb the mechanical behavior was found to be independent of precipitate distribution. The reason for this was both microstructures contain overaged precipitates that are ineffective as dislocation obstacles.

THERMAL FATIGUE TESTS

Thermal fatigue tests were performed using a specimen designed to impose simple shear strain on solder joints in thermal cycling. Both 5Sn-95Pb and 60Sn-40Pb joints were tested with a maximum shear strain of 19% imposed. The nominal thermal cycle was -55°C to 125°C.

• 5Sn-95Pb Joints

The 5Sn-95Pb joints were observed to fail after 120 thermal cycles. The cracks formed at the Pb grain boundaries on planes of maximum shear stress in the joint (parallel and perpendicular to the imposed shear). The precipitation of β-Sn had no effect on crack initiation or propagation in 5Sn-95Pb. Failures occurred because the Pb grains were unable to accommodate the imposed shear by sliding respective to one another. This resulted in the formation of cracks on the grain boundaries.

Thermal fatigue observations were related to isothermal fatigue results[109-111]. The 5Sn-95Pb joints in isothermal fatigue also failed after approximately 100 cycles at Pb grain boundaries. The isothermal fatigue cycles to failure and fracture mode were relatively

independent of temperature. Therefore isothermal fatigue tests can be used as a good representation of the thermal fatigue 5Sn-95Pb joint characteristics.

• 60Sn-40Pb

The failures in 60Sn-40Pb joints were preceded by heterogeneous coarsening of the solder. Both the Pb and Sn-rich phase were found to coarsen. The Pb-rich phase was found to be denuded of precipitates. The heterogeneous coarsening was due to strain imposed in thermal cycling by the thermal expansion differences between joined materials. Only homogeneous coarsening was observed in unconstrained bulk solder specimens. Heterogeneous coarsening was also observed when the only strain imposed was due to the difference in thermal expansion between the solder and the joined material. This indicates that by designing a joint to have matched expansion coefficients only delays thermal fatigue failures, it does not eliminate them.

The heterogeneous coarsening arises at some heterogeneity in the solder that concentrates the shear strain at one point in the joint. The concentrated strain results in recrystallization and phase growth at the heterogeneity. The coarsened region is the weakest point of the joint (as pointed out in mechanical tensile tests on coarsened 60Sn-40Pb solder) leading to further coarsening on continued thermal cycling.

The 60Sn-40Pb joints crack through the heterogeneous coarsened regions. The cracks were intergranular through the interconnected Sn-rich phase at Sn-Sn grain boundaries. The Sn grains are large in the coarsened region so that they can no longer rotate and slide to accommodate the strain. This results in cracks at Sn grain boundaries.

Experiments were performed at low (-55°C to 35°C) and high (35°C to 125°C) thermal cycles. The elevated temperature portion of the cycle was found to be the source of coarsening and failure. The 35°C to 125°C cycled specimens failed in a fashion identical to the -55°C to 125°C cycle. The low temperature cycle also failed, after a larger number of cycles, through a thin heterogeneous coarsened region. Low temperature failures occurred because even at 35°C the solder is at 0.69 of the homologous temperature and there is enough thermal energy for coarsening to occur.

Thermal fatigue results on 60Sn-40Pb joints were compared to isothermal fatigue tests[109-111]. The thermal fatigue life was found to be shorter than the isothermal fatigue results predict. The reason for this poor correlation is that a metallurgical change occurs in the joint in thermal cycling (heterogeneous coarsening) that is not found in isothermal fatigue. Therefore one can not use isothermal fatigue results to predict thermal fatigue behavior in 60Sn-40Pb joints.

8.0 REFERENCES

1. J. Wolters; "Zur Geschichte der Lotternik", Degussa, Frankfort DDR, 1978.
2. L. S. Goldman; "Geometric optimization of controlled collapse interconnections", IBM J. Res. Dev., 13 (1969) p. 251.
3. MIL-STD-883C, "Test methods and procedures for microelectronics", Naval Publications and Forms Center, 5801 Tabor Ave., Philadelphia, PA 19120-5099.
4. M. J. Berkebile; "Investigation of solder cracking problems on printed circuit boards" (Nasa TMX 54653) September 1967.
5. C. L. Lassen; "Use of metal core substrates for leadless chip carrier interconnection", Electronic Packaging and Production, 2,3 (1981) p. 98.
6. C. A. Haper, W. W. Stanley; "Some critical material factors in the application of leadless chip carrier packages", Electronic Packaging and Production, 21, 8 (1981) p. 134.
7. R. Howard, S. Sobeck, C. Sanetra; "A new package related failure mechanism for leadless ceramic chip carriers (LC-3s) solder attached to alumina substrates", Solid State Technology, 26, 2 (1983) p. 115.
8. E. Levine, J. Ordenez; "Analysis of thermal cycle fatigue damage in microsocket solder joints", IEEE Trans. Components, Hybrids, and Manufacturing Tech., CHMT-4 (1981) p. 515.
9. S. K. Kang, N. D. Zommer, D. L. Feucht, R. W. Heckel; "Thermal fatigue failure of soft soldered contacts to Si power transistors", IEEE Trans. Parts, Hybrids, and Packaging, PHP-13 (1977) p. 318.
10. J. T. Lynch, M. R. Ford, A. Boetti; "The effect of high dissipation compoents on the solder joints of ceramic chip carriers attached to thick film alumina substrates", IEEE Trans. Components, Hybrids, and Manufacturing Tech., CHMT-6 (1983) p. 237.

11. J. W. Munford; "The influence of several design and material variable on the propensity for solder joint cracking", IEEE Trans. Parts, Hybrids, and Packaging, PHP-11 (1975) p. 296.

12. R. N. Wild; "Fatigue properties of solder joints", Welding Research Supp., 51 (1972) p. 521s.

13. E. A. Wright, W. M. Wolverton; "The effect of the solder reflow method and joint design on the thermal fatigue life of leadless chip carrier solder joints", Proc. 34th Electron. Components Conf., 34 (1984) p. 149.

14. R. Yenawine, M. Wolverton, A. Burkett, B. Waller, B. Russel, D. Spritz; "Today and tomorrow in soldering", Proc. 11th Naval Weapons Electonics Manufacturing Seminar, China Lake, CA (1987) p. 339.

15. H. B. Ellis; "Aspects of surface mounted chip carrier solder joint reliability", Proc. 11th Naval Weapons Electonics Manufacturing Seminar, China Lake, CA (1987) p. 377.

16. P. M. Hall, T. D. Dudderar, J. F. Argyle; "Thermal deformations observed in leadless ceramic chip carriers surface mounted to printed wiring boards", IEEE Trans. Components, Hybrids, and Manufacturing Tech., CHMT-6 (1983) p. 544.

17. P. M. Hall; "Forces, moments,and displacements during thermal chamber cycling of leadless ceramic chip carriers soldered to printed boards", IEEE Trans. Components, Hybrids, and Manufacturing Tech., CHMT-7 (1984) p. 314.

18. W. T. Chen, C. W. Nelson; "Thermal stresses in bonded joints", IBM J. Res. Dev., 23 (1979) p. 179.

19. Y. Weitsman; "Residual thermal stresses in a symmetric double lap joint", J. of Thermal Stresses, 3 (1980) p. 521.

20. J. F. Burgess, R. O. Carlson, H. H. Glascock, C. A. Neugebauer, H. F. Webster; "Solder fatigue problems in power packages", IEEE Trans. Components, Hybrids, and Manufacturing Tech., CHMT-7 (1984) p. 405.

21. T. C. Taylor, F. L. Yuan; "Thermal stress and fracture in shear-constrained semiconductor device structures", IRE Trans. Electronic Devices, 9 (1962) p. 303.

22. D. R. Olsen, A. M. Berg; "Properties of die bond alloys relating to thermal fatigue", IEEE Trans. Components, Hybrids, and Manufacturing Tech., CHMT-2 (1979) p. 257.

23. H. H. Manko; Solders and Soldering, McGraw-Hill, New York (1979).

24. L. S. Goldmann, R. D. Herdzik, N. G. Koopman, V. C. Marcotte; "Pb-In for controlled-collapse chip joining", IEEE Trans. Parts, Hybrids, and Packaging, PHP-13 (1977) p. 194.

25. R. T. Howard; "Optimization of Pb-In alloys for controlled collapse chip connection application", IBM J. Res. Dev., 26 (1982) p. 372.

26. C. J. Thwaites, W. B. Hampshire; "Mechanical strength of selected soldered joints and bulk solder alloys", Welding Res. Supp., 55 (1976) p. 323s.

25. C. MacKay; "Solder contamination-cause and effect", Fall Meeting Inst. Interconnections and Packaging Electronic Circuits, September (1981) (ICP-TP-380).

26. C. J. Thwaites; "Soldering Technology a decade of developments", Int. Metals Reviews, 29 (1984) p. 45.

27. L. Quan, D. Frear, D. Grivas, J. W. Morris, Jr.; "Tensile behavior of Pb-Sn Solder/Cu joints", J. Electronic Materials, 16 (1987) p. 203.

28. S. V. Lashko, P. I. Lymar, N. F. Lashko; "The effect of Mg additions to the properties of Sn-Pb brazing alloys", Svar. Proiz., 10 (1980) p. 27.

29. W. Englemaier; "Fatigue life of leadless chip carrier solder joints during power cycling", IEEE Trans. Components, Hybrids, and Manufacturing Tech., CHMT-6 (1983) p. 232.

30. P. L. Blum, J. Pelissier, G. Silvestre; "An investigation of soldered Cu-Sn bond brittleness by electron microscopy", Solid State Technology, March (1973) p. 55.

31. H. N. Keller; "Temperature cycling of HIC thin-film solder connections" IEEE Trans. Components, Hybrids, and Manufacturing Tech., CHMT-4, (1981) p. 132.

32. P. M. Hall; "Solder post attachment of ceramic chip carriers to ceramic integrated circuits", IEEE Trans. Components, Hybrids, and Manufacturing Tech., CHMT-4 (1981) p. 403.

33. K. R. Stone, R. Duckett, S. Muckett, M. E. Warwick; "Mechanical properties of solders and soldered joints", Brazing and Soldering, 4 (1983) p. 20.

34. C. Wright; "The effect of solid state reactions upon solder lap shear strength", IEEE Trans. Parts, Hybrids, and Packaging, PHP-13 (1977) p. 202.

35. M. C. Denlinger, D. W. Becker; "Improved solder alloy for printed circuit board application", Welding Res. Supp., 57 (1978), p. 292s.

36. H. S. Rathore, R. C. Yih, A. R. Edenfeld; "Fatigue behavior of solders used in flip chip technology", J. Testing and Evaluation, 1 (1973) p. 170.

37. E. R. Bangs, R. E. Beal; "Effect of low frequency thermal cycling on the crack susceptability of soldered joints", Welding Res. Supp., 54 (1975) p. 377s.

38. R. N. Wild; "Some fatigue properties of solders and solder joints", IBM Report no. 74Z000481, Oct. (1975).

39. J. T. Lynch, G. M. Dydon, M. R. Hepher, J. P. McCarthy; "Environmental assesment of ceramic chip carriers soldered-attached to thick film alumina substrates", Proc. 32nd Elec. Comp. Conf., 32 (1982) p. 385.

40. G. A. Dreyer, A. Koudounaris, I. H. Pratt; "The reliability of soldered or epoxy bonded chip capacitor interconnections on hybrids", IEEE Trans. Parts, Hybrids, and Packaging, PHP-13 (1977) p. 218.

41. P. L. Kinser, J. G. Vaughn, S. M. Graff; "Reliability of soldered joints in thermal cycling environments" Electronic Packaging and Production, 16, 5 (1976).

42. K. U. Snowden; "The effect of atmosphere on the fatigue of Pb", Acta Met., 12 (1964) p. 295.

43. H. S. Blanks; "Accelerated vibration fatigue life testing of leads and soldered joints", Microelectronics and Reliability, 15 (1976) p. 213.

44. C. J. Thwaites, D. McDowall; "A study of the effect on the mechanical properties of soldered joints made to brass in the presence of Sb in 40Sn-60Pb and solders", Brazing and Soldering, 6 (1984) p. 32.

45. H. Solomon; "Low frequency high temperature low cycle fatigue of 60Sn-40Pb solder", presented at Conf. low cycle fatigue - directions for the future, Lake George, NY, 1985 (GE report 85CRD238 Dec. 1985).

46. S. S. Manson; Thermal Stress and Low Cycle Fatigue, New York, McGraw-Hill, (1966).

47. K. C. Norris, A. H. Landzberg; "Reliability of controlled collapse interconnections", IBM J. Res. Dev., 13 (1969) p. 266.

48. J. R. Taylor, D. J. Pedder; "Joint strength and thermal fatigue in chip carrier assembly", Int. J. for Hybrid Microelectronics, 5 (1982) p. 209.

49. H. I. Aaronson; "Decomposition of austenite by diffusional processes", Interscience, (1962) p. 387.

50. K. N. Tu, D. Turnbull; "Morphology of cellular precipitation of Sn from Pb-Sn bicrystals-I", Acta Met., 15 (1967) p. 369.

51. K. N. Tu, D. Turnbull; "Morphology of cellular precipitation of Sn from Pb-Sn bicrystals-II", Acta Met., 15 (1967) p. 1317.

52. D. Turnbull, H. N. Treaftis; "Kinetics of precipitation of Sn from Pb-Sn solid solutions", Acta Met., 3, (1955), p. 43.

53. D. Turnbull; "Theory of cellular precipitation", Acta Met., 3 (1955) p. 55.

54. W. DeSorbo, D. Turnbull; "Kinetics of precipitation in small Pb-Sn spheres", Acta Met., 4 (1956) p. 495.

55. D. Turnbull, H. N. Treaftis; "Micrographic investigation of precipitation in Pb-Sn alloys", Trans. TMS of AIME, 212 (1958) p. 33.

56. H. J. Frost, P. R. Lavery, S. D. Lutender; "Microstructure and mechanical properties of Pb-Sn solder alloys", Proc. 3rd Ann. Electronic Packaging and Corrosion in Miroelectronics Conf., 3 (1987) p. 259.

57. G. Borelius, F. Larris, E. Ohlsson; Arkiv. Matematik Astronomi och Fysik, 31A (1944).

59. R. C. Ecob, B. Ralph; "Habit plane specificivity and cellular precipitation", Proc. Int. Conf. Solid-Solid Phase Transformations, ed. H. I. Aaronson (1982) p. 515.

60. W. Bollmann; Crystal Defects and Crystalline Interfaces, Stringer Berlag, Berlin (1970).

61. R. C. Ecob, B. Ralph; "A model of the equilibrium structure of FCC/BCC Interfaces", Acta Met., 29 (1981) p. 1037.

62. W. A. Tiller, R. MrDjenovich; J. of Applied Phys., 34 (1963) p. 3639.

63. D. Grivas; Deformation of Superplastic Alloys at Relatively Low Strain Rates, Ph.D. thesis, University of California, Berkeley (1978).

64. D. H. Avery, W. A. Backofen; Trans. Quart. ASM, 58 (1965) p. 551.

65. J. D. Verhoeven, D. P. Mourer, E. D. Gibson; "The morphology and crystallography of directionally solidified Pb-Sn eutectic alloys", Met. Trans., 8A (1977) p. 1239.

66. R. H. Hopkins, R. W. Kraft; Trans. TMS-AIME, 242 (1968) p. 1627.

67. N. Takahashi, K. Schenuima; J. Inst. Metals, 87 (1958-59) p. 19.

68. B. Labulle, C. Petipas; J. Crystal Growth, 28 (1975) p. 279.

69. V. C. Marcotte, K. Schroder; "Cu-Pb-Sn ternary system: Low Cu additions to Pb-Sn binary system", Mat. Res. Soc. Symp. Proc., 19 (1983) p. 403.

70. M. Inaba, K. Teshima, O. Hirao, T. Sakurai; "Effect of addtional Fe and Sn on the diffusion reaction on Sn-Cu interface", J. Mat. Sci. Lett., 3 (1984) p. 400.

71. P. J. Kay, C. A. MacKay; "The growth of intermetallic compounds on common basis materials coated with Sn and Sn-Pb alloys", Trans. Inst. Metal Finishing, 54 (1976) p. 68.

72. D. Grivas, D. Frear, L. Quan, J. W. Morris, Jr.; "The formation of Cu_3Sn intermetallic on the reaction of Cu with 95Pb-5Sn solder", J. Electronic Materials, 15 (1986) p. 355.

73. B. S. Berry, I. Ames; "Studies of the SLT chip terminal metallurgy", IBM J. Res. Dev., 13 (1969) p. 286.

74. M. L. Ackroyd, C. A. MacKay; "Solders, solderable finishes and reflowed solder coatings", Circuit World, 3 (1977) p. 1.

75. W. G. Bader; "Dissolution of Au, Ag, Pb, Pt, Cu, and Ni in molten Sn-Pb solder", Welding Res. Supp., 48 (1969) p. 551s.

76. W. G. Bader; "Pb alloys for high temperature soldering of magnet wire", Welding Res. Supp., 54 (1975) p. 370s.

76a. P. L. Brooks, E. Gillam; Acta Met., 18 (1970) p. 1181.

77. M. Omishi, A. Fujibuchi; Trans. JIM, 16 (1972) p. 539.

78. L. daSilva, R. Mehl; Trans. AIME, 191 (1951) p. 155.

79. H. Oikawa, A. Hosoi; Scripta. Met., 9 (1975) p. 823.

80. Z. Lubyova, P. Fellner, K. Mutiasorsky; Z. Metall., 66 (1975) p. 179.

81. M. A. H. Howes, Z. P. Saperstien; "The reaction of Pb-Sn solders with Cu alloys", Welding Res. Supp., 48 (1969) p. 80s.

82. P. E. Davis, M. E. Warwick, S. J. Muckett; "Intermetallic compound growth and solderability of reflowed Sn and Sn-Pb coatings", Plating and Surface Finishing, 70 (1983) p. 49.

83. K. N. Tu; "Interdiffusion and reaction in bimetallic Cu-Sn thin films", Acta Met., 21 (1973) p. 347.

84. D. A. Unsworth, C. A. MacKay; "A preleminary report on growth of compound layers on various metal bases plated with Sn and its alloys", Trans. Insts. Metal Finishing, 51 (1973) p. 85.

85. M. E. Warwick, S. J. Muckett; "Observations on the growth and impact of intermetallic compounds on Sn coated substrates", Circuit World, 9 (1983) p. 5.

86. G. V. Kidson; J. Nuc. Mat., 3 (1961) p. 21.

87. I. Kawakatsu, T. Osawa, H. Yamaguchi; "On the growth of alloy layer betwween solid Cu and liquid Sn", Trans. JIM, 13 (1972) p. 436.

88. D. Gerth; "Untersuchung der zusannerstzing von diffusionschichten in weichlotverbendungen mittels mikrosonde", Metall., 24 (1970) p. 838.

89. P. J. Kay, C. A. MacKay; "Barrier layers against diffusion", Trans. Inst. Metal Finishing, 57 (1979) p. 169.

90. P. E. Davis, M. E. Warwick, P. H. Kay, S. J. Muckett; "Intermetallic compound growth and solderability (electroplated coatings)", Plating and Surface Finishing, 69 (1982) p. 72.

91. J. Kim; "Characterization of ternary Cu-Sn-Au bulk alloys and thin films:, J. Electonic Materials, 13 (1984) p. 191.

92. D. Frear, D. Grivas, J. W. Morris, Jr.; "The effect of Cu_6Sn_5 whisker precipitates in bulk 60Sn-40Pb solder", J. Electronic Materials, 16 (1987) p. 181.

93. E. W. Brothers; Intermetallic compound formation in soft solders, Ph.D. thesis, University of Oklahoma, (1979).

94. K. G. Schmitt-Thomas, M. Hammer; "Bilddung intermetallischer phasen bei weichlotoerbindungen und ihre bideutung fur das bruchverhalten", Shweißen und Schneiden, 29 (1977) p. 258.

95. M. Hansen; Constitution of Binary Alloys, McGraw-Hill, New York, (1958).

96. F. R. N. Nabarro, P. J. Jackson: "Growth of Crystal Whiskers", Growth and Perfection of crystals, editor R. H. Doremus, (1958) p. 13.

97. R. H. Doremus, B. W. Roberts, D. Turnbull; Growth and Perfection of Crystals, Proc. Int. Conf. on Crystal Growth, John Wiley and Sons, Inc., London (1958).

98. J. D. Eshelby; J. Appl. Phys., 24 (1953) p. 176.

99. S. Amelnickx, W. Barmick, W. Dekeyser, F. Seitz; Phil. Mag., 2 (1957) p. 355.

100. W. K. Burton, N. Cabrerar, F. C. Frank; Phil. Trans. Roy. Soc., A243 (1951) p. 299.

101. F. C. Frank; Disc. Faraday Soc., 5 (1949) p. 48.

102. W. C. Ellis, D. F. Bibbons, R. G. Treuting; "Growth of metal whiskers from the solid", Growth and Perfection of Crystals, editor R. H. Doremus, (1958) p. 230.

103. W. W. Webb; "Dislocation structure of whiskers", Growth and Perfection of Crystals, editor R. H. Doremus, (1958) p. 230.

104. Z. Gyulai; Zeits. f. Physik., 125 (1949) p. 1.

105. R. M. Fisher, L. S. Darken, K. G. Carrol; Acta Met., 12 (1954) p. 368.

106. C. J. Thwaites, R. Duckett; "Some effects of soldered joint geometry on their mechanical strength", Revue du la Soudure, 4 (1976) p. 1.

107. G. Becker; "Testing and results related to the mechanical strength os solder joints", IPC Fall meeting IPC-TP-288 (1979) .

108. E. C. Kubik, T. P. L. Li; "Thermal shock and temperature cycling effects on solder joints of hermetic chip carriers mounted on thick films", Microelectronics Center, Martin Marrietta Aerospace, Orlando FL 32855.

109. D. Frear, D. Grivas, M. McCormack, D. Tribula, J. W. Morris, Jr.; "Fatigue and thermal fatigue of Pb-Sn solder joints", Proc. Effects of Load and Thermal Histories on Mechanical Behavior Symp. AIME Spring Conf., Denver, CO (1987) ,in press.

110. D. Frear, D. Grivas, M. McCormack, D. Tribula, J. W. Morris, Jr.; "Fatigue and thermal fatigue testing of Pb-Sn solder joints", Proc. 3rd Ann. Electronic Packaging and Corrosion in Miroelectronics Conf., 3 (1987) p. 269.

111. M. McCormack; Initial research regarding isothermal shear fatigue of solder joints, M. S. thesis, University of California, Berkeley (1987).

112. D. Tribula, D. Grivas, J. W. Morris, Jr.; "Stress relaxation in Sn-Pb solder joints", to be published.

113. R. Berriche, S. Vaynman, M. E. Fine, D. A. Jeannot; "The effect oon environment of fatigue of low Sn-Pb base alloys",Proc. 3rd Ann. Electronic Packaging and Corrosion in Miroelectronics Conf., 3 (1987) p. 169.

114. S. K. Hwang, J. W. Morris, Jr.; "The use of a boron addition to prevent intergranular embrittlement in Fe-12Mn", Met. Trans., 11A (1980) p. 1197.

115. J. Hoyt; "Influence of leg shape and solder joint metallugy on surface mount solder joint strength", Proc. 11th Naval Weapons Electonics Manufacturing Seminar, China Lake, CA (1987) p. 409.

APPENDIX I ELECTRONIC PACKAGING

Modern advances in Integrated Circuit (IC) design technology challenge traditional concepts of electronic packages. As the scale of integration becomes finer, speed increases and more Input/Output (I/O) leads are necessary. The trends in the scale of integration is shown in the table below.

TABLE A1

Integration	# Transistors	I/O Leads	Function
Small Scale Integration (SSI)	1-40	14	
Medium Scale Integration (MSI)	40-400	24	Counter
Large Scale Integration (LSI)	400-4500	48	Hand Calculator
Very Large Scale Integration (VLSI)	4500-300,000	64	Microprocessor
Ultra Large Scale Integration (ULSI)	>300,000	160	Computer on chip*

* Not commercially available yet.

Device speed has increased along with integration. The new Very High Speed Integrated Circuits (VHSIC), which is currently being cultivated by the Department of Defense, use VLSI chips which has increased switching speed from 10 MHz to 25 MHz. GaAs switches are projected to have switching speeds of 2-3 GHz. Packaging schemes used in the past, such as Dual in-line Packages (DiP's) can not provide the small size or speed required. Therefore new packaging schemes are needed. This appendix gives a brief description of electronic packages that have been designed for the new fast IC's.

An electronic package is defined as a housing that interconnects electronic devices (especially IC's) and isolates them from the environment. Traditionally the packaging scheme has been divided into three levels. The first level begins at the metallization on the Si or GaAs and ends at the carrier/chip connection. The second level actually houses the devices and acts as a space transformer from the small and closely spaced contact pads on the chip to the large wiring network on the printed wiring board. It is in the second level that the majority of changes have occurred to compensate for advanced IC's. The third level of the package consists of the printed wiring board and related components.

• First Level Package

The major concern in this level is the electrical connection between the IC and the second level package. Primarily there are two methods to perform this interconnection.

These are diagrammed in Figure A1. The first is wire bonding[1A]. Here 1 mil thick gold wires are ultrasonically bonded from the chip to the carrier. The problem with wire bonding is that it is difficult to reliably wire very closely spaced interconnections. Also parasitic inductance ("cross-talk") between adjacent wires can occur and scramble the signals. The second example is the flip chip technology proposed by IBM[2A]. Here the chip, device side down, is directly soldered to a chip carrier. The surface tension of the solder balls holds the chip up. This design eliminates the problem of wire "cross-talk" because there are no wires present. The chips self align on reflow of the solder (the solder only wets the metal layers on the chip and carrier pads so the chip will align itself when the solder is molten). Therefore the complexity of wiring closely spaced contact pads is eliminated in flip chip technology. However, these solder joints are highly susceptible to thermal fatigue failures, as described in the text, section 4.5.

• Second Level

The first packaging design used in the second level was the Dual in-line Package (DiP). The DiP consists of a rectangular enclosure made of plastic or ceramic with two rows of leads on opposite sides of the rectangle, Figure A2. This package is inserted and soldered into Plated-Through-Holes (PTH) on the Printed Wircuit Board (PWB). A PTH is a small hole drilled through the PWB that has been plated with a thin metallized layer. The problem with the DiP is that it takes up a lot of PWB real estate. As the number of I/O leads increases the DiP must also increase in length. There is also a signal propagation delay associated with travelling over long distances and the possibility of parasitic inductance between leads. Therefore there is a desire to design a package that will have a large number of leads in a compact size.

The second possibility of a compact carrier is the Pin Grid Array (PGA). In the PGA, Figure A3, I/O leads are pins on the bottom of the package rather than on the edge. This results in a package of greatly reduced size. Problems with the PGA are that parasitic inductance is still possible across pin leads. The package design is much more expensive than the DiP (the package itself and the many PTH's on the PWB). Also the PGA is difficult to replace. To replace a PGA all the solder joints on the pins must be remelted. If the PGA is pulled before full melting has occurred a PTH can be lost, resulting in the loss of the entire board.

The most promising design is the leaded, or leadless, chip carrier mounted using Surface Mount Technology (SMT). The chip carrier is made of either plastic or ceramic and has a square shape with I/O connection on all four sides, Figure A4. The chip carrier is surface mounted with solder bonding the pads on the PCB and the metallized

connection of the carrier. A chip carrier has a 60% decrease in area compared with a DiP that has the same number of leads[3A]. The chip carrier is less expensive that the DiP or PGA because no expensive PTH's are required on the PCB. It is also possible to solder carriers to both sides of the PCB. There is low parasitic impedance in surface mount because of the short line lengths in the package. The package is also rugged and easy to handle, there are no pins that can be bent. The package is self aligning in reflow, from with a 7° offset[4A].

- Leaded vs. Leadless Chip Carriers in SMT

Two types of leaded carriers are shown in Figure A5. A Leadless Chip Carrier (LCC) is shown in Figure A4. The leaded carrier has the advantage that flux removal from under the carrier is easy and the lead takes up some of the strain in thermal cycling. However, a leaded carrier does increase lead lengths, and is therefore slower, and self alignment is soldering is not as simple as with LCC[5A]. However, LCC solder joints are susceptible to thermal fatigue failures.

- Plastic vs. Ceramic Chip Carriers in SMT

The Japanese introduced the first commercial plastic chip carrier in 1977[3A]. Plastic packages are inexpensive and facilitate in the size reduction of consumer products[6A]. In the U.S. the primary use of SMT chip carriers is by the military and the packages are made of 90% to 96% Alumina[5A]. The ceramic packages are expensive but have very high reliability. The small size, lightweight and rugged build in the ceramic chip carrier is ideal for high speed operations in missiles and spacecraft where extremely high reliability is required. The reliability of the ceramic package hinges on the hermiticity of the package. Properly sealed, a ceramic package is impermeable to the environment (air and moisture). A plastic carrier is much more susceptible to the environment and errors can occur in device function from impurities polluting the high grade Si or GaAs chips.

The use of SMT has doubled in the years 1983-1984[6A]. Currently SMT makes up 25% of the electronic device market and this is protected to increase to 50% by 1990[3A].

• Third Level

The printed wiring boards that chip carriers are mounted on have also been modified to keep pace with the trends in packaging. The PCB's in the past were commonly made of epoxy-fiberglass or polyimide-fiberglass. Both are inexpensive and have large thermal expansivities which are entirely inappropriate for the mounting of ceramic chip carriers in thermal cycling. New low expansivity boards have been designed, at great expense, to lower the expansivity of the PCB's. These designs include epoxy (polyimide)/Aramid or epoxy/quartz. These boards have been designed with the goal of

tailoring board expansivities to that of the chip carrier. As pointed out in section 4.5 this does not stop thermal fatigue failures of SMT solder joints. Another option[7A] proposes to manufacture ceramic circuit boards with refractory metal lines (W of Mo) that can with stand the curing temperatures for alumina.

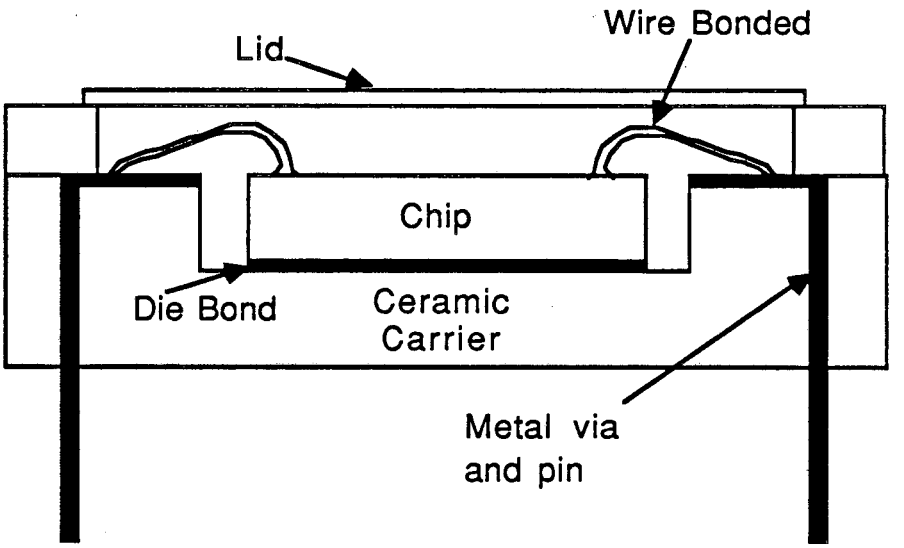

a) Wire Bonded First Level Package.

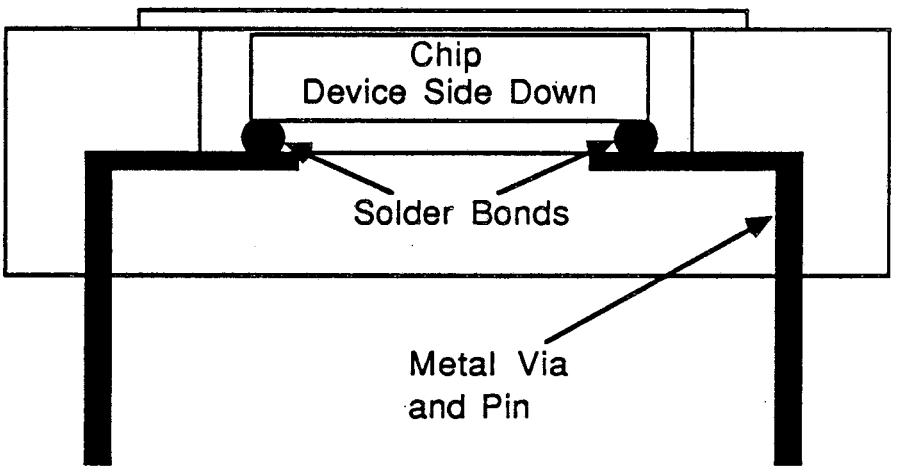

b) "Flip Cip" First Level Package.

Figure A1. Illustrations of two types of first level packages, wire bonded and flip chip. The second level package is a ceramic DiP.

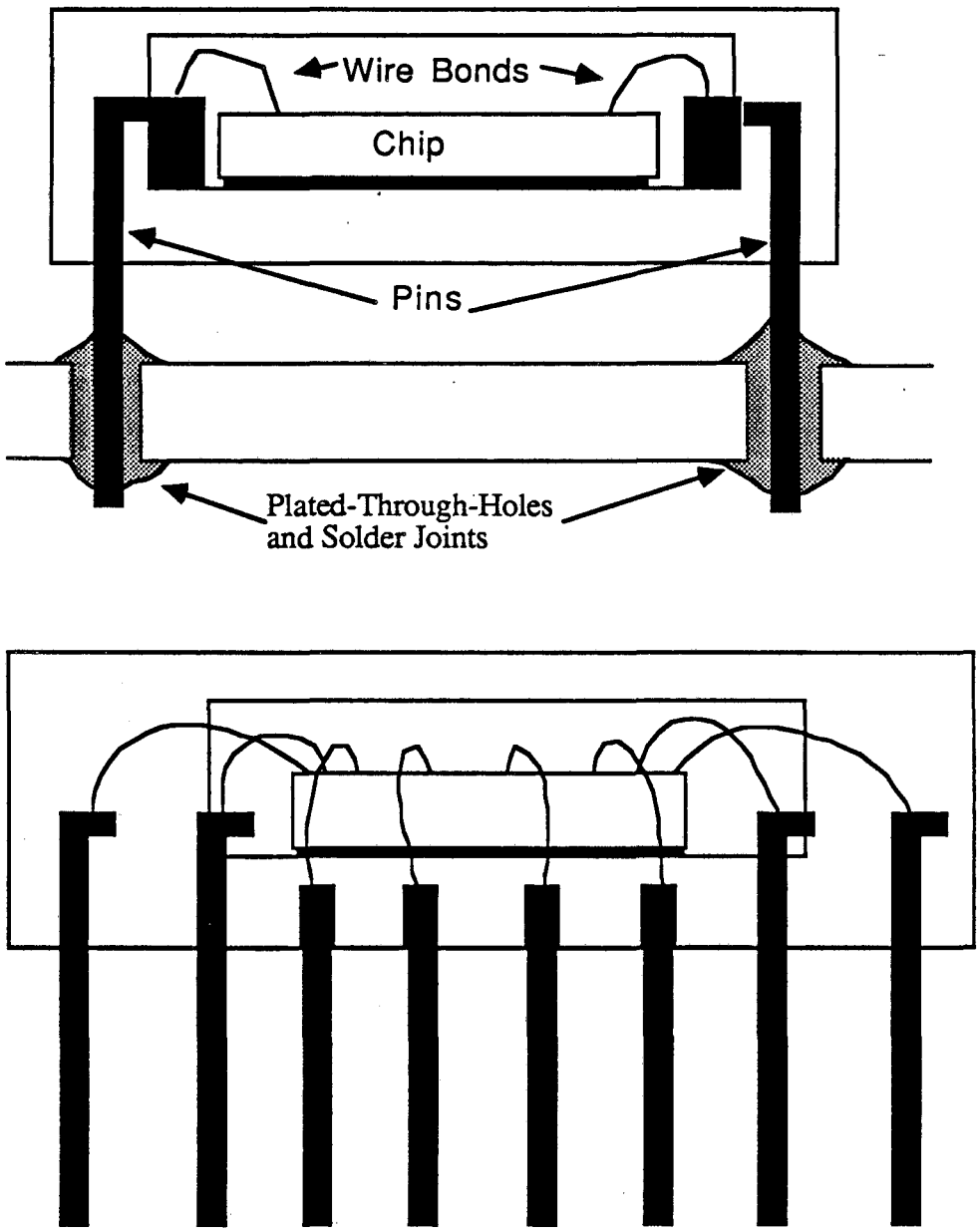

Figure A2. Illustration of two side views of a Dual in-line Package.

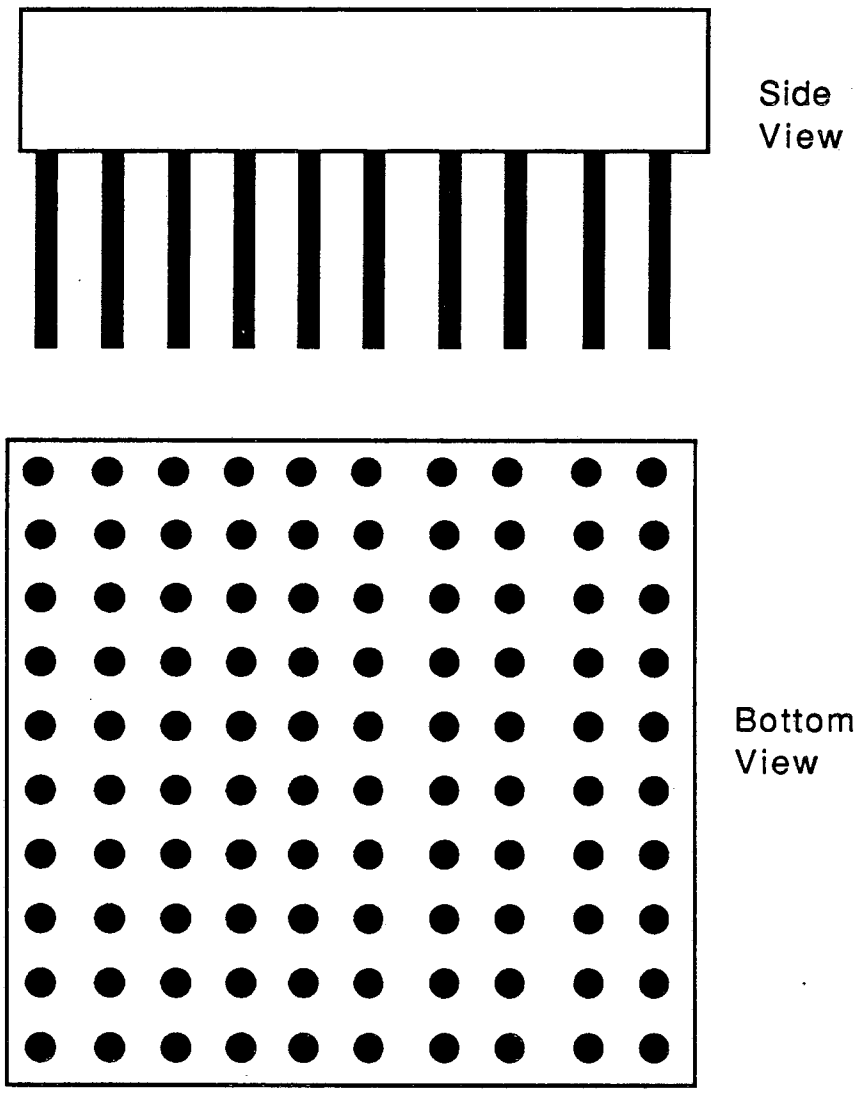

Figure A3. Two views of Printed Grid Arrays (PGA's).

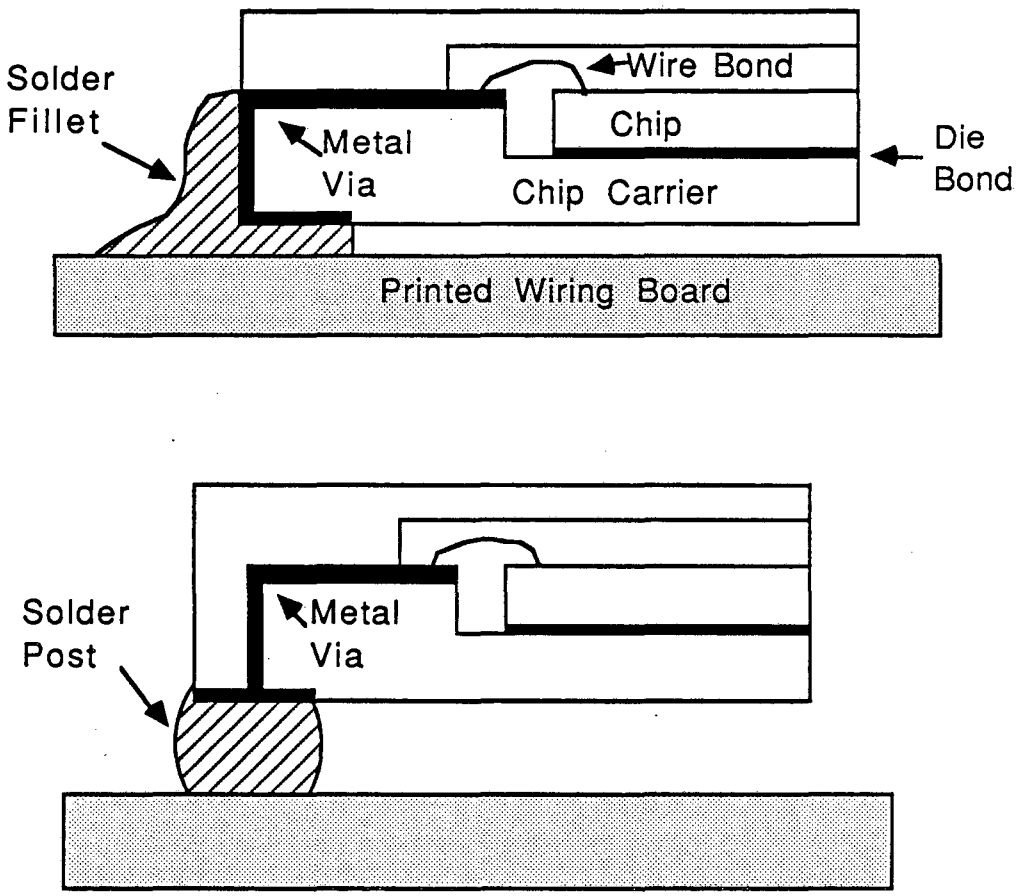

Figure A4. Two examples of Leadless Chip Carriers.

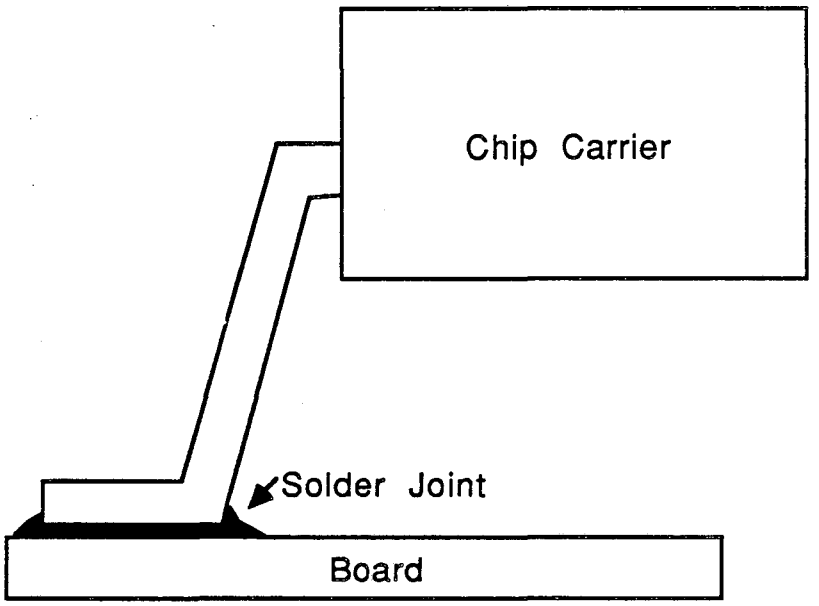

a) Gull Wing Leads

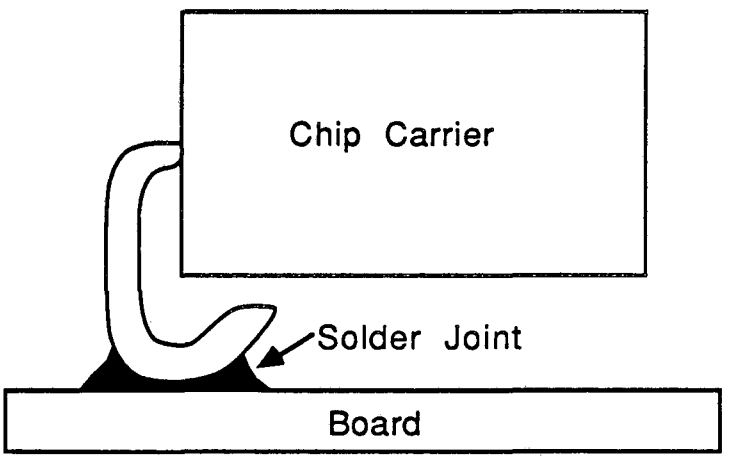

b) J-Bend Leads

Figure A5. Two examples of Leaded Chip Carriers.

APPENDIX II TRANSMISSION ELECTRON MICROSCOPY

A number of the microstructural observations presented in this work were performed using the Transmission Electron Microscope. The purpose of this appendix is to provide some basic background on how these TEM images were formed and how the data can be analyzed.

In TEM a monochromatic beam of electrons are accelerated (ranging from 100 KeV to 1.5 MeV) down an evacuated column, Figure B1. Using a series of electromagnetic lenses and apertures the electrons are collimated on a thin specimen (normally a metallic crystal). The wavelength of the electrons is very small (0.037 Å at 100 KeV and 6.37×10^{-3} Å at 1.5 MeV) and the energy is high so the beam can penetrate through the crystal if it is thin enough. The small wavelength of the electrons also experiences the periodic potential of the crystal lattice. The periodic potential of the crystal lattice causes the electrons to experience constructive interference as they emerge from the specimen. The interference is significant only if the path difference between scattered waves is an integral multiple wavelength of parallel atomic planes, Figure B2. The constructive interference is known as Braggs Law:

$$n\lambda = 2d\sin\theta$$

d = lattice plane spacing
λ = wavelength of electrons
θ = angle of incident beam with lattice plane

Therefore planes parallel to the incident beam produce a diffracted beam that can be recorded on an emulsion (a negative) in the microscope and the diffracted beams produce spots (a diffraction pattern) on the negative. The spacing of the spots is proportional to the lattice spacing of the crystal:

$$\lambda L = rd$$

L = distance electrons travel from specimen to negative
r = distance from incident beam to diffracted beam.

Crystallographic information, such as phase determination, of the specimen is then determined from the diffraction pattern.

Each diffracted beam contains information from the specimen. For instance a single diffraction spot contains all the information from the lattice planes that the diffracted spot represents. Using an objective aperture, located directly after the specimen in the microscope, certain beams can be selected and magnified (using lenses in the projector pole piece) and recombined to form an image. If a diffracted beam is selected, using the objective aperture, the image will contain only regions of the specimen that are scattered into that beam. For instance, if an (002) beam is selected only regions that have (002) planes almost parallel to the incident electron beam will become bright. This form of imaging is called *Dark Field*

Imaging. The central transmitted beam contains all diffracted information. Therefore if the central transmitted spot is selected, by the objective aperture, the result is a *Bright Field Image*.

The techniques described above are called *Diffraction Contrast* or *Amplitude Contrast Imaging* because it is the amplitude of the transmitted and diffracted beam that determines the contrast.

Contrast within the bright field image varies due to variation is diffraction conditions. The intensity of the image goes as the square of the amplitude. This can be stated mathematically by:

$$|\psi|^2_D = \left[\frac{F}{t}\right]^2 \left[\frac{\sin^2(t\,s)}{(\pi s)^2}\right]$$

where:

ψ = Amplitude of wave of electrons

F = Structure factor

t = Specimen thickness

s = Deviation from exact Bragg condition.

Therefore contrast varies with: the thickness of the specimen (wedge thickness fringes), bends in the specimen (bend contour fringes), and changes in crystal orientation (where both t and s vary. Changes in crystal orientation occur at grains, twins, boundaries, and precipitates and are clearly imaged in TEM. Lattice defects such as dislocations are also imaged due to elastic displacements in the crystal that the sensitivity of the electron beam is able to detect. Changes in phase vary the contrast because the structure factor varies between phases.

PHASE CONTRAST IMAGING

The use of phase contrast imaging results in an image that shows extremely fine detail of a crystalline specimen. A summary of the physical explanation of phase contrast imaging is the following.

Most electrons are directly transmitted through the specimen but some pass close to the atoms in the crystal. These electrons deflect through an angle that is dependant on the atomic number of the atoms and closeness of approach of the electrons. These electrons emerge from the bottom of the specimen with uniform amplitude but contain phase variations. This is shown schematically in Figure B3. More than one diffracted beam is allowed to recombine and form an image in the microscope. The contrast is a result of amplitude changes caused by defects and by interference from phase changes from the many diffracted beams allowed into

the image. Inelastic scattering in ignored because it is incoherent and degrades the phase contrast image. Therefore specimens must be very thin so that information is not lost.

The advantage to phase contrast imaging is that it is sensitive to point to point variations in the projected structure rather than the atomic displacements responsible for diffraction contrast. Therefore an image in phase contrast can detect the contrast from individual rows of atoms, and therefore information on a very fine scale. Therefore the image in phase contrast is sometimes called a lattice image.

Phase contrast imaging is complicated because it is severely limited by lens aberration and microscopic instabilities. The contrast transfer function[1B] models the effects of phase distortion due to lens spherical aberrations:

$$e^{ix} = \exp\left\{ i\frac{\pi}{\lambda}\left[\frac{C_s\alpha^4}{2} + \Delta z\alpha^2\right]\right\}$$

where:

α = angle between diffracted beam and forward scattered beam

C_s = spherical aberration coefficient

Δz = defocus defect (minimized by Scherzer defocus[2B]).

It is clear that distortion due to spherical aberration increases greatly as the angle between the diffracted beam and scattered beam increases. Therefore a great deal of effort must be spent to correctly align and correct lens aberrations (the astigmatism) in lattice imaging microscopy.

METHOD TO DETERMINE HABIT PLANE OF PRECIPITATES IN TEM[3B] (FIGURE B4)

1) Obtain structural image and Selected Area Diffraction Pattern (SADP) from the same area of the precipitate and the matrix.

2) Compensate for rotation by the lenses by rotating the image till it corresponds to the diffraction pattern.

3) Index the SADP to determine plane (hkl) and its normal M.

4) Choose a prominent row of reflections and as a reference measure angles **A** and **B** the structural trace directions with respect to the reference row of reflections (as shown in Figure B4).

5) Draw the stereographic projection and indicate **M**. Draw the great circle 90°C away from M that contains both **A** and **B**, and the great circle that corresponds to (hkl). **C** is α_0 degrees away from M and D is γ_0 degrees from **M**.

6) Draw the great circle through **AM** (trace direction) and **BM** (trace normal).

7) **B** is 90° away from **A**, therefore defines the habit plane (HKL), the pole of which is **E**.

8) Repeat this procedure for many precipitates. Eventually a significant crystallographic pole should be indicated by the intersection great circles.

ORIENTATION RELATIONSHIP DETERMINATION[3B]

1) Obtain a diffraction pattern with the reflection of both phases present on one pattern. For ease of determination either the precipitate or matrix should be centered at a low order zone axis.

2) Determine the zone axis for each pattern.

3) Construct stereographic projections for each zone axis.

4) Due to ambiguity obtain several diffraction patterns of different zone axis to check the orientation relationship by tilting the the sample into various orientations.

5) Locate poles of close packed planes and other important planes. These planes give the orientation relationship. This method results in an error of ~ 1°.

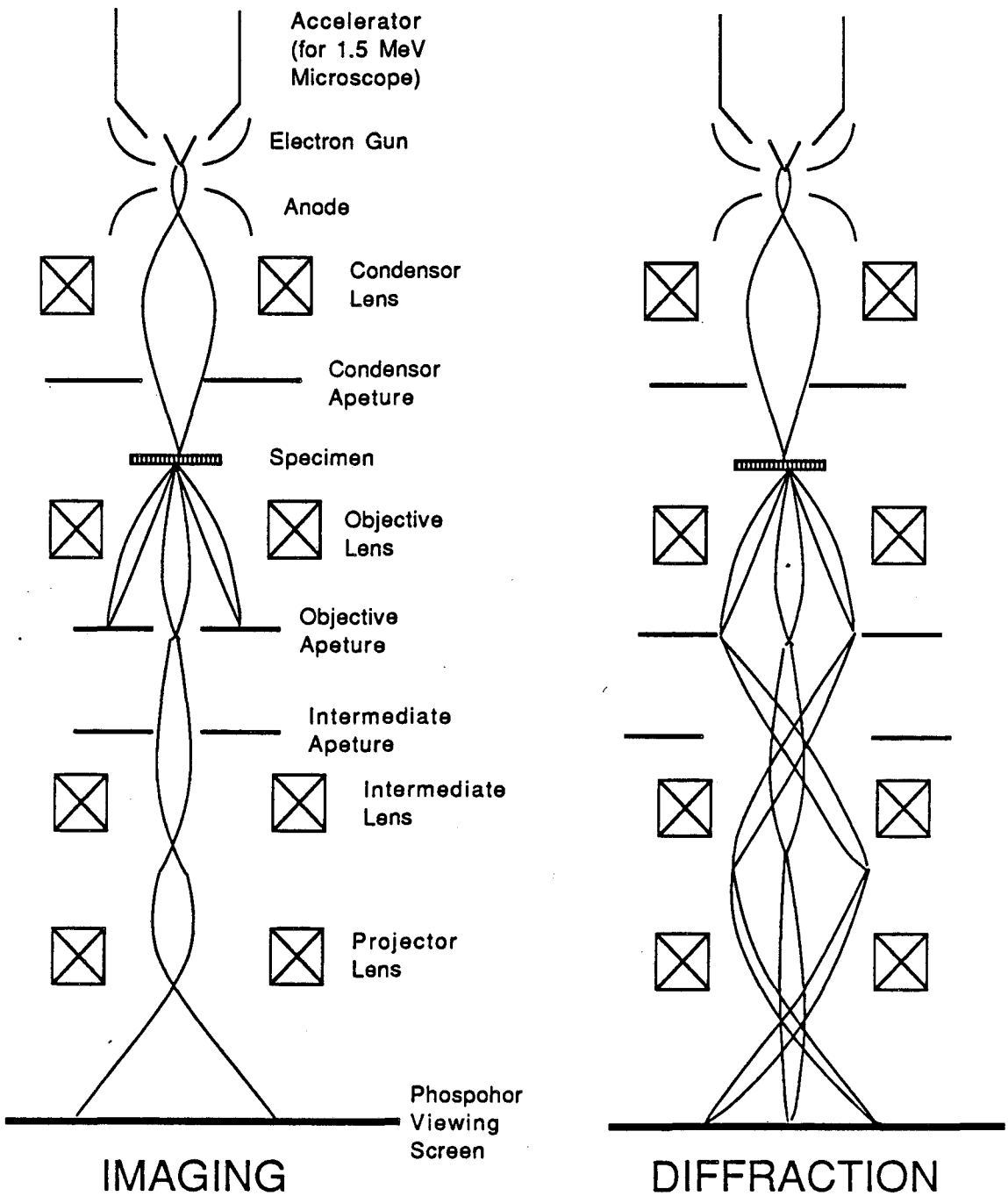

Figure B1. Ray diagrams illustrating the lenses and apertures of a Transmission Electron Microscope.

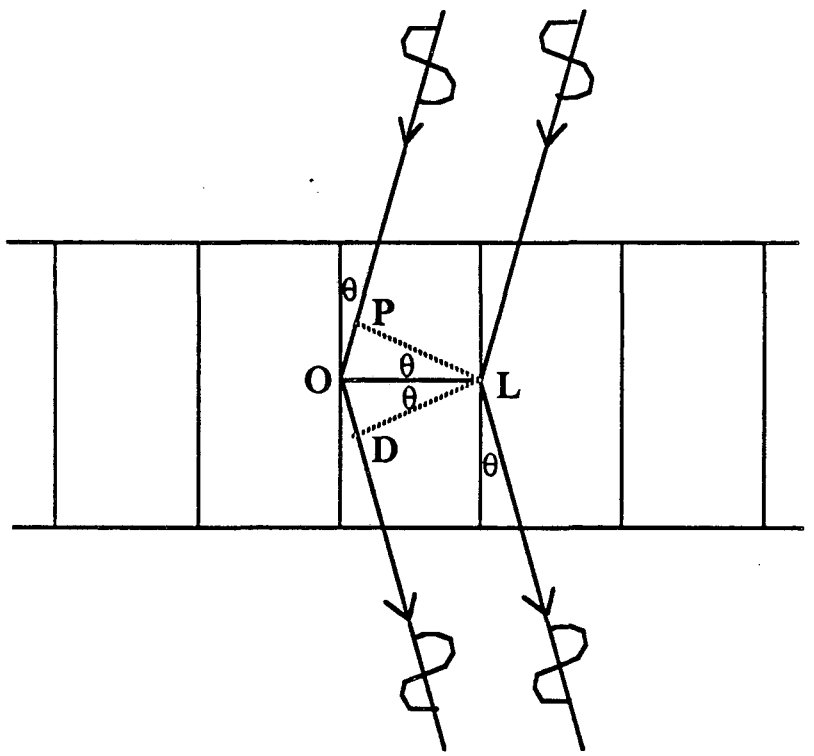

$$PO = OD = OL \sin\Theta$$

$$PO + OD = n\,\lambda$$

$$\boxed{n\,\lambda = 2d\,\sin\Theta}$$

Figure B2 Braggs Law in TEM.

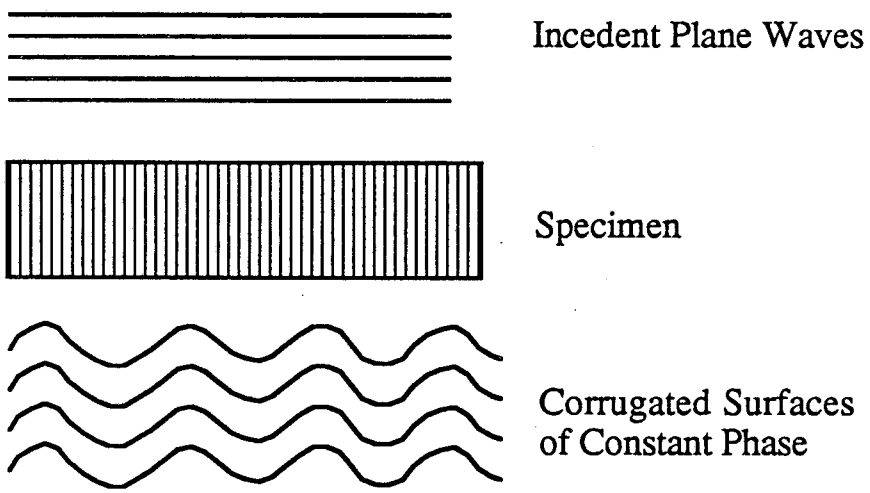

Figure B3 Schematic diagram illustrating phase change of electrons exiting from the bottom of the specimen that allows for lattice imaging.

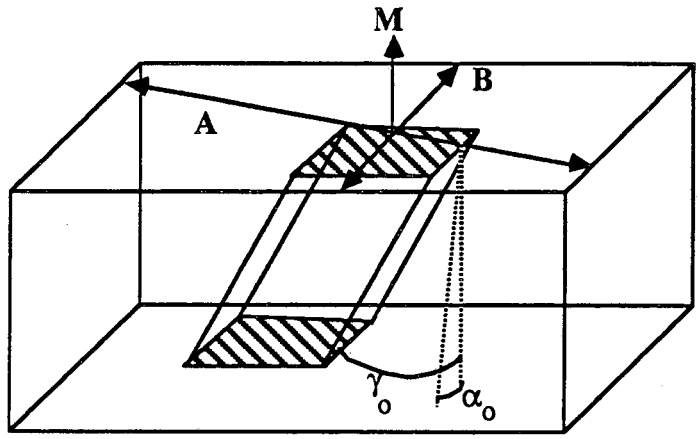

A - Apparent growth direction

B - 90° from **A** in growth direction plane

γ_o - rotated around **B**

α_o - rotated around **A**

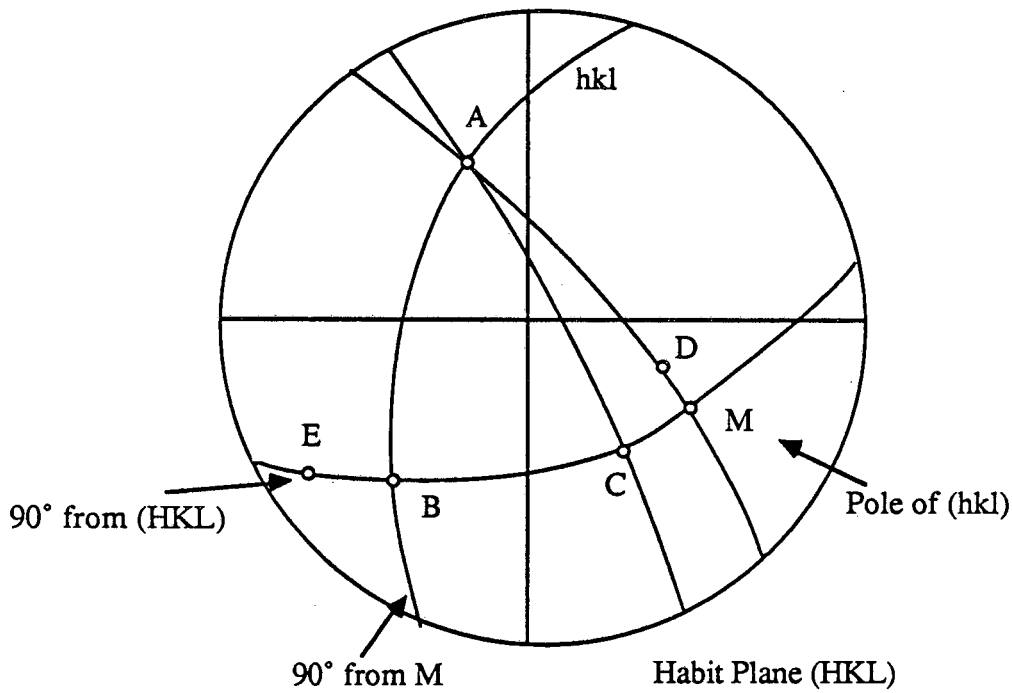

Figure B4 Illustration of method used to determine the habit plane.

APPENDIX REFERENCES

1A. J. Bagrowski, S. G. Konowski, G. D. Spencer; "Intercinnection of monolithic integrated circuits through use of advanced materials and techniques", IEEE Trans Parts, Hybrids, and Packaging, PHP-2, (1966) p. 90.

2A. L. S. Goldmann; "Geometric optimization of controlled collapse interconnections", IBM J. Res. and Dev., 13 (1969) p. 251.

3A. J. Lyman; "Surface mounting alters the PC-board scene", Electronics, Feb. 9 (1984) p. 113.

4A. P. M. Hall; "Solder attachment of leadless ceramic chip carriers", Solid State Technology, March (1983), p. 103.

5A. Guidelines for Surface Mounting and Interconnecting Chip Carriers, Institute for Interconnecting and Packaging Electronic Circuits, 341 Chuch St., Evanston IL 60203 (1983).

6A. D. Brown, M. Freedman; "U. S. surface mounting makes its move", Electronic Packagaing and Production, 25, 2 (1983) p. 208.

7A. A. J. Blodgett; "Microelectronic Packaging", Scientific American, (1985) p. 86.

1B. G. Thomas, M.J. Goringe, "Transmission Electron Microscopy of Materials," John Wiley and Sons, New York (1979), p. 315.

2B. O. J. Scherzer, J. Appl. Phys. 20, 20 (1949).

3B. K. W. Andrews, D. J. Dyson, S. R. Keown; Interpretation of Electron Diffraction Patterns, Plenum Press, New York (1967) pp. 41-45.

LAWRENCE BERKELEY LABORATORY
TECHNICAL INFORMATION DEPARTMENT
UNIVERSITY OF CALIFORNIA
BERKELEY, CALIFORNIA 94720